University of Southampton

Faculty of Engineering and Physical Sciences
School of Physics and Astronomy
Astronomy Group

The Physical Origin of Dusty Winds in Highly Accreting AGN

by

Farin Drewes

ORCID iD: 0000-0001-6039-1988

A thesis for the degree of
Doctor of Philosophy

October 2025

University of Southampton

Abstract

Faculty of Engineering and Physical Sciences
School of Physics and Astronomy

Doctor of Philosophy

The Physical Origin of Dusty Winds in Highly Accreting AGN

by Farin Drewes

Active galactic nuclei (AGN), super-massive and accreting black holes at the centres of galaxies, are some of the most luminous objects in the Universe. Their internal structure is complex and driven by fundamental AGN parameters, such as the accretion rate. However, due to the compact size of AGN, spatially resolved studies of these structures are difficult. In this work, I investigate specifically the physical origins of dusty winds in highly accreting AGN using high angular resolution techniques to resolve the central parsec. I explore the behaviour of the dusty winds, the wind launching region, and the accretion disk, which drives the dusty winds. To observe the dust, I used optical interferometry, and especially the mid-infrared instrument MATISSE, for which I developed a new data reduction method for faint objects. I published the first *LM*-band measurements for Type 1 AGN: the highly accreting objects I Zw 1 and H0557-385, in which the wind launching region has been resolved. For the super-Eddington AGN I Zw 1, I also resolved the accretion disk using reverberation mapping with a sub-daily cadence in seven photometric bands (*uBgVriz*$_s$). Combining my results with archival observations, I constructed the directly measured size-wavelength relation between $3 - 13\,\mu\mathrm{m}$ for H0557-385 and $3000\,\text{Å} - 13\,\mu\mathrm{m}$ for I Zw 1. These relations show several things about highly accreting AGN: firstly, the accretion rate appears to increase the opening angle of the dusty wind such that it is in a preferentially equatorially orientated direction. Secondly, we are directly observing the dusty wind launching region and an inner puffed-up dusty disk for the first time. The accretion disk, however, does not seem to vary noticeably from those in sub-Eddington AGN. The accretion rate does drive AGN structure, particularly in the dusty torus, but the effects vary across the different components studied here. In the future, lower sensitivity limits of optical interferometric instruments will increase the sample size of observable objects considerably and allow for a deeper understanding of internal AGN structure evolution with AGN parameters.

Contents

List of Figures

List of Tables

Declaration of Authorship

I declare that this thesis and the work presented in it is my own and has been generated by me as the result of my own original research.

I confirm that:

1. This work was done wholly or mainly while in candidature for a research degree at this University;
2. Where any part of this thesis has previously been submitted for a degree or any other qualification at this University or any other institution, this has been clearly stated;
3. Where I have consulted the published work of others, this is always clearly attributed;
4. Where I have quoted from the work of others, the source is always given. With the exception of such quotations, this thesis is entirely my own work;
5. I have acknowledged all main sources of help;
6. Where the thesis is based on work done by myself jointly with others, I have made clear exactly what was done by others and what I have contributed myself;
7. Parts of this work have been published as: Drewes, F., Leftley, J. H., Hönig, S. F., Tristram, K. R. W., & Kishimoto, M. 2025, MNRAS, 537, 1369, doi: 10.1093/mnras/staf110

Signed:..... Date:.....

Acknowledgements

> He was determined to discover the underlying logic behind the universe. Which was going to be hard, because there wasn't one.
>
> *Mort*
> Terry Pratchett

An extra special thank you goes to Seb Hönig who supervised me for four long years. Your guidance, knowledge, expertise, and support are incredibly important to me and it is always nice to have a Schnack with you. Sometimes I even heard you when you praised me (although I still pertain it happens less than you think it does).

A special thank you goes to Konrad Tristram who supervised me for one year in Chile, from whom I learned all of the German physics words I never needed to know before. Thank you for giving me the opportunity to work in Chile and to do a project on Paranal, where I had an amazing time.

Another special thank you goes to James Leftley, whom I took inspiration from as to how a good PhD journey should look like. There is an endless number of things you did for me: help with optical interferometry, MATISSE data reduction, and observing proposals; advice on moving to Chile; hanging out at conferences; reading this thesis; the blue pea flower tea; etc.

Thank you to Juan Hernández Santisteban and Roberta Vieliute with whom I collaborated on Chapter 4. Thank you to Juan for being willing to collaborate, lending your expertise, providing the data, and hosting me in St. Andrews for two weeks. Thank you to Roberta for providing the calibration and Fourier analysis code, and for showing me around St. Andrews.

Thank you to my parents who gave me limitless support and thank you to my brother who accompanies me to the front of the crowd at concerts even though he doesn't like it.

Thank you to Rowan and Eloïse who are amazing friends. I love you both so much.

To Mama, Papa, and Jan.

Definitions and Abbreviations

AGN	Active galactic nucleus/nuclei
AO	Adaptive optics
BCD	Beam commuting device
BLR	Broad-line region
CDF	Cumulative distribution function
ISM	Interstellar medium
MATISSE	Multi AperTure mid-Infrared SpectroScopic Experiment
NLR	Narrow-line region
NLS1	Narrow-Line Seyfert 1
OI	Optical interferometry
OPD	Optical path difference
PSD	Power spectral density
RM	Reverberation mapping
SED	Spectral energy distribution
SMBH	Supermassive black hole
VLT	Very Large Telescope
VLTI	Very Large Telescope Interferometer

Chapter 1

Introduction

> [W]here actual evidence had been a bit sparse he had, in the best traditions of the keen ethnic historian, inferred from revealed self-evident wisdom* and extrapolated from associated sources**
> *Made it up.
> **Had read a lot of stuff that other people had made up, too.
>
> *Lord and Ladies*
> Terry Pratchett

1.1 Active Galactic Nuclei

Active galactic nuclei (AGN) are luminous sources at the centre of galaxies with time-variable emission. They are highly luminous across their entire spectral energy distribution (SED) which covers X-ray/gamma ray to radio. Their emission varies on the order of seconds to years and decades. This variability is again seen throughout their SED. Historically, AGN with a visible host galaxy were known as *Seyferts*, and ones without as *quasars*. Currently, quasar is usually used for highly luminous objects ($\gtrsim 10^{45-46}\,\mathrm{erg\,s^{-1}}$), independent of the visibility of the host galaxy (Hickox & Alexander, 2018). However, these terms are also used interchangeably for the same objects, especially one of those studied here. Therefore, we will only be using the general term *AGN*.

The most fundamental observational characteristic of AGN is their enormous power output from a spatially very small, nuclear region – within a few parsecs. As of now, we have been almost entirely unable to resolve the central engine using single-dish and interferometric techniques. The only images successfully resolving this region so far have been taken with the Event Horizon Telescope at millimetre wavelengths, using the entire Earth as a baseline (Event Horizon Telescope

Collaboration et al., 2019, 2022). These results, showing a black hole's 'shadow', support the assumption based on both the luminosity and the spatial restrictions that these objects harbour a supermassive black hole (SMBH) at their centre (Salpeter, 1964; Lynden-Bell, 1969). For instance, the amount of stars needed to generate the same luminosity cannot feasibly fit in the space. The energy that is released in these cases is the potential gravitational energy partially converted into radiation as material falls down the gravitational potential well of the central black hole.

1.1.1 Fundamental AGN properties

The fundamental properties by which AGN are characterised are based on the central black hole and the AGN luminosity. According to the no-hair theorem, a black hole has only three observable properties: mass, angular momentum (usually parametrised as the spin), and electric charge (Israel, 1967, 1968; Carter, 1971). The most important of these for AGN is the black hole mass, $M_{\rm BH}$. In AGN, this mass is usually $\sim 10^6 - 10^9 \mathrm{M}_\odot$, although masses of $10^5 \mathrm{M}_\odot$ and $10^{10} \mathrm{M}_\odot$ have also been measured. More generally, every large galaxy is thought to host a SMBH at its centre, although usually quiescent. For example, the non-active Milky Way has a SMBH with mass $4.30 \times 10^6 \mathrm{M}_\odot$ (GRAVITY Collaboration et al., 2022). Further, black holes in AGN are generally measured to be rapidly spinning (with spins close to 1, Reynolds, 2021). However, this has only been done for a sample size of few tens of AGN and measurements are often poorly constrained. The SMBHs are assumed to have an overall neutral charge.

AGN are further characterised by their luminosity: their *bolometric luminosity* $L_{\rm bol}$ and their *Eddington luminosity* $L_{\rm Edd}$. The bolometric luminosity is the integrated power output over the entire SED. The Eddington luminosity describes the theoretical limit at which the accretion flow is stable. It is kept from collapse through the outwards radiation pressure balancing with the inwards acting gravitational force. In the simple case of a completely ionized gas and under the assumption of spherical symmetry and non-relativistic motion, the radiation pressure experienced by the electrons is

$$P_{\rm rad} = \frac{L}{4\pi r^2 c} \tag{1.1}$$

where L is the luminosity and r is the distance from the centre (the force on protons is negligible). The outwards acting radiation force on an electron is then

$$F_{\rm rad} = \frac{\sigma_e L}{4\pi r^2 c} \tag{1.2}$$

where σ_e is the Thompson scattering cross-section, the interaction cross-section between an electron and a photon. The inward gravitational force experienced by the protons and electrons, with masses m_p and m_e respectively, from a central mass of M is

$$F_{\rm grav} = \frac{GM(m_p + m_e)}{r^2} \simeq \frac{GMm_p}{r^2} \tag{1.3}$$

since $m_p >> m_e$. In the limit of these forces balancing

$$F_{\rm rad} = F_{\rm grav} \tag{1.4}$$

$$\frac{L\sigma_e}{4\pi r^2 c} = \frac{GMm_p}{r^2}. \tag{1.5}$$

Solving for L gives the Eddington luminosity as

$$L_{\rm Edd} = \frac{4\pi G M_{\rm BH} m_p c}{\sigma_e} \simeq 1.26 \times 10^{38} \frac{M_{\rm BH}}{\rm M_\odot}\,{\rm erg\,s^{-1}}. \tag{1.6}$$

While we here only consider a spherical geometry, this limit is applicable to most other geometries (including disks) within a factor on the order of unity. As AGN are powered by the release of energy through accretion, the luminosity of the AGN is based on its accretion rate. The relation between the luminosity and the mass accretion rate $\dot{M}$ is given by

$$L_{\rm bol} = \eta \dot{M} c^2 \tag{1.7}$$

where η is the radiative efficiency. Notably, the radiative efficiency is found to be $\sim 0.01 - 0.1$ for accretion, making this the most efficient mass-energy conversion process in the Universe (e.g. compare with $\eta = 0.007$ for hydrogen burning in stars). The spin of the black hole affects the efficiency; as the spin changes from retrograde to prograde the efficiency increases. A maximally prograde spinning black hole can reach an efficiency of $\eta \sim 0.4$. We further define the dimensionless accretion rate $\dot{\mathscr{M}}$, which is the mass accretion rate scaled by the Eddington luminosity such that

$$\dot{\mathscr{M}} = \frac{\dot{M}c^2}{L_{\rm Edd}} = \frac{\dot{m}_E}{\eta} \tag{1.8}$$

where $\dot{m}_E$ is the *Eddington ratio* or *Eddington (accretion) rate*. The Eddington ratio is defined as

$$\dot{m}_E = L_{\rm bol}/L_{\rm Edd} \tag{1.9}$$

and tells us at what fraction of the Eddington luminosity the AGN is emitting, or the relative strength of the AGN. It is viable for the AGN luminosity to surpass the Eddington limit in that the incoming mass accretion rate exceeds the Eddington limit, and therefore exceeding the Eddington luminosity. This is compensated for by keeping the material from getting close to the black hole and therefore not radiating the full accretion energy, i.e. through outflows, or severely limiting the radiation efficiency close to the black hole (e.g. in the slim disk scenario discussed in Section 1.2.1). The Eddington ratio is one of the most basic classifications used, differentiating AGN based on their relative accretion power, usually under the assumption that different accretion physics apply in the different categories. AGN with $\dot{m}_E < 1$ are sub-Eddington, while super-Eddington denotes $\dot{m}_E \gtrsim 1$. Most AGN have $\dot{m}_E \sim 0.05 - 0.2$. Accordingly, AGN with $\dot{m}_E \gtrsim 0.3$ are called high Eddington. It has arguably been shown that above $\dot{m}_E \sim 0.1 - 0.3$, the physics underlying the disk emission change (Temple et al., 2023). Similarly, for $\dot{m}_E \lesssim 0.01$ observations have shown that the accretion disk may collapse through transition into an inefficient plasma (Hagen et al., 2024b).

1.1.2 The AGN structure

The internal structure of AGN contains different components, all contributing to its complex multi-wavelength emission. This structure is illustrated in Fig. 1.1 and an example of the broadband SED is shown in Fig. 1.2; the individual components will be briefly explored in this section.

The Central Engine. The SMBH and the accretion flow form the central engine which powers the AGN. The accretion flow is in the form of an accretion disk, which is responsible for the bulk of the AGN emission. This emission is usually modelled as a sum of black bodies where each radial ring emits as a black body and whose temperatures are a function of distance from the black hole (the resulting emission spectrum is shown in Fig. 1.2). The disk radiation is often called the 'big blue bump' as it peaks in the far to extreme UV (FUV – EUV) (Shakura & Sunyaev, 1973). As this spectral window is entirely absorbed by neutral hydrogen in the intergalactic medium for local AGN, we are unable to directly observe the majority of the accretion disk emission. This complicates the characterisation of the disk as we cannot see the peak position which is controlled by the black hole mass and accretion rate. Rather, we have to infer the shape of the disk emission from longer wavelength data, which lies on the tail, or emission lines tracing the FUV/EUV. At higher redshifts and for lower luminosities, the peak of the disk emission shifts to longer wavelengths, and gets easier to observe (of course highly conditional on line-of-sight absorption for higher redshift objects). In a standard disk, the temperature profile of the disk is inversely dependent on the black hole mass, while directly dependant on the accretion rate (see Eq. 1.10, Shakura & Sunyaev, 1973). This implies that as the black hole mass increases or the accretion rate decreases, the emission peak will move towards longer wavelengths. The accretion disk occupies spatial radii from $\sim R_{\rm ISCO}$ (innermost stable circular orbit) to a few $10^4 R_g$ (gravitational radii, $R_g = GM/c^2$). The stochastic variability of AGN is very noticeable in the accretion disk continuum.

The Hot X-ray Corona. AGN emit strongly in the X-ray, about 10% of their bolometric luminosity. This emission is characterised by a broad Compton hump which peaks at 30 keV and often the presence of the relativistically-broadened $\rm FeK\alpha$ line at 6.4 keV (Fig. 1.2, Ricci et al., 2017a). This emission is thought to come from a hot plasma close to the central black hole at a few R_g (Uttley et al., 2014; Brandt & Alexander, 2015). The hot plasma is made up of relativistic electrons which upscatter UV and optical photons from the disk through the inverse Compton process (also called 'Comptonization'). Variability in the X-rays is characterised by its rapid nature on the order of seconds to days, including flaring (e.g. Uttley et al., 2014; Edelson et al., 2015, 2017; Wilkins et al., 2021; Kara et al., 2023). Slower spectral changes in which absorption increases/decreases also occur, usually explained by clouds moving into the line of sight within the AGN (e.g. Coffey et al., 2014; Partington et al., 2023). These events reflect evolution in the internal absorption environment on sub-year timescales and that AGN are not just static phenomena, but rapidly changing on human timescales. The X-ray emission is also very useful to probe the relativistic environments of the central black hole, for example through the (partly) gravitationally-redshifted $\rm FeK\alpha$ line (Uttley et al., 2014; Wilkins et al., 2020). In addition, reflected

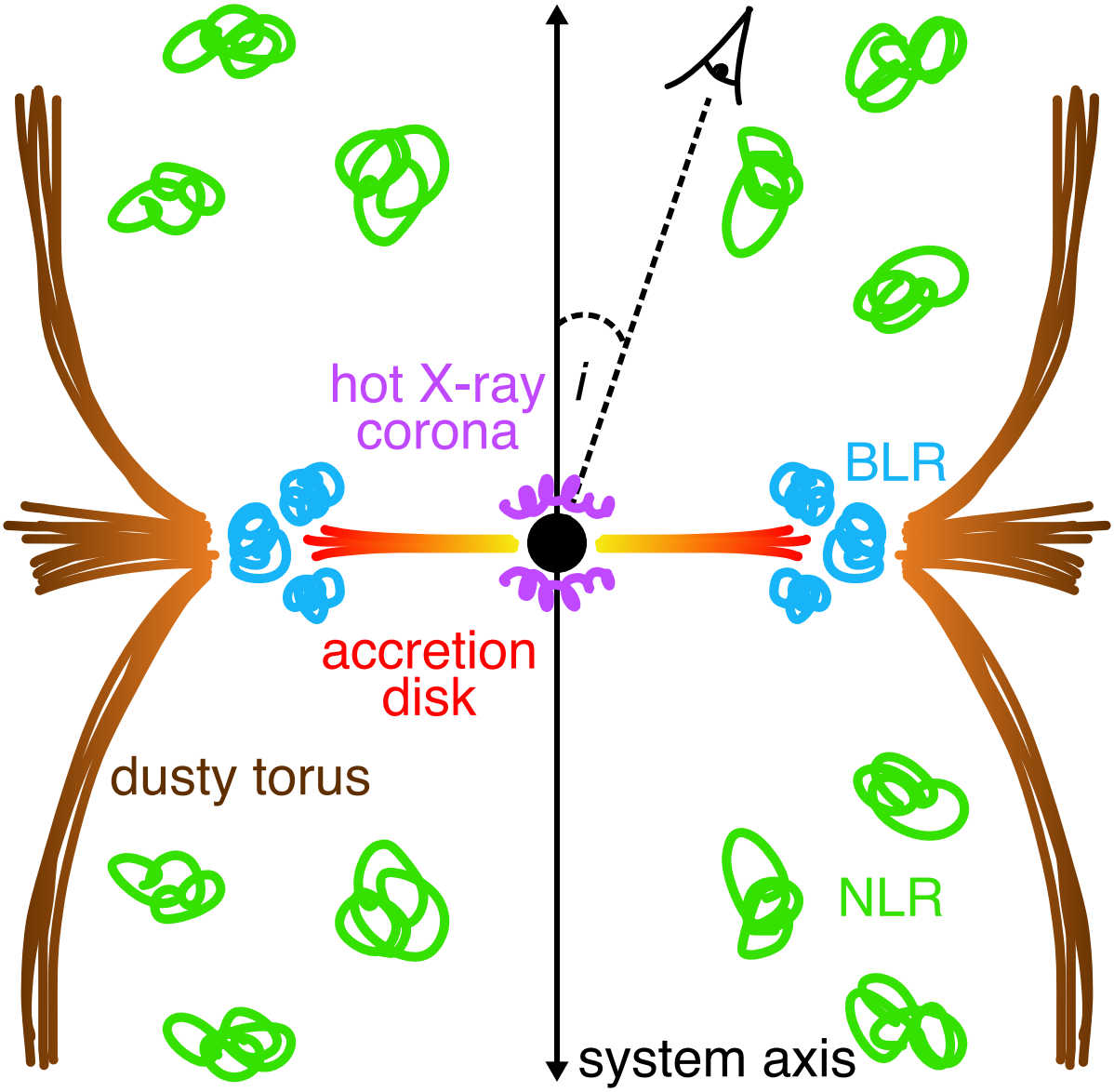

FIGURE 1.1: An illustration of the internal structure of an AGN (not to scale). The centre is occupied by the central engine: a supermassive black hole and the accretion disk (yellow-orange-red). In the close environment, a hot electron plasma upscatters accretion disk emission in the hot X-ray corona (purple). Further out in the equatorial plane, high velocity and high density gas clouds are located in the broad-line region (BLR, blue). In the polar regions, gas is contained in lower density and velocity clouds in the narrow-line region (NLR, green). Dust in the structure of an equatorial disk and a polar hollow outflow cone provides obscuration as the dusty 'torus' (orange-brown). The definition of the inclination i of the AGN is also illustrated: this is the viewing angle as measured from the system axis such that a face-on view has an inclination of 0°, and an edge-on view an inclination of 90°.

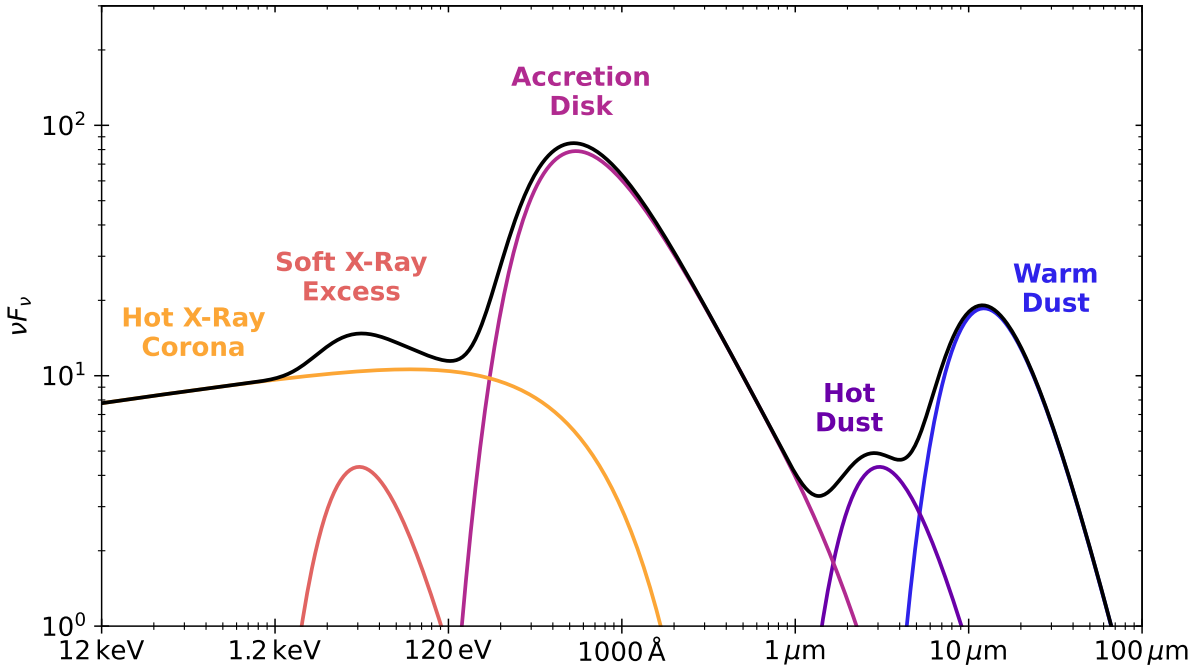

FIGURE 1.2: An example of an AGN SED from the X-ray to the infrared, including all the major broadband emission components. The flux normalisation is arbitrary and the relative component strengths resemble more that of a Type 1; any individual AGN can show different relative component strengths. In the X-ray, the hot X-ray corona emission is described by a power law, and we approximate the soft X-ray excess ($\sim 0.1 - 2\,\mathrm{keV}$) with a black body spectrum. The majority of power in AGN comes from the accretion disk, which peaks in the extreme to far UV. There is a minimum in the SED around $\sim 1\,\mu\mathrm{m}$, at which point emission from the hot dust ($1000 - 1500\,\mathrm{K}$) and the warm dust ($200 - 400\,\mathrm{K}$), dominates in the infrared.

and bent light signals from behind the black hole have been detected (Wilkins et al., 2021). The behaviour of the X-ray signals clearly supports the hypothesis of a black hole at the centres of AGN.

The Soft X-ray Excess. A common feature in AGN X-ray spectra is the soft X-ray excess (Gierliński & Done, 2004; Porquet et al., 2004; Gliozzi & Williams, 2020). When the disk and hot X-ray corona profiles are extrapolated into the $0.1 - 2\,\mathrm{keV}$ region, there is a marked observed excess above the expected emission, as shown in Fig. 1.2. The properties of this feature are remarkably constant. The temperature is usually $0.1 - 0.3\,\mathrm{keV}$ and the strength is uncorrelated with both the primary X-ray spectrum strength and the black hole mass. However, it does appear to be positively correlated with the Eddington ratio. Current interpretations favour a warm, optically thick inverse Compton scenario where electrons upscatter disk photons. This is referred to as the warm corona. The soft X-ray emission may come from the inner disk, puffed-up by radiation from the hot X-ray corona (Gardner & Done, 2017). Even though it is an ongoing struggle to recreate the soft X-ray excess from first principles in simulations, it appears to be a crucial component to describe the behaviour and interaction of the X-ray and optical emission in AGN.

The Broad-Line Region. The broad-line region (BLR) is a region of low filling factor ($\sim 10^{-2}$) filamentary and clumpy gas, at $10^{-3} - 10^{-2}$ pc from the SMBH. This primarily manifests in permitted line emission from the UV to the near-infrared (Netzer, 1990). The term 'broad-line'

refers to the high velocity of this gas seen through the Doppler broadened line widths with velocities of $500 - 10000\,\mathrm{km\,s^{-1}}$ (typically $\sim 5000\,\mathrm{km\,s^{-1}}$). The gas is also highly ionized by photoionization from the central engine. The strongest lines are the hydrogen Balmer lines $\mathrm{H}\alpha$, $\mathrm{H}\beta$, and $\mathrm{H}\gamma$, as well as $\mathrm{Ly}\alpha$. Other common high ionization lines such as C IV, He II, and Mg II are also usually observed. In contrast, forbidden and semi-forbidden lines with broad-line profiles are not observed (with exception of C III]). This is because the BLR clumps/clouds have a high density – $\sim 10^{11}\,\mathrm{cm^{-3}}$ – and high temperature – $10000\,\mathrm{K}$ (Ferland et al., 1992). Therefore, forbidden and semi-forbidden lines are collisionally suppressed. Of course, the BLR also emits continuum, through hydrogen free-free and bound-free processes, often referred to as the diffuse continuum (DC, Korista & Goad, 2001). Most notable is the 'small blue bump' around $3650\,\text{Å}$. This is the Balmer jump (or edge), bound-free emission reaching a peak towards the limit of the Balmer series. A similar (but weaker) feature is present towards the limit of the Paschen series at $8210\,\text{Å}$, called the Paschen jump. Like the disk continuum, BLR emission displays variability. In fact, line emission varies in response to the disk continuum; they are highly correlated and shifted in time, with the continuum leading the lines. In the simplified picture, the disk photons are reprocessed in the BLR after a characteristic time – the light travel time from the disk to the BLR. Therefore, by measuring the lag between the continuum and the line light curves, we can determine distances inside the AGN. This technique is called reverberation or echo mapping (RM) (Peterson et al., 2004). Using this technique, it has been shown that the BLR has a radial (ionization) structure. Higher ionization lines such as C IV and He II are found at smaller radii than lower ionization lines, e.g. Mg II (Clavel et al., 1991; Bentz et al., 2021). Velocity resolved reverberation mapping shows that the BLR is mainly in rotation and virially bound, with additional outflows/infall, and preferentially in the shape of a thick disk (Grier et al., 2013, 2017; Bentz et al., 2021, 2023). High angular resolution studies using optical interferometry (OI) corroborate these results (GRAVITY Collaboration et al., 2018, 2020a, 2021a). The BLR radius as measured using emission lines goes approximately as the square root of the luminosity – this is called the size-luminosity relation ($R \propto L^{1/2}$) (e.g. Bentz et al., 2013). The ionization energy, and therefore the ionization temperature, for a particular line is fixed. As $T^4 \propto L/R^2$ according to the Stefan-Boltzmann law, the radius at which a line will occur is proportional to the luminosity. Nevertheless, there are indications that at very high luminosities, this relation flattens (GRAVITY Collaboration et al., 2024).

The fact that the BLR is primarily in virial motion allows us to use RM and optical interferometry to calculate the mass of the black hole, by measuring the radius and velocity of the emission line which then gives the enclosed mass. Masses of black holes have been directly measured for a number of nearby AGN (Peterson et al., 2004; Bentz & Katz, 2015; GRAVITY Collaboration et al., 2018, 2021b, 2024). These masses are used to calibrate alternate, single epoch methods to measure black hole mass. Single epoch modes rely on the size-luminosity relation to derive the radius, and are primarily based on the $\mathrm{H}\beta$ velocity width and the luminosity at $5100\,\text{Å}$ (Kaspi et al., 2000; McLure & Jarvis, 2002; Woo & Urry, 2002). This is the pre-eminent way to determine black hole masses in AGN. One fundamental problem is that method of black hole mass calculation is only valid for the nearby Universe within a few hundred Mpc, as it is calibrated by nearby AGN. However, optical interferometry shows great promise to directly measure black hole masses, with

the first dynamical mass measurement of an AGN at $z = 2$ already achieved (Abuter et al., 2024; GRAVITY+ Collaboration et al., 2024).

The Narrow-Line Region. The narrow-line region is a region of lower density and velocity gas clouds, virially bound (Davies et al., 2020). This region extends far beyond the outer edges of the BLR and is dominated by photoionization from the central engine. These photoionized, spatially extended regions are arranged in a polar cone shape, which is called the 'ionization cone' (Pogge, 1988; Tadhunter & Tsvetanov, 1989; Wilson et al., 2000). This shape probably derives from anisotropy and collimation of the ionizing accretion disk radiation inside the AGN. These ionization cones are resolved by single dish telescopes and can extend from tens to hundreds of pc close to the AGN to reaching the host galaxy scales, which is called the extended NLR (ENLR) (Schmitt et al., 2003; Veilleux et al., 2003). The narrow line spectrum is populated by the same lines as the BLR spectrum, but far narrower with typical velocities of $200 - 900\,\mathrm{km\,s^{-1}}$. Due to its lower density, forbidden and semi-forbidden lines are not collisionally suppressed, and are strong throughout the spectrum (Ferland & Osterbrock, 1986). One of the most characteristic features is the [O III]$\lambda4959\lambda5007$ doublet, which is commonly used as a tracer of the NLR and warm outflows in AGN. Together with its large spatial extension, the NLR also covers a larger parameter range of density and temperature, which are radially stratified (Baskin & Laor, 2005; Bennert et al., 2006a,b). This is also indicated by a large range of lines with different creation conditions. Temperatures range from $10000 - 25000\,\mathrm{K}$, and electron densities from $10^2 - 10^4\,\mathrm{cm^{-3}}$, with high density clumps (Koski, 1978; Davies et al., 2020). As it is photoionized, the NLR also reprocess the continuum variability of the central engine. However, signals are washed out as a consequence of the large spatial scales and the longer reprocessing timescales due to low densities (Peterson et al., 2013; Barth & Bentz, 2016).

The Dusty 'Torus'. The dusty 'torus' refers to the dusty obscuring structure in AGN, tens of parsecs across. The inner-most, hottest part of this structure at $\sim 0.1\,\mathrm{pc}$ is the sublimation region and preferentially populated by large graphite grains (Kishimoto et al., 2007). The inner boundary is the sublimation radius, where graphite grains sublime at temperatures of $1500 - 2000\,\mathrm{K}$. The sublimation temperature defines the sublimation radius for a given luminosity through the Stefan-Boltzmann law, $T^4 \propto L/R^2$, and therefore the sublimation radius also follows the $R \propto L^{1/2}$ size-luminosity relation (GRAVITY Collaboration et al., 2020b, 2024). Thermal dust continuum emission dominates the infrared (IR) AGN SED. The hot dust in the sublimation region dominates the near-infrared luminosity while the larger structures are seen in the mid-infrared (see Fig. 1.2). In fact, mid-IR optical interferometry observations show that the parsec-scale mid-IR emission is dominated by a polar extended structure (Hönig et al., 2012, 2013; Burtscher et al., 2013; Tristram et al., 2014; López-Gonzaga et al., 2016; Leftley et al., 2018; Gámez Rosas et al., 2022; Isbell et al., 2022, 2025). The structure of the dusty 'torus', rather than being a torus, is made of two principal components (as illustrated in Fig. 1.1, Hönig, 2019). The first is a molecular equatorial dust disk. The second is a dusty wind blown off the disk and located in a hollow polar outflow cone, which may also contain the NLR. The equatorial dust continuum has also been detected at longer wavelengths and at larger scales: submillimetre observations show the existence of a dusty

molecular disk perpendicular to the system axis (Combes et al., 2019; Alonso-Herrero et al., 2021; García-Burillo et al., 2021). This radiates thermal continuum that dominates the $870\,\mu\mathrm{m}$ emission. These parts of the torus have larger sizes as they trace colder dust, with a mean size of tens of parsecs.

Unification of AGN. The dusty torus plays an important role in the observation of AGN. Depending on the angle from which the AGN is viewed, the torus will obscure the BLR and the central engine. In this work, the viewing angle is parametrised as the *inclination angle*, where an AGN at 0 degrees inclination is viewed face-on, and at 90 degrees from the side. AGN which are viewed at low inclinations where the BLR can be seen, are called *Type 1s*. In contrast, AGN which are viewed from the side at high inclinations do not show the BLR and are called *Type 2s*. Alternatively, these are known as Type 1/2 Seyferts, Seyfert 1s/2s, or Sy 1s/2s. Accordingly, UV/optical spectra of Type 1s show broad lines while those of Type 2s do not show broad lines. However, the broad-line region has been observed in Type 2s in polarised light[1] (Antonucci & Miller, 1985; Antonucci et al., 1994). Here, a scattering medium above the torus scatters the BLR emission into our line of sight. Inclination angles from observations of the NLR agree with the interpretation that Type 2s are highly inclined to our line of sight (Fischer et al., 2013). Type 1s are also further categorised into Narrow-Line Seyfert 1s (NLS1s) and Broad-Line Seyfert 1s (BLS1s), based on their emission line widths. NLS1s have $\mathrm{H}\beta$ (or $\mathrm{H}\alpha$) full widths at half maximum (FWHM) less than $2000\,\mathrm{km\,s^{-1}}$ (Jin et al., 2012). They also are defined to have [O III]$\lambda5007/\mathrm{H}\beta$ ratios less than 3. These observational properties appear to be due to underlying physical differences, namely that NLS1s have lower black hole masses and higher Eddington ratios (relative accretion rates) than BLS1s (Jin et al., 2012).

This concept of the 'torus' as an obscurer responsible for differences in Type 1 and 2 observational characteristics is a central component of AGN unification, or the unified model of AGN (Antonucci, 1993). The goal of AGN unification is to explain the large range of observed AGN characteristics with one underlying physics-based model. Essentially, variations in the least number of fundamental parameters should be able to explain differences in observed characteristics. Besides the inclination, these include the central black hole mass, accretion rate, and the presence and/or strength of radio emission and/or jets, as well as temporal evolution (Padovani & Urry, 1992; Urry & Padovani, 1995; Ricci et al., 2023). While we will not discuss radio properties of AGN in detail, AGN are generally divided into two classes: radio loud (RL) and radio quiet (RQ) objects (Kellermann et al., 1989). This is based on their relative level of radio emission, the ratio of optical-to-radio luminosity. Notably, RQ AGN do still emit in radio, but just at lower levels. In the unified model, these differences are related to the existence or size and strength of radio synchrotron jets that are launched in the hot X-ray corona. RL AGN have large and strong jets, up to Mpc sizes outside of the galaxy (e.g. Bridle & Perley, 1984; Bridle et al., 1994). However, RQ objects harbour jets too, albeit weaker and smaller, usually around tens of parsecs in size (e.g. Mundell et al., 2003; Yang

[1] Technically, these are actually 'hidden' Type 1s. There exists another interpretation of Type 1/2s where differences in emission line widths are not due to inclination and obscuration, but an intrinsic feature of the (unobscured) emission. These are 'true Type 2 Seyferts'. In this work we will generally remain in the classic Seyfert regime and use Type 1/2s to refer to unobscured and obscured AGN of the same intrinsic structure and processes.

et al., 2024). Radio jets are an important feedback mode through which the AGN influences its host galaxy (e.g. Nesvadba et al., 2010; Ogle et al., 2010).

1.2 The Accretion Disk

In this section we will further examine the accretion disks in AGN. We will look at theoretical bases of different disk models, the types of observational studies conducted, and the main results of these studies.

1.2.1 Theory

The accretion disk is the central component of the AGN, releasing the huge amounts of energy that characterise it. The accretion disk is a disk around the black hole in which gravitational potential energy is released at least partially through radiation. The annuli of this disk are in quasi-Keplerian motion around the black hole. To release energy, the material must move inward and angular momentum outward. This is thought to occur through the magnetorotational instability (MRI, Balbus & Hawley, 1991). Here, small scale magnetic fields of neighbouring annuli couple with each other, slowing gas in the annuli down. This is generally parametrised as viscosity (Shakura & Sunyaev, 1973).

Accretion disk models are generally distinguished between radiatively efficient and radiatively inefficient accretion flows. Radiatively efficient accretion applies to $0.01 < \dot{m}_E < 1$, while radiatively inefficient accretion occurs for $\dot{m}_E \lesssim 0.01$ and $\dot{m}_E \gtrsim 1$. The standard thin disk model is a radiatively efficient disk (Novikov & Thorne, 1973; Shakura & Sunyaev, 1973). In the super-Eddington regime, the disk is radiatively inefficient due to photon trapping and is described by the optically thick slim disk (Abramowicz et al., 1988). There are further solutions for the radiatively inefficient disk, such as the optically thin case with negligible radiation for $\dot{m}_E \lesssim 0.01$; however we focus on the two aforementioned models because these are those that apply to *active* galactic nuclei (Narayan & Yi, 1994, 1995). It is also expected that real disks will or can be in a mixture of these states or even beyond them.

The *thin disk* is the radiatively efficient, geometrically thin and optically thick disk which is likely the basis for most AGN as it applies to $0.01 < \dot{m}_E < 1$. This range of $\dot{m}_E$ represents the general luminous AGN population. Geometrically thin means that the scale height of the disk is generally very small ($H/R << 1$) and energy is released efficiently from the mid-plane of the disk, with $\eta \sim 0.1$. This disk has a radial temperature profile of

$$T(R) \propto \dot{m}_E^{1/4} M_{\rm BH}^{-1/4} R^{-3/4}. \tag{1.10}$$

Its emission is described by a sum of black bodies, each annulus emitting as a black body. As the peak of this emission is usually in the FUV-EUV, the tail of this emission can be found in the optical and goes as $F_\nu \propto \nu^{1/3}$.

The *slim disk* describes accretion in the super-Eddington regime; as the optically thick disk becomes hotter and radiative cooling becomes inefficient, the disk inflates to $H/R \gtrsim 1$ (Abramowicz et al., 1988). In the disk, matter and photons interact frequently and this keeps photons trapped in the accretion flow, which is referred to as 'photon trapping' (Ohsuga et al., 2002). Rather than the energy getting radiated from the mid-plane, the energy is transported inward through advection. Accordingly, some radiation is accreted into the black hole. These disks are therefore less radiatively efficient with $\eta \sim 0.01$. The temperature profile of this disk is given by

$$T(R) \propto R^{-1/2} \tag{1.11}$$

which is shallower than the thin disk (Wang & Zhou, 1999). Further, the accretion disk emission tail in the optical is expected to go as $F_\nu \propto \nu^{-1}$ (Wang et al., 1999). However, photon trapping only occurs when advective cooling dominates over diffusion of energy from the surface (Wang & Zhou, 1999). The radius of the disk within which photon trapping happens is called the photon trapping radius $R_{\rm tr}$ and is given by

$$R_{\rm tr}/R_g = 2.88\dot{\mathscr{M}} \tag{1.12}$$

and is valid for $\dot{\mathscr{M}} \lesssim 3000 M_{\rm BH}/10^7 {\rm M}_\odot$ (Du et al., 2016). The vast majority of super-Eddington AGN have dimensionless accretion rates of a few tens to a few hundreds, which indicates that they fulfil this condition. If we consider the highest dimensionless rate from the super-Eddington sample in Du et al. (2016), $\dot{\mathscr{M}} \simeq 1000$, this gives $R_{\rm tr} \simeq 2888 R_g$. According to Wien's Law, this radius will emit at 1900 Å, which is in the UV (see Eq. 7 in Cackett et al., 2020). This implies that even for super-Eddington AGN, optical emission will probably come from outside the slim disk regime.

1.2.2 Observational studies of accretion disks

There are two main methods used to study the properties of the accretion disk in AGN: SED fitting and disk reverberation mapping. In SED fitting, a broadband emission spectrum shape for the disk is assumed, extracting information such as black hole mass and accretion rate. Disk reverberation mapping uses the correlated continuum emission at different wavelengths to infer disk sizes and accordingly the radial temperature profile of the accretion disk.

1.2.2.1 Broadband SED fitting

SED fitting targets the big blue bump feature of the accretion disk. The peak of this feature is usually in the absorbed UV region (FUV-EUV), so often X-ray and near UV/optical measurements are used to anchor the fit. A thin disk has radiatively efficient thermal emission so every annulus may be estimated with a black body spectrum. Accordingly, the overall disk emission is a sum of

black bodies, with temperatures according to radial temperature profile of the disk (Fig. 1.2). For a thin disk, Eq. 1.10 shows that this is dependent on black hole mass and accretion rate, so these can be calculated from SED fitting. For internal energetic consistency, the X-ray and disk emission are often coupled energetically (e.g. Kubota & Done, 2018, 2019). To study the underlying accretion disk structure, the disk emission tail in the optical is often used. The thin disk emission tail in the optical is given by $F_\nu \propto \nu^{1/3}$. In contrast, the slim disk slope in the optical is $F_\nu \propto \nu^{-1}$. However, it can be quite difficult to determine the slope of the disk emission. First, there is additional non-variable emission from the AGN that might not originate from the disk. As such, when there is time series information, the RMS of the variable AGN flux is often used, which isolates the variable part of the emission. The variable part is assumed to be dominated by disk emission in the continuum and can therefore estimate the slope of the disk emission. We often also see a bluer-when-brighter effect in AGN emission. The AGN SED is bluer when its flux is higher, as the luminosity is directly dependant on temperature for a black body and therefore as the luminosity increases, the temperature increases. There is also contamination from the host galaxy which usually reddens the observed spectrum. Milky Way extinction is quite easily removed, but intrinsic extinction from both the host galaxy and internally in the AGN can be difficult to determine. This further reddens the spectrum and is present in the RMS flux as well. When the correct amount of intrinsic extinction is unknown, it can be more difficult to distinguish between a thin disk and a slim disk profile (e.g. Donnan et al., 2023). These considerations also apply to broadband SED fitting and must be taken into account. Lastly, we note that while a sum of black bodies provides a good fit to virtually all AGN, it is not the only working model. While the warm Compton emission is often only considered to apply to the soft X-ray excess, it also provides a good fit to the entire disk emission spectrum (e.g. Petrucci et al., 2013; Rogantini et al., 2022; Hagen et al., 2024a). In this model, an optically thick plasma covers the entire disk, equivalent to the warm corona likely responsible for the soft X-ray excess (Petrucci et al., 2018). The entire accretion power is released in the warm corona rather than in the mid-plane of the disk through reprocessing (Comptonization) in the warm corona. When applied to SED fitting, the intrinsic disk emission contribution does not exceed 20%, implying that the entire disk emission can be well reproduced by a warm corona and a passive disk (Petrucci et al., 2018). Notably, the statistical goodness-of-fit does not say much about the 'correctness' of the underlying physics and structure.

1.2.2.2 Reverberation mapping

Disk reverberation mapping is an experiment nominally designed to map the radial temperature profile of the accretion disk. This experiment assumes that the continuum emission is overwhelmingly dominated by disk emission. The underlying geometrical assumption is the 'lamppost' model as illustrated in Fig. 1.3 (Cackett et al., 2007; Fausnaugh et al., 2016). In this model, the hot X-ray corona is situated vertically above the disk. Light is emitted by the disk, goes to the X-ray corona, and is upscattered there. The hot X-ray flux then emitted is variable[2] and shines back down on the disk. In the disk, it is absorbed and re-emitted at longer wavelengths. The

[2]The source of this variability? Don't worry.

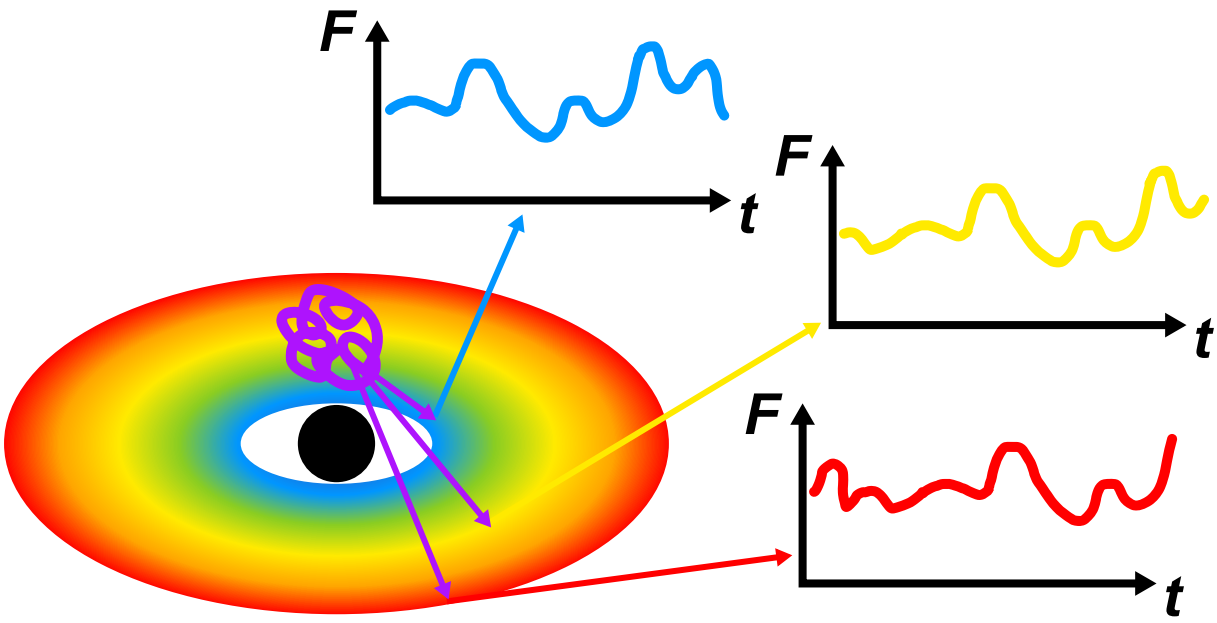

FIGURE 1.3: An illustration of the underlying concept of disk reverberation mapping, including the lamppost model. The hot X-ray corona – the driving light curve – shines on an accretion disk with a radial temperature profile. This light is processed in the disk and re-emitted. The resulting light curves are shifted in time depending on the radii of the accretion disk they were emitted, and therefore their wavelength.

energy of this re-emitted flux is determined by the radius at which it impinges and is re-emitted, as the temperature profile is radially dependant (Eq. 1.10 and 1.11). Flux from further inwards in the disk will be at shorter wavelengths than from further out. The variability of the X-ray flux – the driving light curve – is imprinted on the disk emission, but with a characteristic lag τ. This lag is the time difference between the emission of the driving light curve and the emission of the re-emitted light curve. This lag exists because the light must travel a certain distance from the hot X-ray corona to the disk, approximately the radius of the re-emission annulus[3]. Accordingly, flux at longer wavelengths from larger radii will have longer lags than at shorter wavelengths. The slope of this lag-wavelength relation $\tau(\lambda)$ is directly related to the radial temperature profile of the disk. In the case of a thin disk, the radial temperature profile of the disk is given by Eq. 1.10. The radial temperature profile of the X-ray irradiation goes as

$$T(R) \propto (L_X H_X)^{1/4} R^{-3/4} \tag{1.13}$$

where L_X is the X-ray luminosity and H_X is the height of the hot X-ray corona (Cackett et al., 2007). Both X-ray illumination and intrinsic disk emission give a radial temperature profile $\propto R^{-3/4}$. For black body radiation, using Wien's Law given by

$$T = \frac{hc}{k\lambda X}, \tag{1.14}$$

[3]The height of the hot X-ray corona (a few to tens of R_g) is negligible compared to the radii probed in disk reverberation mapping (thousands to tens of thousands of R_g).

where all constants have their usual meaning, we can convert the temperature to the peak emission wavelength. X is the factor that controls this conversion, based on how the temperature relates to λ in detail. Usually, $X = 2.49$ is used, which considers the flux-weighted mean radius (Fausnaugh et al., 2016). The distance R that the light travels during the lag time τ is simply $R = c\tau$. Combining these gives the standard thin disk lag-wavelength relation $\tau(\lambda) \propto \lambda^{4/3}$. For fitting purposes, this is parametrised as

$$\tau(\lambda) = \tau_0 \left[\left(\frac{\lambda}{\lambda_0} \right)^{\beta} - 1 \right] \tag{1.15}$$

where λ_0 is the wavelength of the reference light curve, the light curve that all lags are calculated with respect to, τ_0 is the normalisation factor, and $\beta = 4/3$ for a thin disk. For a slim disk $\beta = 2$, derived from the temperature profile in Eq. 1.11 (Wang & Zhou, 1999). The normalisation τ_0 holds crucial information in this experiment, and its analytic expression is given by

$$\tau_0 = \frac{1}{c^3} \left[\frac{k\lambda_0 X}{h} \right]^{4/3} \left[\left(\frac{G M_{\rm BH} L_{\rm Edd}}{8\pi\sigma\eta} \right) (3+\kappa) \dot{m}_E \right]^{1/3} \tag{1.16}$$

where all constants have their usual meaning and κ is the ratio of heating from X-ray irradiation to internal disk viscous heating, usually $\kappa = 1$ (Fausnaugh et al., 2016). τ_0 is usually on the order of light-days and is often referred to as the *disk size* at λ_0. It can also be used to infer the Eddington ratio. In this experiment, τ_0 is estimated from fitting the lag-wavelength spectrum and calculated from known quantities according to Eq. 1.16, which is the expected disk size at λ_0.

To perform this experiment, high cadence light curves spanning a reasonably large wavelength range are required. Disk lags are on the order of days, so a sub-day cadence is needed. As this experiment tests the continuum emission of the disk, usually photometric measurements are used. These are observationally less expensive and cover a larger wavelength range than repeated spectroscopic observations. However, broadband filters also contain both continuum emission from the disk and BLR and line emission from the BLR, which creates a mixture of reverberation signals and can impact measurements of distances within the AGN. Large campaigns obtain simultaneous observations in X-ray, UV, and optical to test the correlation between the nominal X-ray driving light curve and the disk emission in addition to mapping the disk (e.g. Fausnaugh et al., 2016; Lewin et al., 2024). Smaller campaigns often only use a range of optical bands to map the disk (e.g. Fausnaugh et al., 2018; Miller et al., 2023; Donnan et al., 2023).

Disk reverberation mapping has been done on an ever-growing number of mostly nearby[4] AGN, within a few hundred Mpc, but the sample size is still in the low tens due to the expense of this method. In general, the lag-wavelengths relation follow the thin disk $\tau(\lambda) \propto \lambda^{4/3}$ profile (e.g. Edelson et al., 2015; Fausnaugh et al., 2016; Cackett et al., 2018, 2023; Hernández Santisteban et al., 2020; Pahari et al., 2020; Miller et al., 2023). In addition, SED slopes generally follow the

[4]Mostly nearby as due to time dilation with redshift, which introduces a factor of $(1+z)$, lags and variability timescales will increase. In addition, at larger distances we observe intrinsically brighter objects which are intrinsically larger. Disk reverberation mapping campaigns are already at least 100 days and higher redshifts mean longer and longer campaigns. Systematic disk reverberation mapping campaigns on a larger number of targets only started in the late 2010s so even if these objects are being/have been observed they are not yet published.

thin disk $F_\nu \propto \nu^{1/3}$ trend. This applies to sub-Eddington AGN, which make up the large majority of the sample, and also to the few super-Eddington objects studied (Cackett et al., 2020; Donnan et al., 2023; Thorne et al., 2025). In fact, fits with $\beta = 2$ for a slim disk do not give significantly better results in super-Eddington objects and the SED slope is not preferentially $F_\nu \propto \nu^{-1}$. This might be explained by the fact that we are not probing the photon trapping radius in UV/optical reverberation mapping and therefore not observing the slim disk state. Emission from the photon trapping radius in super-Eddington AGN studied is usually expected to peak around a few hundred Å, which is unobservable due to absorption by interstellar dust. Accordingly, we are probably probing a similar disk state in both sub- and super-Eddington AGN leading to comparable results from both populations.

In contrast, a fascinating amount of deviations from theory and expectations have been consistently observed in all AGN. Foremost, there is the infamous 'too large disk' problem. This describes the fact that from $\tau(\lambda)$ fitting, τ_0s larger than the expected τ_0 by a factor of $2-3$ are almost ubiquitously observed (e.g. Edelson et al., 2015; Fausnaugh et al., 2016; Cackett et al., 2018, 2023; Hernández Santisteban et al., 2020; Miller et al., 2023). Essentially, it *looks* like we are underestimating the Eddington ratios by a magnitude, implying that all sub-Eddington objects are actually super-Eddington. This is equally the case in sub- and super-Eddington objects (Cackett et al., 2020; Pahari et al., 2020; Donnan et al., 2023; Thorne et al., 2025). Further, there is the '*u*/*U*-band excess'. This is an increase in the lag in the *u*/*U*-band above the overall lag-wavelength spectrum slope (e.g. Fausnaugh et al., 2016; Hernández Santisteban et al., 2020; Kara et al., 2023; Lewin et al., 2023). This is sometimes accompanied by a *r*/*R*-band or *i*/*I*-band excess of lesser amplitude. However, this is not as obvious because light curves from larger radii at longer wavelengths reverberate across a larger area, which washes out the variability amplitude. In addition, the signal-to-noise ratio decreases at longer wavelengths. Finally, the correlation between the X-ray emission and the UV/optical emission appears to be, colloquially expressed, a mess. In some objects, there is little or no correlation between the nominal driving hard X-ray light curve and the UV/optical light curves (Hernández Santisteban et al., 2020; Pahari et al., 2020; Vincentelli et al., 2021; Cackett et al., 2023). Then there are objects where there is correlation but the lags between the X-rays and the UV are much larger than expected (Edelson et al., 2015, 2017; Fausnaugh et al., 2018; Pahari et al., 2020; Vincentelli et al., 2021). In Mrk 335, X-ray emission even appears to take a break but the UV/optical variability is completely unaffected (Kara et al., 2023). All of these present strong challenges to the basic lamppost model.

The variability over different timescales also contains interesting information. It has long been observed that there are long timescale, low order polynomial trends in light curves (Welsh, 1999; Peterson et al., 2004). These are often removed in detrending; that is, fitting a low order polynomial to the light curve and then subtracting it. However, this long-term variability itself holds important information. When evaluating the lag as a function of variability timescale, longer timescales show significantly longer lags than at shorter timescales in the same band (e.g. Pahari et al., 2020; Vincentelli et al., 2021). This is especially clear when using frequency resolved lags calculated using Fourier analysis (Uttley et al., 2014; Cackett et al., 2022; Lewin et al., 2023,

2024). In addition, Fairall 9 has long term variability on the 100 day scale that goes the opposite way – the long wavelengths are leading the short (Hernández Santisteban et al., 2020).

An explanation for these peculiarities is that the assumption that the process of reverberation is highly localised, instantaneous, and overwhelmingly dominated by the disk is not valid. The light curves that we observe are a combination of emission from all components and from different processes. As mentioned in Sec. 1.1.2, it is known and exploited that the BLR also reverberates, although mostly in the lines. However, the BLR does also emit continuum emission, which should respond to changes in the flux from the central engine. That means that rather than sharply peaked and restricted to the disk, the responses to the driving light curve are far more complex with a long tail at large radii. This will lengthen lags and distort the lag-wavelength relation (Korista & Goad, 2001, 2019; Lawther et al., 2018).

The BLR diffuse continuum has a characteristic shape with emission spikes in the Balmer and Paschen jumps. It is generally understood that we can see the imprint of the BLR reprocessing through these features in the broadband lag-wavelength spectrum (Korista & Goad, 2001, 2019; Lawther et al., 2018). The Balmer jump falls into the *u*/*U*-band, most probably being responsible for the *u*/*U*-band excess. Similarly, the Paschen jump is in the *r*/*R*- or *i*/*I*-band (depending on redshift), responsible for the tentative detections of the *r*/*R*- and *i*/*I*-band excess. In fact, the expected shape of the Balmer jump in $\tau\lambda$-space has been clearly resolved in the lag-wavelength spectrum in NGC 4593 using a spectroscopic disk reverberation study (Cackett et al., 2018). The BLR is also probably responsible for at least part of the variability at longer timescales. As the BLR covers a far larger area than the disk, responses to the driving flux occur over much longer timescales. The frequency-resolved lags in NGC 5548, Mrk 335, and Mrk 817 show the need for at least two reverberating structures (Cackett et al., 2022; Lewin et al., 2023, 2024). One, at high frequencies, is the disk, while the other at lower frequencies must be a second reprocessor. The sizes of these secondary reprocessors agree with the BLR sizes calculated from $\mathrm{H}\beta$ RM. In addition, the high frequency lags are well fit with a thin disk profile including the expected disk size. Similarly, removing long-term variations in Mrk 879 through detrending also results in a disk size within expected values (Cackett et al., 2023). More generally, and applying to the majority of AGN with reverberation mapped disks, there is probably a secondary reprocessor emitting diffuse continuum at large radii.

There exist further modifications to the disk geometry and the lamppost model to explain observations, especially the X-ray behaviour. There is the rimmed and rippled disk that might explain the too-large-disk problem (Starkey et al., 2023). Turbulence, inhomogeneity, and fluctuations in the accretion flow, as well as communication over large scales in the disk are all proposed to explain the non-correlation between the X-ray and the UV/optical (Dexter & Agol, 2011; Cai et al., 2018; Hagen et al., 2024a). Here, the warm corona is especially important as it can smooth out the high frequency variability from the hot X-ray corona to better correlate with the UV/optical (Gardner & Done, 2017). However, even in these 'lamppost+' models a secondary reprocessor is needed to reproduce longer continuum lags (Hagen et al., 2024a).

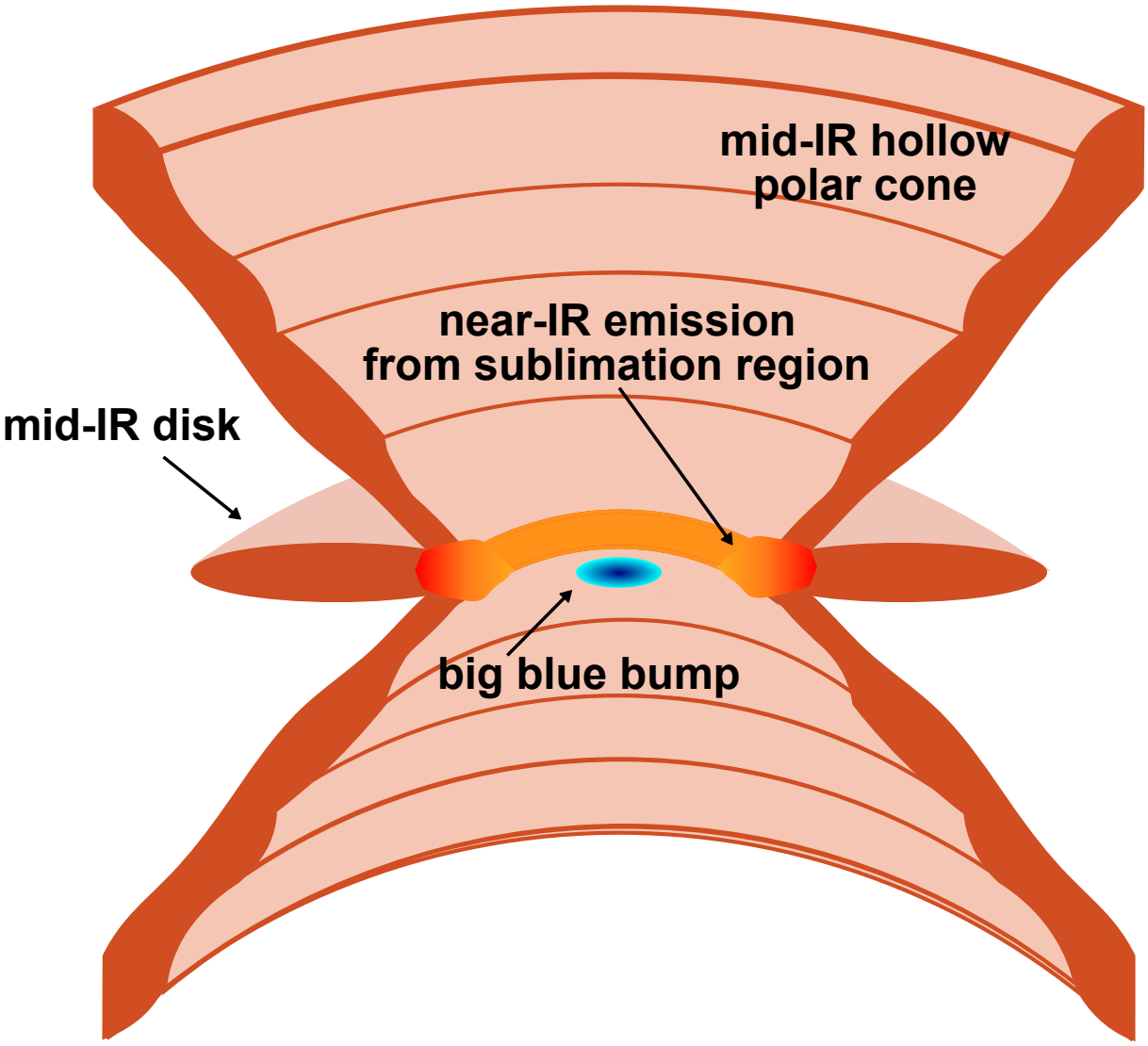

FIGURE 1.4: An illustration of the dusty torus, adapted from Hönig (2019). At the centre is the big blue bump, the central engine, which illuminates the surrounding structures. Surrounding the centre in an equatorial 'ring' structure is the sublimation region which emits in the near-IR. Mid-IR emission comes from both the equatorially-aligned mid-IR disk and the polar hollow outflow cone, often referred to as the dusty wind.

1.3 The Dusty Torus

The dusty 'torus' describes the generally non-toroidal infrared and submillimetre emission region in AGN. Rees et al. (1969) first theorised that the infrared emission in AGN comes from dust irradiated by a luminous central UV source. The dusty torus is generally known as the obscurer central to AGN unification, but it also provides a very important link between the AGN and its host galaxy in the AGN feedback scheme (Krolik & Begelman, 1988; Urry & Padovani, 1995; Hönig, 2019). On one hand, the parsec scale dusty disk and the greater molecular disk are the source of the material for the black hole growth. On the other hand, the dusty winds and associated molecular winds may impact and provide feedback mechanisms back to the host galaxy. It is therefore relevant to study the dusty torus in its own right.

The structure of the dusty torus as assumed nowadays is shown in Fig. 1.4 (Hönig, 2019). There is a dusty parsec-scale disk and a further molecular disk on tens-of-parsec scales in the equatorial plane of the AGN. Near the sublimation radius, dusty winds are launched into the polar direction through radiation pressure. These dusty winds create a hollow cone roughly aligned along the polar/system axis of the AGN. The inner edges of the polar cone appear to trace the edges of the ionization cone and contain the NLR. The dust in the hot regions is thought to primarily consists of large graphite grains, as these are the only ones that can survive in this region (Kishimoto et al., 2007; Netzer, 2015; Hönig & Kishimoto, 2017). Towards colder regions, smaller grains and other species are assumed to be found such that the dust composition in the dusty torus is radially stratified. In the following sections we will explore this structure in further detail, as well as the techniques used to study it. We focus mainly on dust and dusty gas, as this is responsible for the infrared emission studied in this work, but it is important to remember that this is a multiphase structure. We look at the analytical and simulation-based studies of the torus, as well as the overall SED emission and the modelling of it. Then we discuss in detail the structure and physics acting on the hot dust as seen in the near-infrared ($1-5\,\mu\mathrm{m}$) and the warm dust as seen in the mid-infrared ($8-13\,\mu\mathrm{m}$).

1.3.1 Analytical models and simulations

One of the central questions in the study of dusty tori, especially from a theoretical viewpoint, is how the vertical thickness required for obscuration is maintained. Upon the proposal of this obscuring structure by Antonucci & Miller (1985), the torus was an optically and *geometrically thick* disk. Immediately, two different theories for this structure emerged: a warped extension of the accretion disk and a separate dusty structure in the form of a torus (Sanders et al., 1989; Krolik & Begelman, 1988). The former has been largely disfavoured since then by the community and we now regard the dusty torus as a separate, complex, yet integral structure in the AGN (e.g. Netzer, 2015). As an essential component of this structure, the dusty winds are the second major topic investigated through analytical models and simulations; aiming to answer the questions of how the winds are launched and maintained, and what their properties are in relation to the fundamental AGN properties.

As such, analytical models and simulations of the dusty torus focus on the support of the disk's vertical thickness and the wind to investigate the obscuring properties of the AGN dust and how the winds may provide feedback to the host galaxy, and their dependence on fundamental AGN properties. Radiation hydrodynamic (RHD) simulations of the dusty structure make different physical assumptions; nevertheless, they universally show that the dusty winds are launched and sustained through radiation pressure from the central AGN and that this structure is dynamic and non-axisymmetric (Wada, 2012; Chan & Krolik, 2016, 2017; Williamson et al., 2019, 2020; Kudoh et al., 2023). For now, we consider solely the UV radiation pressure from the central engine (i.e. the accretion disk), and not the IR radiation pressure from re-emission by the dust. This latter process will be discussed later. One of the most prominent models is the radiation-fountain model (Wada, 2012, 2015; Wada et al., 2016). These simulations focus on the larger, parsec and

tens-of-parsec scale structure of the dusty torus, leaving the sublimation region unresolved. Immediately, an equatorial disk is formed and biconical outflows appear due to AGN radiation pressure. Dust is blown out in the polar direction and then falls back onto the dusty disk, sustaining the vertical thickness through turbulence. The addition of supernovae further stabilises the height of the disk (Wada et al., 2016). Mid-infrared emission is dominated by the outflows. Notably, obscuration is not only provided by the equatorial dusty structure but also by the dusty outflows (Wada, 2015). Simulations using this setup have also been performed at sub-sublimation radius spatial resolution, to investigate the wind launching mechanisms in the sublimation region (Kudoh et al., 2023, 2024). Here, dust-free-gas-only winds are launched within the sublimation region due to gas pressure. However, as soon as these cross the sublimation threshold, dust is blown off the disk into these winds. The winds are then accelerated rapidly by the UV radiation pressure.

Other RHD simulations also show UV radiation pressure driving the wind (Chan & Krolik, 2016, 2017; Williamson et al., 2019, 2020). They observe that the polar outflows are responsible for the majority of the mid-IR emission (Williamson et al., 2020). Williamson et al. (2019) also showed a two-phase structure; a cold dusty disk and a warm biconical dusty outflow (in the absence of IR radiation pressure). Building on this, Williamson et al. (2020) documented these outflows to be paraboloid in shape, with a hollow outflow cone. However, these outflows were not able to provide the required obscuration. Further, Williamson et al. (2019) found that in contrast to Wada (2012) and Wada et al. (2016) turbulence, gravitational instabilities, and supernovae could not maintain the vertical thickness in the dusty disk. Most importantly, there is a strong dependence of the outflow properties on AGN fundamental properties, particularly the Eddington ratio and anisotropy of the AGN disk emission (Williamson et al., 2019, 2020; Kudoh et al., 2023, 2024). In general, accretion disk emission is anisotropic, i.e. not spherically symmetric (Netzer, 1987). The degree of anisotropy has a large effect on the shape of the sublimation region as well as the direction and outflow properties (Kudoh et al., 2023; Williamson et al., 2019). In an isotropic case, Williamson et al. (2019) observed the dust being completely blown out unlike in the anisotropic case where the wind was produced. Likewise, the Eddington ratio has an effect, but this can vary between studies. Wada (2012, 2015) demonstrated that as the Eddington ratio increases, the more powerful the fountain becomes and more material is blown into the wind while the opening angle decreases. On the other hand, Williamson et al. (2020) observed, primarily due to the anisotropy of the central emission, a larger wind opening angle with increasing Eddington ratio. Here, the wind starts blowing in a preferentially equatorial direction. Nevertheless, it is clear that independent of the simulation and exact wind launching mechanism, the vast majority of the dusty outflows are radiation driven and therefore sensitive to properties such as the shape and strength of the disk radiation.

In contrast to the driving of the winds, the mechanism that sustains the vertical thickness is not well explained by the RHD simulations discussed above. In this case, we must consider IR radiation pressure, as dust is optically thick to its own radiation. This radiation pressure is sufficient to sustain the vertical height of $H/R \sim 0.5 - 1$, especially towards the inner edge within the $10\,\mathrm{pc}$ region (Pier & Krolik, 1992a; Krolik, 2007; Hönig, 2019). This may lead to an inner puffed-up rim within $1 - 5R_{\mathrm{sub}}$ (Krolik, 2007; Hönig, 2019). A similar situation occurs in disks around young

stellar objects (Dullemond et al., 2001). This puffed-up region is also then responsible for the majority of the $3-5\,\mu\mathrm{m}$ emission. This is possibly also the *wind launching region*: IR radiation pressure may launch winds by increasing the scale height of dusty clouds so far that they are decoupled from the disk plane. These clouds are then in a region where they are accelerated by the UV radiation pressure. A semi-analytic model and radiation dynamical simulation, explicitly including IR radiation pressure, demonstrated the occurrence of these effects (Venanzi et al., 2020). The IR radiation pressure contributes to the radiation field, making it more polar. This results in a puffed-up inner rim, maintaining the vertical height in the dusty disk, and boosting the outflows. The last effect is particularly strong when the AGN UV radiation and gravitational force are in equilibrium. Lastly, this results in a hyperboloid outflow shape. This is significant as it matches the results of observation-based detailed radiative transfer calculations done for Circinus (Stalevski et al., 2019).

In conclusion, the structure of the dusty torus is driven and sustained by radiative heating and pressure, both from the central engine (UV) and dust re-radiation (IR). This indicates that AGN properties such as the Eddington ratio and accretion disk emission anisotropy have effects on the structure and dynamics of the dusty torus. This may be particularly important within the inner $10\,\mathrm{pc}$, including the wind launching region.

1.3.2 SEDs and SED modelling

SED modelling is the most widely used technique to study the dusty torus. This is, of course, because it is far more accessible and far less expensive observationally compared to reverberation mapping and optical interferometry. SED fitting commonly explores such topics as the distribution of dust in the torus, the phase of the material, and the geometry of the torus, and more recently the chemistry and grain sizes. The dusty torus emission peaks in the mid-infrared (Pier & Krolik, 1992b, 1993). Data sets used usually cover the near-IR to mid-IR regime ($\sim 1-25\,\mu\mathrm{m}$), with the *N*-band ($8-13\,\mu\mathrm{m}$) specifically providing crucial information to characterise the SED (Lira et al., 2013; Ramos Almeida et al., 2014). Another consideration is the angular resolution of the data. Star formation contributes significantly in the infrared, so data from within the central $100\,\mathrm{pc}$ is required to ensure an SED dominated by AGN emission; otherwise, one needs to consider host galaxy contribution (Hönig et al., 2010).

The general infrared SED of AGN has a few characteristic features. AGN SEDs universally turn upwards at around $\sim 1\,\mu\mathrm{m}$. This is because emission from the dust sublimation region at $\sim 1500\,\mathrm{K}$ peaks at these wavelengths (Barvainis, 1987; Netzer, 2015). The majority of the emission is emitted in the mid-IR, with the peak of the SED at $\sim 40\,\mu\mathrm{m}$ and a significant amount of emission in the $\sim 10-20\,\mu\mathrm{m}$ region (Fuller et al., 2019, 2025). This implies a dominant dusty component at temperatures of $\sim 300\,\mathrm{K}$. This IR emission is also considerably isotropic, i.e. there is little difference in magnitude with inclination and accordingly between Type 1s and Type 2s (Hönig et al., 2011; Ramos Almeida et al., 2011; Stalevski et al., 2016). Furthermore, the slope between the near-IR and the mid-IR, and especially the slope in the near-IR, is dependant on the inclination

angle and possibly the position of individual clouds. In general, Type 1s have shallower slopes than Type 2s (Ramos Almeida et al., 2009, 2011). However, there are exceptions to this: Type 2s do exhibit a large diversity of slopes, with some as shallow as Type 1s (Lira et al., 2013). Nevertheless, this does not translate equally to Type 1s, which consistently only show shallow near-IR slopes. This behaviour might be due to the fact that self-obscuration in Type 2s makes resulting SEDs more complex (Hönig & Kishimoto, 2010). The shallow slope in the near-IR in Type 1s reflects the presence of the '$3-5\,\mu\mathrm{m}$ bump', which is widely observed in Type 1s (Barvainis, 1987; Pier & Krolik, 1993; Mor et al., 2009; Ramos Almeida et al., 2009, 2011; Alonso-Herrero et al., 2011; García-González et al., 2017; García-Bernete et al., 2017). This is commonly attributed to the fact that Type 1s offer a direct view to the hot dust, the fiducial source of this emission (e.g. Barvainis, 1987). Finally, there are the silicate features around $10\,\mu\mathrm{m}$ and $18\,\mu\mathrm{m}$. In a torus comprised of ISM (interstellar medium) dust, we expect to find these silicate features in absorption or emission depending on the line of sight to the hot dust. Silicate features in Type 1s are expected to be in emission and in Type 2s in absorption. However, silicate features portray a large diversity of behaviour independent of inclination and are commonly weak (Ramos Almeida et al., 2009, 2025; Hönig et al., 2010; Asmus et al., 2014; García-González et al., 2017; González-Martín et al., 2023). In fact, strong silicate absorption features are probably related to the host galaxy rather than the torus (Goulding et al., 2012; Asmus et al., 2014).

SED fitting is performed by using SEDs calculated from phenomenologically based radiative transfer models. These models consider different states of dust: a smooth distribution (Fritz et al., 2006), a clumpy one where dust is in clouds (Nenkova et al., 2008a,b; Schartmann et al., 2008; Hönig & Kishimoto, 2010, 2017), or a two-phase distribution, with clumps in a smooth medium (Stalevski et al., 2012, 2016; Siebenmorgen et al., 2015; González-Martín et al., 2023). The dust is generally located in an equatorial flared disk/wedge-shaped configuration (Fritz et al., 2006; Nenkova et al., 2008b; Schartmann et al., 2008; Hönig & Kishimoto, 2010; Stalevski et al., 2012, 2016; Siebenmorgen et al., 2015; González-Martín et al., 2023). This is clearly in tension with the current structural models of the torus, especially considering the fact that the polar regions dominate the mid-IR emission. Accordingly, Hönig & Kishimoto (2017) created an explicit disk+wind model, with an inflowing disk and an outflowing hollow polar cone. Likewise, both Nenkova et al. (2008b) and Siebenmorgen et al. (2015) consider the presence of clumps and smooth material in the polar region, with Nenkova et al. (2008b) clearly documenting that the edge of torus is preferentially soft towards the polar directions. Besides SED libraries, some authors also provide images or interferometric visibilities of the tori configurations corresponding to the SEDs to enable effective synergy between high angular resolution infrared interferometric and low angular resolution SED studies (Schartmann et al., 2008; Hönig & Kishimoto, 2010, 2017; Stalevski et al., 2016).

SED fitting is mainly focused on continuum dust emission and the silicate features. Both photometry and spectroscopy are used, with spectroscopy edited to remove emission lines. This is usually done by either excluding emission line windows outright or extrapolating the continuum over these windows. The best fit model from the SED libraries is usually found by scaling the models to the data and minimising the χ^2 statistic (e.g. Lira et al., 2013). These SED models

often consider a large number of parameters; to constrain the model libraries to reasonable sizes, the parameter ranges may be coarsely sampled. Therefore, SED fitting may not provide a good estimation of the underlying torus properties. To overcome this problem, different methods of parameter interpolation have been used. For example, González-Martín et al. (2019a, 2023, 2025) have used the interpolation inherent to XSPEC to obtain more precise parameter estimates. Asensio Ramos & Ramos Almeida (2009) used Bayesian inference, performing interpolation of SED models based on principle component analysis and artificial neural networks. In addition to the torus SED, other components are also frequently fitted. This includes the AGN disk contribution in the near-IR, host galaxy extinction, and starbursts (although SEDs are also often selected to have minimal starburst contribution).

We summarise results from SED fitting here. Mid-IR data, specifically *N*-band spectra, are crucial in determining the dust distribution in the torus. This data alone can determine the radial power law index of the dust distribution (Hönig & Kishimoto, 2010; Lira et al., 2013; Ramos Almeida et al., 2014). In addition, dusty tori are consistently determined to be compact in size ($\lesssim 10\,\mathrm{pc}$), even though the exact sizes cannot be well constrained (Nenkova et al., 2008b; Alonso-Herrero et al., 2011; García-Bernete et al., 2019). This illustrates that the majority of the emitting dust in AGN is extremely compact, similar to the size scales considered in simulations. Further, there is significant evidence that a substantial amount of dust is concentrated in clumps or clouds, i.e. that the torus medium is either clumpy or two-phase. Due to the distribution of clouds and their effects on each other, e.g. shadowing, silicate features from clumpy and two-phase models are weak both in emission and absorption (Nenkova et al., 2008b; Schartmann et al., 2008; Hönig & Kishimoto, 2010). In addition, as clouds are randomly distributed, silicate features in emission for Type 2 inclinations and in absorption for Type 1 inclinations are created. Further, the strength and direction of the silicate feature is not only dependant on the inclination, but also sensitive to the vertical and radial distribution of clouds, among others (Hönig & Kishimoto, 2010; Stalevski et al., 2012). In addition, the clumpy models provide the isotropic IR emission and anisotropic obscuration seen in AGN SEDs (Nenkova et al., 2008b; Hönig et al., 2010; Hönig & Kishimoto, 2010). Then, there is the case of the $3-5\,\mu\mathrm{m}$ bump, which most models are not able to replicate. The reason for this is assumed to be because this a separate emitting component and often gets treated as such, when an additional hot black body component is introduced to account for it (e.g. Barvainis, 1987; Mor et al., 2009; Lira et al., 2013). Similarly, a two-phase medium with significant emission from the smooth medium around the sublimation region improves fits (Stalevski et al., 2012; Lira et al., 2013). Additionally, a better treatment of the central engine emission anisotropy and sublimation region also improves the behaviour of models in this region (García-González et al., 2017). Nevertheless, supporting the separate component interpretation, the disk+wind model effectively reproduces this feature, with the disk emission responsible for the $3-5\,\mu\mathrm{m}$ bump and the wind emission dominating in the mid-IR (Hönig & Kishimoto, 2017). Results have also shown that there might be an intrinsic difference between the tori in Type 1 and Type 2 AGN. The tori of Type 2s have larger (fitted) covering fractions than Type 1s, and a lower photon escape probability (Alonso-Herrero et al., 2011; Ramos Almeida et al., 2011; García-Bernete et al., 2019). In different parametrisation, Type 2s have a larger number of clouds along the equatorial line of sight, i.e. a

higher cloud density (García-González et al., 2017; García-Bernete et al., 2019). More recently, the chemical composition and dust grain sizes have been investigated. In general, different mixes of dust species all provide a good fit (Reyes-Amador et al., 2024). However, "astronomical" silicates appear to be disfavoured compared with "cosmic" silicates (Draine & Lee, 1984; Ossenkopf et al., 1992; Hatziminaoglou et al., 2015; Reyes-Amador et al., 2024). Fits show that grain sizes tend towards larger sizes, up to $10\,\mu\mathrm{m}$, possibly suggesting depletion of small grains in dusty tori (González-Martín et al., 2023). Nevertheless, in general, any observed SED can either be fit with all SED models – or absolutely none (Netzer, 2015; González-Martín et al., 2025).

In the SED fitting of the dusty torus in AGN there is a general inability to distinguish between models and determine accurate parameter values, with the same parameters determined as different values from different models for the same object. Apart from the behaviour of the silicate feature[5], it is quite difficult to distinguish between a smooth and clumpy torus (Feltre et al., 2012; Stalevski et al., 2012). In one analysis, 50% of the sample was well fit with the disk+wind model, with an even higher proportion of Type 1s (González-Martín et al., 2019b, see also Martínez-Ramírez et al., 2024). For Type 2s, the disk+wind and the classic Nenkova et al. (2008a,b) singular torus model fit similarly well. A naïve conclusion would be that Type 1s are more likely to host a disk+wind geometry and Type 2s a singular torus. However, this contradicts results from optical interferometry where we clearly observe polar emission in Type 2s (e.g. Burtscher et al., 2013; López-Gonzaga et al., 2016). In general, SEDs depend only weakly on inclination and geometry. This rather illustrates that we must be careful in using goodness-of-fit statistics as a marker of "truth", indeed, just because a model fits does not mean it reflects the actual situation in the AGN. Similarly, González-Martín et al. (2025) documents that while all of the 12 reproduceable SEDs (out of 21 total) are well fit with the González-Martín et al. (2023) model, two prefer the disk+wind model, one prefers the Nenkova et al. (2008a,b) model, and 9 are also fit well with other models.

The low prediction power and degeneracy of the SED models have several reasons. As all of the models we discuss are phenomenologically based, they in general produce similar SED shapes, and therefore have less predictive power and are focused on the reproducibility of SEDs (González-Martín et al., 2025). Accordingly, SED fitting is not likely to provide evidence for one model over the other but rather tests how well the torus structure is reproduced in the model. In fact, González-Martín et al. (2019a) showed that the main differences between the different SED models are the slopes below $\sim 7\,\mu\mathrm{m}$ and above $\sim 25\,\mu\mathrm{m}$, and the silicate features. We have already discussed the complexity of the $3-5\,\mu\mathrm{m}$ bump and the silicate features. In addition, the wavelength range above $25\,\mu\mathrm{m}$ is not well probed, especially at high angular resolution, so there is less data to base models on. Parameter results depend heavily on the model and the model assumptions (González-Martín et al., 2019a,b). Feltre et al. (2012) showed that smooth and clumpy models can produce the same SEDs and differences are overwhelmingly due to model assumptions and not basic SED parameters. As such, models that are designed to reproduce the available data in general reproduce the available data, without having the capability to determine

[5]This is, of course, also debated. Stalevski et al. (2012) showed that it was impossible to distinguish between a smooth, clumpy, and two-phase medium based on the silicate feature. Nevertheless, it is generally accepted that a significant amount of dust is concentrated in clouds in the dusty torus, be it in a clumpy or a two-phase medium.

the underlying torus structure. Furthermore, the relationships between some parameters are degenerate and it is not clear which parameters control certain aspects of the SED in actuality. This means that focusing on one parameter might lead to a satisfactory reproducibility of SEDs; however, these SEDs might also be reproduced by another parameter. Therefore, conclusions drawn from the behaviour of these fit parameters about tori can be misleading if they cannot be supported with complementary evidence. This might be demonstrated by the model of González-Martín et al. (2023); with a variable grain size they successfully fit 85-88% of their AGN. However, they also used a simple equatorial torus geometry for their model, and it is unclear if some of the increase in goodness-of-fit might equally be achieved with a more complex geometry, such as a disk+wind model. Therefore, results that indicate a depletion of small grains in dusty tori might be spurious. Most importantly, we have to consider host galaxy extinction and its impact on SED fitting. The magnitude of this extinction is unknown in most cases and fit concurrently with the underlying SED model. This can create an extremely degenerate situation: depending on the amount of intrinsic extinction applied, different parameters and models can be fit satisfactorily.

The fact that geometry, including inclination angle and covering factor, are very poorly constrained within and between models can be compensated for by using complimentary infrared interferometric observations. For instance, the interferometric visibilities in the *N*-band can constrain the radial distribution power law index in Type 1s (less so in Type 2s due to the complex self-obscuration; Hönig & Kishimoto, 2010). On the other hand, Type 2s allow for easier determination of the radial temperature distribution in the wind. Interferometric observations can uncover the geometry of the dusty torus that cannot be constrained using SEDs, specifically the polar emission and the disk+wind structure (Hönig, 2019). In contrast, properties such as dust composition cannot currently feasibly be investigated using spectroscopic optical interferometry in most objects[6], due to the low throughputs.

It is therefore important not to rely on a single technique to characterise the dusty torus. In addition, SED models that concurrently provide images are crucial. Furthermore, it is also clear that our current models are not complex enough to reliably reproduce SEDs. This is illustrated by large residuals in fits and significant proportions of samples that remain unfit (González-Martín et al., 2019b, 2023, 2025). In addition, the new era of high angular and spectral resolution spectra provided by JWST show a whole array of features, especially molecular such as water-ice, not considered in currently available models (González-Martín et al., 2025; Ramos Almeida et al., 2025).

1.3.3 The hot dust seen in the near-infrared

Here we will discuss the hot ($\sim 1000 - 1500\,\mathrm{K}$) dusty torus region as seen in the near-IR ($1 - 5\,\mu\mathrm{m}$[7]). This includes the sublimation region as well as the source of the $3 - 5\,\mu\mathrm{m}$ bump. Of

[6] In all objects besides NGC 1068 and Circinus because they are very special girls (Jaffe et al., 2004; Gámez Rosas et al., 2022; Isbell et al., 2022, 2023).

[7] The near-IR is usually only considered to be $1 - 2.2\,\mu\mathrm{m}$, the *JHK*-bands, while the mid-IR starts from $\sim 3.5\,\mu\mathrm{m}$, the *L*-band. However, in this context it is structurally more useful to group the *LM*-bands with the near-IR. Notably,

course, the dusty torus does not exist of clearly delineated structures at different wavelengths, but is a continuous, multi-temperature structure. However, especially interferometric observations show that the inner, hotter, and more compact structures dominate the $1-5\,\mu\mathrm{m}$ regime while longer wavelengths are dominated by extended, cooler structures (e.g. GRAVITY Collaboration et al., 2020c; Gámez Rosas et al., 2022; Isbell et al., 2022, 2023; Leftley et al., 2024). The general structure *observed* in the near-IR is inclination-dependant. While with a direct view (Type 1s) we can directly observe the shape and properties of the innermost hot dust, an inclined view (Type 2s) will only show the imprints of the hot dust in the obscured nuclear region. Therefore, we focus our discussion on Type 1s unless otherwise indicated. There are two main ways to study the near-IR region in a spatially resolved manner, reverberation mapping and optical interferometry. In RM, the photometric light curves in the *JHK*-bands ($1.2, 1.6, 2.2\,\mu\mathrm{m}$) as well as in the *LM*-bands (3.5 and $4.6\,\mu\mathrm{m}$; Spitzer channels 1 and 2; WISE bands W1 and W2) are correlated with optical light curves, e.g. *B* or *V*, to derive a time lag and the associated radius (e.g. Clavel et al., 1989; Koshida et al., 2014; Sobrino Figaredo et al., 2020; Chen et al., 2023). Optical interferometry of hot dust until recently has mainly focused on the *K*-band (Keck Interferometer, VLTI/AMBER, VLTI/GRAVITY, CHARA), but VLTI/MATISSE is now contributing valuable information in the *LM*-bands (e.g. Kishimoto et al., 2011a, 2022; Weigelt et al., 2012; Gámez Rosas et al., 2022; GRAVITY Collaboration et al., 2024). Reverberation mapping and optical interferometry both contribute size information; however, the size measured using RM in a given band does not necessarily need to correspond to the size measured using OI in the same band. This is because the RM size is a response-weighted radius, and the OI size a flux-weighted radius. Therefore, the relation between the RM and OI sizes can give us further information about the hot dust distribution (Kishimoto et al., 2009a, 2011a). In the case where $R_{\mathrm{RM}} \sim R_{\mathrm{OI}}$, that is $R_{\mathrm{OI}}/R_{\mathrm{RM}} \sim 1$, the hot dust distribution will be compact and sharply peaked. When $R_{\mathrm{OI}}/R_{\mathrm{RM}} > 1$, the hot dust distribution is shallower. The inner dust dominates the response for RM while OI sees a larger average radius over a wider dust distribution. In addition, the size-wavelength relation can give a radially resolved picture of temperature, for example, the spatial relationship between the sublimation region in the *JHK*-bands and the emission region that dominates the $3-5\,\mu\mathrm{m}$ bump. Finally, optical interferometry provides spatially and directionally resolved information of the hot dust distribution such as its shape and orientation with respect to other components in the AGN[8].

Reverberation mapping has been conducted for several tens of objects in the *K*-band (Suganuma et al., 2006; Koshida et al., 2014; Minezaki et al., 2019; GRAVITY Collaboration et al., 2023). WISE (Wide-field Infrared Survey Explorer; Wright et al., 2010) monitoring has provided several hundred of objects time lag measurements in the *LM*-bands (Lyu et al., 2019; Yang et al., 2020; Chen et al., 2023; Mandal et al., 2024). The size in the *K*-band has been consistently measured to be smaller than the putative sublimation radius when using a standard ISM dust mix, by up to

in this work we will also refer to the *LM*-bands as part of the mid-IR. After all, this is astrophysics and "terminology [is] used quite loosely" (Netzer, 2015).

[8]Optical interferometry cannot (currently) provide absolute astrometry, i.e. position, so alignment of structures observed in different bands and with different instruments can be subjective (see e.g. the case of NGC 1068 as observed with GRAVITY and MATISSE; GRAVITY Collaboration et al., 2020c; Gámez Rosas et al., 2022; Leftley et al., 2024).

three times (Kishimoto et al., 2007; Koshida et al., 2014; Pozo Nuñez et al., 2014; Ramolla et al., 2018; Sobrino Figaredo et al., 2020). However, it is also consistently measured to be significantly larger than the BLR radius (as measured using RM), indicating that the BLR lies within the dust according to the classic picture of unification (Clavel et al., 1989; Antonucci, 1993; Urry & Padovani, 1995; Suganuma et al., 2006; Koshida et al., 2014; Ramolla et al., 2018; Minezaki et al., 2019; Chen et al., 2023). The size-wavelength relation across the *KLM*-bands appears to be remarkably consistent, with $R_K : R_L : R_M = 0.6 : 1 : 1.2$ across several different studies (Lyu et al., 2019; Yang et al., 2020; Chen et al., 2023; Mandal et al., 2024). This might also suggest that the *KLM*-band emitting regions are located in the same regions and therefore dominated by the same dust (Clavel et al., 1989; Guise et al., 2022).

Optical interferometry observations in the *K*-band have been modelled well with a thin ring or a disk, with sizes of $0.028 - 1.33\,\mathrm{pc}$ near the sublimation radius, for a total sample of about 30 objects (Swain et al., 2003; Kishimoto et al., 2009a, 2011a,b, 2022; Pott et al., 2010; Weigelt et al., 2012; GRAVITY Collaboration et al., 2020b, 2024; Leftley et al., 2021). This thin disk is orientated along the *equatorial* direction of the AGN (Pott et al., 2010; Leftley et al., 2021; Kishimoto et al., 2022). Image reconstruction of the Type 1 Seyfert NGC 3783 shows an accreting or outflowing hot cloud that lies near the edge of the ionization cone (GRAVITY Collaboration et al., 2021a). The reconstructed image of the Type 2 Seyfert NGC 1068 in the *K*-band shows a thin ring-like structure, at the basis of the outflow detected in the *N*-band (GRAVITY Collaboration et al., 2020c). In the *LM*-bands, the reconstructed images are far less polar than the *N*-band and almost spherical; but indicate the beginnings of the polar outflows from the central structure (Gámez Rosas et al., 2022). In the Type 2 Seyfert Circinus, the *LM*-band structures resemble the thin disk in the equatorial direction that is present in the *N*-band, however no hot dust was observed – this is obscured (Isbell et al., 2023). Finally, optical interferometry sizes are consistently larger than reverberation mapping sizes by a factor of $2 - 2.5$ (Kishimoto et al., 2009a, 2011a; Pott et al., 2010; Weigelt et al., 2012; Koshida et al., 2014; Leftley et al., 2021; GRAVITY Collaboration et al., 2020b, 2023, 2024).

These observations have consequences for the hot dust structure in AGN. Foremost, finding that $R_{\mathrm{RM},K} < R_{\mathrm{sub}}$ can indicate several things. One, that the sublimation radius is smaller as it is dominated by large graphite grains, which can survive at higher temperatures and therefore further inwards (Kishimoto et al., 2007). Two, there are geometric effects that make it appear such that the RM size is smaller than the sublimation radius, particularly a foreshortening effect. Here, the reverberation signal is dominated by the response from hot dust at a significant height above the equatorial plane, making it appear closer to the central engine. This can certainly be reproduced by any geometry with considerable scale height at the inner rim such as a puffed-up inner rim or a slim disk (e.g. Dullemond et al., 2001; Pozo Nuñez et al., 2014; Chen et al., 2023). However, the bowl-shaped/concave model as described by Goad et al. (2012) has been particularly successful in explaining the *JHK* reverberation mapping results (Pozo Nuñez et al., 2014; Ramolla et al., 2018; Sobrino Figaredo et al., 2020). This model also explains the fact that $R_{\mathrm{OI}}/R_{\mathrm{RM}} > 1$. GRAVITY Collaboration et al. (2024) successfully simultaneously replicated *K*-band measurements from OI

and RM using a simple, bowl-shaped model. In addition, the large $R_{\rm OI}/R_{\rm RM}$ fraction indicates a shallower hot dust distribution in contrast to the steep and compact structure that would be indicated by $R_{\rm OI}/R_{\rm RM} \sim 1$(Kishimoto et al., 2009a; Weigelt et al., 2012; Guise et al., 2022). Finally, simultaneous chromatic modelling of the interferometric *KLMN*-band data of NGC 1068 confirms a Type 2 structure, with the emission visible in the *KLM*-bands from hot dust located in an obscured nuclear region and at the basis of the outflow (Leftley et al., 2024). Interestingly, modelling of current interferometry of the *K*- or *L*-band alone cannot distinguish between a Type 1 or Type 2 view of the central region because the observed structures of unobscured and obscured hot dust are not significantly different at these wavelengths.

Finally, we discuss whether the hot dust geometry and properties depend on fundamental AGN properties such as bolometric luminosity and the Eddington ratio. Fundamental for this is the size-luminosity ($R-L$) relation, which, analytically is predicted to be $R \propto L^{1/2}$. Both reverberation mapping and optical interferometry results in the *KLM*-bands consistently show a shallower relation, especially at higher luminosities, and less scatter than in the BLR $R-L$ relation (Lyu et al., 2019; Minezaki et al., 2019; GRAVITY Collaboration et al., 2020b, 2023; Sobrino Figaredo et al., 2020; Chen et al., 2023; Mandal et al., 2024). This implies that as the luminosity increases, the hot dust gets more compact, increasing the effect of self-shielding. However, GRAVITY Collaboration et al. (2024) showed that when using a non-linear correction for the bolometric luminosity (the SED changes shape as the luminosity increases), this effect disappears in the *K*-band and the sizes follow the expected $R \propto L^{1/2}$ relation. This non-linear correction has not been tested for the *LM*-band sizes; however, Yang et al. (2020) did show the $R \propto L^{1/2}$ relation exists over four magnitudes in the *L*-band. This is in contrast with all other studies (Lyu et al., 2019; Chen et al., 2023; Mandal et al., 2024). In addition, the *K*-band sizes do not show any correlation with Eddington ratio (Koshida et al., 2014; GRAVITY Collaboration et al., 2020b). Further, the surface emissivity is constant with bolometric luminosity (GRAVITY Collaboration et al., 2020b). In general, the BLR size to hot dust size ratio is constant and uncorrelated with AGN properties[9] (Chen et al., 2023). However, there are indications of a correlation between *LM*-band sizes and Eddington ratio: as the Eddington ratio increases, the relative *LM*-band sizes decrease and get more compact (Chen et al., 2023; Mandal et al., 2024). In the picture of a puffed-up rim or a slim disk that increases in scale height with increasing Eddington ratio, this means that the *LM*-band emission is increasingly dominated by the puffed-up region. This region shadows regions further out, leading to more compact *LM*-band sizes (Chen et al., 2023; Mandal et al., 2024).

In conclusion, the hot dust region responsible for the near-IR ($1-5\,\mu$m) emission sits outside the BLR around the sublimation radius in a thin ring, which is located in the equatorial plane. There is evidence that this inner rim has a significant scale height and shallow dust distribution, be it in a bowl-shaped/concave, puffed-up, or slim disk geometry. There are possibly also indications that this scale height increases with increasing Eddington ratio. The hot dust sizes probably follow the

[9]This might also indicate that the shallow $R-L$ relation found for BLR sizes might be due to the non-linear correction for the bolometric luminosity (GRAVITY Collaboration et al., 2024). Nevertheless, there are indications that the BLR $R-L$ relation is more complex than the hot dust $R-L$ relation, suggesting that the hot dust sizes are better for measuring black hole masses (GRAVITY Collaboration et al., 2023).

$R \propto L^{1/2}$ relation. While Type 1 inclinations offer a direct view to the hot dust region (and the dust responsible for the $3-5\,\mu\mathrm{m}$ bump), this is obscured in Type 2 Seyferts.

1.3.4 The warm dust seen in the mid-infrared

The dusty torus structure as seen in the mid-IR (here, primarily the *N*-band) has been characterised principally through the results of high angular resolution observations with optical interferometry (e.g. Hönig et al., 2013; Tristram et al., 2014). Optical interferometry provides access to the sub-parsec scale structure of the innermost $10\,\mathrm{pc}$, while the highest angular resolution mid-IR imaging is on scales of tens to hundreds of parsecs. In this section, we will discuss the mid-IR dust structure on these different scales.

Small scales ($< 10\,\mathrm{pc}$) can only be probed with optical interferometry and image the warm dust at $\sim 200-400\,\mathrm{K}$. Results show that the structure does not resemble the classical thin ring/toroidal expectation and is well represented by a shallow and extended power-law (Kishimoto et al., 2009b, 2011b). Sizes for the mid-IR emission – usually represented by the half-light radius, which is model independent – are on the scales of $\lesssim 5\,\mathrm{pc}$, approximately up to a few tens of sublimation radii (Kishimoto et al., 2011b; Hönig et al., 2012, 2013; Burtscher et al., 2013; Tristram et al., 2014; López-Gonzaga et al., 2016; Leftley et al., 2018). These mid-IR sizes also follow a far shallower size-luminosity relation than the usual $R \propto L^{1/2}$ with a large scatter (Kishimoto et al., 2011b; Burtscher et al., 2013; Leftley et al., 2019). Furthermore, these results are independent of inclination and show no correlation between size and Type 1s or 2s (Burtscher et al., 2013; López-Gonzaga et al., 2016; Leftley et al., 2019). All these results suggest that the structure of the dust in the mid-IR is more complex. Rather, it is a two-component structure: a polar component, which are outflowing dusty winds, and an equatorial component, which is a disk (Hönig, 2019). The polar component is indicated by prominent elongations of the mid-IR emission along the polar direction observed using mid-IR optical interferometry. Polar elongations so far have been observed in $\sim 6-9$ sources (Hönig et al., 2012, 2013; Burtscher et al., 2013; Tristram et al., 2014; López-Gonzaga et al., 2016; Leftley et al., 2018). Out of all the sources that have sufficient angular coverage to constrain elongations, 80% have elongations in the polar direction and none in the equatorial (Leftley et al., 2018). These polar components dominate the resolved mid-IR emission with $\sim 60-90\%$ (Hönig et al., 2012, 2013; Tristram et al., 2014; Leftley et al., 2018; Isbell et al., 2022). The major-to-minor axis ratios are substantial, with $1.3-3:1$ (Hönig et al., 2013; Tristram et al., 2014; López-Gonzaga et al., 2016; Leftley et al., 2018). The polar components also have a shallow radial dust distribution, with low density of dust or dusty clumps (Hönig et al., 2013; Tristram et al., 2014; Isbell et al., 2022). Notably, these structures are observed in both Type 2s and Type 1s (Hönig et al., 2013; Leftley et al., 2018). This indicates that this is a universal feature in AGN. In fact, Hönig & Kishimoto (2017)'s disk+wind model predicts the observation of polar structures at low inclinations and successfully reproduces these for the Type 1 AGN NGC 3783 and ESO 323-G77 (Leftley et al., 2018). Image reconstructions of the Type 2 AGN NGC 1068 and Circinus clearly show these polar structures. The polar extended emission in NGC 1068 has two

polar horns, which agrees well with the predicted structure of a hollow polar outflow cone – emissions at the edges of a hollow cone are enhanced (Gámez Rosas et al., 2022). Circinus has a low density, patchy structure in the polar region, which is consistent with a clumpy dust structure (Isbell et al., 2022). Circinus also shows the two component mid-IR structure with striking clarity: perpendicular to the polar extension, there is a clear equatorially aligned disk (Tristram et al., 2014; Isbell et al., 2022). This equatorial disk has a steep temperature profile, contributing $\sim 10\%$ of the mid-IR emission. Further, this disk is also smaller in size than the polar extension. Due to these reasons, this secondary disk component has only been observed in the very nearby and mid-IR luminous AGN Circinus. However, a similar structure may be present in NGC 1068 in absorption. Partial obscuration of the southern polar outflow in NGC 1068 points towards the existence of a thin sheet or disk with a size of $\sim 10\,\mathrm{pc}$ (Gámez Rosas et al., 2022; Isbell et al., 2025). In general, high angular resolution mid-IR interferometric observations have uncovered a complex dust structure, consisting of a hollow polar outflow cone and an equatorial disk.

Akin to optical interferometric observations, mid-IR images also show polar extended emission on the scales of tens to hundreds of parsecs (Asmus et al., 2014, 2016; Alonso-Herrero et al., 2021). This extended mid-IR emission is aligned along the ionization cone, which delineates the nuclear area of material heated/photoionized by the AGN, particularly the NLR (Asmus et al., 2014). Indeed, the mid-IR luminosity scales with the luminosity of the [O IV] emission line, which is an NLR tracer (Asmus et al., 2016). As such, it is likely that the extended mid-IR emission originates from dust in the NLR heated by the AGN and/or shocks rather than being an extension of the dusty winds (Hönig, 2019). In fact, simulations of mid-IR imaging observations of disk+wind realisations indicate that the polar elongations would be unresolved or only slightly resolved, making it unlikely that these are related to the nuclear extended emission we see in mid-IR images (Alonso-Herrero et al., 2021). Studies of dust emissions at longer wavelengths ($30 - 40\,\mu\mathrm{m}$) show that where mid-IR emission is of AGN origin (rather than star formation) the dust is in the NLR and heated by the AGN (Fuller et al., 2019, 2025). This dust is at temperatures of $\sim 100\,\mathrm{K}$, which at these distances can be heated by the central AGN emission (Fuller et al., 2019). JWST imaging of ESO 428-G14 reveals a relatively compact dust emission region, with a size of $100\,\mathrm{pc}$, co-linear with the radio jet (Haidar et al., 2024). The authors demonstrate that this dust may be heated by AGN radiation and/or jet-induced shocks. Jet-induced shocks in general probably also play a significant role in inducing mid-IR dusty emission on these scales. Observations of NGC 1068 with the Large Binocular Telescope Interferometer (LBTI) clearly show the transition from dusty wind dominated mid-IR emission to dust heated by jet-induced shocks by accessing intermediate scales with parsec resolution (Isbell et al., 2025). Near the base of the extended polar emission, the morphology clearly resembles the two-horned morphology of the dust in the very high angular resolution observations that image the hollow dusty polar outflow cone (Gámez Rosas et al., 2022). However, as the emission is traced outwards, there are clear indications of mid-IR emission arising from dust heated by a jet-induced shock. While dusty winds in AGN clearly do not extend beyond the $\sim 10\,\mathrm{pc}$ scale, the dusty torus is connected to larger scales through the equatorial disk. Observations in the submillimetre regime clearly show thermal emission from a dust disk that sits in the equatorial plane, with sizes of a few tens of parsec (Combes et al., 2019; Alonso-Herrero et al.,

2021; García-Burillo et al., 2021). They provide a connection between the host galaxy and the dusty torus, probably acting as the region through which material flow into the dusty torus and the central engine (Hönig, 2019). However, even though dusty winds do not affect the AGN environment beyond $10\,\mathrm{pc}$ directly, they do impact the shape and direction of AGN feedback through outflows and the ionization cone. It is very likely that the outflows and the NLR are collimated at radii of $\lesssim 5\,\mathrm{pc}$, where the dusty wind dominated the AGN environment and mid-IR emission (Tristram et al., 2022; Kakkad et al., 2023). This indicates that the hollow polar outflow cone might not have a strong direct feedback impact but that it does shape the AGN radiative and kinetic feedback.

Chapter 2

Optical Interferometry

> It's still magic even if you know how it's done.
>
> *A Hat Full of Sky*
> Terry Pratchett

In most optical astronomical observations, the photons on the detector and the basic observables have a direct relationship to the flux emitted by the object observed. However, in optical interferometry, where our observables are *visibility*, *correlated flux*, *differential phase*, and *closure phase*, the connection to the astronomical object is not as apparent. In this chapter we will explore how optical interferometry works and how our observables are connected to the source properties. We will also look at the particular interferometric instrument MATISSE, primarily used in our work. Then we will present our new data reduction method for faint sources in MATISSE.

2.1 Basic Interferometry Theory

In this section, we will discuss basic interferometry theory. This discussion is based on the course notes from the 1999 Michelson Summer School (Lawson, 2000) and the doctoral thesis of K. R. W. Tristram (Tristram, 2007).

Let us start with the basic two telescope interferometer, as sketched in Fig. 2.1. The source in the sky is at position $\underline{S}$, with the source direction represented by the position vector $\underline{s} = \underline{S}/|\underline{S}|$. The telescopes A and B are at positions $\underline{x}_A$ and $\underline{x}_B$ respectively. The *baseline* $\underline{B}$ is the separation vector between the telescopes, $\underline{B} = \underline{x}_B - \underline{x}_A$. As the source is far away, we can estimate the light as arriving as a plane wave. The light beams then make their way through the telescopes and telescope infrastructure until they arrive at the beam combiner. At the beam combiner, the two beams are interfered. There are two basic designs of beam combiner: the pupil plane or Michelson

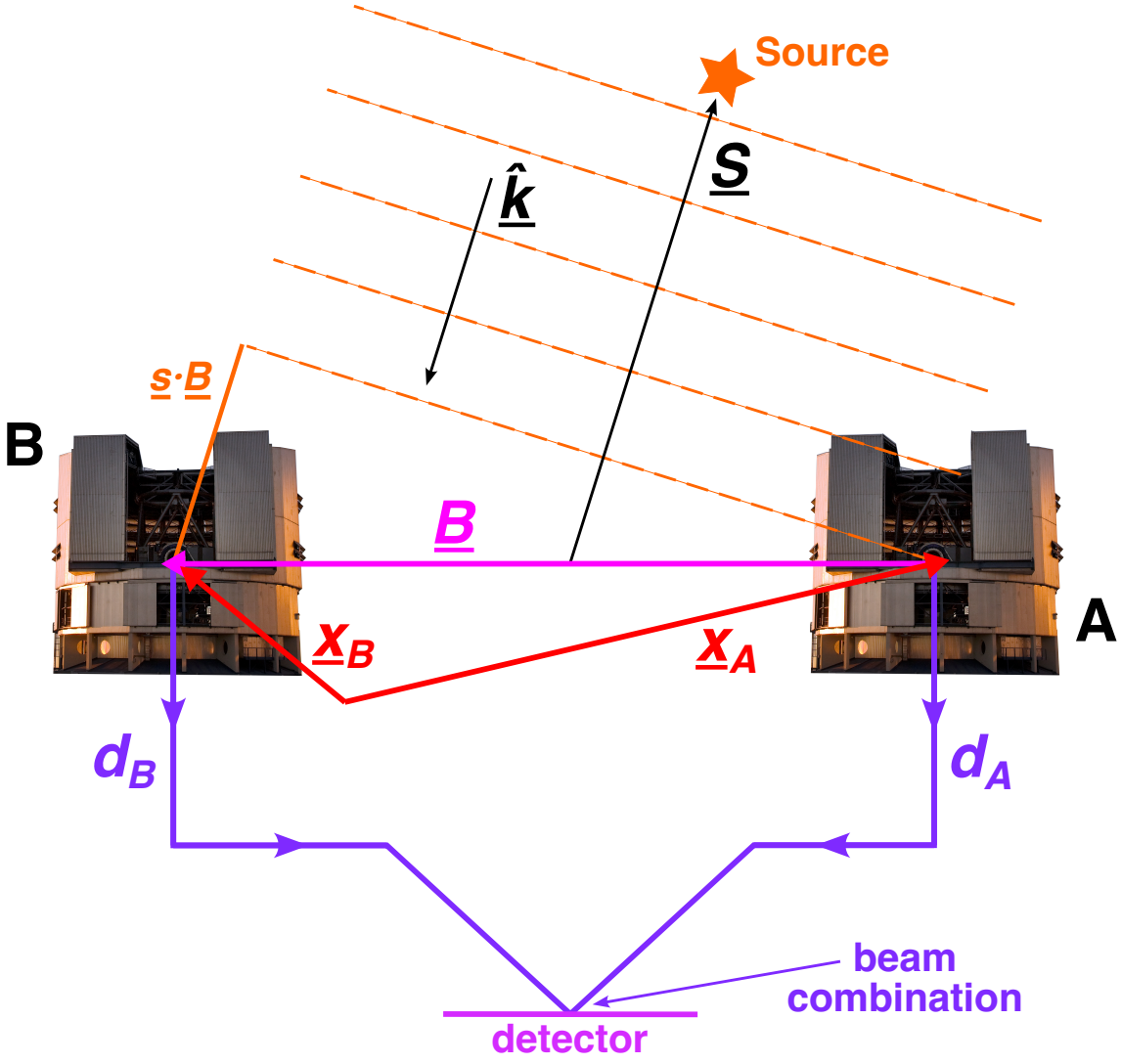

FIGURE 2.1: A sketch of a basic two telescope interferometer. The source in the sky is at position $\underline{S}$, and the telescopes A and B are at positions $\underline{x}_A$ and $\underline{x}_B$ respectively. The baseline $\underline{B}$ is the separation between the two telescopes, with $\underline{B} = \underline{x}_B - \underline{x}_A$. The source is far away so the arriving light can be estimated as plane waves. The light arrives at telescope A with its phase ahead by $\underline{s} \cdot \underline{B}$. The light then traverses two different optical paths with path lengths d_A and d_B. The two beams then arrive at the beam combination site, combining on the detector. This is a Fizeau or image-plane interferometer.

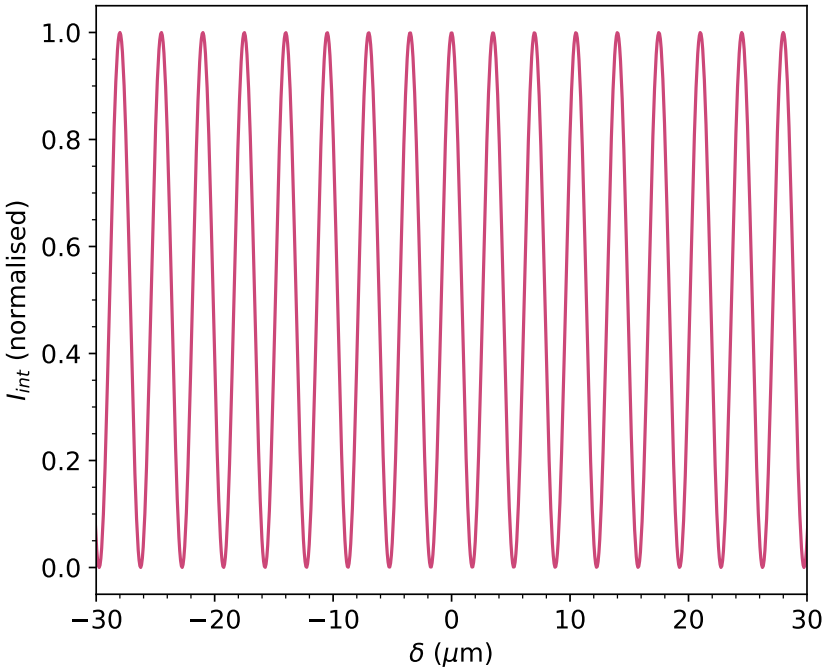

FIGURE 2.2: The interferometric intensity I_{int} as a function of the optical path difference δ for a monochromatic point source according to Eq. 2.3. This oscillatory pattern is called *fringes*. These fringes are calculated at a wavelength of $\lambda_0 = 3.5\,\mu\text{m}$, the *L*-band. At OPD values of 0, λ_0, $2\lambda_0$,... the signals interfere positively while at $\lambda_0/2$, $3\lambda_0/2$, $5\lambda_0/2$,... they interfere negatively.

interferometer and the image plane or Fizeau interferometer. In a Michelson interferometer, the beams are superposed in parallel in the pupil plane using a half-silvered mirror. In a Fizeau interferometer, the images from the two telescopes are superposed on the detector, i.e. in the image plane. In effect, neither of these designs is better than the other, and usage in instruments comes down to design constraints. For instance, both the first generation Very Large Telescope Interferometer (VLTI) instrument MIDI and the second generation VLTI instrument GRAVITY are Michelson interferometers (Leinert et al., 2003; GRAVITY Collaboration et al., 2017). MATISSE, the focus of this research, is an image plane combiner and therefore we will focus the following analysis on the Fizeau interferometer (Lopez et al., 2022).

2.1.1 Fringes and fringe modulation

For simplicity, we first discuss a monochromatic point source. To determine the result of the beam combination on the detector, we must trace the light from the sky through the telescopes. More concretely, we are looking at the phase shift that arises from the difference between the optical paths that the two beams take. This is the *optical path difference* or OPD, δ. When the light arrives at the telescope apertures, beam B will already have obtained a phase shift with magnitude $\underline{s} \cdot \underline{B}$ with respect to beam A due to the difference in position between the telescopes ($\underline{B} = \underline{x}_B - \underline{x}_A$). On their way to the detector, the beams will further traverse optical paths with

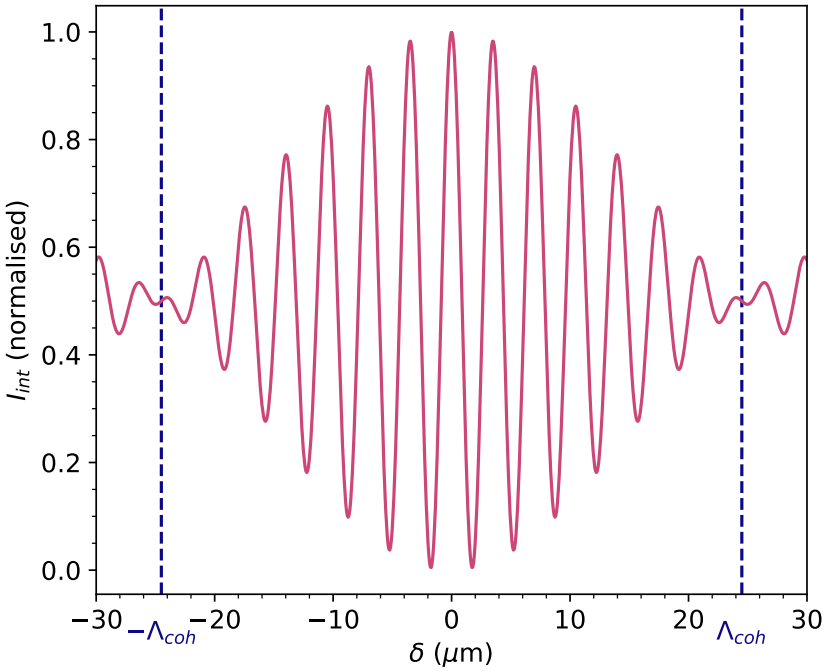

FIGURE 2.3: The interferometric intensity I_{int} as a function of the optical path difference δ for a polychromatic point source according to Eq. 2.7. This is for a filter with central wavelength of $\lambda_0 = 3.5\,\mu\text{m}$ and a filter width of $\Delta\lambda = 0.5\,\mu\text{m}$, approximately the *L*-band. The coherence length is $\Lambda_{\text{coh}} \simeq 25\,\mu\text{m}$ (Eq. 2.4). At this point, the intensity difference between the fringes is effectively zero.

lengths d_A and d_B respectively. Accordingly, at the detector, the light beams can be described by

$$\underline{E}_A = \underline{E}_{A,0} e^{ikd_A} e^{-i\omega t} \text{ and } \underline{E}_B = \underline{E}_{B,0} e^{ikd_B - ik\underline{s}\cdot\underline{B}} e^{-i\omega t}. \tag{2.1}$$

where the wave vector $\hat{\underline{k}}$ is anti-parallel to $\underline{s}$ such that $\hat{\underline{k}} \cdot \underline{s} = -ks$ (as shown in Fig. 2.1). The electric field of beam A is given by $\underline{E}_A$ and that of beam B by $\underline{E}_B$. On the detector, these two fields are superposed such that they make one wave with $\underline{E} = \underline{E}_A + \underline{E}_B$. The interferometric signal recorded by the detector is the time averaged intensity $I_{\text{int}} = |\underline{E}|^2 = \underline{E} \cdot \underline{E}^*$. Using the expressions for the electric fields from Eq. 2.1, this is then

$$I_{\text{int}} = I_{\text{src}}(\eta_A + \eta_B + 2\sqrt{\eta_A \eta_B} \cos k\delta) \tag{2.2}$$

where I_{src} is the source intensity. Further, $|\underline{E}_A|^2 = \eta_A I_{\text{src}}$ and $|\underline{E}_B|^2 = \eta_B I_{\text{src}}$, with η_A and η_B the transmission efficiencies of optical paths A and B respectively. The optical path difference is $\delta = d_A - d_B + \underline{s} \cdot \underline{B}$. Varying d_B will lead the intensity to oscillate. In an ideal situation where $\eta_A = \eta_B = 1$, I_{int} reduces to

$$I_{\text{int}} = 2I_{\text{src}}(1 + \cos k\delta). \tag{2.3}$$

This is plotted in Fig. 2.2 for a wavelength of $3.5\,\mu\text{m}$, which is in the *L*-band. This oscillatory pattern is what is referred to as *fringes*, akin to the results of Young's double slit experiment (Young, 1804). The interferometric signal is also referred to as the *interferogram*.

It is clear that in a perfectly monochromatic situation this fringe pattern will repeat at full intensity infinitely, for an ever larger value of δ. In a realistic scenario, we will have a bandpass of finite width Δk. As $I_{\rm int}$ is a function of the wave number $k = 2\pi/\lambda$, chromatic dispersion will occur. At larger values of δ, the two beams will stop interfering coherently. The intensity of the fringes will decrease rapidly. The OPD amplitude at which this approximately occurs is the *coherence length*, $\Lambda_{\rm coh}$. For a bandpass with width $\Delta\lambda$ and central wavelength λ_0, the coherence length is given by

$$\Lambda_{\rm coh} \simeq \lambda_0^2/\Delta\lambda \tag{2.4}$$

under the assumption that $\Delta\lambda << \lambda_0$. The OPD must be smaller than $\Lambda_{\rm coh}$ to obtain fringes. In the case of spectral dispersion of the signal, with resolution $R = \lambda_0^2/\Delta\lambda$, $\Lambda_{\rm coh} = R\lambda_0 - \lambda_0/4R$. We can illustrate the effect of chromatic dispersion on the interferometric signal by considering a polychromatic set-up with a simple top-hat bandpass. The transmission coefficients $\eta_A(k)$ and $\eta_B(k)$ are wavelength dependent and have a finite width such that

$$\eta_A(k) = \eta_B(k) = \eta(k) = \begin{cases} \eta_0 & \text{for } k_0 - \Delta k/2 < k < k_0 + \Delta k/2 \\ 0 & \text{else} \end{cases} \tag{2.5}$$

where Δk is the width of the filter and k_0 the centre. The source intensity is assumed to be constant at $I_{\rm src}(k) = I_0$. To get the total interferometric signal, we must integrate Eq. 2.2 over all relevant wave numbers, as given by

$$I_{\rm int} = \int_{k_0-\Delta k/2}^{k_0+\Delta k/2} 2I_0\eta_0(1+\cos k\delta)\mathrm{d}k. \tag{2.6}$$

Integration leads to

$$I_{\rm int} = 2I_0\eta_0\Delta k(1+\cos k_0\delta\,\mathrm{sinc}\,\delta\Delta k/2). \tag{2.7}$$

$I_0\eta_0\Delta k$ is also referred to as the bandpass power $I_{\rm bp}$, which is the total power collected in the bandpass. We plot this interferometric signal in Fig. 2.3 for a central wavelength of $3.5\,\mu$m and a filter width of $\Delta\lambda = 0.5\,\mu$m, approximating the *L*-band. We can clearly see that the fringes from Fig. 2.2 are modulated by the sinc function and quickly disappear at $|\delta\Delta k/2| > 1$. This limit is the coherence length described by Eq. 2.4. The coherence length of the set-up here is $\simeq 25\,\mu$m, as seen in the plot[1]. Notably, the sinc function modulating the fringe pattern is the Fourier transform of the original top-hat bandpass. We can generalise this for all shapes of bandpasses and source intensities as

$$I_{\rm int} = 2I_{\rm bp}(1 + M(\Lambda_{\rm coh},\delta)\cos k_0\delta) \tag{2.8}$$

where $M(\Lambda_{\rm coh},\delta)$ is the fringe envelope or fringe modulation function. The fringe envelope is the Fourier transform of the system bandpass, also called the transfer function;
$M(\Lambda_{\rm coh},\delta) = \mathcal{F}[\eta(k)](\Lambda_{\rm coh},\delta)$.

[1] This is only the case for one bin covering the entire *L*-band. In reality, we observe several bins over the *L*-band.

2.1.2 van-Cittert-Zernike theorem

In general, the *van-Cittert-Zernike theorem* states that the interferometric signal, which is called the *complex visibility* $\mathcal{V}(\underline{u})$, is the Fourier transform of the source intensity distribution on the sky. In other words,

$$\mathcal{V}(\underline{u}) = \mathcal{F}[I(\underline{s})](\underline{u}) = \tilde{I}(\underline{u})e^{i\phi(\underline{u})} \tag{2.9}$$

where $I(\underline{s})$ is the intensity distribution of the source in the sky and $\underline{u}$ is the *spatial frequency* given by $\underline{u} = \underline{B}_{\text{proj}}/\lambda$, the number of wavelengths per metre. $\underline{B}_{\text{proj}}$ is the *projected baseline* separation between the two telescopes with respect to the source. Further, $\tilde{I}(\underline{u})$ is the real amplitude of the complex visibility, also called the *correlated flux*, and $\phi(\underline{u})$ is the *phase*. The amplitude of the complex visibility is directly related to the normalised (real) *visibility* $V(\underline{u})$ given by

$$V(\underline{u}) = \frac{|\mathcal{V}(\underline{u})|}{|\mathcal{V}(0)|} = \frac{\tilde{I}(\underline{u})}{\tilde{I}(0)} \tag{2.10}$$

where $\tilde{I}(0)$ is the total source flux such that $V(0) = 1$. The normalised visibility and the phase are the main interferometric observables. Since $\mathcal{V}(\underline{u})$ and $I(\underline{s})$ are a Fourier pair, the inverse transform from $\mathcal{V}(\underline{u})$ to $I(\underline{s})$ also applies. This implies that we can reconstruct the source intensity distribution from our visibility and phase measurements. However, due to a series of limitations discussed later, this is practically unfeasible for most sources in optical interferometry.

We can illustrate the van-Cittert-Zernike theorem by considering the interferometric signal from an extended (monochromatic) source with a brightness distribution $I(\underline{s})$ on the sky. The extended source is a superposition of sources that are mutually incoherent. The interferometric signal over the whole sky is then

$$I_{\text{int}} = \int I(\underline{s})(\eta_A + \eta_B + 2\sqrt{\eta_A\eta_B}\cos\left(k(d - \underline{s}\cdot\underline{B})\right))\mathrm{d}\underline{s} \tag{2.11}$$

where we have expanded $\delta = d - \underline{s}\cdot\underline{B}$. The integral of the first term $(\eta_A + \eta_B)I(\underline{s})$ is simply the total detected source flux. The second term can be written as

$$\sqrt{\eta_A\eta_B}\left[e^{ikd}\int I(\underline{s})e^{-ik\underline{s}\cdot\underline{B}}\mathrm{d}\underline{s} + e^{-ikd}\int I(\underline{s})e^{ik\underline{s}\cdot\underline{B}}\mathrm{d}\underline{s}\right]. \tag{2.12}$$

It is clear that both integrals are the 2D Fourier Transform of $I(\underline{s})$. Using the visibility $V(\underline{u})$, the interferometric signal is then

$$I_{\text{int}} = I_{\text{src}}(\eta_A + \eta_B + 2V(\underline{u})\sqrt{\eta_A\eta_B}\cos\left(kd - \phi(\underline{u})\right)). \tag{2.13}$$

Based on this interferometric signal it is apparent that our observables in interferometry are the visibility $V(\underline{u})$ and the phase $\phi(\underline{u})$, as a function of the spatial frequency.

2.1.3 Phase

The phase holds a lot of information about the morphology of the source. However, due to the atmosphere it is relatively difficult to measure. Atmospheric turbulence will introduce an unknown phase shift $\phi_{\rm atm}$ to the light. There are several ways to account for this in use today. The first is phase referencing. Here, a phase referencing object with known phase $\phi_{\rm pr}$ is observed simultaneously to the science object with phase $\phi_{\rm obs}$. Since this phase is known, the atmospheric phase shift can be derived using $\phi_{\rm atm} = \phi_{\rm obs} - \phi_{\rm pr}$. Another technique of phase referencing is referencing with respect to the continuum. The phase of a continuum band is set to zero and the phase of the line emission is referenced to this. This is called the *differential phase*.

Closure phases are an alternative to phase referencing. The closure phase is the sum of the measured phases from three baselines and can therefore only be observed with 3+ telescopes. Here, each baseline combination of two telescopes A and B measures a total phase $\Phi_{\rm AB}$, which consists of the source phase $\phi_{\rm AB}$ and the atmospheric phase of each telescope $\varphi_{\rm A} - \varphi_{\rm B}$. For three telescopes with baseline combinations AB, BC, and CA, this gives the measured phases of each baseline as

$$\begin{aligned} \Phi_{\rm AB} &= \phi_{\rm AB} + \varphi_{\rm A} - \varphi_{\rm B} \\ \Phi_{\rm BC} &= \phi_{\rm BC} + \varphi_{\rm B} - \varphi_{\rm C} \\ \Phi_{\rm CA} &= \phi_{\rm CA} + \varphi_{\rm C} - \varphi_{\rm A}. \end{aligned} \tag{2.14}$$

The closure phase $\phi_{\rm cp}$ is the sum of these phases such that

$$\begin{aligned} \phi_{\rm cp} &= \Phi_{\rm AB} + \Phi_{\rm BC} + \Phi_{\rm CA} = \phi_{\rm AB} + \phi_{\rm BC} + \phi_{\rm CA} + \varphi_{\rm A} - \varphi_{\rm B} + \varphi_{\rm B} - \varphi_{\rm C} + \varphi_{\rm C} - \varphi_{\rm A} \\ &= \phi_{\rm AB} + \phi_{\rm BC} + \phi_{\rm CA} \end{aligned} \tag{2.15}$$

and the atmospheric contents cancel out. However, we cannot disentangle the individual intrinsic phases from the source from each baseline; nonetheless it can provide important structural information.

2.1.4 Practical considerations in optical Interferometry

While we now have the theoretical basics for optical interferometry, there are some practical issues we must consider. These necessarily inform our observing strategies, data analysis, and interpretation of results.

A central concept in interferometry is the uv-*plane*, shown in Fig. 2.4. In essence, it is the geographic locations of the telescopes where v is North and u is East. More correctly, the uv-plane is the Fourier plane that contains the spatial frequency (u, v) coordinates. Each Interferometric measurement from a particular telescope combination is located at a spatial frequency $\underline{u} = (u, v)$ that can be placed in the uv-plane. While the uv-plane is strictly correct in units of spatial frequency, for ease it is commonly expressed in terms of projected baseline length $B_{\rm proj}$. The

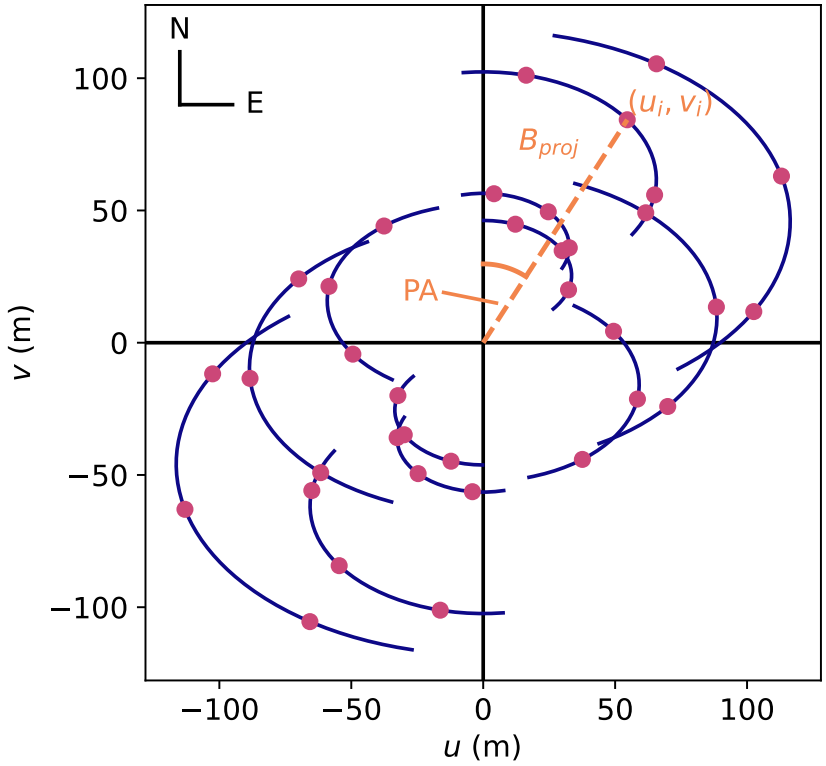

FIGURE 2.4: The uv-plane with example uv-points (filled circles) and tracks (lines) as would be obtained using the VLTI with the UTs. The uv-plane is expressed in metres, derived from spatial frequencies at a wavelength of $3.5\,\mu$m. For the point (u_i, v_i) the definitions of the projected baseline $B_{\rm proj}$ and position angle PA have been illustrated, where $B_{\rm proj}$ is the distance from the origin and PA is the angle measured from the v-axis. The cardinal directions are also indicated.

projected baseline length for an observation with coordinates (u, v) is the distance from the origin of the uv-plane, that is

$$B_{\rm proj} = \sqrt{u^2 + v^2}. \tag{2.16}$$

Further, the position of the uv-point is defined by its angle measured from the v-axis, the *position angle* PA (see Fig. 2.4 for an illustration). The position angle is defined as

$$\mathrm{PA} = \arctan\left(\frac{u}{v}\right). \tag{2.17}$$

Coverage of the uv-plane can be achieved in two ways: moving the sky (through rotation of the Earth) and moving the telescopes. The paths followed by the combinations of two telescopes at set stations in the uv-plane as the Earth rotates are called uv-tracks and are illustrated by the curved lines in Fig. 2.4. Fig. 2.4 also shows that by definition, the uv-points only cover 180 degrees and the points are mirrored to cover the entire plane. To reconstruct the source image from the measured visibility according to the van-Cittert-Zernike theorem it is important to sample the uv-plane evenly; that is in all directions and different baseline lengths.

The uv-plane also shows another important feature of optical interferometers: the resolution. The resolution of an optical interferometer can be expressed in two ways. The resolution as derived

from the Rayleigh Criterion, $\zeta_{\mathrm{Rayleigh}}$, as commonly used in optical interferometry, is

$$\zeta_{\mathrm{Rayleigh}} = \frac{\lambda}{2B_{\mathrm{proj}}}. \tag{2.18}$$

On the other hand, considering the ability to distinguish neighbouring fringes, the resolution ζ_{fringe} is merely the inverse of the spatial frequency:

$$\zeta_{\mathrm{fringe}} = \frac{\lambda}{B_{\mathrm{proj}}}. \tag{2.19}$$

Both these expressions are inversely proportional to the projected baseline length. This means that measurements at larger uv-points – longer baseline lengths – provide higher resolutions. Essentially, the projected baseline length is comparable to the diameter of a single aperture telescope when considering the resolution. This also means that different baseline lengths sample different size scales of the source, such that at longer baseline lengths larger scale features get resolved out. In addition, we can see that for a non-spherical sampling of the uv-plane we have different resolving power depending on the direction.

We will now explore how these considerations affect the real usage of optical interferometry. First of all, we are mostly unable to reconstruct images from our complex visibility according to the van-Cittert-Zernike theorem. This is in part due to the fact that we do not have access to the absolute phase of the object, and can only use relative measures such as the closure phase or the differential phase. Nevertheless, these are useful in modelling the source morphology.

Further, we do not have the capabilities of sampling the uv-plane densely enough to successfully reconstruct images in the majority of cases. In millimetre and radio interferometers, which have tens to thousands of stations and provide image reconstruction, signals are first recorded at the individual stations and then interfered electronically where signals can be boosted artificially. In contrast, in optical interferometry the interferometric signal is recorded after physical interference[2], and the light from one telescope is split between each two-pair baseline combination it is involved in. N number of telescopes gives $N(N-1)/2$ baseline combinations, which means that the more telescopes, the weaker interferometric signal becomes. To obtain a reasonably strong interferometric signal for a feasible source magnitude limit, telescope numbers in optical interferometry facilities are limited to a handful. One of these optical interferometry facilities is the VLTI, where one can choose between four Unit Telescopes (UTs, 8.2 m mirrors) or four Auxiliary Telescopes (ATs, 1.8 m mirrors) at a time. This means that one observation only produces six uv-points, which is not nearly enough to reconstruct an image. For faint objects, the UTs are necessary. The UT configuration is static, and three of the four UTs are aligned along one direction. This leads to one direction always being severely under sampled. Sufficient movement in the uv-plane is also limited by practical considerations. uv-coverage through rotation of the Earth means repeated observations over long timescales to fill the uv-plane sufficiently. This might not be possible for intrinsically variable objects, like rotating stars with hotspots, disks around stars

[2] "No one knows the reason for all this, but it is probably quantum." (*Pyramids*, Terry Pratchett)

with brightness asymmetries, and AGN. All of these are major targets for optical interferometry. Moving the telescopes is possible, which is what the AT array exists to serve; although only between nights, so there are still inter-night variability effects. The four ATs are fixed on rails that allow them to be moved to four different array configurations: the small, medium, large, and extended arrays. Unfortunately, the light collecting area of the ATs is not large enough to observe AGN[3] (with exception of NGC 1068 and Circinus).

However, under the assumption of simple geometries and structures, we can successfully model our visibilities and phases and get a good understanding of source morphologies. This is achieved through creating a model image of the source, applying Fourier transforms to the image, and extracting visibilities and phases to fit the data. The basic geometries, such as disks, point sources, rings, power law distributions, binaries, and Gaussian distributions represent the resolvable structures well, especially in combination (e.g Menu et al., 2015; GRAVITY Collaboration et al., 2021c; Corporaal et al., 2021). This is of course enhanced by the vast wavelength range offered by optical interferometry today ($1.6 - 13\,\mu\mathrm{m}$), which allows us to extract temperature and radially stratified structure information.

Nevertheless, the success of this modelling approach heavily depends on the degree of resolution of the object. A resolved object is usually needed to apply this approach. In this case, resolved refers to the fact that the visibility has reached zero for the first time. The Fourier transforms of a lot of common morphologies like disks and binaries behave in an oscillatory pattern, where the (squared) visibility will reach zero and then bounce up and down. These successive bounces are called 'lobes', with the first lobe holding overall structure information, and successive lobes holding more and more detailed morphological information (the first and second lobes are shown in the example visibility curve in Fig. 2.5). To apply this modelling technique in reasonable detail, at least the first lobe should be resolved; however, information can be extracted even with less information as long as assumptions about the source morphology are made.

Let us now consider the sublimation radius of an AGN. The NLS1 I Zw 1 is one of the two main objects of our further study and has a sublimation radius of $\sim 0.2\,\mathrm{pc}$ at a distance of 250 Mpc. Its size in the sky is therefore $0.2\,\mathrm{mas}$. We can also calculate the resolution of our interferometer according to Eqs. 2.18 and 2.19. It is commonly assumed that $2.2\,\mu\mathrm{m}$ (*K*-band) is an appropriate observation wavelength for dust at the sublimation radius. We also consider the longest baseline possible for the UTs, 130 m. This gives us resolution powers of $\zeta_{\mathrm{Rayleigh}} = 1.7\,\mathrm{mas}$ and $\zeta_{\mathrm{fringe}} = 3.5\,\mathrm{mas}$. This is a magnitude larger than the sublimation radius, so we will not be able to formally resolve it. Still, if we observe this object, we will see the visibility decrease with increasing baseline length, but not reach zero. This is a *partially resolved* object, which is the case for the vast majority of AGN we observe. An illustration of this situation is shown in Fig. 2.5, where we plot the visibility curve of a radial power law brightness distribution as observed in the *L*-band, which simulates the dust distribution in AGN. The maximum baseline length of the UT configuration is

[3]It is actually, but the rapid movement of the atmosphere necessitates shorter integration times so the UTs are required for even relatively bright objects. Optical interferometry is just an exercise in continuously losing against the laws of physics.

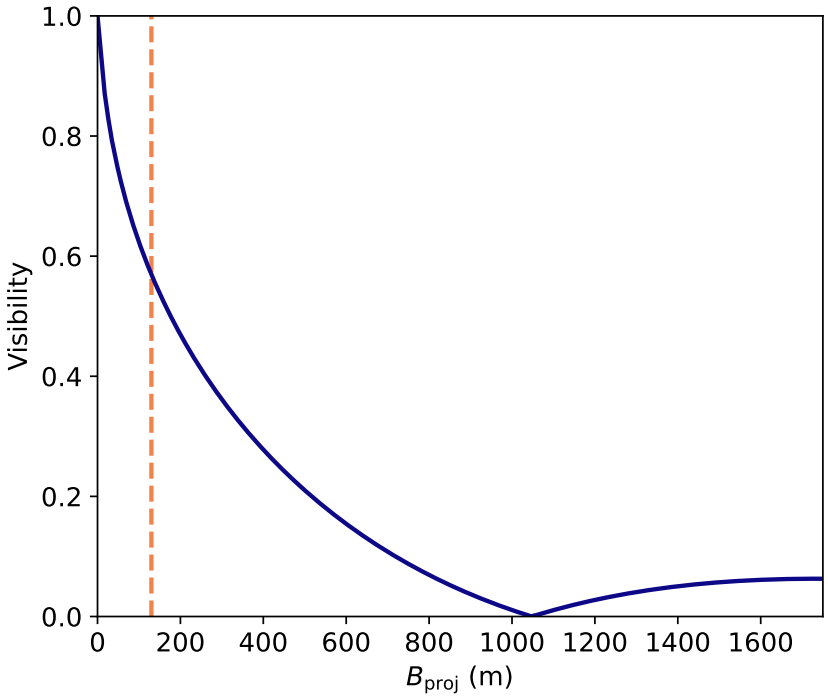

FIGURE 2.5: The visibility curve as a function of projected baseline length B_{proj} in metre of a radial power law brightness distribution with $r^{-2.4}$ in the *L*-band, simulating the dust distribution of an AGN in the *L*-band. The maximum baseline length of the UT configuration of $\sim 130\,\mathrm{m}$ is indicated with the vertical dashed line. Within this limit, this source will only be partially resolved.

indicated with the vertical line, which clearly demonstrates that the observable section of the visibility curve does not reach zero. Nonetheless, this data holds important information. Under the assumption of a simple Gaussian or power law source intensity distribution, we can derive the size of the object[4]. Accordingly, we usually go beyond the nominal resolution limit. In addition, this characterisation does not require a full covering of the uv-plane – usually a few (2 or 3) observations are enough. These are called *snapshot observations* and can also give a first order approximation of the shape of the emission region. This is achieved through comparing the visibility curves along different directions in the uv-plane. If the visibility curve along one direction indicates a larger size than along another direction, the perpendicular direction, that this is a clear indication that the source is elongated in that direction. This can be determined using a simple elliptical model source intensity distribution. This basic measure has proven to be extremely powerful in AGN science. Studies of the dusty torus in the *N*-band with MIDI showed elongations of the dust along the *polar* axis of the AGN (Hönig et al., 2012, 2013; Burtscher et al., 2013; Tristram et al., 2014; López-Gonzaga et al., 2016; Leftley et al., 2018). These observations are in conflict with the classical equatorial toroidal structure of the torus and provided evidence for the existence of the dusty polar outflow (Hönig, 2019). Further, this data analysis was developed without closure phases as MIDI did not deliver closure phases. As aforementioned, another powerful tool to study the morphologies of these structures is the large wavelength range available. This gives access to

[4]The size of an extended astronomical object is often a nebulous concept. Here, we adopt the measure of the half light radius $R_{1/2}$. This is the radius in which half of the light is included.

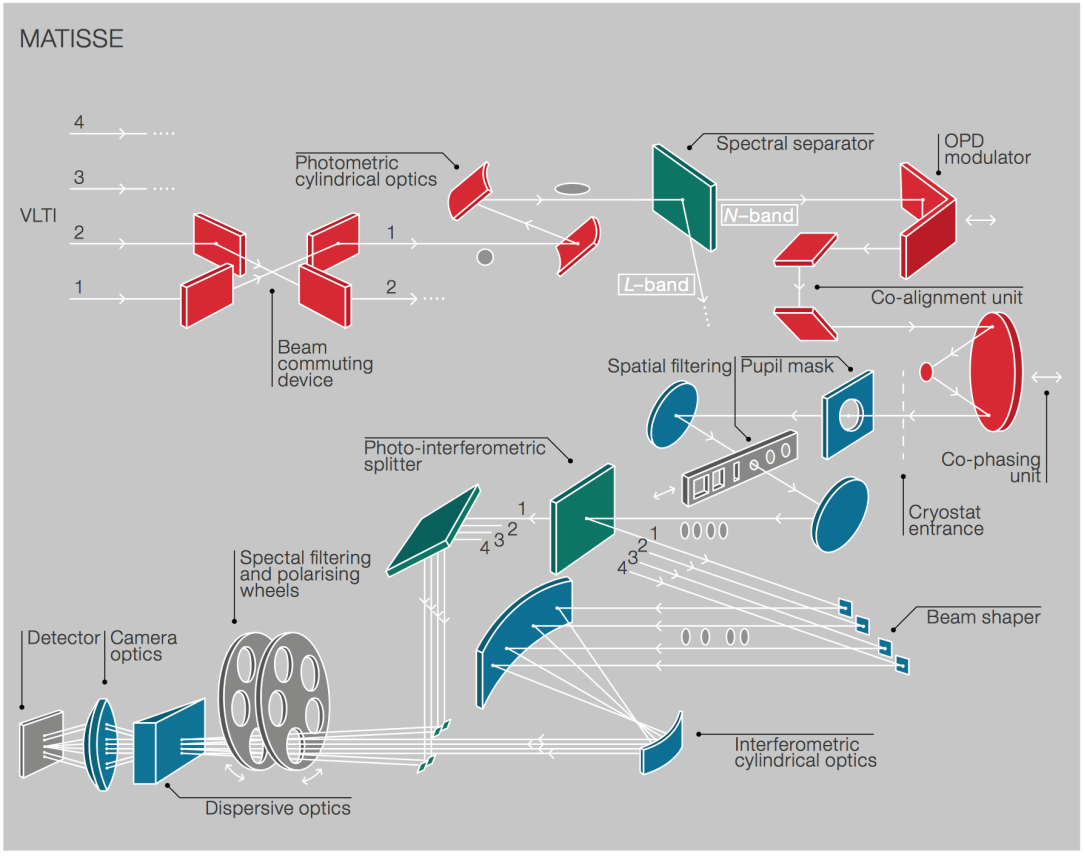

FIGURE 2.6: Schematic of the MATISSE instrument. Taken from Lopez et al. (2022).

the temperature stratified structure, which shows that hotter AGN dust is less extended and more concentrated in the equatorial plane and cooler dust emission is dominated by the polar outflow (GRAVITY Collaboration et al., 2020c; Gámez Rosas et al., 2022; Isbell et al., 2022, 2023; Leftley et al., 2024). Even in the most extreme cases, such as AGN, optical interferometry is a very powerful tool to access the innermost regions and has the potential to redefine our view of AGN.

2.2 MATISSE

MATISSE (Multi AperTure mid-Infrared SpectroScopic Experiment) is the second generation mid-infrared spectro-interferometer at the VLTI (Lopez et al., 2022). The VLTI is the optical interferometry infrastructure at the Very Large Telescope (VLT) on Cerro Paranal in Chile, operated by the European Southern Observatory (ESO). The VLTI collects the light from the four UTs or the four ATs through underground tunnels and delay lines to the VLTI lab, where the instruments are located. Currently, the VLTI lab houses the infrared tilt sensor IRIS, the *H*-band instrument PIONIER, the *K*-band instrument GRAVITY, and MATISSE (Gitton et al., 2004; Le Bouquin et al., 2011; GRAVITY Collaboration et al., 2017). MATISSE is currently the only interferometer that operates in the *LM*-bands ($3-5\,\mu\mathrm{m}$). It also operates in the *N*-band ($8-13\,\mu\mathrm{m}$). Due to the large wavelength difference between these bands, different optics and

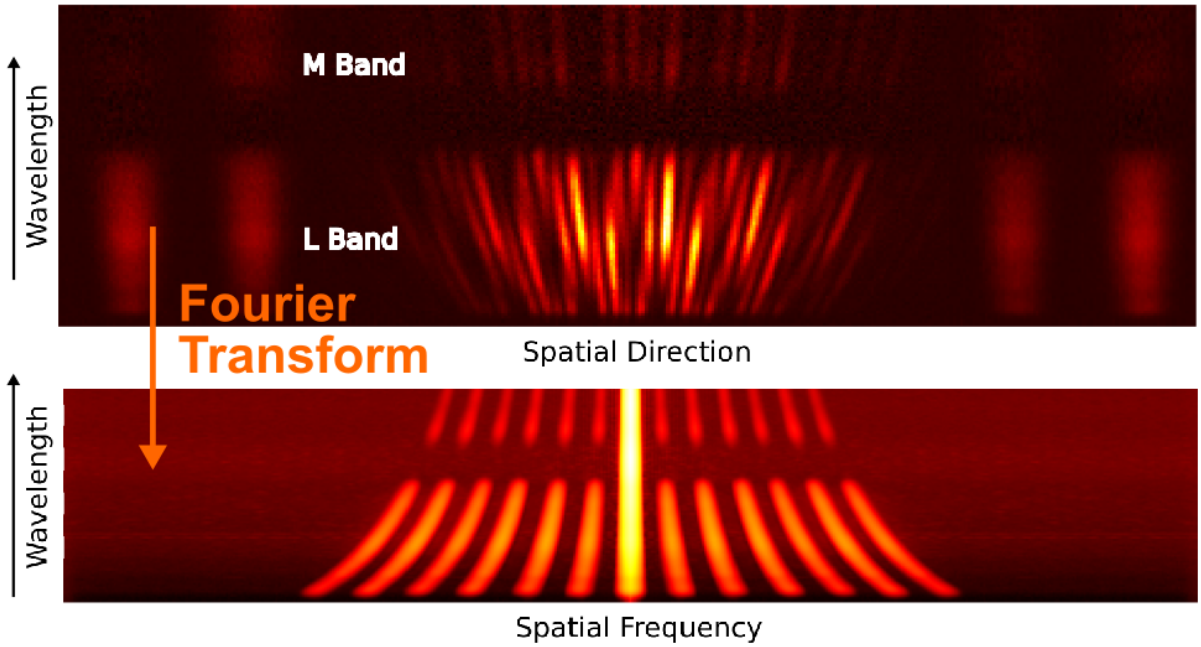

FIGURE 2.7: The interferometric signal as recorded on the detector (upper panel) and the power spectral density distribution (PSD) of the interferometric signal (lower panel). Wavelength increases going up. The x-dimension of the upper panel is spatial direction across the detector, and the x-dimension in the lower panel is spatial frequency. The lower panel is the Fourier transform of the upper one, such that each fringe (peak) contains the signal of one baseline. Due to the spatial encoding applied before combination, the fringes are separated according to $3D/\lambda$, $6D/\lambda$, $9D/\lambda$, $12D/\lambda$, and $18D/\lambda$. The bright peak at the centre that bridges the atmospheric gap is the low frequency white light peak which contains the thermal background and the object's photometry. The rectangular signals at the edges of the upper panel are the photometric signals. Adapted from Lopez et al. (2022).

detectors are used such that the *LM*- and *N*-bands can be observed simultaneously. MATISSE is a multi-axial, all-in-one Fizeau spectro-interferometer. It can provide visibilities, closure phases, and differential phases. First fringes were observed on February 18, 2018. A schematic of the internal optical path of MATISSE is presented in Fig. 2.6.

MATISSE is a multi-axial, all-in-one interferometer. This means that all four beams from the telescopes are combined at once rather than in individual pairs. The beam combination occurs in the camera optics in front of the detector, as shown in Fig. 2.6. To isolate the different beam combinations in spatial frequency space the beams are spatially encoded. This means that the beams are spatially separated from each other in a non-redundant configuration before combination. The beams are separated by distances of by $3D$, $9D$, and $6D$, where D is the beam diameter. The power spectral density (PSD) function of the fringe pattern on the detector is then obtained by evaluating the Fourier transform of the fringe pattern. The six fringe peaks in the PSD – corresponding to the six pairwise combinations of the four beams – are located at the spatial frequencies of $3D/\lambda$, $6D/\lambda$, $9D/\lambda$, $12D/\lambda$, and $18D/\lambda$. Since the beams are spectrally dispersed, they are arranged in a characteristic fanning configuration (Fig. 2.7). The PSD is mirrored exactly across the zeroth spatial frequency. The PSD, i.e. the Fourier transform of the interferometric

signal (the interferogram), per spectral channel is given by

$$\mathcal{I}(u) = M_{\rm B}(u)\sum_{i=1}^{4} n_{{\rm B},i} + M(u)\sum_{i=1}^{4} n_{*i} + \sum_{i=1}^{4}\sum_{j=2,j>i}^{4} M(u-u_j)\mathcal{V}_{ij}\sqrt{n_{*i}n_{*j}}, \tag{2.20}$$

Eq. 1 in Lopez et al. (2022). The modulus of $\mathcal{I}(u)$ is the correlated flux $F_{\rm corr}$; the intensity of the PSD. The telescope beam indices are i and j, with ij indicating telescope pairs. The flux contribution from the thermal background for beam i is $n_{{\rm B},i}$ and the flux from the source is n_{*i} and n_{*j} for the respective beams i and j. $\mathcal{V}_{ij}$ is the complex visibility for the beam combination ij, such that the third term gives the flux for each baseline. This is the flux contained within each fringe peak in the PSD. Here, $M(u-u_j)$ is the relevant instrument function for these fringe peaks (i.e. the fringe envelope). There is also a low spatial frequency fringe peak, called the 'photometry' or white light peak (central peak in Fig. 2.7). This is not the pure photometric signal of the object but is instead a combination of the thermal background emission and the object's photometry (it noticeably bridges the atmospheric gap). It is the combination of the first two terms in Eq. 2.20, with $M_B(u)$ the thermal background transfer function and $M(u)$ the low spatial frequency peak of the instrument transfer function. Focusing the thermal background to the photometry peak keeps it from contaminating the interferometric fringe signal. The spectro-photometric signal of the object is recorded at the edges of the detector in Fig. 2.7 and contains the total flux spectra, one from each telescope.

MATISSE also includes the beam commuting device (BCD). This is located at the entrance of the instrument (see Fig. 2.6). It commutes the beams, that is, it exchanges the beams and the corresponding optical paths in MATISSE through mirrors. For instance, instead of beam 1 going down path 1, it is switched with beam 2 such that beam 1 goes down path 2 and beam 2 goes down path 1. By going through all possible combinations of the set-up, the contribution to the phase shift from the different internal MATISSE optical paths will be cancelled out. The effect of switching of the beams is that the pair-wise fringe peaks also switch positions in the PSD (Fig. 2.7). For example, the beam combination 12 fringe peak now moves to the last peak instead of being the first one. The fringe peak widths get smeared out when moving to larger spatial frequencies. This leads to a lower total fringe intensity collected depending on the fringe peak location. This difference is constant for different BCD set-ups, is known, and can be corrected for. The BCD is made up of two sets of mirrors. These can be in ('IN') the optical path, switching the beams, or out ('OUT') of the optical path. Accordingly, there are four possible BCD positions: OUT-OUT, IN-IN, OUT-IN, and IN-OUT.

2.2.1 MATISSE observation procedure

To understand the data products produced by MATISSE, we must first discuss the MATISSE observation set-up and procedure. MATISSE observations are solely conducted in *Hybrid* mode. In this mode, the *LM*-bands are observed in *SiPhot* mode and the *N*-band in *HighSens* mode (Lopez et al., 2022). In *SiPhot* mode, interferometric and photometric data is taken simultaneously (e.g.

Fig. 2.7) while in *HighSens* mode they are taken consecutively. This is due to limitations of *N*-band detector and set-up, which we will not further discuss as we do not consider the *N*-band here at all and is therefore inconsequential. Each observation consists of 14 exposures, 2 on the sky and 12 on the target. After the sky exposures, 4 exposures are conducted that cycle through all four BCD positions (one exposure per position). These exposures are done without chopping. Chopping is a technique commonly used in infrared astronomy where the object and the sky are rapidly alternatively observed over a number of cycles. This gives an accurate estimate of the background flux (sky and thermal background from e.g. the VLTI tunnels and lab) and is necessary to extract reliable photometry. The next 8 exposures are done with chopping, 4 with the BCD in IN-IN and 4 with the BCD in OUT-OUT. Each exposure is about 1 minute long and consists of *N* detector integrations (NDIT, i.e. frames). Actual integration times (DIT) are limited by the atmospheric *coherence time* (in MATISSE standalone[5]). The coherence time is the time over which the atmosphere is stable. For interferometric observing conditions, coherence times above $4\,\mathrm{ms}$ are considered 'good'. The DIT for observations used here is 0.111 s. Typically, accounting for detector read-out time, each exposure consists of ~ 200 frames on target, but of course half that when chopping.

2.2.2 MATISSE pipeline

The MATISSE data reduction pipeline is described in the MATISSE Pipeline User Manual v2.2.0[6]. Here we outline the process, paying specific attention to the first part contained in the master recipe `mat_raw_estimates` which extracts the raw interferometric observables and is applied both to the science target and any calibrator observations. All steps therein are applied frame by frame unless stated otherwise. The input for the pipeline is the interferogram, i.e. the raw detector image (upper panel in Fig. 2.7). First, the raw interferogram is calibrated to correct for detector and instrument effects, resulting in the calibrated interferogram. This includes application of the flat field, bad pixel, non-linearity, and spectral distortion maps. Next, the photometric breams (see Fig. 2.7) are extracted from the calibrated interferogram. The κ-matrix, which describes the linear transformation of the photometric intensities into the interferometric beams, is used to derive the photometric contribution to the interferometric beams. In addition, the photometric beams are extracted and the background signal obtained from chopping is subtracted. The calibrated interferogram is then Fourier transformed to produce the uncontaminated calibrated correlated flux (contained in the OBJ_CORR_FLUX files). The OPD is estimated from the correlated flux. Next, the correlated flux is processed through incoherent or coherent processing.

MATISSE offers two different types of products, the incoherent and coherent estimators. Coherent estimators rely on knowledge of the atmospheric OPD contribution, such that the frames can be

[5]MATISSE now offers a mode in which GRAVITY tracks and stabilizes the fringes, allowing for longer integration times and therefore increased sensitivity in the *LM*-bands (GRA4MAT, Woillez et al., 2024). Observations used in this work were made before the implementation of GRA4MAT, so we only consider the performance of MATISSE working alone, called MATISSE standalone.

[6]MATISSE Pipeline User Manual v2.2.0

aligned by phase before summing. For incoherent estimators, frames are added blindly. Incoherent processing gives lower signal-to-noise ratio but does not need the atmospheric OPD. Estimation of the atmospheric OPD is difficult, requires knowledge of the atmospheric behaviour, and can carry large amounts of uncertainties; coherent processing can also degrade the signal significantly if not calculated carefully. In contrast, incoherent processing is simpler and more robust, so we use the incoherent estimators. The most pertinent of these products is the squared visibility calculated as

$$V_i^2 = \frac{\sum_u \langle |F_{\rm corr}(u_i, \lambda, t)|^2 - \beta \rangle_t}{2 \sum_x \langle F_{{\rm tot},a} \cdot F_{{\rm tot},b} \rangle_t}, \tag{2.21}$$

taken from the MATISSE Pipeline User Manual v2.2.0. The squared visibility V_i^2 is evaluated for the baseline i with u_i the corresponding spatial frequency of that measurement. $F_{\rm corr}$ is the correlated flux, i.e. the integrated intensity of the fringe peaks, with a bias estimate β that corrects for white noise. The total photometric fluxes are given by $F_{{\rm tot},a}$ and $F_{{\rm tot},b}$, also referred to as *total flux*. The averages are evaluated over time t, which means they are averaged over all frames. As expected, this is simply the squared normalised visibility from Eq. 2.10.

When incoherent processing is performed in the pipeline (recipe `mat_proc_incoher`) the uncontaminated complex correlated flux and extracted photometric beams (which give the total flux) to calculate the raw squared visibilities according to Eq. 2.21, contained in the file RAW_VIS2. In addition, the total flux spectra are output into RAW_SPECTRUM and the closure phases are calculated. Alternatively, the correlated flux can be incoherently estimated; in this case RAW_VIS2 contains the correlated flux and only the closure phases are additionally calculated. Coherent processing (`mat_proc_coher`) outputs the raw visibility and differential phases. At the end of the first part of the pipeline, all raw interferometric observables are concatenated to be further processed. The second part of the pipeline, `mat_cal_oifits`, calibrates these interferometric observables and concatenates them into the finished data products.

2.3 A New MATISSE Data Reduction Method for Faint Objects

The vast majority of AGN observed using MATISSE are 'faint', that is close to the detection limits of MATISSE. For example, the objects studied in this work have *L*-band fluxes of $\sim 0.1\,{\rm Jy}$ and *M*-band fluxes between $\sim 0.1 - 0.2\,{\rm Jy}$ (Kishimoto et al., 2011b; Shangguan et al., 2018). In contrast, the best weather condition MATISSE standalone flux limits in the *LM*-bands for low resolution are $0.06\,{\rm Jy}$ and $0.5\,{\rm Jy}$ respectively. Observing in low flux conditions close to the limit amplifies statistical and instrumental effects. From the outset, we are positively biased in correlated flux and visibility measurements as we cannot measure negative fluxes[7]. Atmospheric turbulence, short integration times, and instrumental effects make the spread in the observed correlated flux

[7] Interferometric signals can be negative, but these cannot be measured. Consider a disk; according to the van-Cittert-Zernike theorem, the interferometric signal is the Fourier transform of the disk, which is a Bessel function and goes negative at points. For a detailed discussion on how this affects the analysis of resolved objects see Varga et al. (2024).

distribution of faint objects quite large (Fig. 2.9). An important instrumental effect varying on short timescales that also broadens the correlated flux distribution is the adaptive optics (AO). Adaptive optics perform poorly for faint objects, which leads to lower coherence and sensitivity to atmospheric turbulence. This correlated flux distribution is also very skewed, with a peak at low fluxes and a long high flux tail (Fig. 2.9). Therefore, averaging fluxes according to the incoherent squared visibility or correlated calculated by the official MATISSE pipeline in Eq. 2.21 and contained in RAW_VIS2 will introduce an additional positive bias. The average of this distribution is not a good estimator of the peak position and overestimates the peak. This implies that in worst case scenarios, a partially resolved object (visibilities at longer baselines < 1) will not be recognised as such because visibilities are overestimated. Therefore, we decide not to use the squared visibilities/correlated flux contained in RAW_VIS2. We correct for and remove these statistical and instrumental contributions when reducing the data using a bootstrapping method. This method allows us to leverage a larger amount of the data, including the 'low quality' parts, and base our results on a robust statistical foundation.

In this section, we will describe this data reduction method, starting with a discussion of calibrators, observations, and intermediate MATISSE pipeline products. Then we discuss our methods for background removal, flagging, fringe masking, and BCD corrections. After, we explain our approach to deconvolving the science target's correlated flux distributions through resampling the calibrator's correlated flux distributions. Finally, we describe the final calibrations and visibility calculations.

2.3.1 Calibrators, observations, and intermediate MATISSE pipeline products

The observing strategy for infrared interferometric observations of AGN generally includes two different calibrator stars, the bright and the red. The bright calibrator is an A, G, or K star that has good AO performance due to its optical brightness. We use the bright calibrator to determine the fringe peak positions and create the masks to isolate the fringe peaks due to its high signal-to-noise ratio. However, as these stars are optically bright, they quickly fall off in the IR and have steep IR SED slopes. This causes flux at shorter wavelengths to be overweighted. Calibration will then make the AGN slopes bluer. To account for this we use 'red' calibrators, which are red M giants. These have similar slopes in the IR to AGN. However, they are also fainter with poorer AO performance, but not as faint as AGN. Observation sequences for AGN are usually CAL-SCI-RED, with possible additional AGN observations tacked on as SCI-RED. CAL refers to the bright calibrator, RED to the red calibrator, and SCI to the science target, i.e. the AGN.

Preliminary data reduction is performed using the MATISSE pipeline in incoherent mode. The `mat_raw_estimates` task provides several intermediate products, most pertinently OBJ_CORR_FLUX, RAW_SPECTRUM, and RAW_VIS2, all of which are uncalibrated. We use the correlated flux contained in OBJ_CORR_FLUX in our data reduction, which we obtain by taking the modulus of the real and imaginary components of the Fourier transform. RAW_SPECTRUM contains the spectro-photometry, i.e. the total flux spectra from the four telescopes. We only use the chopped spectra for total flux determination. RAW_VIS2 contains the

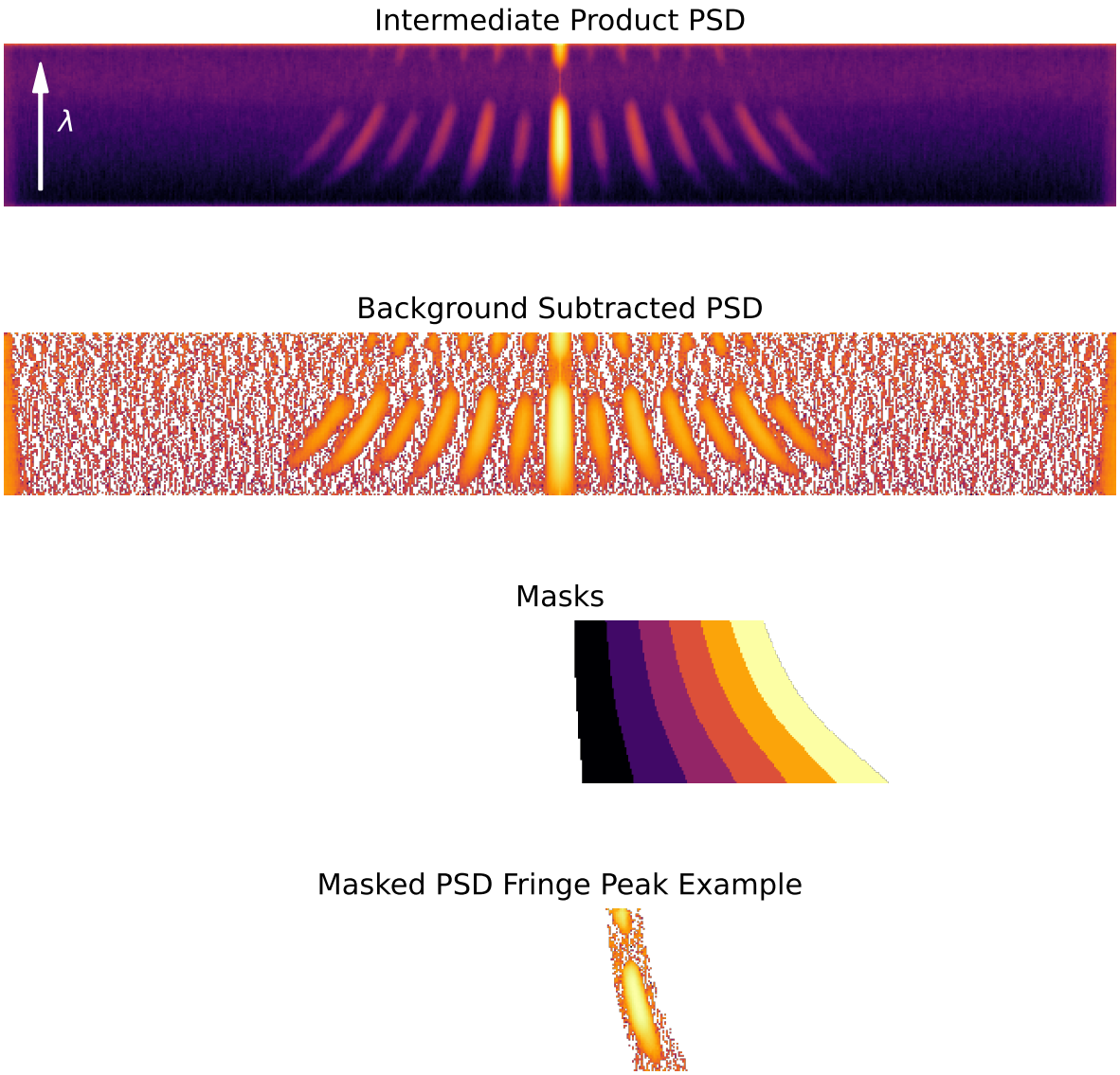

FIGURE 2.8: The initial data reduction steps, top to bottom. The first panel shows the intermediate product of the MATISSE pipeline: the median PSD of one exposure, flat-fielded and dark and sky-subtracted. The chromatic background signal is very noticeable. The second panel shows the PSD but with this chromatic background subtracted. The third panel shows the fringe peak masks which are described in Section 2.3.2. The last panel shows an example of a masked fringe peak.

incoherently calculated squared visibilities/correlated flux; we only extract the uv-coordinate information it also holds. The fringe peaks are separated into the *L*- and *M*-bands; *L*-band: $3.0 - 3.8\,\mu\mathrm{m}$, *M*-band: $4.5 - 4.9\,\mu\mathrm{m}$. All following steps are done for the science target and the red calibrator equally, unless stated otherwise.

2.3.2 Background removal and fringe masking

The fringe peaks have a chromatic background signal (see the first panel in Fig. 2.8). We evaluate this background based on the median of all frames, per exposure. The signal-to-noise ratio of the

median is high enough to distinguish between the fringes and the background. This is done per wavelength bin, independently for each bin. First, we approximately mask out the fringe peaks and then smooth and fit the remaining background signal. We then subtract this chromatic background from each frame individually. Next, we also flag wavelength bins with low signal-to-noise ratio in the peak. Again, this is applied to each wavelength bin independently, flagging bins where the signal-to-noise ratio of the peak is less than 2. Additionally, each fringe peak (i.e. baseline combination) is here treated independently such that there are six different signal-to-noise flagging maps per frame, one for each peak.

The masks to extract the fringe peaks are created using the bright calibrator as it has the highest signal-to-noise ratio. Independent masks are created for each exposure, matching the exposures with the same set-ups to the red calibrator and science target. First, we create the background signal as described above and subtract it from the median of the bright calibrator exposure. We then use the dispersion relation for the fringe peaks from the spatial encoding to determine the positions of the fringes. We estimate the beam diameter in pixel coordinates for each fringe, anchoring the dispersion relations. This is achieved by finding the maximum correlated flux in a certain wavelength bin and using the corresponding position to get the beam diameter:

$$D_i[\mathrm{m\,pix}] = \lambda_D[\mathrm{m}]\, p_{\mathrm{max},i}[\mathrm{pix}]/F_i. \tag{2.22}$$

D_i is the beam diameter for fringe peak i, λ_D is the wavelength of the particular wavelength bin, and $p_{\mathrm{max},i}$ is the position of the maximum flux in that wavelength bin in fringe peak i. F_i is the spatial encoding factor for the fringe peak, i.e. 3, 6, 9, 12, 15, or 18. The edges of the fringe peak masks are set halfway between neighbouring fringe peaks, at a relative distance of $\Delta F = 1.5$. The edges of the fringe peaks, $u_{i,\mathrm{low}}$ and $u_{i,\mathrm{high}}$, are given by

$$u_{i,\mathrm{low}} = (F_i - \Delta F)\lambda/D_i \text{ and } u_{i,\mathrm{high}} = (F_{i+1} - \Delta F)\lambda/D_{i+1}. \tag{2.23}$$

An example of the fringe peak pattern and the corresponding masks can be seen in Fig. 2.8.

2.3.3 BCD correction

There are two main ways to combine the data of the different exposures in an observation: after the final calibrated visibilities or before calibration. As the BCD switches the fringe peaks in which the individual beam combinations are contained within, it also switches the amount of flux registered in the fringe peaks. This is because the width of the peaks is wavelength-dependent and a function of subsequently higher products of three. This means that the outer fringe peaks will disperse more than inner. Therefore, the correlated fluxes of a particular beam combination cannot be blindly combined. One way to correct for this is to apply the whole data reduction and calibration for each exposure separately, matching these to the same calibrator exposure. This should get rid of any BCD position effects as they are present in both the target and the calibrator, cancelling out. However, only a relatively small number of frames are available, which can have

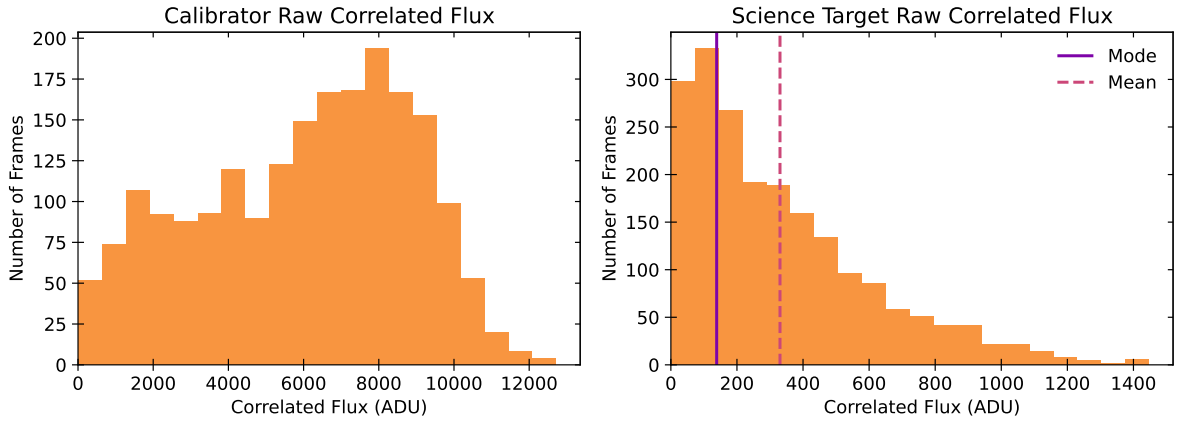

FIGURE 2.9: The raw flux distributions for the red calibrator (left) and the science target (right). Also indicated for the science target is the position of the mode and the mean to characterise the distribution, with the mean clearly skewed by the long high flux tail and the mode representing the peak of the distribution better.

large effects on the statistics. This is especially relevant to us as we want to deconvolve the correlated flux distribution. We can also combine the correlated flux measurements from all exposures before calibration, using the BCD corrections. These BCD corrections correct the flux offsets due to the beam spreading of a single beam combination between different BCD positions with respect to one BCD position, OUT-OUT. To estimate this factor, a large sample of calibrators was taken and the ratio of each BCD position and OUT-OUT was calculated, which is the conversion factor between that BCD position and OUT-OUT with wavelength. This is mostly linear with wavelength so it was fit with a line for a given wavelength range (e.g. *L*-, *M*-, or *N*-band). With this, we correct the flux from the BCD positions IN-IN, IN-OUT, and OUT-IN with respect to OUT-OUT. This then allows us to collate all frames from all exposures, giving us a much larger data set to perform the rest of the data reduction on. We have observed that our method provides much better results when correcting for BCD effects at the beginning.

2.3.4 Resampling

Atmospheric turbulence and instrumental effects are convolved with the 'clean' correlated flux distribution, resulting in the observed and skewed correlated flux distribution. The main effects are instrumental: the quality of the AO correction and the fringe tracking, which differ between the calibrator and the science target, as well as on a frame-by-frame basis. These effects depend on the coherence time. The shorter the coherence time, the more stochastic noise is added, which results in a bias floor that needs calibrating out. To calibrate this out we effectively match the noise properties between the science target and calibrator distributions by resampling the calibrator distribution. We resample the calibrator correlated flux distribution such that it looks like the science target distribution. In effect, our resampled calibrator distribution RD is given by

$$RD = CD \circledast TF \Rightarrow RD(p) = \int_p CD(p')TF(p-p')\mathrm{d}p'. \tag{2.24}$$

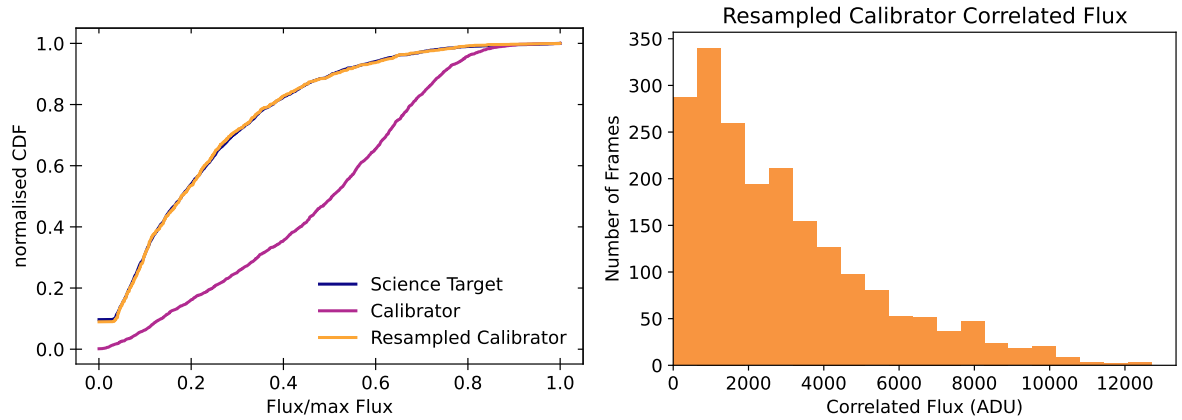

FIGURE 2.10: The CDF of the science target, raw calibrator, and resampled calibrator distributions (left), and the resampled calibrator flux distribution (right).

The resampled distribution is the convolution of the calibrator distribution CD and a transfer function TF. In practice, we accomplish this by resampling the calibrator distribution such that its cumulative distribution function (CDF) matches the CDF of the science target distribution.

We obtain the correlated flux distributions by taking the median of the *L*-band flux over the entire band. Each fringe peak in each frame therefore has one corresponding flux value. Six distributions are built, one for each baseline (example in Fig. 2.9). We then calculate the CDFs of the distributions, normalised by the maximum flux. The science target CDF is a function of $F_{\mathrm{SCI}}/F_{\mathrm{SCI,max}}$ and the calibrator CDF is a function of $F_{\mathrm{CAL}}/F_{\mathrm{CAL,max}}$. This assures that both CDFs are on the same scale as the calibrator flux is higher by at least a magnitude. We then generate a random number between 0 and 1 to choose a CDF value for the science target CDF. Next, we find the $F_{\mathrm{SCI}}/F_{\mathrm{SCI,max}}$ that corresponds to this CDF position. We then look for the closest observed $F_{\mathrm{CAL}}/F_{\mathrm{CAL,max}}$ value to the $F_{\mathrm{SCI}}/F_{\mathrm{SCI,max}}$ value. This $F_{\mathrm{CAL}}/F_{\mathrm{CAL,max}}$ value is returned into the flux dimension and both flux and the associated frame are saved. This is done until the resampled distribution has the same size as the original calibrator distribution. Both the resampled calibrator distribution and the science target distribution are now the same, as are the corresponding CDFs (Fig. 2.10). Only the *L*-band is used for resampling as it has a higher signal-to-noise ratio. Instrumental effects in the *M*-band are the same as they situated next to each other on the same detector. Therefore, the resampled distributions can be applied to the *L*- and *M*-band equally.

We now match the frames, that is, match a science target frame to a resampled calibrator frame. This science target frame will then be calibrated using the matched calibrator frame, applying frame by frame calibration. We match the frames by matching their distance to the mode of the distribution. The mode of the science target distribution is found, and the distance normalised with respect to the mode from the science target frame to the mode is evaluated. Then the mode of the resampled calibrator distribution is determined, and a frame is found that has the same normalised distance to the mode. A single calibrator frame can be the match for multiple science frames. Frame matching is done for *L*- and *M*-band separately.

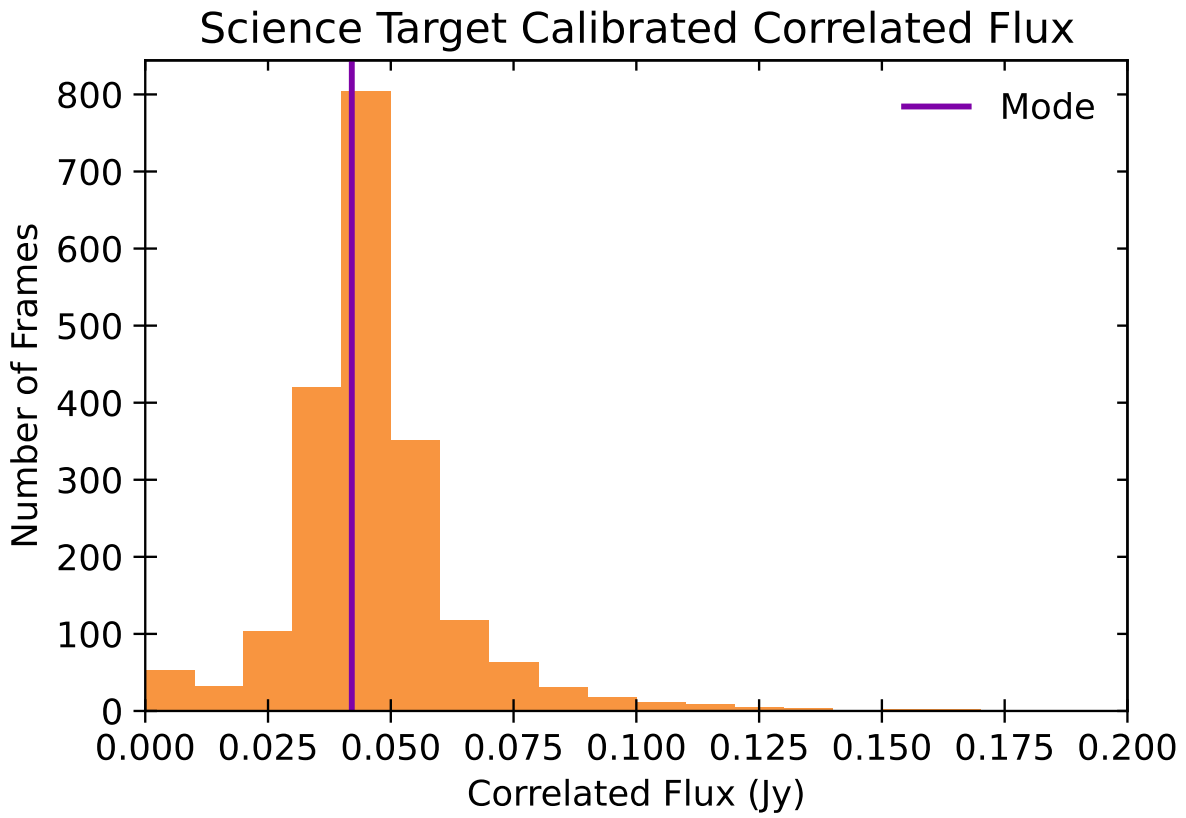

FIGURE 2.11: The calibrated correlated flux distribution. The correlated flux is characterised using the mode as indicated.

2.3.5 Calibration and visibility calculation

Finally, we calibrate the correlated and total fluxes and calculate the visibility. Based on Eq. 2.10, the visibility $V(\underline{u})$ for the different baselines is simply given by

$$V(\underline{u}) = F_{\mathrm{corr}}(\underline{u})/F_{\mathrm{tot}}, \tag{2.25}$$

where $F_{\mathrm{corr}}(\underline{u})$ is the correlated flux of the different baselines and F_{tot} is the total flux. The *LM*-band fluxes of the calibrator are estimated through a black body fit to available photometry. *LM*-band spectra are extracted using a linear fit over the corresponding wavelength ranges.

As aforementioned, we calibrate the correlated flux frame by frame, matching science target frames to calibrator frames. Frames are calibrated individually to retain as much information as possible before collapsing the data. In contrast to the resampling, this is done spectrally dispersed, that is we calibrate the correlated flux spectra. This accounts for the calibrator and the science target having different slopes in the infrared. Next, we take the median over the entire *L*/*M*-band again, per baseline per frame to increase the signal. This gives us the final calibrated correlated flux distributions as seen in Fig. 2.11. Compared with the raw distributions in Fig. 2.9, the calibrated correlated flux distributions are now well defined. In addition, correlated flux values are well below the nominal MATISSE limits. This demonstrates the power of our method to characterise the

faintest MATISSE objects. To characterise these distributions and find the overall correlated flux for each baseline, we use the mode of the distribution. The mode characterises the peak better than the mean. We sigma-clipped the correlated flux distribution with a sigma limit of 2 (removing all frames outside of this limit) and calculated the new standard deviation, which we use to estimate the uncertainties in the correlated flux.

Next, we calibrate the total flux. The raw total flux is contained within the RAW_SPECTRUM files, and is recorded from each of the telescopes, such that there are four total flux spectra per frame. We only use exposures with chopping. For calibration, we use the mean calibrator flux over all relevant frames and exposures per telescope, i.e. we calibrate each telescope separately. We then calibrate each science target total flux frame individually, matching the corresponding telescopes. The total flux spectrum per telescope is calculated as the median of all frames. A final total flux spectrum is then calculated from the four telescope spectra, with the error given by associated standard deviation. To calculate the visibilities, we collapse the total flux in the spectral direction as we did the correlated flux, taking the median over the entire L/M-band respectively.

The visibility is calculated using Eq. 2.25 for all baselines and the LM-bands. The uncertainty in the visibility is the propagation of the correlated flux error, under the assumption that the correlated flux error dominates over the error on the total flux. We further determine the projected baseline lengths and the position angles as described in Section 2.1.4. The results for the main set of data that will be analysed in this thesis are plotted in Fig. 2.12 compared to the outputs from the official MATISSE pipeline. Note that our analysis is done on visibility as shown in the figure, while the MATISSE pipeline works on the squared visibilities. The uncertainties in our data reduction method are more representative of the scatter in the data than from the MATISSE pipeline. Further detailed discussion of the data is presented in the next chapter.

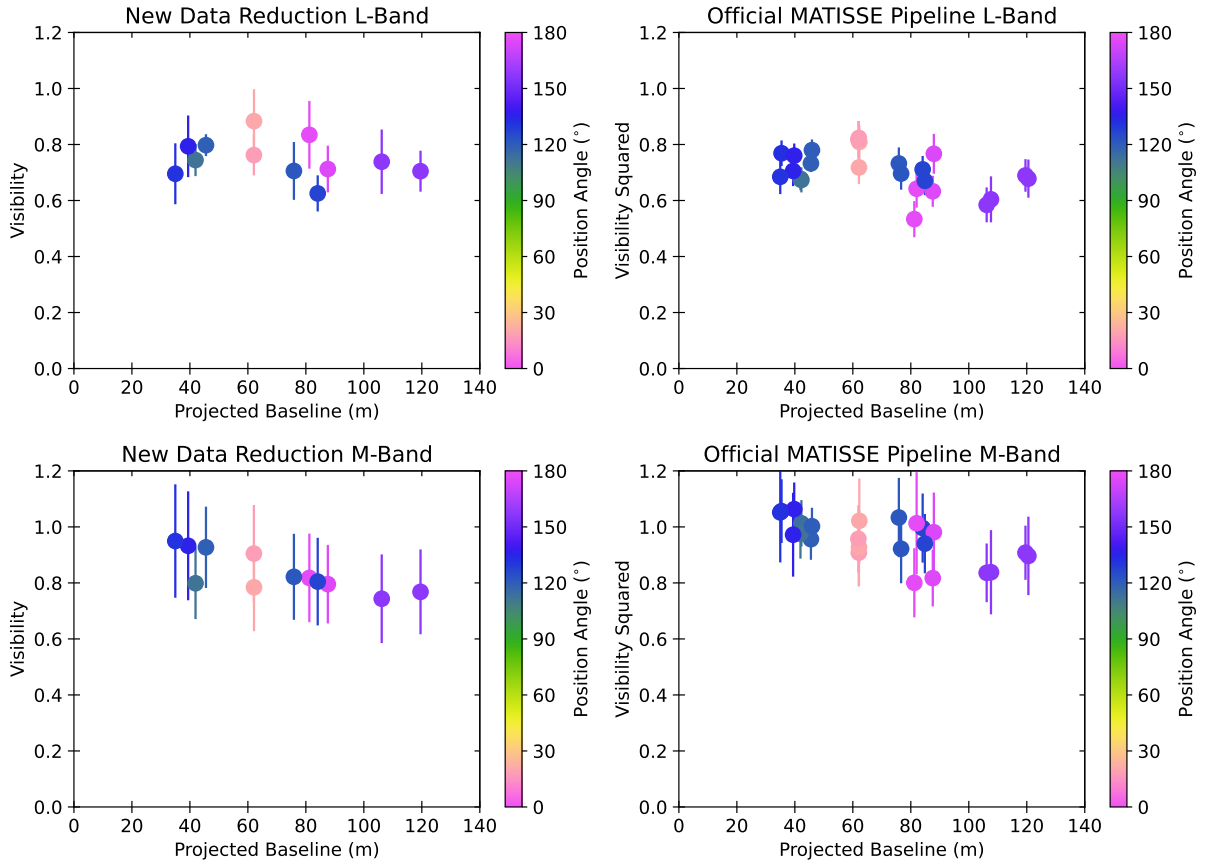

FIGURE 2.12: Comparison between the official MATISSE pipeline products (right, in visibility squared) and the products of our new data reduction method (left, in visibility). There are more data points in the MATISSE pipeline products because these have been reduced per BCD positions.

Chapter 3

I Zw 1 and H0557-385: the dusty tori of two high Eddington AGN observed in the MATISSE *LM*-bands

> He'd learned in recent days, though, that rather than drown in uncertainty it was best to surf right over the top of it.
>
> *Mort*
> Terry Pratchett

In this chapter we investigate the inner structure of the dusty torus in two highly accreting AGN. In particular, we examine high angular resolution optical interferometric observations with MATISSE in the *LM*-bands ($3.5 - 4.6\,\mu\mathrm{m}$). At these wavelengths, we expect to observe the putative dusty wind launching region. Therefore, high angular resolution observations of this region can tell us about its structure and how these are related to the accretion rate. These are the first published MATISSE observations of Seyfert 1 AGN, and the first published optical interferometric observations in the *LM*-bands of Seyfert 1s. This chapter contains the work published in Drewes et al. (2025).

I led this study and was responsible for developing the data reduction for the MATISSE data (described in Section 2.3), analysing the data, modelling the SEDs, and assembling the results. The discussion is based on my own work as well as input from my co-authors: James H. Leftley, Sebastian F. Hönig, Konrad R. W. Tristram, and Makoto Kishimoto. The GRAVITY team kindly provided the reduced I Zw 1 GRAVITY data before publication (GRAVITY Collaboration et al., 2024). This work is based on observations collected at the European Southern Observatory under ESO programmes 085.C-0172, 0105.B-0346(A), and 1103.D-0626(C). The raw data is publicly available from the ESO Science Archive Facility at archive.eso.org. The CAT3D-WIND suite of models used in this work are publicly available at cat3d.sungrazer.org (Hönig & Kishimoto, 2010, 2017).

3.1 Introduction

Active galactic nuclei are some of the most powerful objects in the universe, yet much of their defining structure is highly concentrated to the central few parsecs of their host galaxies. These spatial scales have made it difficult to study the central engine (the supermassive black hole and the accretion disk) and its surrounding material. The dusty material is concentrated in the so-called dusty 'torus', the obscuring medium, a few tens of parsecs across. The gas and dust in this obscuring medium are a source of material for the accretion disk and provide a feedback connection to the rest of the galaxy. This obscuring medium was first proposed by Antonucci & Miller (1985) based on the idea that the viewing angle and an axisymmetric obscuring medium are responsible for the differences between Type 1 and Type 2 Seyferts. Observations show that the composition in the hotter, inner part of the torus is dominated by large graphite grains (e.g. Kishimoto et al., 2007). Assuming dust is accreted from the host galaxy with an originally standard ISM dust composition, this implies that both grain size and composition will be radially stratified (Hönig, 2019).

High-resolution infrared interferometry has enabled us to directly resolve the dusty tori in several nearby galaxies. In particular, data from the former mid-infrared interferometer on the VLTI, MIDI (MID-infrared Interferometer, Leinert et al. 2003), has indicated that this torus has a two-component structure: an equatorial disk and a polar outflow cone (e.g. Hönig et al., 2012, 2013; Burtscher et al., 2013; Tristram et al., 2014; López-Gonzaga et al., 2016).

Recently, the second generation VLTI instruments GRAVITY (*K*-band, GRAVITY Collaboration et al. 2017) and MATISSE (*L*, *M*, and *N*-band, Lopez et al. 2022) have provided high quality data to enable the reconstruction of images of the central few parsecs in AGN for the first time. The hottest dust near the sublimation radius (at temperatures of $\sim 1500\,\mathrm{K}$), as traced by GRAVITY, is inferred to be showing an equatorially oriented ring in Type 1 AGN (GRAVITY Collaboration et al., 2020b). MATISSE imaging of NGC 1068 and the Circinus Galaxy illustrates the multi-phase structure of the dust: the hotter dust imaged in the *L*- and *M*-bands, whilst still showing a polar extension, is significantly more concentrated and more luminous in the equatorial directions (Gámez Rosas et al., 2022; Isbell et al., 2023; Leftley et al., 2024). Finally, *N*-band data clearly shows the elongated polar structures in these objects (Gámez Rosas et al., 2022; Isbell et al., 2022; Leftley et al., 2024). This implies that the hot, near-IR emitting dust is located close to the sublimation region in the plane of the accretion disk. In contrast, the cooler mid-IR dust is divided into two components, an equatorial disk and a polar outflow, with most of the flux located in the polar region (Hönig et al., 2012; Hönig, 2019).

High spatial resolution ALMA imaging has revealed dusty molecular tori that are preferentially aligned perpendicular to the AGN axes (Combes et al., 2019; Alonso-Herrero et al., 2021; García-Burillo et al., 2021). As these are disconnected from the galactic disk, they appear to be the larger scale (median radius $\sim 42\,\mathrm{pc}$) and lower temperature components of the equatorial dusty disk. In these structures, thermal dust emission is responsible for the majority of the $870\,\mu\mathrm{m}$ continuum flux. The same structure is found in a variety of molecular lines as well.

Radiation-hydrodynamic simulations have confirmed this arrangement. Radiation pressure launches winds at the inner edge of the dusty disk, forming a hollow polar cone (Wada et al., 2016; Chan & Krolik, 2016, 2017; Williamson et al., 2019). Using detailed radiative transfer modelling of a multi-wavelength and resolution data set of the nucleus of the Circinus Galaxy, Stalevski et al. (2019) managed to reproduce existing images with a dominant hollow polar cone. However, this is not the case for all AGN – simulations and observations imply a combination of dust densities and AGN accretion rates, above which dust will be blown out before it can be launched in a polar wind (Ricci et al., 2017b, 2023; Venanzi et al., 2020; Alonso-Herrero et al., 2021; García-Burillo et al., 2021). Increasing the accretion power at more moderate levels ($\dot{m}_E < 0.1$) will widen the opening angle of the cone, decreasing the prominence of the polar elongation (Williamson et al., 2020).

So far, the focus in interferometry studies of the polar winds has been AGN in the mid-Seyfert regime ($\dot{m}_E \lesssim 0.05$). AGN in the blowout region (see Fig. 4 in Alonso-Herrero et al. 2021), especially with high accretion rates, have been undersampled, due to the severe flux limitations in VLTI observations. These limitations have led us to speculate about dust structure in powerful AGN. Leftley et al. (2019) tentatively found that as Eddington ratio increases, the resolved source fraction increases with respect to the unresolved source fraction in the *N*-band, where the polar outflows are strongest. This implies that in strong AGN, more dust is blown into the dusty winds by radiation pressure. For the hot dust in the near-IR, GRAVITY Collaboration et al. (2020b) found that two luminous quasars with $\dot{m}_E \sim 1$ have sharply peaked dusty emission profiles and comparably small hot-dust sizes. This contrasts with the other, lower luminosity AGN in their sample, which have more extended emission profiles and larger dust sizes. These are signs that the structure of the dust, including relative sizes and other parameters, evolves with Eddington ratio. With the new generation of VLTI instruments it is now possible to go fainter and expand our high-Eddington sample.

Studying the high end of the AGN accretion parameter space is important to constrain the physical mechanism that govern the dust structure in AGN. It has been shown that the accretion rate has a large impact on the inner parts of AGN structure, in particular the nature of the accretion flow and observed SED shapes and outflow properties (e.g. Czerny et al., 2003; Temple et al., 2023). This is arguably related with a change in underlying accretion physics at Eddington ratio of approximately $0.1 - 0.3$. Here, we are interested in tracing changes of the circumnuclear dusty structure with accretion rate and extend IR interferometric studies from the low Eddington regime at $\dot{m}_E < 0.3$ to high Eddington ratios > 0.3. For this purpose we have observed two sources with high Eddington ratios.

I Zw 1 is the prototypical narrow line Seyfert 1, at a redshift of ~ 0.061 (255 Mpc) (Asmus et al., 2016). Its black hole mass is estimated between $\log M_{\rm BH} \sim 6.97 - 7.16$, based on reverberation mapping and line width results respectively (Hao et al., 2005; Huang et al., 2019). It is accreting at super-Eddington rates of $\dot{m}_E \sim 2.14$ (Hao et al., 2005). This puts it very clearly into the blowout region shown in Fig. 4 in Alonso-Herrero et al. (2021), making it an ideal object to study the importance of strong accretion.

H0557-385 is also a Seyfert 1 galaxy, until now mostly studied in the X-ray, at redshift $z = 0.034$ and at a distance of 157 Mpc (Coffey et al., 2014; Leftley et al., 2019). The black hole has an intermediate mass, measured at about $\log M_{\rm BH} \sim 7.81$ using Hβ line widths. With an accretion rate of $\dot{m}_E \sim 0.4$ it also belongs to the higher accreting objects (Coffey et al., 2014). In addition, its infrared spectrum shows a significant bump in the *L*- and *M*-bands, which was not explainable using the MIDI *N*-band data (Kishimoto et al., 2011b). We will investigate the source of this SED feature in this paper.

In this work we investigate the dust structure in these two high-accretion AGN, specifically with regards to the presence and/or orientation of the polar wind and the inner disk structure, using high angular resolution mid-IR interferometry data from MATISSE. Both AGN have been previously observed in the *N*-band using MIDI, but failed to show any prominent elongations (Kishimoto et al., 2011b; Burtscher et al., 2013; López-Gonzaga et al., 2016). GRAVITY data also exists for I Zw 1, which will provide a more coherent view of the multiphase structure of the dust. To examine the physical mechanisms in those sources, we also performed SED fits and produced model images using CAT3D-WIND to compare to our observations (Hönig & Kishimoto, 2017). In Section 3.2, we will present our data acquisition and reduction, specifically with regards to MATISSE. In Section 3.3, we will explain our SED modelling procedure and our model image creation. In Section 3.4, we will collate our results, and compare our data with our mock observations of the model images. In Section 3.5, we will discuss these results in the context of prior interferometric studies of the dusty torus as well as what our modelling and observations tells us about the physical wind launching mechanism.

3.2 Data and Data Reduction

In the following section, we describe our data acquisition and reduction for the interferometric data. We also present the photometric and spectroscopic data we collected from the archives to build our SEDs. Finally, we discuss the geometric model that we used to derive sizes from the interferometric data.

3.2.1 Interferometry

3.2.1.1 MATISSE

MATISSE observations for I Zw 1 and H0557-385 were taken in the same night (24.09.2021), with the same settings, under program 0105.B-0346(A). Low resolution mode with UT baseline configuration was used to observe the faint dust continuum in the *L*- and *M*-bands, with a central wavelength of $3.5\,\mu$m. *N*-band observations were also attempted but no fringes were detected, as they are below the current bias limit of MATISSE standalone observations (Lopez et al., 2022).

Generally, A, G, and K stars are used to calibrate infrared interferometric data since their brightness in the optical gives a good AO performance. However, these stars are considerably bluer than AGN, and the stars' IR SED slopes are steeply declining. This will lead to flux at shorter wavelength to be overweighted, and in calibration this will shift the AGN slopes bluer. To correct for this, we instead used red M giants which have a more similar IR SED slope compared to AGN. Stars were selected according to their *V-K* colours and small proper motions to weed out nearby red dwarf stars.

Data reduction was performed partly using version 1.7.6 of the MATISSE pipeline, and partly by using an algorithm developed by us specifically for faint objects. We used the MATISSE pipeline for a preliminary reduction, using its intermediate data products for our further analysis. This data reduction method is described in detail in Section 2.3.

Fig. 3.1 and 3.2 show that both sources are partially resolved: the visibility decreases with increasing baseline length. Since they are not resolved completely, we are unable to do complex geometric modelling of the sources. Therefore, we focus on two main observables: elongations and sizes. The visibilities in Fig. 3.1 and 3.2 are colour coded by position angle. As can be seen, no clear position angle dependency of the visibilities is present. To further test the presence of elongations, we modelled the source emission as a 2D elliptical Gaussian distribution. In this case, the real space flux distribution is given by

$$F_\nu(x,y) = F_0 e^{-0.5((x\cos\theta+y\sin\theta)^2/\sigma_x^2-(x\sin\theta-y\cos\theta)^2/\sigma_y^2)} \tag{3.1}$$

where F_0 is a normalisation factor and θ is the position angle of the major axis of the ellipsis. In the case of elongation, we expect the angular sizes in the perpendicular directions, σ_x and σ_y, to be significantly different. However, in modelling we found no constraints on σ_x, σ_y, and θ. Therefore our data rules out any significant elongation in these objects. In addition, the closure phases are zero, implying an absence of any asymmetrical off-centre structure in the dust. Therefore, we interpret this as viewing a circular projected dust distribution and we can use a one-dimensional (1D) Gaussian model with only two parameters to recover the brightness-weighted size of a partially resolved circular dust distribution. This is the same method to determine sizes as in GRAVITY Collaboration et al. (2020b, 2024).

In a 1D Gaussian model, the visibility V is given by

$$V = V_0 e^{-2\pi^2 B_{\rm proj}^2 \sigma^2/\lambda^2} \tag{3.2}$$

where V_0 is the visibility normalisation, $B_{\rm proj}$ is the projected baseline length, λ is the wavelength of the data, and σ is the size of the Gaussian in radians, which we convert to mas (GRAVITY Collaboration et al., 2024). It should be noted that in this model, we do not force $V_0 = 1$. The single telescope fluxes may include contamination from astrophysical sources extending outside of the field-of-view of the interferometer, e.g. from nuclear stellar clusters, or the interferometer may suffer from instrumental losses, all leading to an effective $V_0 < 1$.

We used an MCMC method to fit the data with this model, with 16 walkers and 10^5 iterations each. As the burn-in, we discarded the first 5000 steps and thinned by 50% to avoid autocorrelation. The complete set of results with one sigma (68%) confidence intervals is presented in Table 3.1. For I Zw 1, we determine Gaussian sizes of $\sigma_L = 0.46 \pm 0.22$ mas and $\sigma_M = 0.71 \pm 0.41$ mas, for the *L* and *M*-band emission, respectively. The *L*-band emission of H0557-385 is well constrained with a size of $\sigma_L = 0.79 \pm 0.11$ mas. In contrast, the *M*-band in H0557-385, is unconstrained, with a maximum size of $\sigma_{M,\max} = 0.36 \pm 0.27$ mas. The fits are also shown in Fig. 3.1 and 3.2.

An alternative model to recover sizes from interferometric observation is adoption of a power law brightness distribution. Such a model is motivated by evaluating radiative transfer models and may have a more direct relation to physical brightness distributions (e.g. Kishimoto et al., 2007; Hönig & Kishimoto, 2010; Kishimoto et al., 2011b). However, such models require assuming zero baseline visibility $V_0 = 1$ as the anchor due to the lack of sufficiently high quality data to recover the baseline-dependent visibility slope without this assumption. Astrophysical contamination of the single-telescope flux will be significantly less at longer wavelengths (and effectively absent in the *N*-band, see Kishimoto et al., 2011b; Asmus et al., 2016). As such, we consider the power law modelling approach a reasonable alternative to the Gaussian model in the *L*- and *M*-bands.

For the power law model, we created a grid of 10000×10000 pixels and fill it with a circularly symmetric brightness distribution, with a central hole. The brightness distribution follows $r^{-\alpha}$ where α is the power law index and r the distance from the centre. The radius of the central hole is set by the sublimation radius $r_{\rm in}$. Visibilities are extracted from the Fourier transformed grid, normalised such that $V_0 = 1$. In this model, α and $r_{\rm in}$ are the fitting parameters. We fitted the data by minimising the χ^2. It should be noted that $r_{\rm in}$ is not well constrained in this model as the observed baseline lengths do not resolve the corresponding spatial scales. Therefore, we calculate the best fit power law index marginalised over $r_{\rm in}$, shown in Table 3.2 and provide with one sigma (68%) confidence intervals. For I Zw 1 the marginalised power law index in the *L*-band is $\alpha = 2.48 \pm 0.12$. In the *M*-band, $\alpha = 2.60 \pm 0.38$. For H0557-385 the *L*-band marginalised power law index was found to be $\alpha = 2.40 \pm 0.10$, and in the *M*-band $\alpha = 2.22 \pm 0.13$. In addition, we evaluate the one sigma χ^2 contours over all model parameters to find the uncertainty range for our models. These are plotted together with best fit models in Fig. 3.3 and 3.4. These sizes were determined under the assumption that $V_0 = 1$; if we were to use the V_0 evaluated using the Gaussian fits (Table 3.1), the sizes found by using a power law model would decrease.

3.2.1.2 GRAVITY

GRAVITY data is only available for I Zw 1, taken as part of program 1103.D-0626(C) on 25.07.2021. It was observed in dual-field off-axis mode with low spectral resolution and UT baseline configuration, using the fringe tracker to record the fringes using 100% of the light, while the science combiner was pointing at the sky. For data reduction, we used version 1.4.2 of the GRAVITY pipeline. In addition, according to GRAVITY Collaboration et al. (2020b), we selected frames with group delays of $< 3\,\mu$m to account for visibility losses due to the atmosphere. The

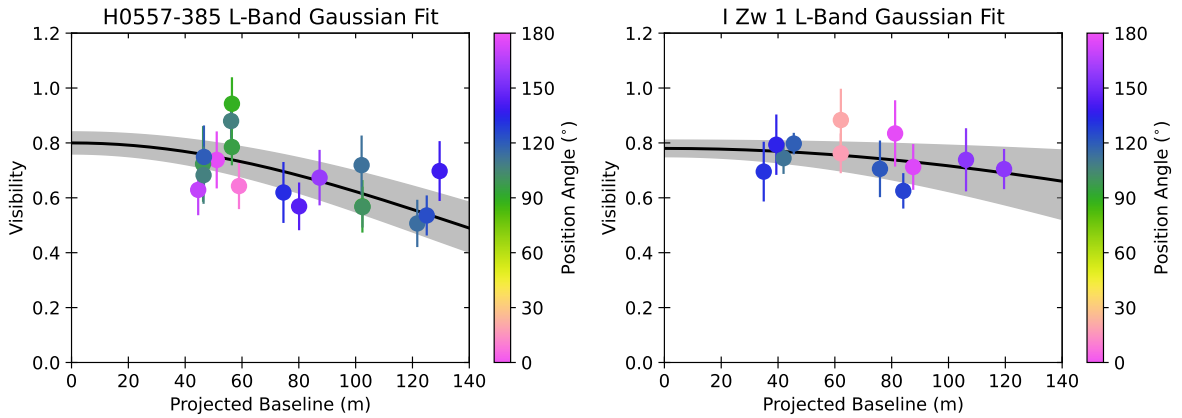

FIGURE 3.1: *L*-band visibilities and 1D Gaussian fit at $3.4\ \mu\mathrm{m}$ for H0557-385 (left) and I Zw 1 (right). Data is coloured based on its position angle, and the 1D Gaussian fit according to Eq. 3.2 is plotted with the black line, with the shaded region the error of the fit.

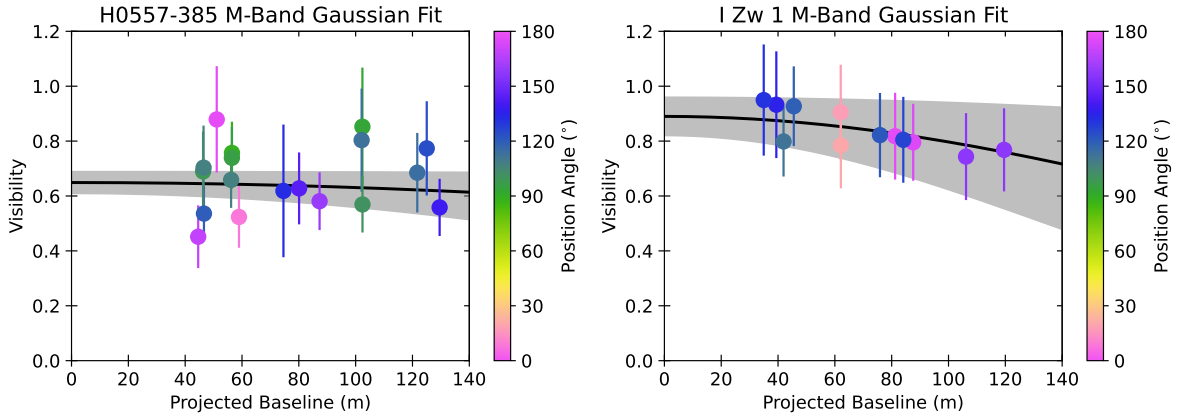

FIGURE 3.2: *M*-band visibilities and 1D Gaussian fit at $4.6\ \mu\mathrm{m}$ for H0557-385 (left) and I Zw 1 (right). Data is coloured based on its position angle, and the 1D Gaussian fit according to Eq. 3.2 is plotted with the black line, with the shaded region the error of the fit.

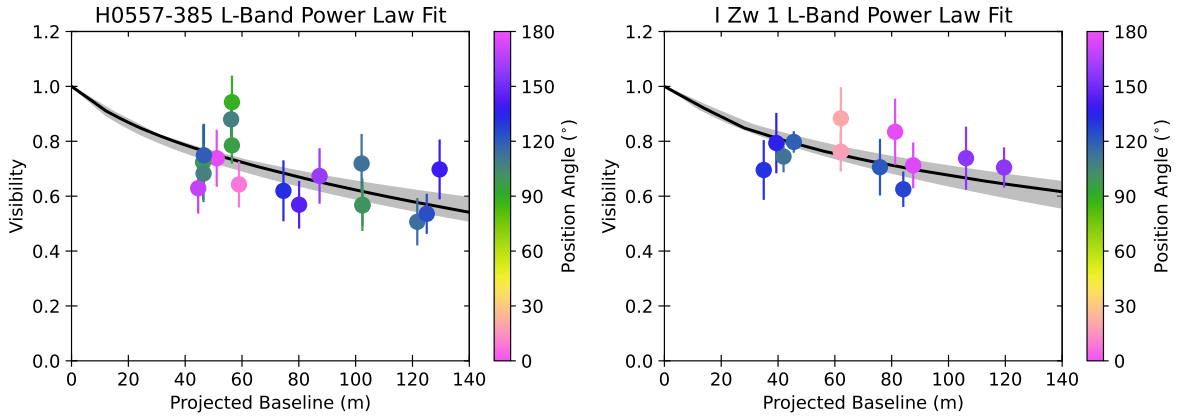

FIGURE 3.3: Power law fit of the *L*-band visibilities at $3.4\ \mu\mathrm{m}$ for H0557-385 (left) and I Zw 1 (right). Data is coloured based on its position angle, and the power law fit is plotted with the black line, with the shaded region the error of the fit.

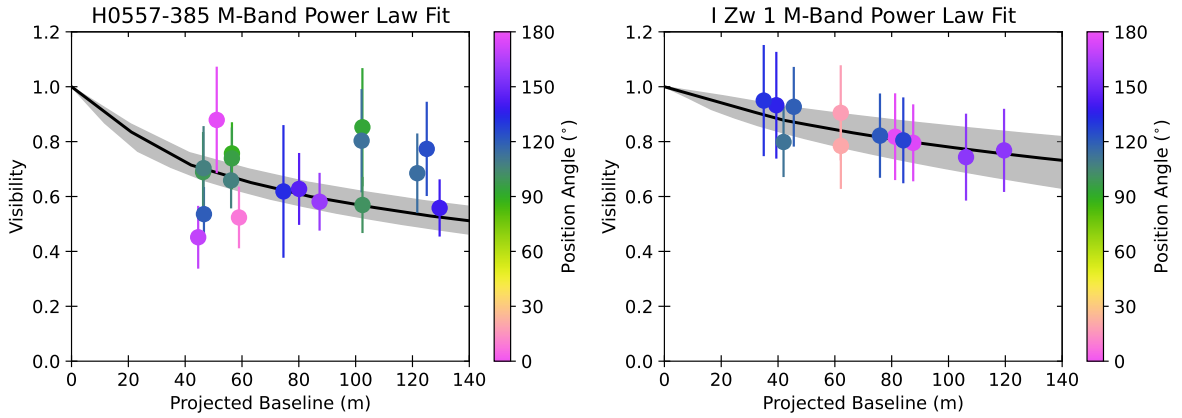

FIGURE 3.4: Power law fit of the *M*-band visibilities at $4.6\,\mu\mathrm{m}$ for H0557-385 (left) and I Zw 1 (right). Data is coloured based on its position angle, and the power law fit is plotted with the black line, with the shaded region the error of the fit.

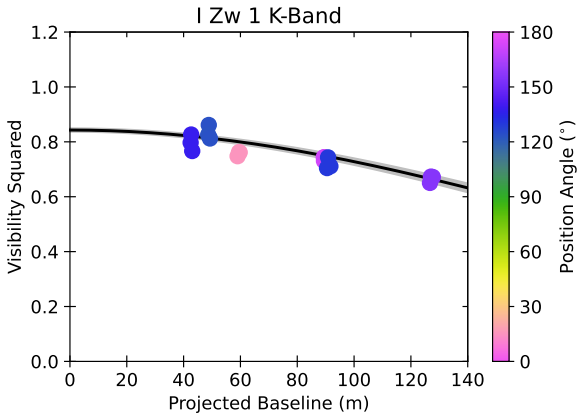

FIGURE 3.5: *K*-band squared visibilities at $2.2\,\mu\mathrm{m}$ for I Zw 1. Data is coloured based on its position angle, and the 1D Gaussian fit according to Eq. 3.2 is plotted with the black line, with the shaded region the error of the fit. Errors are too small to be visible.

visibilities squared are plotted in Fig. 3.5. In this case, we constrained our models to the 1D Gaussian model. The dust that dominates *K*-band emission is emitted within a small radius. In this case, the size measured by the Gaussian half light radius is a good approximation of the power law half light radius (Kishimoto et al., 2011b). Like for the *L* and *M* bands, we cannot make the assumption that $V_0 = 1$, due instrumental effects and contaminations, which are significant in the *K*-band (GRAVITY Collaboration et al., 2020b). We used the same 1D Gaussian to fit the data as we did for MATISSE data (Eq. 3.2), to estimate the maximum size of the hot dusty region, using V^2 instead of V. However, the tail end of the accretion disk emission contributes significantly to the near-IR luminosity. To estimate this, we fit $F_\nu \propto \nu^{1/3}$ to the optical flux of I Zw 1 as shown in the SED in Fig. 3.6. In the *K*-band, the point source contribution is $f_{pt} = 0.07$. This agrees well with the range of values of $5 - 25\%$ typically found in Type 1 AGN as measured by Kishimoto et al. (2007). With this, we use Eq. 5 from GRAVITY Collaboration et al. (2020b) to account for the point source contribution. We get a final size of the partially resolved hot dust region in the *K*-band in I Zw 1 of $\sigma_K = 0.29 \pm 0.01$ mas, with $V_0^2 = 0.843 \pm 0.007$. Results are summarised in Table 3.1.

Object	λ	V_0	Angular Size σ (mas)	$R_{1/2}$ (pc)	$R_{1/2}$ ($R_{\rm sub}$)^c
H0557-385	$3.4\,\mu$m	0.80 ± 0.04	0.79 ± 0.11	0.71 ± 0.10	5.9 ± 0.8
	$4.6\,\mu$m	0.65 ± 0.04	$\leq 0.36 \pm 0.27$	$\leq 0.32 \pm 0.24$	$\leq 2.7 \pm 2.0$
	$8.5\,\mu$m			$0.77^{+0.48,a}_{-0.29}$	$6.4^{+4.1}_{-2.4}$
	$12.4\,\mu$m		$18^{+15,b}_{-4.7}$	$< 2.4^b$	< 20.0
	$13.0\,\mu$m			$1.89^{+1.17,a}_{-0.72}$	$15.8^{+9.8}_{-6.0}$
I Zw 1	$2.2\,\mu$m	0.918 ± 0.004	0.29 ± 0.01	0.42 ± 0.01	2.3 ± 0.06
	$3.4\,\mu$m	0.78 ± 0.03	0.46 ± 0.22	0.67 ± 0.32	3.7 ± 1.6
	$4.6\,\mu$m	0.89 ± 0.07	0.71 ± 0.41	1.03 ± 0.60	5.7 ± 3.3
	$12.7\,\mu$m		$10.2^{+8.5,b}_{-6.4}$	$< 4.01^b$	< 22.5

Notes.
[a] Sizes from Kishimoto et al. (2011b), measured using a power law and corrected with a factor of 1.5.
[b] Sizes from Burtscher et al. (2013), measured using a point source and a Gaussian, which introduces upper limits for $R_{1/2}$ at point source fractions above 0.5. Corrected with a factor of 1.5.
[c] Sublimation radii used are $R_{\rm sub} = 0.12\,$pc for H0557-385 and $R_{\rm sub} = 0.18\,$pc for I Zw 1 (see Section 3.4.1).

TABLE 3.1: The Gaussian fit results to the interferometry (V_0 and σ) and additional sizes of the objects at different wavelengths. The angular size is the σ of the Gaussian fit to the visibility data, in the *K*-band corrected for the accretion disk contribution. The physical radii are the half light radii (here, the HWHM).

3.2.2 SEDs

For this work, we collated IR SED data from archival sources to construct the SED of the dusty torus and to then model the SED using CAT3D-WIND. We focus on the IR emission, in the range from $1\,\mu$m to $\sim 100\,\mu$m. This covers emission originating predominantly from within the central $\sim$ 100 pc (Asmus et al., 2014), which corresponds to an angular size of $\sim 0\farcs08 - 0\farcs13$ for our objects. These resolutions are very difficult to attain with single dish photometric and spectroscopic observations. We aim for higher resolutions to examine galactic contributions such as starbursts, especially in larger aperture measurements. From this, we can judge to what extent the SED reflects the dusty torus emission and the applicability of SED modelling.

For H0557-385, we have compiled a set of high resolution photometry from *Y*-band to *N*-band, taken with the explicit goal of studying the dust in the AGN (Kishimoto et al., 2011b; Asmus et al., 2014). Furthermore, we have included two long wavelengths measurements from IRAS to characterise the behaviour of the colder dust (Moshir et al., 1990). Due to the large aperture, these can be seen as strict upper limits. Finally, we have overlaid the SPITZER point source spectrum in Fig. 3.6 to clearly illustrate the unusual mid-IR features. These include an unusually high *LM*-band

Object	λ	Power Law Index α	$R_{1/2}$ (mas)	$R_{1/2}$ (pc)	$R_{1/2}$ ($R_{\rm sub}$)[c]
H0557-385	$3.4\,\mu$m	2.40 ± 0.10	0.87 ± 0.19	0.66 ± 0.14	5.5 ± 1.2
	$4.6\,\mu$m	2.22 ± 0.13	1.45 ± 0.38	1.10 ± 0.29	9.2 ± 2.4
	$8.5\,\mu$m			$0.51^{+0.32,a}_{-0.19}$	$4.3^{+2.7}_{-1.6}$
	$12.4\,\mu$m		$18^{+15,b}_{-4.7}$	$< 1.6^{b}$	< 13.3
	$13.0\,\mu$m			$1.26^{+0.78,a}_{-0.48}$	$10.5^{+6.5}_{-4.0}$
I Zw 1	$3.4\,\mu$m	2.48 ± 0.12	0.73 ± 0.19	0.90 ± 0.23	5.0 ± 1.3
	$4.6\,\mu$m	2.60 ± 0.38	0.58 ± 0.29	0.72 ± 0.36	4.0 ± 2.0
	$12.7\,\mu$m		$10.2^{+8.5,b}_{-6.4}$	$< 2.7^{b}$	< 15.0

Notes.
[a] Sizes from Kishimoto et al. (2011b), measured using a power law.
[b] Sizes from Burtscher et al. (2013), measured using a point source and a Gaussian, which introduces upper limits at point source fractions above 0.5.
[c] Sublimation radii used are $R_{\rm sub} = 0.12\,$pc for H0557-385 and $R_{\rm sub} = 0.18\,$pc for I Zw 1 (see Section 3.4.1).

TABLE 3.2: The power law fit results to the interferometry and additional sizes of the objects at different wavelengths. The power law is characterised by its power law index α, where the brightness is radially distributed according to $r^{-\alpha}$, and the sublimation radius $r_{\rm in}$. The power law index here shown is marginalised over $r_{\rm in}$. All radii are half light radii, measured at $V = 0.5$. *K*-band results are not included as due to the small physical size of the region, it is approximated well using a Gaussian.

bump and a $10\,\mu$m silicate feature in absorption – in a Type 1. However, the Spitzer data will not be further used in the analysis since the aperture is $\gtrsim 3\times$ the AGN infrared emitting region. Nevertheless, we do not expect significant starburst activity since the star formation rate is $\lesssim 1.6\,{\rm M}_\odot{\rm yr}^{-1}$ (Shimizu et al., 2017). Regarding variability, while the X-ray emission has seen significant flux variability due to absorption events, during these times optical emission has stayed nominal (Coffey et al., 2014). Full SED data can be found in Table A.3, and the SED is displayed in Fig. 3.6.

I Zw 1 is a more complex case due to the presence of a nuclear starburst and near-IR accretion disk contribution (Schinnerer et al., 1998; Kishimoto et al., 2007). Using ALMA data, Fei et al. (2023) showed that the starburst is within the central 1 kpc of the galaxy ($0\farcs8$). On the other hand, the VISIR spectrum of I Zw 1 does not show significant starburst emission, which implies that only apertures $\gtrsim 0\farcs4$ contain significant contamination from star formation (Jensen et al., 2017). Consequently, as illustrated in Table A.2 with the extraction aperture sizes, the majority of the available data is contaminated by starburst emission. We have amassed data from $\sim 1\,\mu$m to $70\,\mu$m, both spectroscopic and photometric, that include starburst SED signatures (Hickox & Alexander, 2018). Starbursts predominantly emit in the mid-IR, overlapping directly with the dusty torus emission. In addition, star formation has an irregular shape with prominent emission features. PAH features in particular, especially the $11.3\,\mu$m feature, are often used as starburst tracers

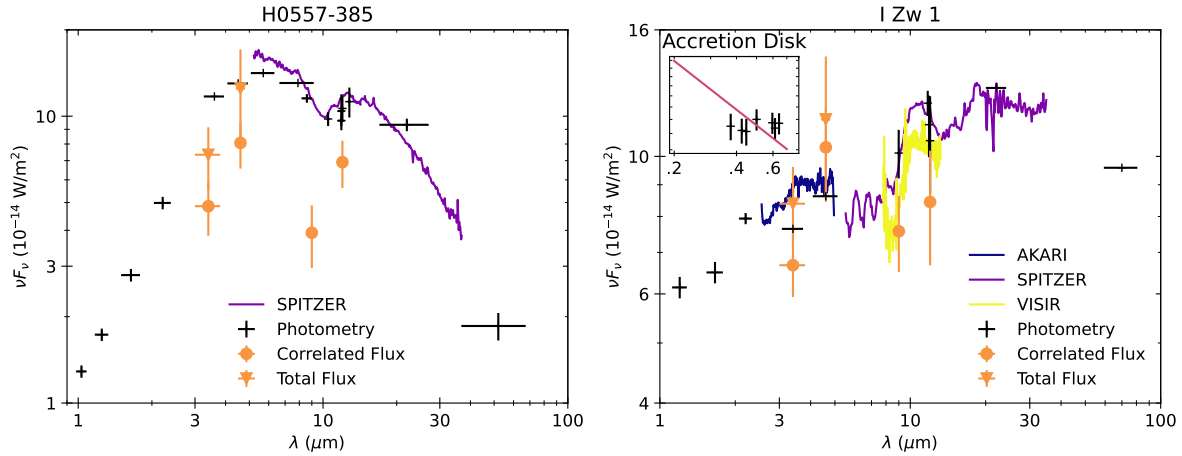

FIGURE 3.6: SEDs for H0557-385 (left) and I Zw 1 (right), with interferometric measurements from MATISSE in the *L*- and *M*-bands, and from MIDI in the *N*-band overplotted in orange circles. Higher circles are total flux measurements and lower circles are correlated flux measurements, except in the *N*-band where only correlated flux measurements exist.

(Peeters et al., 2004; Brandl et al., 2006; Diamond-Stanic & Rieke, 2010). I Zw 1 does have a clear $11.3\,\mu\mathrm{m}$ emission feature even within 0.″4; Jensen et al. (2017) have shown that these are likely to have been excited by nuclear AGN radiation and not a starburst. This emission line also does not significantly impact the shape of the silicate emission (Asmus et al., 2014). Other PAH features at shorter wavelengths are commonly washed out by AGN continuum (Diamond-Stanic & Rieke, 2010). Further, emission lines can be neglected because we are dealing with broadband SED fitting and not spectral fitting. Adding a starburst SED's sub-$10\,\mu\mathrm{m}$ emission, which peaks in the *L*-band region, will offset the balance between the sub-$10\,\mu\mathrm{m}$ and $\gtrsim 10\,\mu\mathrm{m}$ emission by overestimating the sub-$10\,\mu\mathrm{m}$ contribution (Hickox & Alexander, 2018). This makes it very difficult to model the underlying torus emission accurately, except through high spatial resolution measurements particularly in the *LM*-band region.

The near-IR emission will be impacted by the tail of the accretion disk. Crucially, this will impact the *K*-band size of the dust as measured with GRAVITY. To estimate the accretion disk contribution used in Section 3.2.1.2, we obtained continuum fluxes from a UVES spectrum (ID 085.C-0172). The continuum is relatively flat, which matches with previous optical spectra (e.g. Baldwin et al., 2004). We do have high resolution *N*-band coverage, both in photometry and spectroscopy, which is dominated by dusty torus emission (Asmus et al., 2014; Jensen et al., 2017). Comparing the high resolution VISIR spectrum to the low resolution SPITZER spectrum, in the mid-IR, we see not only a difference in flux levels but also a change in the spectral shape especially around the silicate feature at $\sim 10\,\mu\mathrm{m}$. Variability is not a large concern as the ASAS-SN light curve from $2012 - 2019$ shows long term flux stability (Huang et al., 2019). In the short term (cadence of several days), variability is unimportant, with the optical flux varying between 3–9% (Huang et al., 2019). We note that our interferometric flux in the *M*-band is larger than the AKARI spectrum, which is likely due to flux calibration issues. Full SED data can be found in Table A.2, and the SED is displayed in Fig. 3.6.

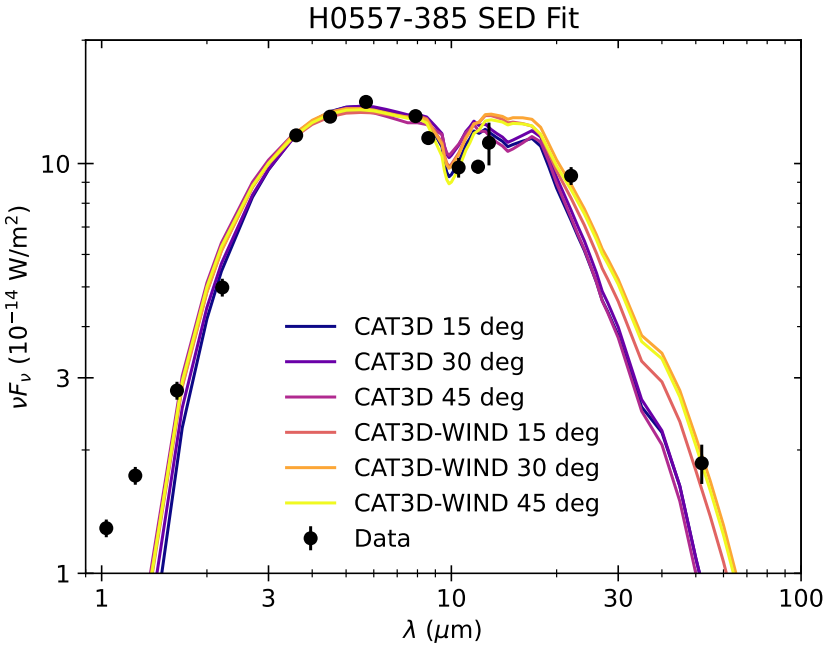

FIGURE 3.7: Best-fit SED fits for H0557-385, without and with wind, over inclinations of 15, 30, and 45 degrees. The data is plotted with the black dots. Table A.1 contains the best-fit model parameters.

3.3 CAT3D-WIND

In this section, we simultaneously model the SEDs and visibilities. We focus particularly on whether there is a polar wind present. SED modelling alone is insufficient to reveal structural information due to degeneracies (Feltre et al., 2012). Therefore, we test our best fit SED models against visibilities to recover information about structure.

We use the radiative transfer code CAT3D-WIND to model the dust structure (Hönig & Kishimoto, 2010, 2017). This model assumes a two-phase disk+wind structure, which has been inspired by IR interferometry of a set of AGN and matches the geometric distribution obtained from radiation hydrodynamic simulations. In this model, the wind is described as a hollow polar cone with a mass distribution independent of the disk (Wada et al., 2016; Williamson et al., 2020). The dust is contained in randomly distributed clouds, assuming a clumpy torus. Through Monte Carlo and radiative transfer and ray tracing, the SEDs for different parameter values are extracted. In addition, images of the torus at different wavelengths can be obtained. The model parameter that is of specific interest to us here is the wind to disk ratio, i.e. the amount of dust contained within the wind versus within the disk. Furthermore, the wind opening angle is of interest. Using this model enables us to compare our observations to a realistic representation of the dust structure, which includes the wind (which can also be switched off). Specifically, we are able to examine the importance of the wind in comparison to the disk and how large the wind opening angle is. The provision of images allows us to extract interferometric information from the model to compare to our observations.

3.3.1 H0557-385

Examining the SED of H0557-385 (Fig. 3.6), we can clearly see a prominent silicate absorption feature around $10\,\mu\mathrm{m}$. However, in Type 1s, such as H0557-385, we expect to see the silicate feature in emission (Hönig & Kishimoto, 2010). The host galaxy of this source is highly inclined. Therefore, the silicate absorption is probably of host-galactic origin (Goulding et al., 2012). In fact, through analysis of the optical spectrum, Coffey et al. (2014) found considerable intrinsic extinction. Accordingly, we included ISM extinction in our SED fitting to account for the deep absorption feature (Chiar & Tielens, 2006). For modelling, we used the photometric data as seen in Fig. 3.6 and Table A.3. We combined the three photometric points around $12\,\mu\mathrm{m}$ into one, so as to not overweight the fit in that region. We did not interpolate between parameter values of the initial model library. In addition, we added constraints on some model parameters as fitting these models unconstrained does not lead to conclusive results. As we know this is a Type 1, we restricted possible inclinations to below 60 degrees. From Rokaki & Boisson (1999) we can also presume that the torus is probably not viewed face on, likely between $20-40$ degrees. Therefore, we limit inclination angles to $15-45$ degrees. We restricted the value of the optical depth τ_{OD} such that the silicate feature is in absorption. All fit results are shown in Table A.1 and Fig. 3.7.

Host galaxy extinction (Fig. 3.7) clearly improves the shape of the fit, reproducing the SED shape. Using modelling of the optical spectrum and the $\mathrm{H}\alpha/\mathrm{H}\beta$ line ratio, Coffey et al. (2014) found the intrinsic extinction in H0557-385 to have $E(B-V)=0.53-0.54$. Adopting our best-fit optical depths of $2.2-2.6$ gives $E(B-V)=7-8$ (assuming $A_K/E(B-V)=0.36$; Fitzpatrick, 1999). This is certainly much higher than the amount derived by Coffey et al. (2014); however, we introduced the quite strong constraint that the silicate feature must be in absorption. As can be seen in e.g. Fig. A.1 the silicate feature produced by CAT3D and CAT3D-WIND can be quite strong for Type 1s, so a considerable amount of extinction is needed to suppress it. In contrast to the models, silicate features in AGN SEDs are commonly weak, such that the intrinsic extinction may not need to be as extreme to result in the observed SED (e.g. Ramos Almeida et al., 2009; Hönig et al., 2010). However, the introduction of intrinsic extinction also introduces degeneracies and constraints on parameters become less tight. Goodness-of-fit values for the CAT3D and CAT3D-WIND fits do not differ significantly. In addition, as can be seen in Fig. 3.7, there is very little difference between the fits. Essentially, simply adjusting the amount of extinction leads to a viable fit. At the longest wavelengths, the data does prefer the wind-added model. The reason for this is that the modelled wind has a flatter dust distribution than the disk. Therefore, at larger distances, there is comparably more dust in the wind than at the same distance in the disk. This means that predominantly cooler, longer-wavelength emission at those distances will be dominated by the wind. However, the long-wavelength data from IRAS has a very large aperture, roughly $4'\times5'$. Therefore, this data includes an unknowable amount of host galaxy contribution and is too unreliable to use it as a differentiating tool between the two models. In the near-IR ($1-1.2\,\mu\mathrm{m}$) there is a clear excess in the data compared to the fits, this is due to noticeable contribution from the accretion disk at these wavelengths (Kishimoto et al., 2007). This is illustrated in the total

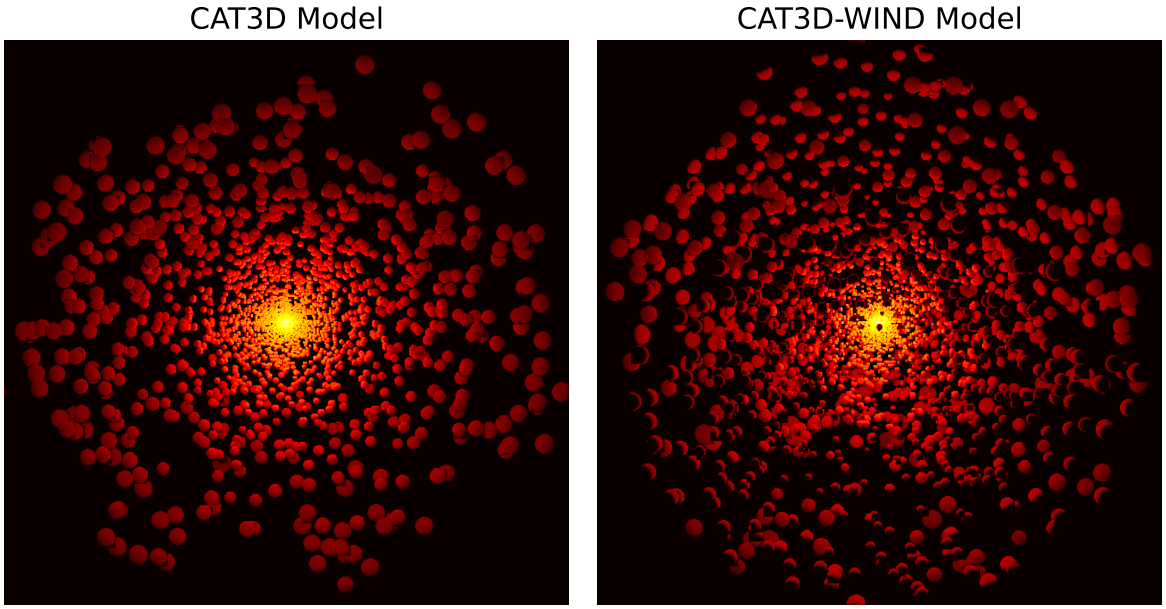

FIGURE 3.8: Images of the best fit CAT3D (left) and CAT3D-WIND (right) models with an inclination of 30 degrees in the *L*-band.

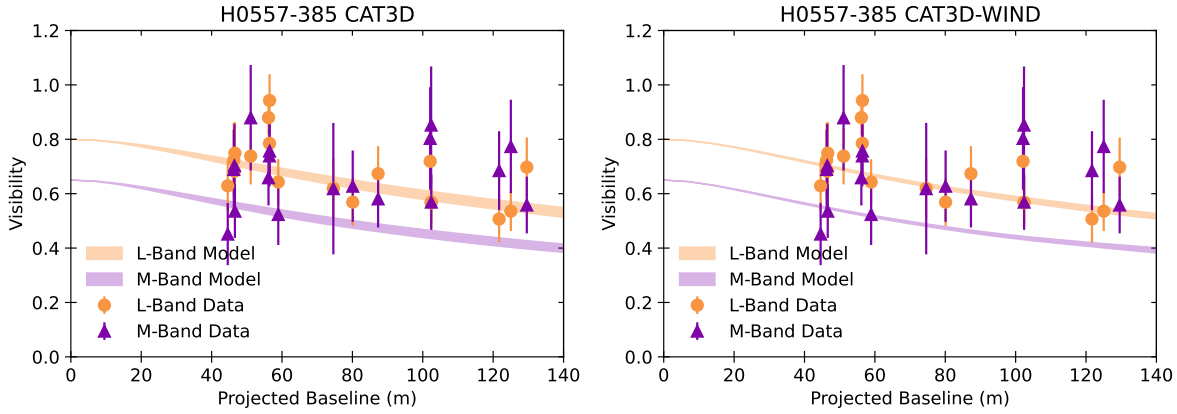

FIGURE 3.9: Interferometric results for the best fit models for H0557-385 with our observations overlaid. The shaded regions of the models cover the visibilities for all position angles. The *L*-band is in orange and the *M*-band is in purple. On the left is the best fit model without wind and on the right is the best fit model with wind.

AGN SED in Fig. 1.2, where the total flux at $1 - 1.2\,\mu\mathrm{m}$ is significantly above the hot dust component due to the addition of the accretion disk flux.

Furthermore, we created images of the torus based on the best fit models, using the models with an inclination of 30 degrees. These images as seen in the *L*-band are shown in Fig. 3.8. We then mock observed these with a set of ideal uv-points, maximising the coverage in all directions. Our aim here is to examine how strongly the emission is elongated for these models. Further, we want to see whether this elongation could be detected with interferometry. The results, overlaid with the observations, are shown in Fig. 3.9. It appears that polar structure is naturally suppressed. In addition, for inclinations of Type 1s, it is not sufficiently detectable in this object with current

interferometric instrumentation – a visibility accuracy of the order of 1% would be needed. The images in Fig. 3.8 also clearly show that there is little difference between with and without a wind, for this inclination and at these wavelengths.

3.3.2 I Zw 1

The complexity of the SED of I Zw 1 makes a fit with a torus model very ambiguous and hence does not provide any meaningful constraints on the dust distribution. Specifically, the shape at $\lesssim 10\,\mu\mathrm{m}$ is badly defined, in contrast to the $\gtrsim 10\,\mu\mathrm{m}$ emission (see Section A.2). This is shown in the right plot in Fig. A.1 which shows sample CAT3D and CAT3D-WIND fits. Even shifting the near-IR flux as in the left plot in Fig. A.1 does not markedly improve the quality of the fit. It is appears to be very difficult for the models to produce reasonable fits to both the data $\lesssim 10\,\mu\mathrm{m}$ and $\gtrsim 10\,\mu\mathrm{m}$. Since SED fitting is not the focus of this work, we have decided not to pursue this problem further.

3.4 Results

3.4.1 Bolometric luminosity and the sublimation radius

Our goal is to compare the interferometric sizes between our two objects, as well as simple dust emission models and objects with lower Eddington ratios. Through this, we can look at the influence of the Eddington ratio on the structure of the torus. However, the physical radii are to the first degree dependent on the bolometric luminosity of the central engine. To account for this, we scale the interferometric sizes by the sublimation radius, removing any bolometric luminosity dependencies (GRAVITY Collaboration et al., 2020b). We hence first determine the bolometric luminosities of our objects. There are a variety of techniques to find L_{bol}, e.g. based on the mid-IR luminosity, $\lambda L_{5100\,\text{Å}}$, or X-ray luminosities, especially $14 - 195\,\mathrm{keV}$. Here, our goal is to determine L_{bol} in the most self-consistent way for maximum comparability, rather than the intrinsic value. To achieve this, we collected L_{MIR} and $L_{2-10\,\mathrm{keV}}$ for both objects, and $L_{14-195\,\mathrm{keV}}$ for H0557-385, from Asmus et al. (2015). The intrinsic I Zw 1 5100Å luminosity is taken from Huang et al. (2019) and for H0557-385 from Coffey et al. (2014). From the hard X-ray and optical luminosities we found the bolometric luminosity directly through established relations. For the $L_{2-10\,\mathrm{keV}}$ and L_{MIR}, we first transformed these into a hard X-ray luminosity, and then calculated the bolometric luminosity based on that. Our method is based on Appendix A of GRAVITY Collaboration et al. (2020b) and the luminosity relations used therein: the $L_{\mathrm{bol}} - L_{14-195\,\mathrm{keV}}$ relation from Winter et al. (2012), $L_{\mathrm{bol}} - \lambda L_{5100\,\text{Å}}$ from Trakhtenbrot et al. (2017), and $L_{14-195\,\mathrm{keV}} - L_{2-10\,\mathrm{keV}}$ from Winter et al. (2009). The $L_{2-10\,\mathrm{keV}} - L_{\mathrm{MIR}}$ relation is taken from Asmus et al. (2015).

In I Zw 1, we find a spread in L_{bol} of 1 dex, giving a factor of 3 for the uncertainty in R_{sub}. This is mainly driven by its relative faintness in the $2 - 10\,\mathrm{keV}$ band in comparison to its mid-IR luminosity (Asmus et al., 2015). In general, I Zw 1 exhibits highly complex behaviours in the X-ray, including

reflections from behind the black hole and ultra-fast outflows (Wilkins et al., 2021; Rogantini et al., 2022). This implies that the X-ray based luminosity is not reliable in this object.

On the other hand, H0557-385 is far more compact in the spread in $L_{\rm bol}$, ~ 0.5 dex. Again, X-ray based luminosities are assumed not to be particularly reliable in this object due to a peculiar absorption event in the 2000s, that solely impacted the X-ray emission but not the optical (Coffey et al., 2014).

As the $\lambda L_{5100\,\text{Å}}$ derived bolometric luminosities approximately cover the center of both distributions, we have decided to use these here. For I Zw 1, the intrinsic $\lambda L_{5100\,\text{Å}} = 10^{44.50}$ erg/s, which gives $L_{\rm bol} = 10^{45.36}$ erg/s (Trakhtenbrot et al., 2017; Huang et al., 2019). For H0557-385 , $\lambda L_{5100\,\text{Å}} = 10^{44.12}$ erg/s, giving $L_{\rm bol} = 10^{45.01}$ erg/s (Coffey et al., 2014). To estimate the sublimation radius we used the relation between $R_{\rm sub}$ and $L_{\rm bol}$ as presented in GRAVITY Collaboration et al. (2020b) (see their Fig. 7 and Section 5.2 for details). In I Zw 1, $R_{\rm sub} = 0.18\,\text{pc}$, and in H0557-385 $R_{\rm sub} = 0.12\,\text{pc}$. This bolometric-luminosity-derived sublimation radius of H0557-385 is very consistent with sublimation radii derived from SED fitting, $0.1 - 0.12$ pc (Table A.1). This corroborates our usage of $\lambda L_{5100\,\text{Å}}$ derived bolometric luminosities.

3.4.2 Interferometric sizes

With a large wavelength coverage of interferometric sizes from GRAVITY, MATISSE, and MIDI, we can examine the radial distribution of the dust, assuming the *K*-, *LM*- and *N*-band emission mainly trace the hot ($T > 1000\,\text{K}$), warm ($T \sim 600\,\text{K}$) and cool ($T \sim 300\,\text{K}$) dust respectively. This will give us important insights into the structure of the dusty disk in these high accretion objects. For comparable size estimates of these emission regions we determined their half light radii $R_{1/2}$, which includes half of the emission within it. For the Gaussian sizes σ we obtained by fitting the interferometric data in Section 3.2.1, we determined the half width at half maximum (HWHM $= 1.1775\sigma$). This is the half light radius for a radially symmetric 2D Gaussian model. Resulting half light radii in both pc and in units of the sublimation radius $R_{\rm sub}$ can be seen in Table 3.1. Since the data quality for H0557-385 in the *M*-band is so low, we have only managed to obtain an estimated upper limit. For our power law model fits, we determined the half light radius $R_{1/2} = R_{V=0.5}/4.5$ with $R_{V=0.5}$ as the spatial wavelength at $V = 0.5$ (see Kishimoto et al., 2011b, for details). The uncertainties are derived from the one sigma contours seen in Fig. 3.3 and 3.4 and discussed in Section 3.2.1.1. These are presented in Table 3.2, in units of mas, pc, and scaled by the sublimation radius $R_{\rm sub}$.

For *N*-band sizes we used the results from Burtscher et al. (2013). Instead of a single Gaussian, the authors used a Gaussian and an unresolved point source to fit the MIDI correlated fluxes. Consequently, for source point fractions above 0.5, only an upper limit – the maximum size of the unresolved region – can be determined. This is the case for both of our objects. An alternative analysis of the MIDI data for H0557-385 is presented in Kishimoto et al. (2011b). Here, sizes were determined by fitting a power law instead of a Gaussian (see Section 3.2.1.1). As the authors

illustrate in their Fig. 5, depending on the size and spatial frequency, the HWHM of a Gaussian and $R_{1/2}$ of a power law show significant differences. Based on the visibilities, we converted the power law half light radii into Gaussian HWHM, using this figure. We multiplied the power law derived sizes by a factor of 1.5. At low spatial resolutions, power law and Gaussian + unresolved point source models lead to approximately the same results. Accordingly, we applied the same correction method to sizes from Burtscher et al. (2013), for which we determined the correction factor to be 1.5 as well. Uncorrected sizes from Burtscher et al. (2013) and Kishimoto et al. (2011b) are included in Table 3.2 along our other power law measurements. Sizes corrected for a single Gaussian model are presented in Table 3.1. In addition, Gaussian normalised half light radii as a function of wavelength are plotted in Fig. 3.10, and normalised power law half light radii are plotted in Fig. 3.11. The *K*-band data point in the plot depicting the power law sizes (Fig. 3.11) is the single Gaussian half light radius, as discussed in Section 3.2.1.2.

Angular sizes and physical radii presented in this paper can be compared with results reported previously for other AGN. The (uncorrected for accretion disk contribution) angular FWHM of I Zw 1 in the *K*-band, 0.65 mas, corresponds to the value measured by GRAVITY Collaboration et al. (2024). After correcting the physical radius for a thin ring geometry, as applied by the authors, our measurements also arrive at the same value at 0.59 pc. In the *LM*-band, sizes have been reported only for 2 other sources so far, none of which are Type 1s. Sizes have only been published for the nearest and brightest AGN, NGC 1068 and Circinus, both of which are Type 2s. In NGC 1068, the *LM*-band is measured to have a size of $1.7 \times 0.9\,\mathrm{pc}$, which, assuming a sublimation radius of 0.15 pc (in line with our analysis), corresponds to $\sim 11.3 \times 6\,R_{\mathrm{sub}}$ (Burtscher et al., 2013; Gámez Rosas et al., 2022). For Circinus, the analysis of the *LM*-band emission is more detailed. With an $R_{\mathrm{sub}} \sim 0.02\,\mathrm{pc}$, the *L*-band size is $\sim 6 \times 3\,R_{\mathrm{sub}}$ $(0.12 \times 0.06\,\mathrm{pc})$ (Burtscher et al., 2013; Isbell et al., 2023). The *M*-band is modelled with two components: a large and a small one. The large component has an estimated size of $30 \times 4.3\,R_{\mathrm{sub}}$ $(0.6 \times 0.08\,\mathrm{pc})$. Interestingly, the small component appears to be smaller than the *L*-band, just $5 \times 2.2\,R_{\mathrm{sub}}$ $(0.1 \times 0.044\,\mathrm{pc})$. While these are on the same scales we are measuring, comparing the components, our results show sizes towards the smaller end for both the Gaussian and power law models. It should be noted again, that our objects are Type 1 AGN, meaning that more of the central hot dust emission is exposed to the observer. As such, smaller sizes compared to Type 2s can be expected.

To put our results into the context of a model for the circumnuclear environment in these sources, we assume the dust distribution to be primarily located within or projected onto a disk, given the lack of significant polar extension. If a wind is present it must emerge from close to the disk with a wide opening angle or fully projected onto the disk. To test this, we adopt a simplified torus/disk model consisting of a power law dust distribution $\eta(r) \propto (r/r_{\mathrm{in}})^{-a}$ and a black body temperature distribution $T(r) = T_{\mathrm{in}} \cdot (r/r_{\mathrm{in}})^{1/2}$ with $T_{\mathrm{in}} = T(r_{\mathrm{in}}) = 1500\,\mathrm{K}$ (e.g. Hönig & Kishimoto, 2011). We calculated normalised interferometric sizes ($R_{1/2}/R_{\mathrm{sub}}$) as a function of wavelength for $a = 0$ (homogeneous dust distribution), $a = 0.2$ and $a = 0.5$. Sizes from the model images have been extracted in the same way as for the observations (see Section 3.2.1.1). For the 1D Gaussian model, we assume that $R_{\mathrm{sub}} = 0.6 \cdot R_K$ where R_K is the observed interferometric *K*-band size.

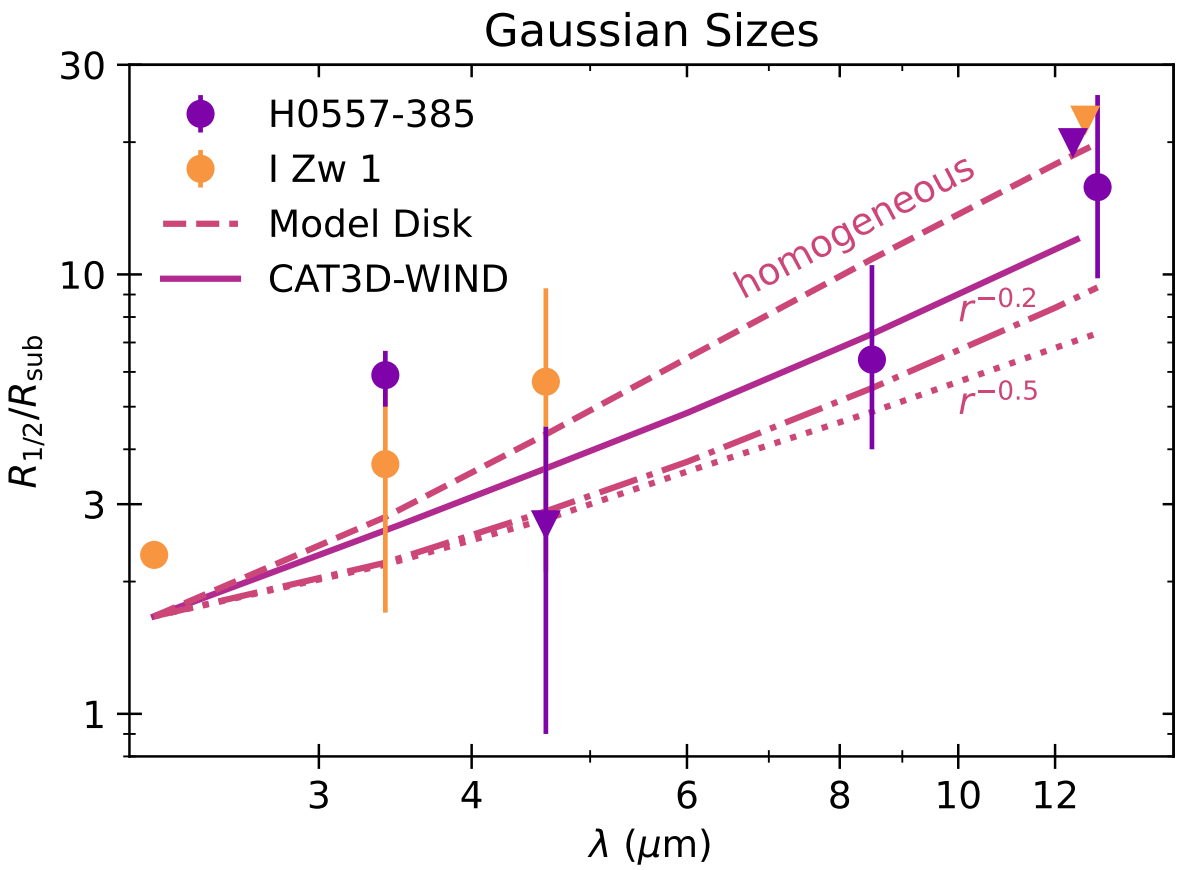

FIGURE 3.10: The scaled Gaussian half light radii shown as a function of wavelength, with upside down triangles marking upper limits. Errors are derived solely from the interferometric sizes, uncertainties in $R_{\rm sub}$ and $L_{\rm bol}$ have not been considered. Also shown are the Gaussian half light radii tracks for a disk with a radial dust distribution. The dashed line shows the size profile extracted from a homogeneous disk model, the dashed-dotted line a disk with a radial power law of $r^{-0.2}$, and the dotted line a power law with $r^{-0.5}$. The solid line shows the sizes extracted from a CAT3D-WIND model with a wind opening angle of $60°$.

This accounts for the well-documented difference between the brightness-weighted interferometric size estimates compared to the "true" inner radii as determined from response-weighted reverberation mapping (e.g. Kishimoto et al., 2007, 2011a; GRAVITY Collaboration et al., 2020b). Fig. 3.10 shows the Gaussian size tracks for these model disks and in Fig. 3.11, we plot the corresponding power law size tracks.

For a more realistic comparison, we also extracted the interferometric size as a function of wavelength from CAT3D-WIND images of a disk and a wind with a large opening angle. We used a wind opening angle of $60°$ with all other parameter values taken from the CAT3D-WIND best fit model at $30°$ inclination (Table A.1). The same method as for the simple disks was used to calculate the interferometric sizes here. Interferometric sizes of the CAT3D-WIND model calculated using a 1D Gaussian model are plotted as a solid line in Fig. 3.10, and those calculated using a power law model are plotted as a solid line in Fig. 3.11.

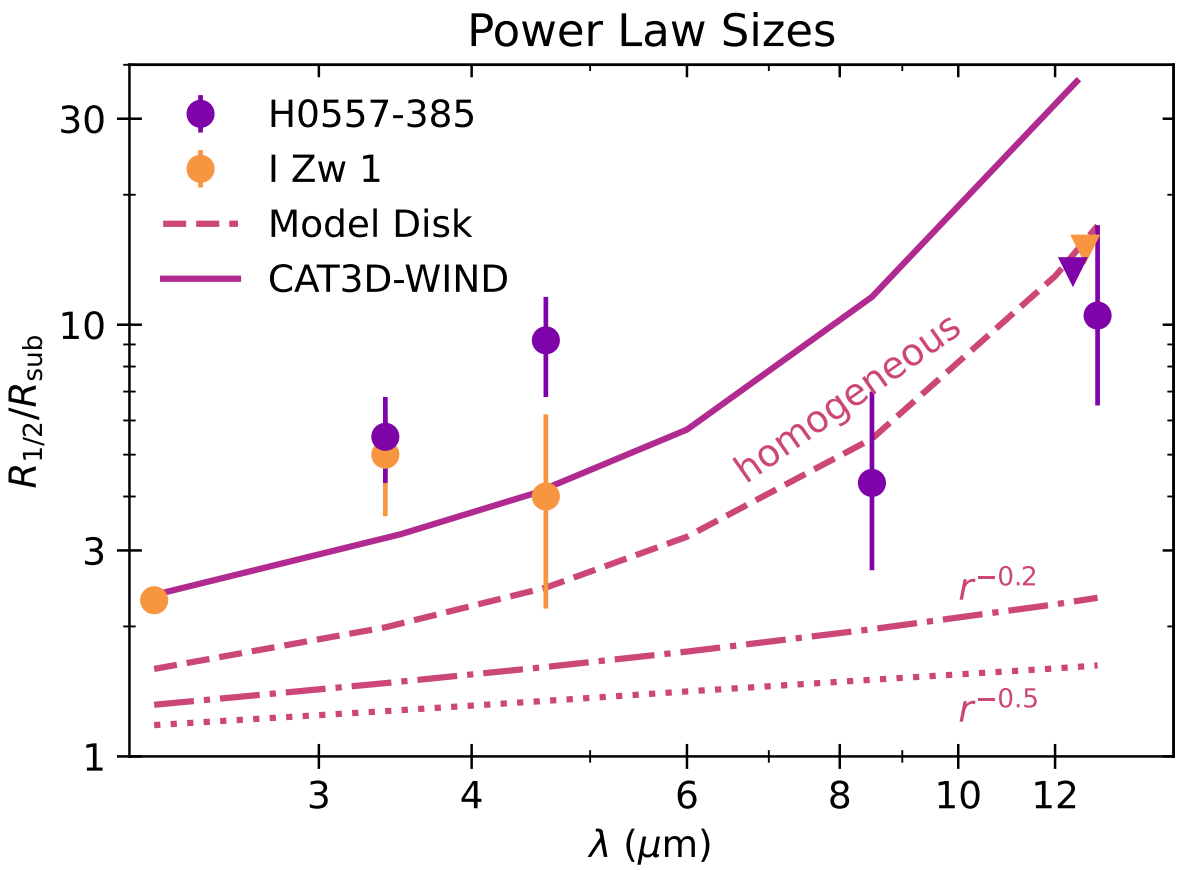

FIGURE 3.11: The scaled power law half light radii shown as a function of wavelength, with upside down triangles marking upper limits. The *K*-band half light radius is the derived from a single Gaussian fit, as discussed in Section 3.2.1.2. Errors are derived solely from the interferometric sizes, uncertainties in $R_{\rm sub}$ and $L_{\rm bol}$ have not been considered. Also shown are the power law half light radii tracks for a disk with a radial dust distribution. The dashed line shows the size profile extracted from a homogeneous disk model, the dashed-dotted line a disk with a radial power law of $r^{-0.2}$, and the dotted line a power law with $r^{-0.5}$. The solid line shows the sizes extracted from a CAT3D-WIND model with a wind opening angle of $60°$.

3.5 Discussion

In this section, we test and discuss the disk+wind model for the dusty torus as described in Hönig (2019). Particularly, we look at the consequence of high Eddington ratios on this model: as the Eddington ratio increases, theory predicts that the opening angle of the dusty wind will increase, changing it from a *polar* to a predominantly *equatorial* direction. This model is illustrated in Fig. 3.12.

3.5.1 No polar wind

Our modelling results do not indicate the presence of a prominent polar structure in H0557-835. In Fig. 3.9, the measured visibilities are compared to those for the CAT3D and CAT3D-WIND models

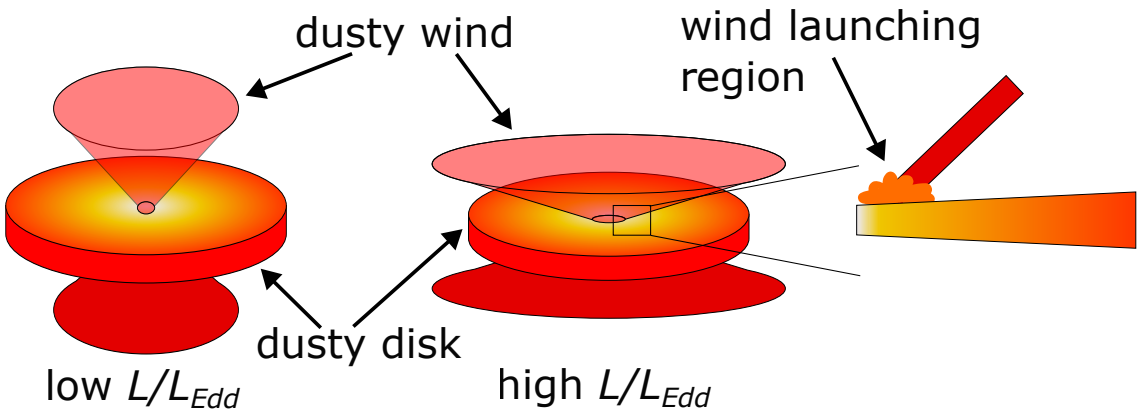

FIGURE 3.12: This illustration is an approximation of the torus structure in low (left) and high Eddington ratio AGN (right), as the opening angle of the wind outflow cone increases. It also depicts a vertical slice of disk and wind at the inner boundary of the disk. Here, infrared radiation pressure launches the wind off of the disk. The colour gradient from white/yellow to red depicts the temperature gradient of the dust. Credit: Rowan Dayton-Oxland

best fitting the SED. The model visibilities were extracted from the corresponding radiative transfer model images at $3.4\,\mu\mathrm{m}$ and $4.6\,\mu\mathrm{m}$. The best fit parameters show that while the CAT3D iteration does not have a wind by construction, neither does the CAT3D-WIND iteration have a significant wind. Here, the wind contains less than a third of the entire infrared-emitting dust and has the largest opening angle available in the model, of 45 degrees. The shaded regions in the plots encompass the entire range of visibilities covered in perpendicular directions when simulating the interferometric observations of the images. They are narrow for both iterations, showing very little directional dependence, which is also reflected in our observations. In addition, the model results with and without wind are very similar in the visibility space, indicating that the addition of a weak polar wind does not make a significant impact on interferometric observations. Even with more precise data, it would not be possible to distinguish between these two instances of models. There, we assume for further discussion that H0557-385 does not harbour any significant *polar* wind.

3.5.2 Inferring the dust distribution within $10\,R_{\mathrm{sub}}$

Fig. 3.10 shows the single Gaussian interferometric sizes of our two objects as a function of wavelength. It also shows the Gaussian half light radii for a dusty disk with a homogeneous radial dust distribution, and two radial power law dust distributions, $r^{-0.2}$ and $r^{-0.5}$, as well as those of a CAT3D-WIND model with a wind opening angle of 60° (as described at the end of Section 3.4.2). The CAT3D-WIND model lies between the homogeneous disk and the disk with $r^{-0.2}$ profile. H0557-385, in purple, has a large *L*-band size, clearly above the homogeneous dusty disk at that point. As wavelength increases, the relative sizes appear to flatten out (or even possibly dip in the *M*-band), within $\sim 10\,R_{\mathrm{sub}}$. The size then increases almost up to the homogeneous disk track again at the longest wavelengths of $12 - 13\,\mu\mathrm{m}$. The sizes of I Zw 1 in orange consistently follow

the profile of the homogeneous disk, while staying just above it. The *KLM*-bands are concentrated within sizes below $\sim 5\,R_{\rm sub}$.

The power law interferometric sizes as a function of wavelength are presented in Fig. 3.11. Power law half light radii for a dusty disk with a homogeneous radial dust distribution, a radial power law dust distribution with $r^{-0.2}$, and a radial power law dust distribution with $r^{-0.5}$ are also shown. The power law sizes of the CAT3D-WIND model with the large wind opening angle are consistently above those of the homogeneous disk. H0557-385 *LM*-band sizes (purple circles) are offset to larger sizes from the homogeneous disk distribution. At longer wavelengths, the sizes follow the homogeneous disk model more closely. Interestingly the *LM*-band sizes are consistent with the longer wavelength sizes implying that the bulk of the brightness in the 3.4 μm to 12.5 μm wavelength region emerges from the same spatial region ($\sim 4-10\,R_{\rm sub}$). For I Zw 1 (orange circles), the short wavelength sizes in the *KLM*-bands roughly follow the CAT3D-WIND tracks, with sizes $\lesssim 5\,R_{\rm sub}$. Those tracks are slightly offset from the homogeneous disk but follow a similar slope. On the other other hand, the upper limit in the *N*-band indicates a deviation from the shorter wavelength trend towards a flatter dust distribution (approximately parallel to the $r^{-0.2}$ track).

It is worth highlighting that both the Gaussian model sizes as well as those extracted from the more physically motivated power-law model are consistent with each other within errors. This demonstrates that the analysis of our results is not dependent on the chosen model. Both approaches imply that a significant fraction of the total infrared emission is concentrated at about the radius constrained by the *LM*-bands.

3.5.3 Where is the dusty wind – evidence for a wind launching region

The presence of a dusty wind is often inferred through a *polar* elongation in mid-IR interferometry and imaging (e.g. Hönig et al., 2012; Asmus et al., 2016). Both I Zw 1 and H0557-385 show no evidence of polar elongations in the *N*-band (Burtscher et al., 2013; López-Gonzaga et al., 2016), although we expect the wind emission to dominate the mid-IR (Tristram et al., 2014; Isbell et al., 2022). Radiative hydrodynamic (RHD) simulations of the dust around AGN show that due to anisotropy of the accretion disk radiation an increase in the accretion will increase the opening angle of the polar dust cone (e.g. Williamson et al., 2020). In this picture, higher accretion rates will flatten out the winds into the equatorial direction close to the disk (Fig. 3.12). We can now test if this model is consistent with our observations.

In H0557-385, the sizes between 3.4 and $12.5\,\mu$m are more or less independent of wavelength. This implies that the bulk of the emission is concentrated within the $\sim 3-10\,R_{\rm sub}$ region. In I Zw 1, this flattening is prominently seen in the power law sizes, constrained to within $\sim 5\,R_{\rm sub}$ in the *KLM* bands. Within the model of a radiatively driven wind, these observations are consistent with a wind launching region. In this region, a combination of infrared and AGN radiation pressure blows dust off of the disk into the wind (Fig. 3.12). This region represents a conglomeration of the dust in the disk ("puffed-up disk") and would dominate the emission in the bands corresponding to the

size of this region. Both H0557-385 and I Zw 1 show such a flattening in sizes at the expected distances (Hönig & Kishimoto, 2017).

Puffed-up regions are regularly seen in young stellar objects (Dullemond et al., 2001; Hönig, 2019). This bulge in the dust distribution will throw a shadow on the dust in the disk behind it, decreasing the temperature of that dust. As a result, sizes measured at longer wavelengths will be artificially decreased. This will lead to a "bump feature" in the size-wavelength relation where sizes remain constant.

3.5.4 Where is the dusty wind – equatorial outflow or blow out?

As mentioned previously, one important factor in the dusty wind model is the dependence of the wind direction on Eddington ratio. Both I Zw 1 and H0557-385 are high-Eddington ratio sources. As such, the model would predict an equatorial wind. This may appear as if the polar wind seen in lower Eddington ratio sources is blown out. Evidence for such blow out has been found in mid-infrared and sub-mm observations of some local AGN as shown in Alonso-Herrero et al. (2021) and García-Burillo et al. (2021). Indeed, the objects that appear to lack a polar wind preferentially have either higher luminosities and/or accretion rates than typical Seyfert galaxies or are very low luminosity AGN where significant radiative feedback is not expected.

For our data, aside from the absence of a polar wind, we find that CAT3D-WIND models with large wind opening angles match the H0557-385 observations relatively well, in particular for our Gaussian size estimates. They do not reproduce the puffed-up region as it is not included in the model. While not being proof of an equatorial wind, this highlights that our observations are consistent with such a scenario. Interestingly, when focusing on the Gaussian sizes, I Zw 1 at higher Eddington rate follows closer the homogeneous disk model than H0557-385. This may be interpreted as a sign of a stronger blow-out of the wind or flattening of the wind launching region, in line with the overall radiatively driven dusty wind picture.

3.5.5 The NIR dust structure in I Zw 1

In addition, we want to discuss the *K*-band size of I Zw 1 and its implications for the near-IR dust structure. Previous work has shown that the NIR emission region, the hot dust, is likely in the shape of a thin ring (Kishimoto et al., 2011a; GRAVITY Collaboration et al., 2020b, 2024). For consistency with previous works, we also assume here that this is the case. As the measured half light radii are model-dependent in the partially resolved limit, we divide our Gaussian size by a factor $\sqrt{\ln 2}$ to convert to a thin ring size (Kishimoto et al., 2011b). The thin ring size is then $2.8\,R_{\rm sub}$. The normalised size of the hot dust ($R/R_{\rm sub}$) can be used to get a qualitative picture of the dust emissivity and density slopes (Kishimoto et al., 2011b; GRAVITY Collaboration et al., 2020b). If more hot dust is concentrated close to the sublimation radius, then $R/R_{\rm sub} \to 1$ – the dust emissivity and density slopes are steep. On the other hand, a more spread out NIR emitting

region will result in a large value of $R/R_{\rm sub}$. Given that the *K*-band value of $R/R_{\rm sub}$ in I Zw 1 is relatively large, this is in agreement with a shallow dust emissivity and density slope, and an extended NIR emitting region. This is in contrast to results found by Kishimoto et al. (2011a) and GRAVITY Collaboration et al. (2020b), who looked at the dependency of $R/R_{\rm sub}$ on the bolometric luminosity. They found that in general, $R/R_{\rm sub}$ decreases with increasing luminosity, meaning that emissivity and density slopes get steeper with higher luminosity. However, I Zw 1 is in the first quartile of normalised sizes when put in context of the GRAVITY Collaboration et al. (2020b) sample. In its corresponding luminosity bracket, it is larger than any other object. This suggest that there might be secondary effects driving the NIR dust structure, such as the Eddington ratio.

Another explanation for the comparatively large relative *K*-band size in I Zw 1 is the uncertainty in the sublimation radius. While we adopted $R_{\rm sub} = 0.18\,{\rm pc}$, the 1 dex spread in $L_{\rm bol}$ allows for an up to 50% increase in the size of the sublimation radius. With a sublimation radius of $\sim 0.3\,{\rm pc}$, the relative *K*-band size will decrease to $\sim 1.5\,R_{\rm sub}$, much more similar to other objects. However, going to the other extreme of $L_{\rm bol}$ decreases the sublimation radius even further, resulting in a relative *K*-band size of $\sim 4\,R_{\rm sub}$. Uncertainties in the calculation of the bolometric luminosity and the sublimation radius can have large effects on the interpretation of the results.

3.6 Conclusions

In this paper, we present the fist VLTI/MATISSE data of Type 1 AGN, focusing on the infrared structure of highly accreting sources. We used Gaussian and power law models to fit the interferometric data to recover the sizes from our MATISSE *LM*-band and archival GRAVITY *K*-band data. Using these data together with prior results from longer wavelength MIDI data, we were able to construct a multi-wavelength view of the dust structure. This shows that:

1. There is no evidence for a polar wind in both objects. This could be either due to a wind being launched equatorially, projection effects, or the wind region being blown out at high Eddington ratios.
2. Interferometric data implies a preferentially disky equatorial dust distribution in both objects.
3. We find evidence that the near- to mid-IR emission is concentrated in the disk plane at distances $\sim 3 - 10\,R_{\rm sub}$, which we interpret as signs of a puffed-up wind launching region.

The presence of a puffed-up inner region with absence of a *polar* wind in these high Eddington ratio objects is notably different to previously observed lower accreting Seyferts. However, it matches predictions of a radiation pressure driven wind model. To further examine the relationship between the behaviour of the dusty 'torus' and the Eddington ratio, we need to expand our current sample of multi-wavelength interferometrically observed high-Eddington objects. The use of GRA4MAT in mid-IR observations will increase the quality of data and enable new *N*-band

observations which will provide us with phases for the first time. Currently ongoing upgrades of GRAVITY into GRAVITY+ will further increase capabilities.

Chapter 4

A Phenomenological Study of the Accretion Disk in the Super-Eddington AGN I Zw 1

"No! Please! I'll tell you whatever you want to know!" the man yelled.
"Really?" said Vimes. "What's the orbital velocity of the moon?"
"What?"
"Oh, you'd like something simpler?"

Night Watch
Terry Pratchett

In this chapter we investigate the accretion disk structure, particularly its temperature profile, in the super-Eddington AGN I Zw 1, one of the two objects studied in Chapter 3. As discussed in the last chapter, the accretion disk emission appears to play an important role in shaping the dusty torus. Therefore, we now study how the accretion disk structure is influenced by high Eddington ratios and how this connects to the structures at larger radii, particularly the BLR and the dusty torus. We use continuum reverberation mapping to temporally resolve the temperature profile of the accretion disk. The work contained within this chapter has been submitted.

This work was carried out in close collaboration with Roberta Vieliute and Juan V. Hernández Santisteban. I designed and led the study, with data calibration and Fourier analysis tools provided by Roberta Vieliute (the data calibration method is published in Vieliute et al., 2025). I carried out the data analysis and composed the discussion based on my own work. I also received valuable input from further collaborators: Keith Horne, Aaron J. Barth, Edward M. Cackett, Encarni Romero Colmenero, Michael R. Goad, Shai Kaspi, Hermine Landt, Paulina Lira, Hagai Netzer, Marianne Vestergaard, and Hartmut Winkler. This work is based on observations collected at Las

Cumbres Observatory (LCO) robotic telescope network, under LCO Key Projects KEY2020B-006 and KEY2023B-001 (PI: J. V. Hernández Sanstisteban) (Brown et al., 2013). The raw data is publicly available on the LCO Archive at archive.lco.global. The inter-calibrated light curves are publicly available on Zenodo at dx.doi.org/10.5281/zenodo.16599407. Additional publicly available data was obtained from the XMM-Newton Science Archive (obsIDs 0743050301, 0743050801, and 0851990101) at nxsa.esac.esa.int/nxsa-web/ and the *Swift* archive at swift.ac.uk.

4.1 Introduction

AGN are some of the most luminous objects in the Universe; maintaining this luminosity primarily through accretion onto a supermassive black hole through an accretion disk (Salpeter, 1964; Lynden-Bell, 1969). The structure of this disk is most often approximated with a thin disk (geometrically thin and optically thick; Novikov & Thorne, 1973; Shakura & Sunyaev, 1973). To probe the radial temperature profile of this disk, we usually use continuum reverberation mapping studies. Disk reverberation studies have all shown correlated continuum light curves, with short wavelength light curves temporally leading those at longer wavelengths on the order of days (e.g. Cackett et al., 2007, 2018; Fausnaugh et al., 2016, 2018; Edelson et al., 2017; Hernández Santisteban et al., 2020). This implies the presence of a structure with a radial temperature profile reprocessing light from a central, variable source. In the vast majority of objects, the lag-wavelength spectrum is well fit with a thin disk $\tau(\lambda) \propto \lambda^{4/3}$ relation (e.g. Collier et al., 1999; Cackett et al., 2007; Fausnaugh et al., 2016; Edelson et al., 2019). However, several frequently found discrepancies suggest that the accretion disk and observations are significantly more complicated. First, there is the '*u*/*U*-band excess'. This is an excess lag observed in the *u*/*U*-band, at times accompanied by a similarly increased lag in the *r*/*R*- or *i*/*I*-band. In addition, there is the 'too large disk' problem. The normalisation of the lag-wavelength relation lets us infer a size, or alternatively an accretion rate, of the disk (under the assumption of the classical thin disk-lamppost model, Cackett et al., 2007; Fausnaugh et al., 2016). The majority of studies have found a disk several times larger than predicted by their bolometric luminosity, usually around a factor of $2-3$ (also observed via microlensing e.g. Morgan et al., 2010). Another feature often noticed is continuum variability on different timescales (Hernández Santisteban et al., 2020; Vincentelli et al., 2021; Cackett et al., 2023; Donnan et al., 2023; Miller et al., 2023; Lewin et al., 2024). While variability on a daily scale appears to be related to disk reprocessing, additional variability on longer timescales (tens – hundreds of days) has also been found and contains important information about the internal structure of the AGN. Recently, frequency[1]-resolved Fourier analysis of continuum light curves has shown great power to unravel different sources of reverberation signals (Uttley et al., 2014; Cackett et al., 2022; Lewin et al., 2023, 2024; Panagiotou et al., 2025).

It has been frequently noted and demonstrated that these discrepancies can be created by a contamination of the disk continuum by diffuse continuum emission from a second reprocessing

[1]Frequency in this study is only used to refer to Fourier frequencies, i.e. the variability frequency, and not the frequency of radiation. Radiation energy is only referred to using its corresponding wavelength.

region at larger distances, usually interpreted as the broad line region (Korista & Goad, 2001, 2019; Lawther et al., 2018; Netzer, 2022). The BLR is a region of high velocity and density clouds at larger radii than the accretion disk. This BLR diffuse continuum is particularly strong at the Balmer and Paschen jumps, i.e. the *u/U*- and *i/I*-bands. Further, the BLR continuum likely 'artificially' lengthens lags through a second reprocessing at larger distances at all wavelengths and may therefore be partially responsible for the too-large-disk problem.

Of course, one of the main reasons for the complexity of these studies is that the underlying disk may not be a simple thin disk, but rather more complex, such as a slim disk (Abramowicz et al., 1988). It is generally presumed that AGN accretion mechanisms and disk structures change at the Eddington limit. In the basic picture, sub-Eddington AGN as described above are presumed to host thin disks, and super-Eddington AGN slim disks. This transition is probably rather gradual as advective cooling becomes more and more important, even at moderate to high sub-Eddington rates.

There have been fewer super-Eddington objects studied, but they mostly present with the same features as sub-Eddington objects. The lag-wavelength spectra are well fit with the thin disk profile of $\tau(\lambda) \propto \lambda^{4/3}$ and the slim disk profile of $\tau(\lambda) \propto \lambda^{2}$ corresponding to the slim disk temperature profile $T \propto R^{-1/2}$ (Wang & Zhou, 1999; Cackett et al., 2020; Donnan et al., 2023; Thorne et al., 2025). In addition, an excess in the *u/U*-band lag has been observed, and there is evidence of the too-large-disk problem. Further, the SED is used to analyse the temperature profile of the underlying disk, where a thin disk has a long-wavelength tail with $F_\nu \propto \nu^{1/3}$, while a slim disk has $F_\nu \propto \nu^{-1}$ (Wang et al., 1999). Results are inconclusive as both profiles are found to fit, especially depending on the amount of internal host galaxy extinction applied (Cackett et al., 2020; Donnan et al., 2023).

AGN disks and the study thereof is complex. Therefore, we aim to foremost phenomenologically describe the disk structure of the prototype Narrow Line Seyfert 1 galaxy I Zw 1. I Zw 1 is super-Eddington with a central black hole mass of $\log(M_{\rm BH}/{\rm M}_\odot) \sim 6.97$, accreting at an Eddington ratio of $\dot{m}_E \sim 2$ and at a redshift of $z \sim 0.061$ ($255\,{\rm Mpc}$, Asmus et al., 2016; Huang et al., 2019). This enables us to observe an accretion disk in an extreme state, which can reveal more information about the underlying physics. The structure of this AGN has also been extensively studied across the electromagnetic spectrum, including the X-ray, UV/optical observations and reverberation mapping of the BLR, and radial mapping of the dusty torus (Silva et al., 2018; Rogantini et al., 2022; Huang et al., 2019; Juráňová et al., 2024; Burtscher et al., 2013; GRAVITY Collaboration et al., 2024, Chapter 3). This enables us to also put our results in the wider context of multi-wavelength AGN structure.

We have obtained photometric monitoring of I Zw 1 using the Las Cumbres Observatory (Brown et al., 2013), over three years in 7 optical bands with an average cadence of $\simeq 0.75$ days. We set out three aims for this study. Firstly, we want to phenomenologically describe the accretion disk in I Zw 1. Next, we will discuss our observations in the context of other super-Eddington and sub-Eddington disks to compare and contrast their underlying disk structure. Lastly, we will

Facility	Observation Date	Filters	Cadence (days)
LCO	Year 1: 02.07.2020 – 09.02.2021	*uBgVriz*$_s$	1.14
	Year 2: 23.05.2021 – 19.02.2022		0.86
	Year 3: 09.06.2022 – 15.02.2023		0.56
	Year 4: 23.05.2023 – 08.02.2024		0.91
XMM-Newton OM	19.01.2015	*UVW2, UVM2, UVW1, U, B, V*	
	21.01.2015	*UVW2, UVM2, UVW1, U, B, V*	
	12.01.2021	*UVW2, UVW1, U, B, V*	
Swift UVOT	13.07.2023	*UVW2, UVM2, UVW1, U, B, V*	

TABLE 4.1: Observation log for the data used in this paper. Details about the observations and reductions are in Section 4.2.

examine the multi-wavelength structure of I Zw 1, for the first time assembling physical sizes from the optical accretion disk to the mid-IR dust. In Section 4.2, we describe our data collection and reduction processes. In Section 4.3, we conduct the time series analysis of the light curves, using the cross-correlation and PyROA methods, as well as Fourier analysis. In Section 4.4, we analyse the SED. In Section 4.5, we discuss our results in relation to a phenomenological description of the disk structure, in the context of other AGN disk studies, and the multi-wavelength structure of I Zw 1.

4.2 Data Collection and Reduction

In this section we describe our data collection and reduction procedures. Our main data set is four years of optical photometric observations of I Zw 1 with a sub-day cadence from the Las Cumbres Observatory. We supplement this with UV/optical observations from *XMM-Newton* OM and *Swift* UVOT. Even though only one of these observations was taken concurrently with the LCO monitoring, we include these data to characterise the UV emission generally. The observation logs are presented in Table 4.1.

4.2.1 Las Cumbres Observatory

The multiband observations of the light of curve of I Zw 1 were acquired with the Las Cumbres Observatory robotic telescope network (Brown et al., 2013). The observations were made under

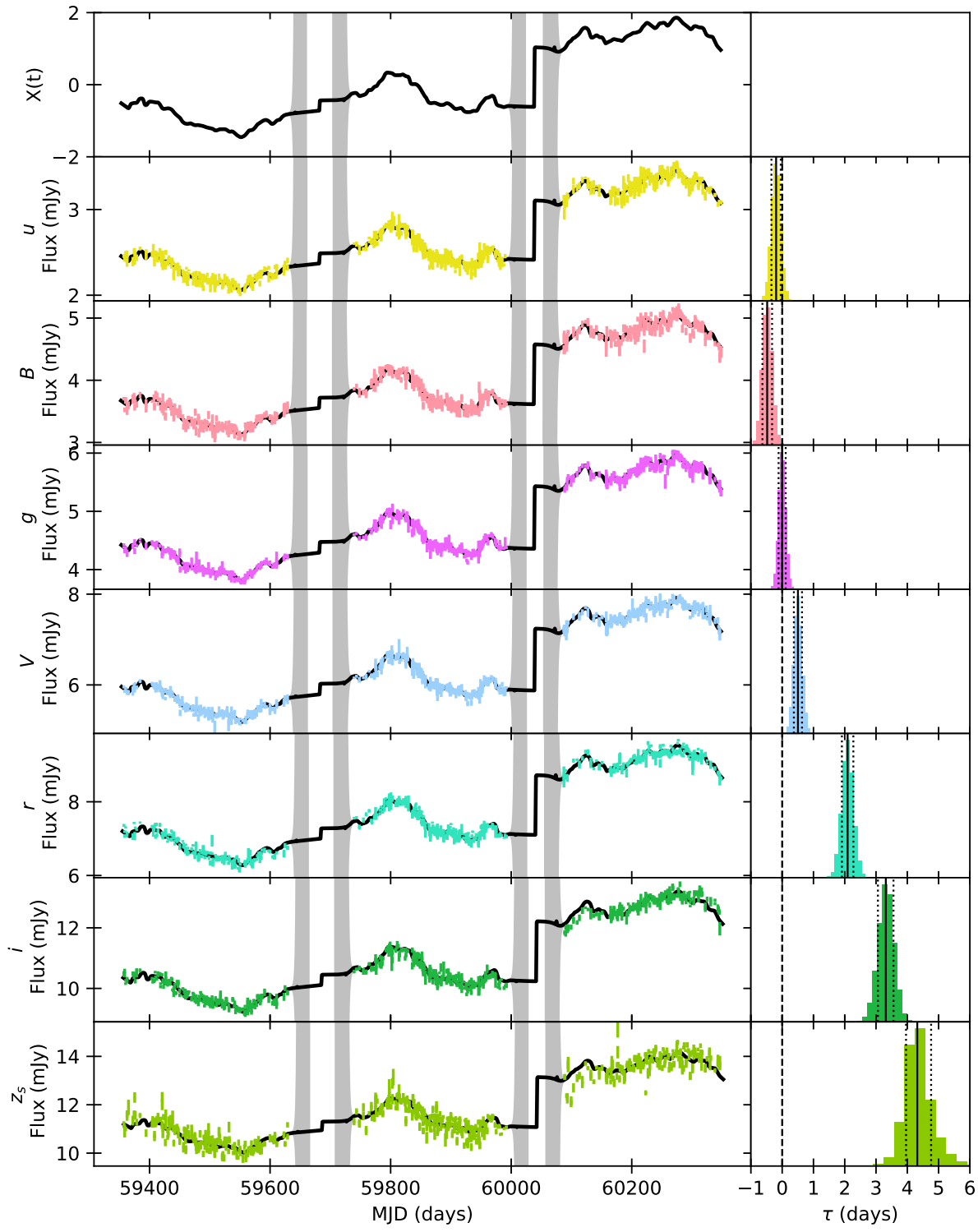

FIGURE 4.1: The light curves in all bands for Years 2 – 4, the PyROA model (solid line), and its 68% confidence interval shown in grey, including the driving light curve $X(t)$ (top panel). The right panel shows the marginalised posterior distributions for the inter-band lags as calculated by PyROA, with its mean (solid line) and 68% confidence interval denoted by the dotted lines. The reference light curve is the g-band.

LCO Key Projects KEY2020B-006 and KEY2023B-001 (PI: J. V. Hernández Sanstisteban). An overview of the observations can be found on the AGN Variability Archive (AVA)[2]. The telescopes are 1 m telescopes and host Sinistro CCD cameras with a field of view of $26.5' \times 26.5'$ and a resolution of $0\farcs389\ \mathrm{pix}^{-1}$. We obtained high cadence photometry in 7 filters: Bessell *BV*, SDSS *ugri*, and Pan-STARSS z_s. At each observation, two exposures were made with exposure times $(BVugriz_s) = 2 \times (30, 30, 120, 30, 30, 30, 60)$ s. Fig. B.1 shows the average observed spectrum of I Zw 1 across the LCO campaign overlaid with the LCO filter transmission curves. While the campaign on I Zw 1 is still ongoing, here we look at the first four years of data. In these four years, we had four observing seasons, each between 250 – 270 days long. Apart from Year 1 (1.14 days), all other years have observations at a sub-day cadence. The average cadence of the latter three years is 0.75 days. A summary of the observations is presented in Table 4.1. We do not use Year 1 due to its particularly low cadence and lower variability amplitude, and generally worse light curve quality and instead only use Years 2, 3, and 4 in our analysis. We downloaded the data from the LCO archive, flat-fielded and bias corrected internally using BANZAI (McCully et al., 2018). Sources are extracted using SEXTRACTOR with an extraction aperture radius of $5''$ (Bertin & Arnouts, 1996). This is to ensure the effect of the variable PSF over the observing season due to atmospheric changes is minimal. The background is calculated using a global background model made by smoothing the image in a 200 point pixel mesh. We use the field stars to calculate the zero-point, using the AAVSO Photometric All-Sky Survey (APASS) DR10 for all filters except *u* (Henden et al., 2018). The *u*-band is calibrated using the Sloan Digital Sky Surveys (SDSS) DR16 (Ahumada et al., 2020). For additional details on the data reduction process see Hernández Santisteban et al. (2020) and Donnan et al. (2023).

To calibrate and adjust the light curves between the different telescopes we use a new intercalibration method, PyTICS, based on comparison field stars described in Vieliute et al. (2025)[3]. This method corrects for effects from the small systematic differences of the telescopes in the LCO network, such as filter transmissions and camera sensitivities, and the large range of observing conditions, including variations in weather, airmass, seeing, and sky transparency. PyTICS also estimates the additional uncertainty that arises from these effects, for example increasing noise for telescope faults or bad nights. This allows for precise and accurate determination of bad data points in contrast to simply using large offsets from the average AGN light curve. The correction factors and their uncertainties are calculated incrementally through an iterative process. They are then blindly applied to the AGN light curve, conserving the AGN's inherent variability structure. This is done independently in each filter. For details, see Vieliute et al. (2025).

4.2.2 *XMM-Newton* OM

I Zw 1 was observed with the optical monitor (OM) onboard *XMM-Newton* in 2015 and 2021 (Jansen et al., 2001; Mason et al., 2001). Here we use the two observations from 2015 (obsIDs

[2] alymantara.com/ava/
[3] https://github.com/Astroberta/PyTICS

0743050301 and 0743050801) and one observation from 2021 (obsID 08519901). In 2015 the object was observed with the *UVW2, UVM2, UVW1, U, B, V* filters while in 2021 only the *UVW2, UVW1, U, B, V* filters were used (see Table 4.1). We downloaded the processed data from the XMM-Newton Science Archive and extracted the relevant information. The data were processed with the Science Analysis System (SAS) version 18.0.0. Fluxes were extracted from a source region calculated by the `omdetect` task. The extraction apertures for I Zw 1 vary between 2.″0 and 2.″5.

4.2.3 *Swift* UVOT

We use archival ultraviolet/optical data from the Neil Gehrels *Swift* Observatory (Gehrels et al., 2004) serendipitously taken throughout the optical LCO monitoring. One epoch from 2023 was processed through the standard UVOT (Roming et al., 2005) pipeline (v.4.5) to obtain photometric measurements with a $5''$ radius aperture centred at the coordinates of the AGN, to be consistent with the ground-based photometry and avoid different host-galaxy contributions. The background estimation was selected from a $30''$ radius aperture located in a nearby blank part of the image.

4.3 Time Series Analysis

The light curves of I Zw 1 over all three years show both short and longer term variability. They are also correlated – distinctive features are repeated across the seven bands (see Fig. 4.1). The reference band is usually taken to be the shortest wavelength. However, in our case this is the *u*-band for which we expect significant BLR contamination, which will then dilute the disk signal in the lags from all other bands. We chose to measure these lags using as reference the *g*-band as this is the shortest wavelength that will have the least BLR contamination, with the highest data quality.

Multiple methods can be used to calculate time lags, but here we focus on two: the cross correlation function (CCF) and PyROA (Donnan et al., 2021, 2023). Cross correlation is the most direct mathematical method, shifting light curves with respect to a reference light curve and evaluating how well they correlate as a function of lag. PyROA instead directly models the light curves and a driving light curve, which takes into account a scaling of the light curve amplitudes in addition to the time shift. In the following section we further describe these methods and evaluate the time lags.

4.3.1 Cross correlation

Here we use the interpolated cross correlation function (ICCF) method with flux randomisation/random subset sampling (FR/RSS) as demonstrated in Peterson et al. (2004), using the PyCCF code (Sun et al., 2018) to retrieve the inter-band lags. This method accounts for uneven sampling of the light curves and uncertainties in the data, and estimates reliable errors on

Band	$\lambda_{\rm eff}$ (Å)	Year 2		Year 3		Year 4	
		$\tau_{\rm peak}$	$\tau_{\rm cent}$	$\tau_{\rm peak}$	$\tau_{\rm cent}$	$\tau_{\rm peak}$	$\tau_{\rm cent}$
u	3540	$0.20^{+0.20}_{-0.55}$	$-1.90^{+1.26}_{-1.07}$	$0.15^{+0.10}_{-0.35}$	$-1.82^{+0.82}_{-0.80}$	$-0.25^{+0.10}_{-0.10}$	$-1.96^{+0.64}_{-0.45}$
B	4361	$-0.20^{+0.45}_{-0.15}$	$-2.38^{+1.09}_{-1.16}$	$0.10^{+0.10}_{-0.25}$	$-1.04^{+0.79}_{-0.92}$	$-0.05^{+0.10}_{-0.10}$	$-0.46^{+0.56}_{-0.69}$
g	4770	$0.00^{+0.00}_{-0.00}$	$-0.02^{+0.96}_{-0.92}$	$0.00^{+0.00}_{-0.00}$	$0.01^{+0.64}_{-0.64}$	$0.00^{+0.00}_{-0.00}$	$0.00^{+0.46}_{-0.48}$
V	5448	$-0.25^{+0.55}_{-0.10}$	$1.38^{+1.20}_{-1.49}$	$0.15^{+0.10}_{-0.05}$	$1.37^{+0.72}_{-0.77}$	$-0.05^{+0.40}_{-0.05}$	$0.63^{+0.65}_{-0.59}$
r	6215	$5.35^{+1.25}_{-2.80}$	$7.92^{+1.41}_{-1.84}$	$0.95^{+1.40}_{-0.65}$	$1.81^{+0.70}_{-0.76}$	$1.30^{+2.30}_{-0.75}$	$2.83^{+0.56}_{-0.62}$
i	7545	$2.60^{+2.50}_{-3.10}$	$7.87^{+1.67}_{-2.06}$	$2.25^{+2.10}_{-0.95}$	$6.15^{+0.67}_{-0.83}$	$1.40^{+1.35}_{-0.90}$	$7.14^{+3.67}_{-2.02}$
z_s	8700	$9.55^{+0.85}_{-2.08}$	$10.8^{+1.4}_{-2.2}$	$0.20^{+2.65}_{-0.55}$	$4.77^{+1.87}_{-1.75}$	$6.85^{+5.45}_{-1.10}$	$8.05^{+4.55}_{-2.10}$

TABLE 4.2: Lags in days (observed frame) using the cross correlation method, measured between each light curve and the reference light curve in the *g*-band. The interpolated cross correlation function was applied to each year of data separately. From this, the lag at the peak of the CCF $\tau_{\rm peak}$, and the centroid above $0.8r_{\rm peak}$, $\tau_{\rm cent}$, are calculated (see Section 4.3.1). Uncertainties are the 68% confidence intervals.

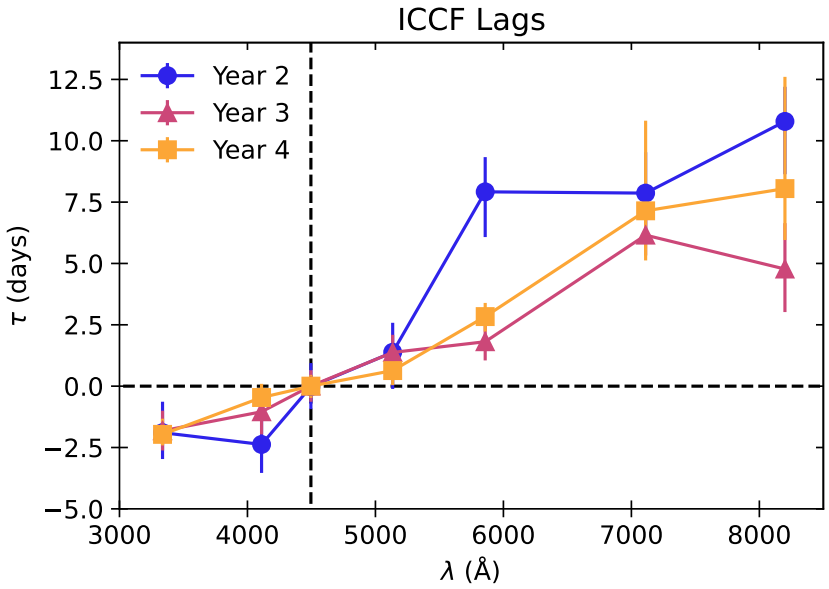

FIGURE 4.2: Lag spectrum for Years 2–4 as calculated using ICCF, using the centroid lag $\tau_{\rm cent}$ and with reference to the *g*-band in the AGN rest frame. Year 2 is denoted by the circles, Year 3 by the triangles, and Year 4 by the squares. Lags plotted here are presented in Table 4.2. Lags increase with wavelength for all years.

	u	B	g	V	r	i	z_s
	3540 Å	4361 Å	4770 Å	5448 Å	6215 Å	7545 Å	8700 Å
τ	$-0.19^{+0.15}_{-0.15}$	$-0.48^{+0.15}_{-0.16}$	$0.00^{+0.11}_{-0.11}$	$0.50^{+0.13}_{-0.13}$	$2.09^{+0.18}_{-0.18}$	$3.31^{+0.24}_{-0.25}$	$4.32^{+0.44}_{-0.36}$

TABLE 4.3: Lags in days (observed frame) as calculated using PyROA, measured between each light curve and the reference light curve in the g-band. PyROA was applied to Years 2–4 simultaneously (see Section 4.3.2). Uncertainties are the 68% confidence intervals.

	β	τ_0 (days)	y_0
thin disk	$4/3$	4.23 ± 0.24	1.00 ± 0.02
slim disk	2	1.71 ± 0.09	1.03 ± 0.04
free β	2.51 ± 0.34	$1.19^{+0.33}_{-0.26}$	1.04 ± 0.06

TABLE 4.4: The fit results for three different disk profiles to the lag-wavelength spectrum calculated by using PyROA, based on Eq. 4.2. For the thin and slim disk profiles β was fixed while the free β fit varied β. Uncertainties are the 68% confidence intervals.

the lags. Notably, however, it has been shown that ICCF overestimates errors (Cackett et al., 2018; Yu et al., 2020).

We use RSS to create a large number ($N_{\rm sim}$) of realisations of the light curves, which is sampling with substitution. The errors on the data points are scaled according to the number of times that point has been picked. Then, applying FR, we add Gaussian noise where the mean is the flux of the point and sigma is the error on the flux. The ICCF is evaluated by linearly interpolating one light curve first, and then cross correlating both curves. Next, the second light curve is interpolated and both curves are again cross correlated. The final ICCF is the average CCF of both instances. To determine the lag, we calculate both the lag at the peak $\tau_{\rm peak}$ and the centroid lag $\tau_{\rm cent}$ (above $0.8r_{\rm peak}$) of the final CCF. We repeat this process $N_{\rm sim} = 10^4$ times. We use a lag search interval of -50 to 50 days, with a sampling step of 0.05 days. The final lags are determined as the median of the peak and centroid distributions, with uncertainties from the 16% and 84% quantiles. We analysed each year individually, as the considerable gap between each observing season (~ 100 days) is not approximated well by linear interpolation when considering variability on the timescale of days. All lags (peak and centroid) for Years 2–4 are presented in Table 4.2. The peak correlation coefficients $r_{\rm peak}$ are further tabulated in Table B.1. We also use the centroid lag, $\tau_{\rm cent}$, as the main ICCF-derived lag from here on. The lag-wavelength spectrum for Years 2–4 as calculated using ICCF is plotted in Fig. 4.2.

4.3.2 PyROA

For a more detailed analysis of the light curves, we use PyROA (Donnan et al., 2021, 2023). PyROA uses a running optimal average to model the light curves, and MCMC methods to estimate

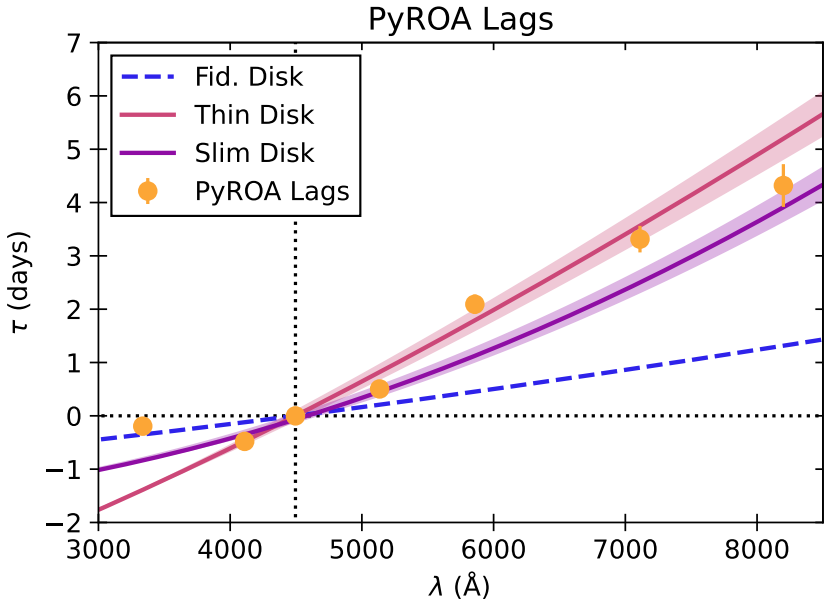

FIGURE 4.3: Lag spectrum as calculated using PyROA simultaneously for all three years in the AGN rest frame (shown in Table 4.3). As in Fig. 4.2, lags increase with wavelength. A thin disk profile with $\tau \propto \lambda^{4/3}$ and a slim disk profile with $\tau \propto \lambda^{2}$ is fitted to this data (Table 4.4). These are shown with the solid lines and their error regions are shaded. As a comparison, the fiducial thin disk profile for I Zw 1 with its mass and bolometric luminosity is illustrated with the dashed line, with $\tau_0 = 1.07\,\mathrm{days}$ as calculated in Section 4.5.1.

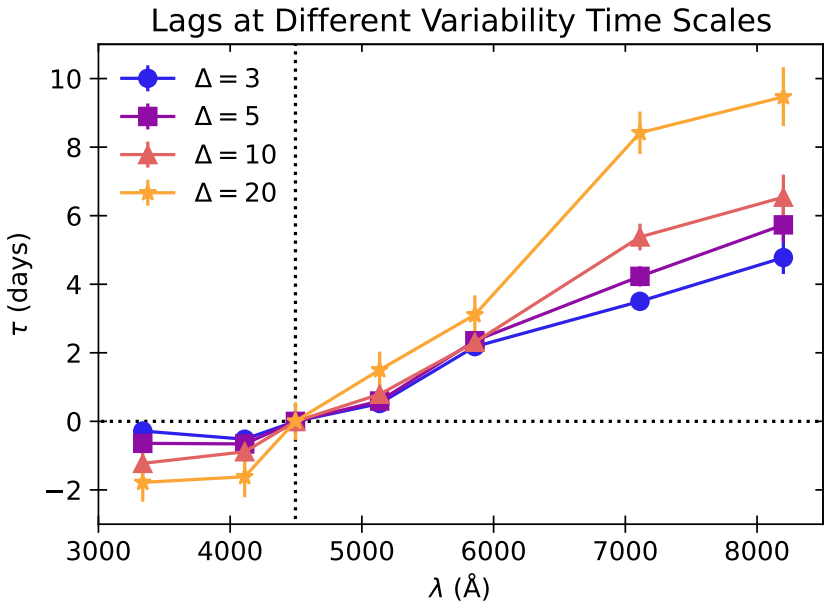

FIGURE 4.4: Lags calculated using PyROA while varying the variability stiffness parameter Δ with $\Delta = 3, 5, 10, 20\,\mathrm{days}$ in the AGN rest frame. $\Delta = 3$ is denoted by the circles, $\Delta = 5$ by the squares, $\Delta = 10$ by the triangles, and $\Delta = 20$ by the stars. As Δ increases, the driving light curve stiffens and longer variability timescales are probed. The plot shows that as that variability timescale increases, the magnitudes of the lags increase.

the uncertainties of the light curve parameters. To take advantage of all available information, all light curves are fitted simultaneously. From this, PyROA calculates a dimensionless driving light curve $X(t)$, with a mean of zero, and a variance of one. To translate the driving light curve to the observed ones, we use the basic light curve model in PyROA. In this, $X(t)$ is scaled and re-normalised to the mean flux of the observed flux, and shifted in time by the lag τ as given by the basic model

$$F_i(t) = A_i X(t - \tau_i) + B_i \tag{4.1}$$

after Eq. 9 in Donnan et al. (2021). $F_i(t)$ is the model flux of the light curve in band i, A_i is the RMS flux, B_i is the mean flux, and τ_i is the lag. The flexibility of the driving light curve is controlled by a Gaussian memory function with a width Δ. As Δ increases, $X(t)$ stiffens and cannot respond well to rapid variability in the light curves. Accordingly, we can analyse different variability timescales by controlling Δ and the timescales over which the light curves are fit. As the fundamental model, we simultaneously fitted the data from Years 2, 3, and 4 with PyROA, with reference to the *g*-band. This fit optimizes A_i, B_i, and τ_i for each band and a common Δ. The results from this fit and the entire set of light curves are presented in Fig. 4.1 and the lag-wavelength spectrum in Fig. 4.3. The lags are also included in Table 4.3. This fit gives $\Delta = 2.55 \pm 0.07\,\mathrm{days}$ when left as a free parameter. To examine behaviour of the lag spectrum at different variability timescales, we repeated this process but setting Δ to $\Delta = 3, 5, 10, 20\,\mathrm{days}$, as this parameter controls how sensitive the fit is to certain features in the light curves. The lag-wavelength spectra from this are shown in Fig. 4.4 and the lags are tabulated in Table B.2. As the best fit Δ of our initial model is also $\simeq 3\,\mathrm{days}$, the first of these variability timescale fits is essentially equivalent to our initial fit.

Figures 4.2 and 4.3 show that independent of the method for lag-calculation, there is a positive relationship between the lag and the wavelength. The PyROA lags are smaller than the ICCF lags because PyROA tends to concentrate on the smallest reasonable variability timescale, i.e., Δ tends to the smallest reasonable value. On the other hand, the ICCF lags are measured using the centroid, which is generally drawn from an asymmetric CCF, with a significant contribution at larger lag values. This means that the ICCF lags are skewed towards larger delays. ICCF errors are also larger than the PyROA ones. This is to be expected as the FR/RSS implemented in PyCCF overestimates the uncertainties (Cackett et al., 2018, see also discussion in Donnan et al., 2021). From here on we will concentrate our analysis and discussion on the PyROA lags as with this method we can fit a larger data set and therefore more information simultaneously. With ICCF, only individual years are accessible and the results of these show significant scatter from year to year. This indicates that these results are more susceptible to variations in quality of the light curves between and in observing season. In addition, we are interested in the disk at small sizes and lags, therefore PyROA is more likely to extract more relevant lags than ICCF. In general, the ICCF results appear to be less robust than PyROA, in the context of measuring the disk.

To characterize the lag-wavelength spectrum we fit $\tau(\lambda)$ according to the standard disk profile power law parametrised as

$$\tau(\lambda) = \tau_0 \left[\left(\frac{\lambda}{\lambda_0} \right)^{\beta} - y_0 \right], \tag{4.2}$$

where $\lambda_0 = 4770/(1+z)$ Å, as lags are calculated in reference to the *g*-band. The factor y_0 normalises the lag at $\lambda = \lambda_0$ to zero and is therefore expected to be 1 in an ideal scenario (see Eq. 1.15). For a thin disk $\beta = 4/3$ and for a slim disk $\beta = 2$ (Shakura & Sunyaev, 1973; Wang & Zhou, 1999). We also perform this fit leaving β as a free parameter. We use a MCMC routine with 16 walkers and 10^5 steps, discarding the first 5000 steps and thinning by 50% to avoid autocorrelation. The fitting results with 68% confidence intervals are shown in Table 4.4. The thin and slim disk fits are also overplotted in Fig. 4.3. The other disk profile has an extremely similar track in the wavelength space explored here. We have also plotted the track for the fiducial disk in I Zw 1 with $\tau_0 = 1.07\,\mathrm{days}$, based on the mass and bolometric luminosity (see Section 4.5.1).

4.3.2.1 The lag-frequency spectrum

A powerful tool for the analysis of times series are Fourier techniques. Figure 4.4 shows that the lags in I Zw 1 change with the variability timescales, with longer lags at longer variability timescales. To further probe this behaviour, we look at the frequency-resolved lags, similar to Cackett et al. (2022) and Lewin et al. (2023, 2024). We create evenly sampled light curves by using PyROA to model the light curves independently, with Δ set to $2\,\mathrm{days}$ to retain as much short term variability as possible, without overfitting the white noise level. We then calculate the cross-spectrum from the Fourier transforms of the reference light curve and light curve of interest. The lag is evaluated from the phase of the cross-spectrum, per frequency bin (for further details see Uttley et al., 2014). We analyse all three years together, with three segments each covering one year of data. These segments have a length of $155\,\mathrm{days}$ each. We use seven frequency bins, covering the frequency range between $0.006 - 2.9\,\mathrm{days}^{-1}$ ($7 \times 10^{-8} - 3 \times 10^{-5}$ Hz). The lag-frequency and coherence spectra for all bands are plotted in Fig. 4.5. In this plot, we have already removed the lowest frequency bin, $\sim 0.01\,\mathrm{days}^{-1}$, as it is sensitive to small variations in the binning parameters. This is likely due to bias effects that have been shown to exist for the lowest frequency bin (e.g. Cackett et al., 2022). The frequency-resolved lags in the *g*-band are flat at zero because it is used as the reference band. Further, all frequencies above $0.5\,\mathrm{days}^{-1}$ are uninformative since the highest frequency we modelled our light curves with was on a variability timescale of $\Delta = 2\,\mathrm{days}$, which we denote with the vertical dotted lines in Fig. 4.5. The PyROA modelling washes out the variability at higher frequencies and correlates adjacent points. This effect is illustrated in the coherence spectra: above $0.5\,\mathrm{days}^{-1}$, the coherence is ~ 1 and then drops towards lower frequencies. This frequency region is where real signal is probed in the light curves and it rises again towards the lowest frequencies, as expected. There is a clear presence of a variability-dependant lag behaviour, with lags significantly increasing in the lowest frequency bin, especially at the longest wavelengths. To analyse this behaviour, we evaluate the predicted frequency-resolved lags for a simple thin disk and fit a model of a thin disk with an additional secondary reprocessor.

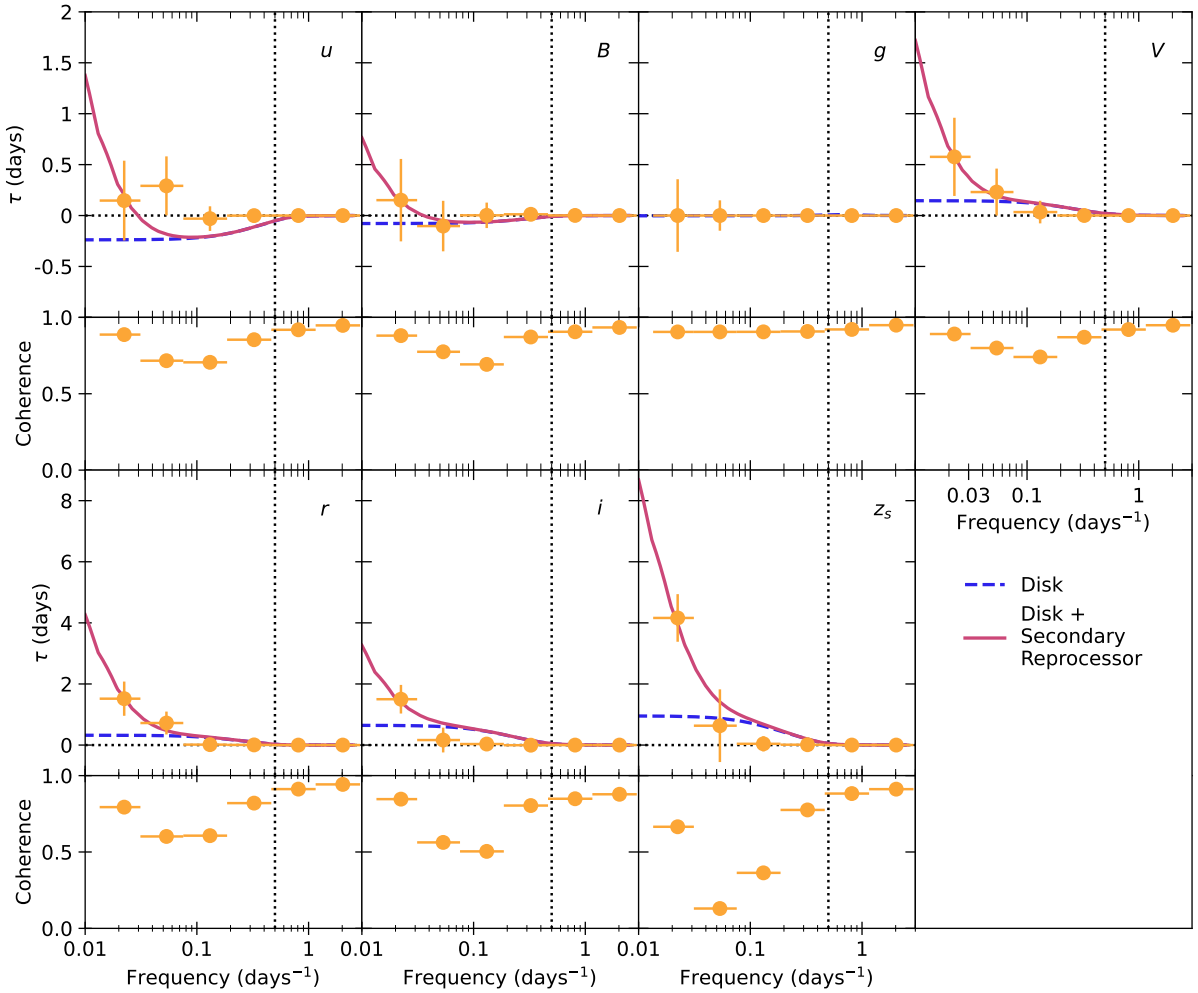

FIGURE 4.5: The lag-frequency and coherence spectra for all bands derived from Fourier analysis. The studied frequency range is $0.013 - 2.9\ \mathrm{days}^{-1}$ ($1.5 \times 10^{-7} - 3 \times 10^{-5}$ Hz); however, data at frequencies above $0.5\ \mathrm{days}^{-1}$ (vertical dotted lines) is uninformative as the ROA washes out the variations (and correlates adjacents points, also increasing its coherence). The data points are plotted with circles, the simple thin disk is denoted with the dashed line, and the disk + secondary reprocessor model is denoted by the solid line. The median delay of the secondary reprocessor in this model is $\tau_M = 20\ \mathrm{days}$.

To produce the frequency-resolved lag expectation of this model, we require the corresponding transfer functions for the accretion disk and the secondary reprocessor models for each band observed. In reverberation mapping, the geometry of a reverberating structure determines its response to a change in the impeding continuum; this response is described by the *transfer function* (Blandford & McKee, 1982). For the accretion disk, we used the thin disk transfer function, ψ_{disk}, which is a function of black hole mass, mass accretion rate and inclination angle (see details in Collier et al., 1999; Cackett et al., 2007; Starkey et al., 2016). We parametrise the transfer function of the secondary reprocessor ψ_{SR} as a log-normal distribution as implemented in Cackett et al. (2022) and Lewin et al. (2023, 2024):

$$\psi_{\mathrm{SR}}(t) = \frac{1}{S\sqrt{2\pi}t} \exp\left[-\frac{\ln\left(t/\tau_M\right)^2}{2S^2}\right], \tag{4.3}$$

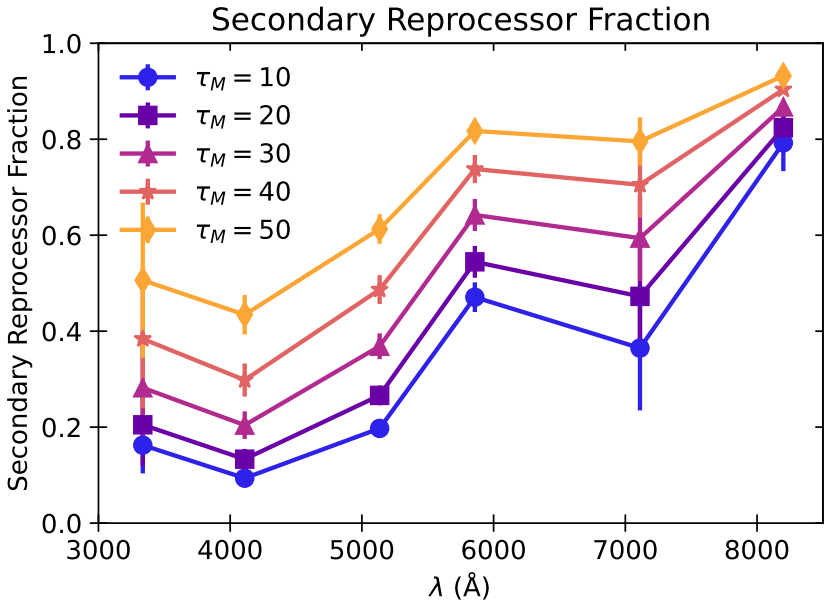

FIGURE 4.6: The fractional contribution of the secondary reprocessor ($f(\lambda)$ in Eq. 4.4) as a function of wavelength as fitted with the disk + secondary reprocessor model in Fig. 4.5, with the median delay of the secondary reprocessor at $\tau_M = 10$, 20, 30, 40, and 50 days. While the fractional contribution increases with increasing distance of the secondary reprocessor, the general shape is retained.

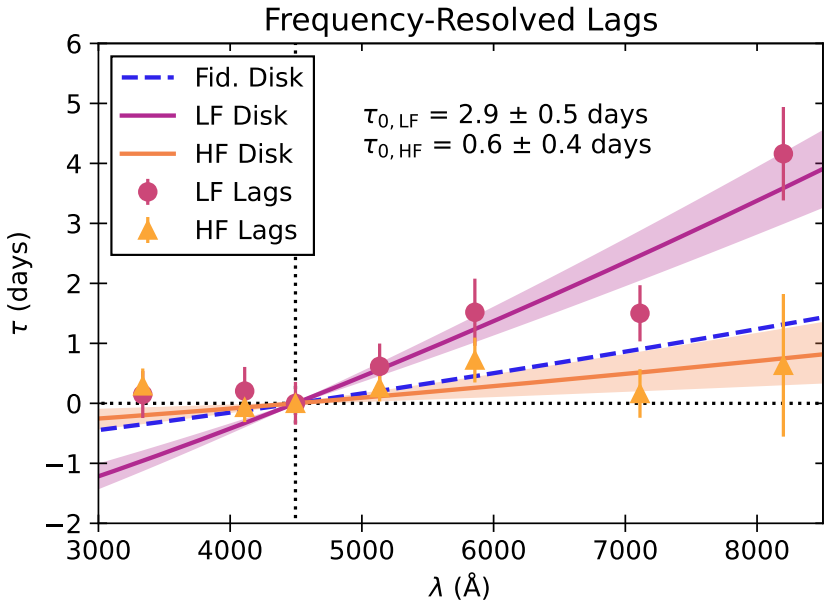

FIGURE 4.7: The high frequency (HF, $0.031 - 0.076\ \mathrm{days}^{-1}$) and low frequency (LF, $0.013 - 0.031\ \mathrm{days}^{-1}$) lag-wavelength spectra in the AGN rest frame. The high frequency lags are plotted with the triangles and the orange line and shaded region denote the thin disk fit and associated uncertainty region with $\tau_{0,\mathrm{HF}} = 0.59 \pm 0.36$ days. The low frequency lags are represented by the circles and the magenta line and shaded region denote the thin disk fit and associated uncertainty region with $\tau_{0,\mathrm{LF}} = 2.86 \pm 0.45$ days. The fiducial thin disk profile discussed in Section 4.5.1 is plotted with the dashed line.

where τ_M is the median of the distribution and S is the standard deviation. In the physical context, τ_M is the median delay of the reprocessor, that is, the distance at which the median reprocessor response occurs. The standard deviation S is that of the transfer function, and does not indicate the physical size of the reprocessor. As S increases at a fixed median delay, the response at short delays increases. Therefore, S is better understood as a measure of the skewness of the transfer function towards short delays; that is how well τ_M characterise the peak of the response. For small S, the median delay is approximately at the peak of the response function and the response clusters around the median delay. For large S, the peak rapidly shifts towards short delays, the function spreads out, and the response is increasingly dominated by short delays. This also implies that for larger S, the median delay needs to be increased greatly to account for the increase of response at short delays. The total transfer mixture model, $\psi_{\rm tot}$, of both reprocessors is thus given by:

$$\psi_{\rm tot}(t) = (1 - f(\lambda))\psi_{\rm disk}(t) + f(\lambda)\psi_{\rm SR}(t)\,, \tag{4.4}$$

where $f(\lambda)$ is the fractional contribution of the secondary reprocessor.

The thin disk is the predicted disk based on the Eddington ratio of I Zw 1 of 1.95, with an approximate face-on inclination, as outlined in Section 4.5.1 and plotted with the dashed blue line in Fig. 4.5. This disk largely reproduces lags in the second lowest frequency bin ($0.031 - 0.076\,{\rm days}^{-1}$) but fails to predict the lag behaviour at even lower frequencies, which consistently lie above it. To recreate the lags at the lowest frequencies, we fit the thin disk and additional BLR-like secondary reprocessor according to Eq. 4.3 and 4.4, optimising $f(\lambda)$. We do not fit the *g*-band as it is the reference band. The median delay of the secondary reprocessor is varied between $\tau_M = 10 - 50\,{\rm days}$, which makes little difference to the goodness-of-fit, so we choose to show the fits for a size of $\tau_M = 20$ days. At shorter and longer distances the goodness of fit drops significantly. The standard deviation S is fixed at 1 day, as results from previous studies show $S = 1 - 2$ with the majority at ~ 1 (Cackett et al., 2022; Lewin et al., 2023, 2024). Notably, setting the standard deviation to 2 days also reproduces the data well, with an increase in $f(\lambda)$. Since the response amplitude at longer lags has decreased relative to shorter lags, the fractional contribution needs to increase to compensate for this. The disk + secondary reprocessor model is denoted with the solid magenta line in Fig. 4.5 and clearly accounts for the higher lags at the lowest frequencies. This fit also estimates the fractional contribution $f(\lambda)$ from the secondary reprocessor, which is plotted in Fig. 4.6 (for $\tau_M = 10 - 50\,{\rm days}$). The fractional contribution does vary with the distance at which the secondary reprocessor is placed, increasing as the distance increases, but retains the same overall shape. For $10\,{\rm days}$, the lowest fractional contribution in the *B*-band is 9% and the highest in the z_s-band is 79%; for $50\,{\rm days}$ the *B*-band fractional contribution is 43% and the z_s-band contribution is 93%. The fits in Fig. 4.5 indicate that the reverberation signals in the second lowest frequency bin ('high frequency', $0.031 - 0.076\,{\rm days}^{-1}$) are dominated by the disk and in the lowest frequency bin ('low frequency', $0.013 - 0.031\,{\rm days}^{-1}$) by the secondary reprocessor. We extract the lag-wavelength spectra of these two bins and fit them with a thin disk according to the method described in Section 4.3.2, with y_0 fixed to 1 to constrain the fits. For the high frequency fit, $\tau_{0,{\rm HF}} = 0.61 \pm 0.37\,{\rm days}$ and for the low frequency fit

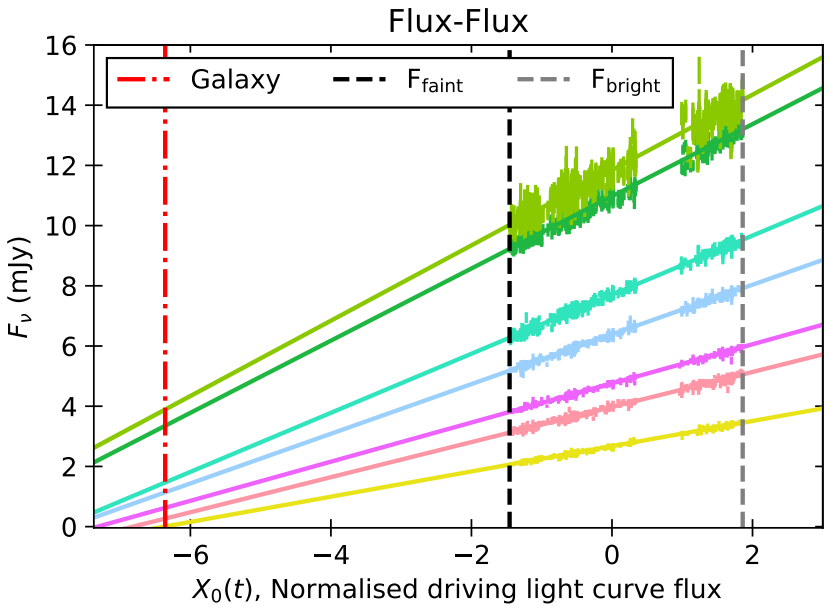

FIGURE 4.8: The flux-flux ($F_\nu - X(t)$) plot, used to determine the host galaxy contribution. The $X(t)$ at which the first filter intersects $F_\nu = 0$ (here *u*) is taken as $X_{\rm gal}$ (red dash-dotted line). The flux in all other bands at $X_{\rm gal}$ is the host galaxy contribution in those bands. The colours correspond to the individual filter light curves in Fig. 4.1, from bottom to top *uBgVriz*$_s$.

$\tau_{0,\rm LF} = 2.92 \pm 0.47$. The lag-wavelength spectra with their fits and the fiducial thin disk profile according to Section 4.5.1 are plotted in Fig. 4.7.

4.4 SED Analysis

To further explore the structure of the disk, we analyse the SED of the optical continuum. This houses the long-wavelength plateau of the accretion disk emission, predicted to be $F_\nu \propto \nu^{1/3}$ for a thin disk, and $F_\nu \propto \nu^{-1}$ for a slim disk (Wang et al., 1999). We use a flux-flux analysis to isolate the constant host galaxy contribution from the variable AGN flux (Winkler et al., 1992; Winkler, 1997). Accordingly, we examine the $F_\nu - X(t)$ (flux – driving light curve) space, $X(t)$ taken from PyROA, and plotted in Fig. 4.8 (Donnan et al., 2023). The light curves are corrected for Galactic extinction using $E(B-V) = 0.057$ and then de-redshifted to the AGN rest frame (Fitzpatrick, 1999; Schlafly & Finkbeiner, 2011). The data in each filter are well-described by a straight line, indicating that the AGN SED does not change shape with changes in flux within our observation window (Fig. 4.8). We fit a line to the data in each band, and extrapolate these to $F_\nu = 0$, essentially 'winding down' the AGN. The $X(t)$ at which the first filter intersects at 1σ above $F_\nu = 0$ is $X_{\rm gal}$. Subsequently, we evaluate the flux of all other bands at $X_{\rm gal}$. This is the lower limit host galaxy contribution. The band which reaches $F_\nu = 0$ first is the *u*-band, the shortest wavelength we have available. Contrary to our assumptions, we do still expect significant host galaxy contribution in the *u*-band due to circumnuclear star formation and are therefore underestimating the host galaxy flux (Fei et al., 2023). The SED fluxes can be found in Table B.3 in the Appendix.

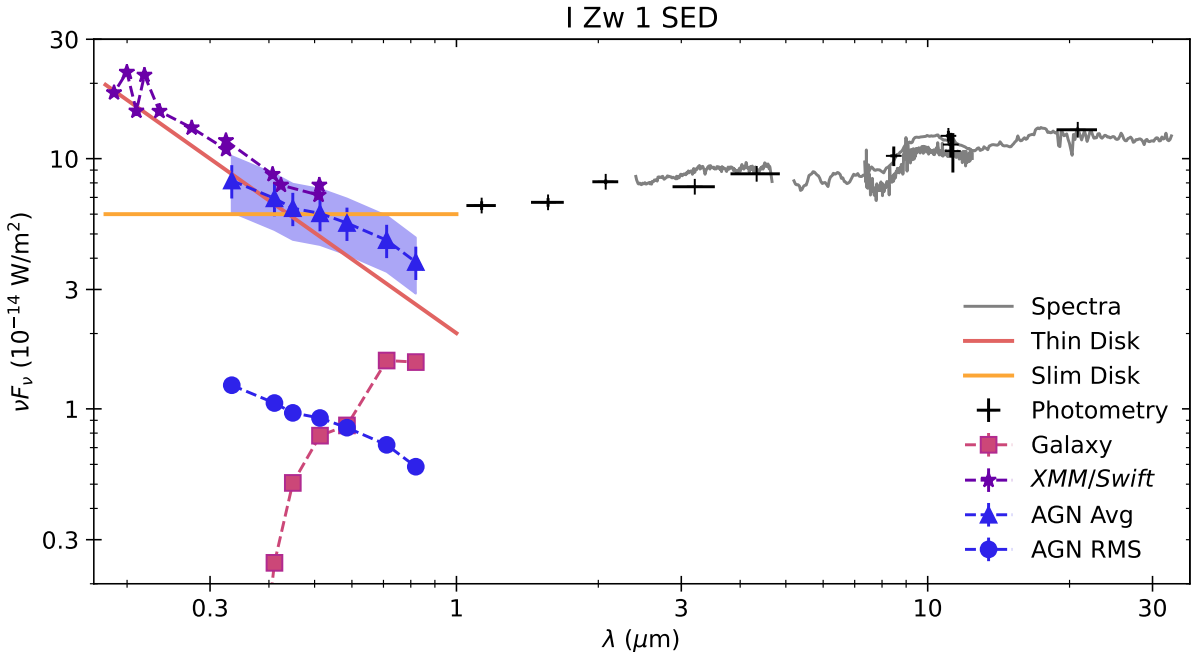

FIGURE 4.9: The near-UV to mid-infrared SED of I Zw 1, in the rest frame of the AGN, and corrected for Galactic (IR) and intrinsic extinction (UV/optical). The LCO AGN flux during years 2, 3, and 4 spans the shaded region with the average flux denoted by the triangles with errorbars given by the RMS flux. The RMS of the AGN is denoted by the circles, and has the same slope as the average AGN. The host galaxy flux determined using the flux-flux technique is shown by the squares, and is only corrected for Galactic extinction. The stars show the *XMM-Newton* OM and *Swift* UVOT measurements and the IR photometry points and spectra tabulated in Table A.2. The SED slopes of the thin and slim disks are also overplotted using thick lines.

The resulting SED (not pictured) is flat, even slightly decreasing towards shorter wavelengths. This was similarly noticed by Juráňová et al. (2024) and is a sign of intrinsic absorption. Rogantini et al. (2022) used a Milky Way extinction curve with $E(B-V) = 0.13$, derived from O I line ratios. In fact, this value is a 'compromise value', where Rudy et al. (2000) adjusted the value derived from the line ratios to a lower value based on previous results which produced less reddening. In contrast, Juráňová et al. (2024) used a custom extinction law fit based on the SMC bar average model by Gordon et al. (2003). Their extinction law is flattened below 1550 Å. This curve, lacking the Galactic 2175 Å bump and flattened in the UV, matches well with average extinction curve found by Gaskell et al. (2004) for quasars.

We correct our LCO data for intrinsic extinction according to Juráňová et al. (2024), as this extinction is more robust and physical for a quasar such as I Zw 1 than the one used by Rogantini et al. (2022). The resulting mean and RMS AGN fluxes and host galaxy flux are plotted in Fig. 4.9. We use the same model to correct the *XMM-Newton* OM and *Swift* UVOT data described in Section 4.2.2 and 4.2.3 for intrinsic extinction. We are focusing on the average flux, so we average the data between the *XMM-Newton* and *Swift* in the corresponding filters, with uncertainties taken as the standard deviation, and we use this data in fitting. The UV data plotted in Fig. 4.9 and Fig. 4.10 are the weighted mean of the three *XMM-Newton* epochs as well as the *Swift* data separately. Further, we subtracted host galaxy contribution from the bands for which have this

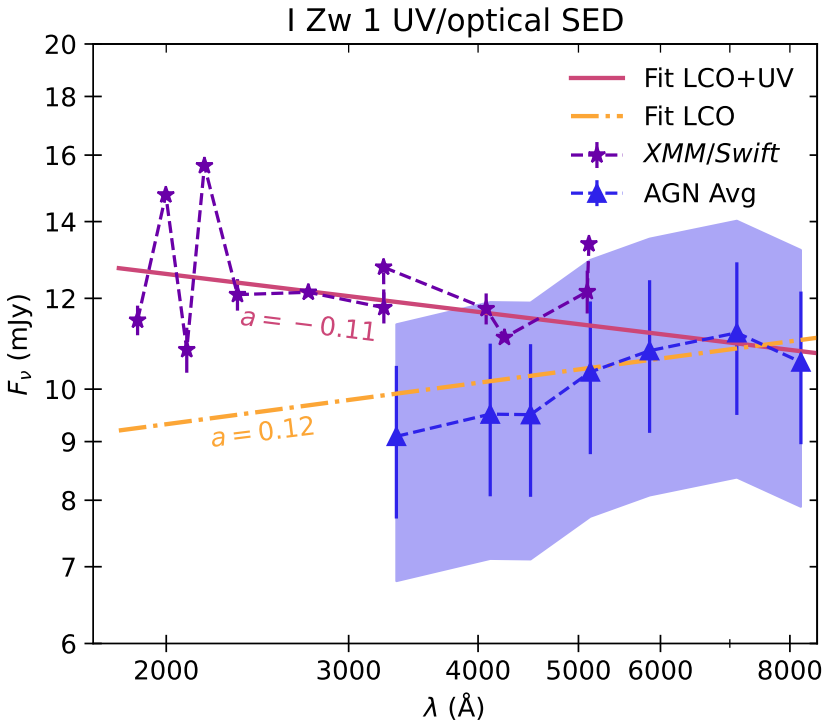

FIGURE 4.10: The UV/optical SED of I Zw 1 including the average LCO AGN flux (triangles), with errorbars representing the RMS flux, and the *XMM-Newton* and *Swift* flux (stars). The fits for the slope are performed according to $F_\nu \propto \lambda^a$, where a thin disk has $a = -1/3$ and a slim disk $a = 1$. The fit to only the LCO average AGN data is denoted by the dash-dotted line with $a = 0.12 \pm 0.13$ and the fit to all of the data is the thick line with $a = -0.11 \pm 0.12$.

information from the LCO flux-flux analysis (*UBV*). To compare the UV/optical slope to the thin and slim disks we overlaid their profiles in Fig. 4.9 (with arbitrary normalisation). To provide a more expansive picture of the AGN emission, we added the IR SED assembled in Section 3.2.2 and compiled in Table A.2. This was only corrected for Galactic extinction using the ISM profile from Chiar & Tielens (2006) and the Galactic $A_K/E(B-V) = 0.36$ ratio from Fitzpatrick (1999). The complete SED is plotted in Fig. 4.9. Both the average AGN and RMS AGN flux follow the same slope. In comparison with the example slopes of a thin and a slim disk, the slope of the AGN emission is not easily classifiable. Accordingly, we fit the optical and UV slope. Similarly to the lags, we use a MCMC routine with 16 walkers and 10^5 steps, discarding the first 5000 steps and thinning by 50% to avoid autocorrelation. These fits are parametrised as $F_\nu \propto \lambda^a$ where a thin disk has $a = -1/3$ and a slim disk $a = 1$. First, we only fit the average AGN LCO data which gives a slope of $a = 0.12 \pm 0.13$. Including the average *XMM-Newton* and *Swift* measurements steepens the slope to $a = -0.11 \pm 0.12$. The relevant data and fits are plotted in Fig. 4.10.

4.5 Discussion

In this section we discuss our results in the context of our aims to phenomenologically describe the accretion disk in I Zw 1, examine the results in the context of other super- and sub-Eddington

AGN, and analyse the multi-wavelength internal structure of I Zw 1. Accordingly, we first examine the actual sources of the reverberation signals we measure. In the context of those results we then analyse the underlying accretion disk structure based on the lag-wavelength spectra and the UV/optical SED profile. Finally, we collate the optical to mid-IR size-wavelength relation of I Zw 1 and discuss the resulting implications on BLR formation models.

4.5.1 The source(s) of reverberation signals

4.5.1.1 The accretion disk

The lag-wavelength spectrum as shown in Fig. 4.2 and 4.3 clearly displays larger lags with increasing wavelengths, implying an emission region with a radially stratified temperature profile. Moreover, it necessitates the existence of non-local large-scale communication in the AGN. Independent of the source of variability, it must be in some way communicated over large distances, e.g. in a reprocessing scenario or large-scale fluctuations throughout the entire disk (Cai et al., 2018; Hagen et al., 2024a). If we assume the classical lamppost-disk reprocessing model we can estimate the size of the disk from the AGN properties, further assuming an underlying thin disk. We use Eq. 1.16 to evaluate a fiducial value for τ_0 (Fausnaugh et al., 2016). As is common practice, we take X, the correction factor for the conversion between wavelength and temperature for a certain radius, to be 2.49. Similarly, we take the ratio of external to internal heating $\kappa = 1$, and $\log M_{\rm BH} = 6.97$ (Huang et al., 2019). We derive the bolometric luminosity $L_{\rm bol}$ from the $5100\,\text{Å}$ luminosity $\lambda L_{5100\,\text{Å}}$ according to Trakhtenbrot et al. (2017) (for a further discussion see Section 3.4.1). The intrinsic luminosity of I Zw 1, $\lambda L_{5100\,\text{Å}} = 10^{44.50}\,\mathrm{erg\,s^{-1}}$, gives a bolometric luminosity of $L_{\rm bol} = 10^{45.36}\,\mathrm{erg\,s^{-1}}$ (Trakhtenbrot et al., 2017; Huang et al., 2019). The resulting Eddington ratio is $\dot{m}_E = 1.95$. We then calculate the accretion efficiency η using Eq. 1.8 and the dimensionless accretion rate $\dot{\mathscr{M}}$. This is found to be $\dot{\mathscr{M}} = 130$ according to Eq. 2 in Du et al. (2015), which gives $\eta = 0.015$, for a face-on disk. This is similar to the accretion efficiency calculated for another super-Eddington AGN Mrk 142 and what is generally expected in slim disk flow (Cackett et al., 2020). Applying these values, we calculate a fiducial $\tau_0 = 1.07$ days, which is the predicted size of the disk at $4495\,\text{Å}$. Our fitted τ_0 for a thin disk profile is $4.23 \pm 0.24\,\mathrm{days}$, larger by a factor of 4.0 ± 0.2. Using our fitted τ_0, we get a large dimensionless mass accretion rate of $\dot{\mathscr{M}} = 9970$. Assuming $\eta = 0.015$, this implies $\dot{m}_E = 150$ and hyper super-Eddington accretion. A similar offset was also found in the other super-Eddington AGN, Mrk 142, PG 1119+120, and 3C 273 (Cackett et al., 2020; Donnan et al., 2023; Thorne et al., 2025). We must note, however that the expression for τ_0 is only valid for sub-Eddington objects. Nevertheless, even in sub-Eddington objects studies consistently find the disk measured through RM to be larger by a factor of $2-3$, similar to our case (e.g. Edelson et al., 2015; Fausnaugh et al., 2016; Cackett et al., 2018; Hernández Santisteban et al., 2020; Miller et al., 2023). From this we instead infer that the source(s) of the RM signals we measure are rather similar in super- and sub-Eddington AGN.

It has been shown that an inclined disk can reproduce some of the results of continuum reverberation mapping; namely overall longer lags and skewed lag distributions. The lag distribution of an inclined disk peaks at smaller lags that correspond to fast variability and has a long tail at larger lags which responds to slower variability (Starkey et al., 2016). This emulates the skewed CCF distributions that are commonly found and have a long tail at large lags, such that $|\tau_{\rm peak}| < |\tau_{\rm cent}|$ (e.g. Edelson et al., 2017, 2019; Hernández Santisteban et al., 2020). Table 4.2 shows that this behaviour is also present in I Zw 1. To further investigate the possibility of an inclined disk, we compare the frequency-resolved lags with the prediction for a thin disk at an inclination of 60° and with $\dot{m}_E = 50$, plotted in Fig. B.2. This disk does reproduce the majority of the data well. However, the lowest frequencies in the z_s and especially *u*-band are not modelled well by this inclined disk. In addition, the skewed lag distributions can result from other factors, most relevantly a secondary reprocessor located at larger distances.

4.5.1.2 A continuum secondary reprocessor

In fact, there is ample evidence that there is more than one source of continuum RM signals in I Zw 1. The second source besides the fiducial accretion disk is a secondary reprocessor emitting continuum flux. This secondary reprocessor is located at larger radii than the disk and responds to the driving light curve with larger lags, increasing the overall observed lags. The continuum emitted is usually assumed to be diffuse continuum, from hydrogen bound-free recombination and free-free emission processes (Korista & Goad, 2001, 2019; Netzer, 2022). Accordingly, this diffuse continuum is particularly strong around the Balmer ($3650\,\text{Å}$) and Paschen ($8210\,\text{Å}$) jumps, which map to our *u*- and *i*-band filters. The continuum strength in these features then maps to the lag-wavelength spectrum and we expect to see an increase in the *u*- and possibly *i*-band lags, the *u*/*i*-band excess (e.g. Cackett et al., 2018). In fact, the lag-wavelength spectrum in Fig. 4.3 does appear to show a *u*-band excess. The *u*-band lag is noticeably larger than predicted by both fits.

There are two general theories for the nature of this secondary reprocessor: the classical, virially bound BLR or a wind (Korista & Goad, 2001, 2019; Lawther et al., 2018; Hagen et al., 2024a). Of course, depending on interpretation the difference between these might solely be semantic as the BLR itself has been shown to be mainly in Keplerian motion but includes inflows and/or outflows (e.g. GRAVITY Collaboration et al., 2018; Bentz et al., 2021). Here we differentiate between the BLR winds detected in absorption ($v_{\rm out} = 1950\,{\rm km s^{-1}}$) and the BLR as described by the reverberation mapping of the $\rm H\beta$ emission line (Juráňová et al., 2024; Huang et al., 2019). Assuming that the minimum launching radius of the wind is set by the escape velocity, approximated by the virial velocity, the wind is launched from at least 10–25 ld (light days, $0.01 - 0.02\,{\rm pc}$). In contrast, the size of the BLR estimated using $\rm H\beta$ is $37.2^{+4.5}_{-4.9}\,{\rm ld} \sim 0.031\,{\rm pc}$ (I Zw 1 lies on the $R_{\rm BLR} \propto L^{1/2}$ relation). The modelled size of the secondary reprocessor based on the frequency-resolved lags is $10 - 50\,{\rm ld}$ $(0.008 - 0.04\,{\rm pc})$. The low frequency lags and the secondary reprocessor model from our Fourier analysis are consistent with the region inhabited by the BLR and associated winds, likely indicating that indeed the BLR is responsible. However, we

cannot distinguish the location of the secondary reprocessing material between the BLR winds and the BLR radius traced by the $\mathrm{H}\beta$ line. It is probable that this material is not actually located at one specific distance but rather spread throughout the entire $0.01 - 0.04\,\mathrm{pc}$ region.

A similar picture of contribution from a secondary processor can be seen in other super-Eddington as wells as sub-Eddington AGN. Super-Eddington AGN Mrk 142 and PG 1119+120 have *u/U*-band excesses, and it is a well-documented feature in sub-Eddington AGN (Cackett et al., 2020; Donnan et al., 2023; Fausnaugh et al., 2016; Hernández Santisteban et al., 2020). In fact, in NGC 4593 the Balmer jump is clearly resolved in the lag-wavelength spectrum (Cackett et al., 2018). Further, PG 1119+120 shows much larger lags, especially in the *u*-band, on a variability timescale of 100 days (Donnan et al., 2023). Again, this is also seen in a number of sub-Eddington AGN (Pahari et al., 2020; Vincentelli et al., 2021). The frequency-resolved lags of (sub-Eddington) Mrk 335 and Mrk 817 show a marked increase in lags at low frequencies, below $0.01\,\mathrm{days}^{-1}$ and $0.05\,\mathrm{days}^{-1}$ respectively (Lewin et al., 2023, 2024). The secondary reprocessors modelled for these objects have sizes that concur with BLR sizes derived from reverberation mapping of $\mathrm{H}\beta$ in both cases.

There is consistent evidence that a secondary reprocessing diffuse continuum is mixed into general continuum lags and lengthens these in a multitude of objects. Notably, this secondary reprocessor significantly contributes to the continuum lags across the entire optical spectrum, not just where it is especially strong in the *u/U*-band. This can be seen when studies remove the *u/U*-band lag to remove the impact of the diffuse continuum, but fits still produce disk sizes several times too large (Fausnaugh et al., 2018; Cackett et al., 2020). On the other hand, using solely the high frequency lags which are expected to be significantly less contaminated by the secondary reprocessor results in disk sizes which are in line with expectations (Lewin et al., 2023, 2024). Substantial contribution across the optical spectrum is also evidenced by our results: low frequency lags which require a secondary reprocessor to replicate are on the order of the overall best-fit PyROA lags. Further, the modelled fractional contribution of the secondary reprocessor in Fig. 4.6 is significant and above $\sim 20\%$ in the majority of bands. In addition, the high frequency lag-wavelength spectrum in Fig. 4.7 is fit with a notably smaller size, more similar to the fiducial thin disk. It is evident that the presence of this secondary reprocessor is a consequence of the basic Seyfert AGN structure. In general, there appears to be a secondary reprocessor at larger radii co-spatial with the BLR emitting diffuse continuum that considerably lengthens observed continuum lags at all wavelengths, independent of Eddington ratio.

4.5.1.3 Fe II

I Zw 1 has strong Fe II emission, which can be seen in the average spectrum in Fig. B.1 (e.g. Boroson & Green, 1992; Véron-Cetty et al., 2004). For comparison, we also plot the Fe II template constructed by Véron-Cetty et al. (2004) based on I Zw 1, arbitrarily scaled. Finally, we overlay the LCO filter transmission curves. With this combination, it is apparent that the Fe II emission is particularly strong in the *BgV*-bands. Fe II emission arises from the BLR and reverberates in response to the continuum (Gaskell et al., 2022). Studies have shown the Fe II lag to be around

twice the size of the Hβ lag, placing it towards the outer BLR (e.g. Barth et al., 2013; Hu et al., 2015; Zhang et al., 2019). However, the variability amplitude of Fe II is dampened relative to Hβ, mainly because it sits at larger distances and reverberates over a larger area. As such, Fe II can introduce additional reverberation signals in I Zw 1 at lags approximately twice the size of Hβ, $\sim 80\,\mathrm{days}$, in primarily the *BgV*-bands. This then indicates that our choice of the *g*-band as an 'uncontaminated' reference band may be problematic. Using an UV reference band might then provide a more 'uncontaminated' option, which we unfortunately do not have. An UV reference light curve might also directly uncover the signature of Fe II reverberation in the lag spectrum through increased lags in the *BgV*-bands, similar to the *u*-band excess as a sign of the Balmer jump from the diffuse continuum. However, I Zw 1 also shows significant Fe II and Fe III emission in the UV – whether this further affects reverberation signals is unknown (Vestergaard & Wilkes, 2001). Further, detecting evidence of Fe II reverberation in frequency-resolved lags like we have shown with the diffuse continuum is probably not feasible with our data. This is because if the fiducial Fe II is located at a delay of $\sim 80\,\mathrm{days}$, our light curve segment size is less than double that (155 days), making it extremely difficult to detect without a longer season of intensive reverberation mapping.

4.5.2 The underlying accretion disk structure

With regards to the underlying disk structure in I Zw 1, we can look at the lag-wavelength spectrum, which reflects the radial temperature profile of the disk, and the SED slope in the UV/optical, which contains the long-wavelength tail of the disk emission. Parameter results for the power law fits to the lag-wavelength spectrum of the PyROA lags are shown in Table 4.4. Both fits with a fixed β – the thin and slim disk – shown in Table 4.4 perform similarly, with comparable fit parameter errors ($\sim 5\%$) and $y_0 \sim 1$ as expected (Eq. 1.15). As the lag-wavelength spectrum in Fig. 4.3 illustrates, the data can also not sufficiently differentiate between these different profiles. The free β fit has larger fit parameter uncertainties due to the larger number of fit parameters. This agnostic fit has a shallow slope, i.e. temperature falls of slowly with radius in the disk (similar to Cackett et al., 2020). It also has the smallest disk size, within errors of the fiducial size. In addition, it shows that the disk size and β are degenerate to an extent, as τ_0 decreases as β increases. There is additional information about the disk structure in the frequency-resolved lags at high frequencies ($0.031 - 0.076\,\mathrm{days}^{-1}$) which we expect to be dominated by the disk rather than the secondary reprocessor. These lags are reproduced by the fiducial thin disk generally well in Fig. 4.5. The extracted high frequency lag-wavelength spectrum is shown in Fig. 4.7 compared with the fiducial thin disk profile and size. While the uncertainties and scatter are larger, there is still a trend of increasing lag with wavelength, probing a radially stratified temperature profile. Assuming a thin disk, the disk size of these high frequency lags is $\tau_{0,\mathrm{HF}} = 0.61 \pm 0.37\,\mathrm{days}$. This is smaller than the fiducial disk size of 1.07 days and shows that at higher variability frequencies we probe increasingly smaller structures in the AGN. In addition, it indicates the disk size based on the overall best-fit PyROA lags is likely to be too large, and the actual disk sizes tend towards the fiducial disk size or even smaller.

Considering the SED, both the RMS and mean AGN profiles have the same slope (Fig. 4.9). This implies that both the variable components and the dominant constant component in the AGN have the same SED shape, with dominant emission from the accretion disk. The variable SED also shows no bluer-when-brighter behaviour. The exact shape of the SED profile is difficult to determine, depending on the amount of internal extinction applied and host galaxy contribution. First, if we only consider the LCO derived SED we find that for $F_\nu \propto \lambda^a$, $a = 0.12 \pm 0.13$. This is closer to a thin disk than a slim disk. When we then add UV/optical data from archival *XMM-Newton* and *Swift* observations the resulting slope steepens to $a = -0.11 \pm 0.12$, shifting even closer to a thin disk slope with $a = -1/3$. Notably, the *XMM-Newton* data was collected before our campaign, and only one *Swift* data set is simultaneous with our observations. Long term monitoring with ASAS-SN shows the optical variability in I Zw 1 to be $\sim 3 - 6\%$, so even earlier *XMM-Newton* data should be within the flux range covered by our campaign (Huang et al., 2019). There appears to be an offset between the *XMM-Newton* and *Swift UBV* and the LCO data, which may be due to intrinsic variability. Shifting up the LCO SED to match the optical *XMM*/*Swift* data would result in a flat ($a \sim 0$) SED slope. Further, if we consider only the *Swift* points (stars at lower flux in Fig. 4.10), the result would be similar, with an essentially flat SED. We might also be underestimating the host galaxy contribution, especially in the bluer bands, as we anchor the flux-flux decomposition in the *u*-band. While host galaxy spectra are generally red, there can be significant contribution in the blue optical and UV when there is active star formation. In fact, I Zw 1 hosts a nuclear starburst within 1 kpc, which is within our extraction aperture (Fei et al., 2023). However, fitting a galactic template, Juráňová et al. (2024) found a red spectrum and negligible contribution at shorter wavelengths, especially in the UV. The red slope of the LCO SED can also be considered in the context of contribution from diffuse continuum. The diffuse continuum spectrum increases from the local minimum at the Balmer jump to the local maximum at the Paschen jump, which corresponds to our *BgVriz*$_s$-bands (Korista & Goad, 2019). Therefore, in a case of significant DC contribution (as we are likely to be observing RM signals), this could account for a reddened SED slope at these wavelengths. However, this would also mean an even larger contribution in the *u*-band, which covers the Balmer jump. As the *u*-band has the lowest flux (Fig. 4.10), it is difficult to argue for this case. While the inclusion/exclusion of certain data does change the SED slope, all results are closer to a thin disk than a slim disk.

The exact SED slope is highly sensitive to the amount of intrinsic extinction applied. The presence of internal reddening has been noted in I Zw 1 for a long time, due to its uncharacteristically flat/red optical spectrum compared to the large amount of AGN emission (e.g. Laor et al., 1997; Rudy et al., 2000). However, the estimates of the internal extinction varies considerably: from $0.1\,\mathrm{mag}$ in Laor et al. (1997), Rudy et al. (2000)'s compromise value of $0.13\,\mathrm{mag}$, their calculated value of $0.19\,\mathrm{mag}$, to $0.206\,\mathrm{mag}$ as fitted for by Juráňová et al. (2024) (assuming a thin disk SED). A higher extinction appears more likely in I Zw 1. Rudy et al. (2000) calculated a $E(B-V) = 0.19\,\mathrm{mag}$ based on O I emission line ratios, even though they then adopted a lower value based on Laor et al. (1997). This is consistent with the value of $0.206\,\mathrm{mag}$ found by Juráňová et al. (2024) using an independent technique and data taken more than 15 years later. In addition, the extinction law we use (and fitted by Juráňová et al., 2024) is characteristic for quasars,

eschewing the Galactic 2175 Å bump and flattening out below 1550 Å (Gaskell et al., 2004). The LCO SED in Fig. 4.10 has this extinction applied and is consistent with a slim disk slope. The application of additional extinction, which we cannot rule out, will make the SED blue and bring it in line with a thin disk. A similar situation is noted in PG 1119+120 by Donnan et al. (2023).

Nevertheless, the question presents itself whether we can actually probe a slim disk profile in I Zw 1 using optical reverberation mapping. A slim disk, which heats up as radiative cooling becomes ineffective and therefore puffs up, is only expected to dominate inside the photon trapping radius (Wang & Zhou, 1999). The photon trapping radius $R_{\rm tr}$ can be estimated using the dimensionless accretion rate $\dot{\mathscr{M}}$ where we here take $\dot{\mathscr{M}} = 130$ as calculated above. Using Eq. 1.12, we find $R_{\rm tr} \sim 374 R_g$. Emission from this accretion disk regime will peak at 817 Å (Eq. 7 in Cackett et al., 2020). In this study we consider $\lambda > 3000$ Å for reverberation mapping, far away from the putative photon trapping radius, and therefore should not expect the lag to follow λ^2. Even in the SED we only consider $\lambda > 1700$ Å, while the slim disk with $F_\nu \propto \nu^{-1}$ should only appear at shorter wavelengths. Indeed, Kubota & Done (2019) show that the SED profile of an accretion disk partly in the slim disk state is almost identical to that of a thin disk at the wavelengths considered here. It is therefore probable that we are not in fact probing the slim disk in I Zw 1, even with it being super-Eddington. Similar situations have been found in the super-Eddington AGN Mrk 142 and PG 1119+120 (Cackett et al., 2020; Donnan et al., 2023). Instead, we are probably looking at an outer disk region. This outer disk region might be like a standard thin disk, implying that we are indeed probing similar disk structures in sub- and super-Eddington AGN with UV/optical reverberation mapping. Therefore, we should not expect a turnover in results when crossing the Eddington limit. Indeed, a gradual change in disk structure occurs as $\dot{m}_E < 1$ increases, with super-Eddington AGN presenting the extremes of this transition.

Clearly, we cannot make any conclusions as to the exact underlying structure of the accretion disk. We can however say that we are probably observing an optically thick, thermally emitting disk with a radial temperature profile, in which the temperature decreases with radius. This is of course under the assumption of the lamppost model (irrespective of the exact X-ray-UV/optical relationship), where lags between light curves are directly related to the physical distances across the disk and in the AGN (Cackett et al., 2007; Fausnaugh et al., 2016; Kammoun et al., 2021). If there is another method of communication over large scales in the disk, such as large-scale temperature fluctuations the lags are likely to have a different more complex relationship with physical distance (e.g. Cai et al., 2018). The lag-wavelength spectrum in I Zw 1 holds little differentiating power between different radial temperature profiles. For one, this is due to the comparatively small wavelength range probed in this optical-only study. Nevertheless, even across a larger wavelength range, another study on a super-Eddington object has failed to find conclusive evidence for either a thin or slim disk profile (Cackett et al., 2020). The other reason, of course, is the significant contribution in the lag spectrum from the secondary reprocessor. As demonstrated, we have found evidence for the presence of such a structure in I Zw 1. However, after isolating high and low frequency lags, with the high frequency lags reproduced solely using the fiducial thin disk, it is likely that the actual disk size is on the order of the fiducial disk size 1.07 days or smaller, as

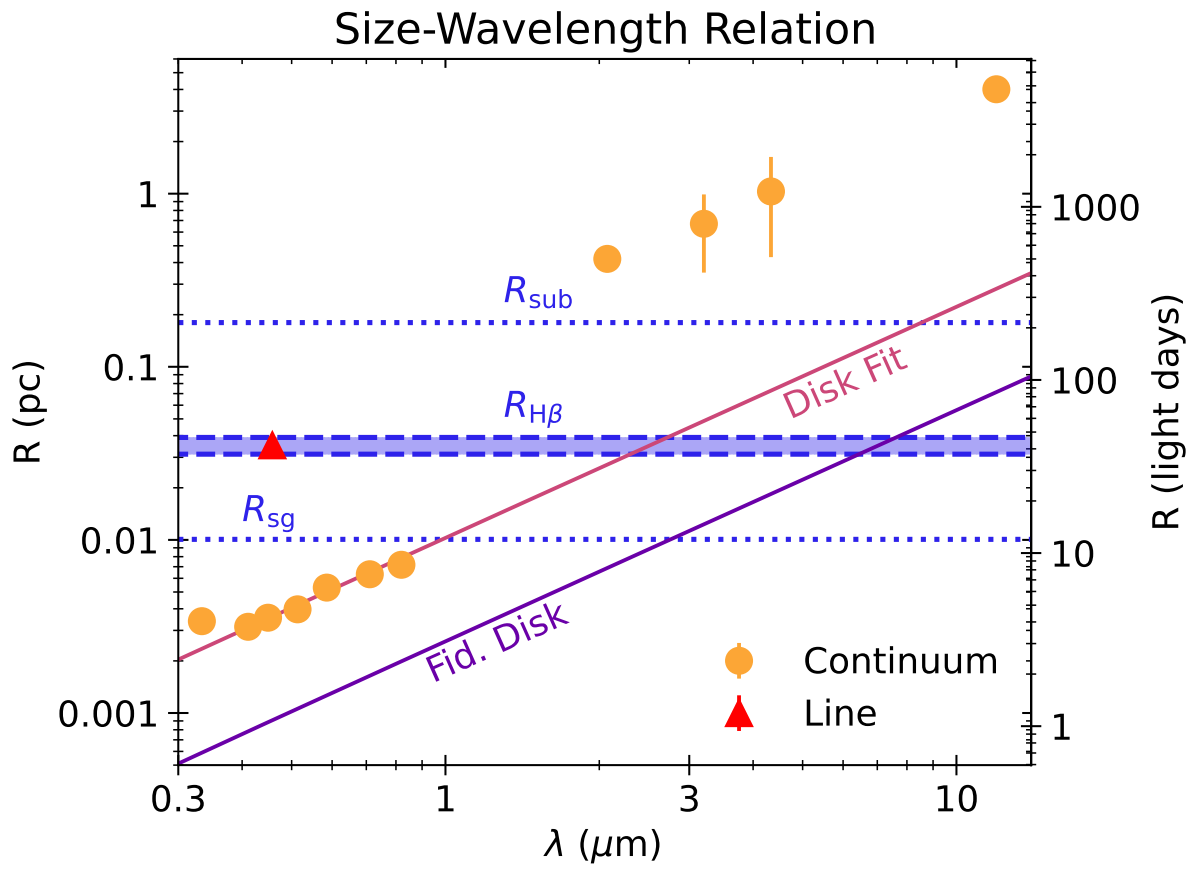

FIGURE 4.11: The directly measured size-wavelength relation in I Zw 1, from the optical to the mid-IR. Circles represent sizes measured using continuum emission, using reverberation mapping for the optical and optical interferometry for the infrared, which are presented in Chapter 3. The triangle and the shaded region represents the radius $R_{\mathrm{H}\beta}$ measured using the $\mathrm{H}\beta$ emission line with reverberation mapping by Huang et al. (2019). As the optical continuum lags were measured with respect to the *g*-band, we add the disk size in the *g*-band, τ_0, to get the absolute size. Here we assume thin disk so we use $\tau_0 = 4.23\,\mathrm{days}$. We also add this size and the measured *V*-band lag to $R_{\mathrm{H}\beta}$ as the $\mathrm{H}\beta$ lag was evaluated with reference to the *V*-band. This fitted thin disk profile is also plotted, and the fiducial thin disk profile with $\tau_0 = 1.07\,\mathrm{days}$. Finally, we indicate the sublimation radius $R_{\mathrm{sub}} = 0.18\,\mathrm{pc}$ (Section 3.4.1) and the self-gravitating radius of the disk $R_{\mathrm{sg}} = 12\,\mathrm{ld}$ using the dotted lines, which are assumed to be the outer and inner boundaries of the BLR respectively (Lobban & King, 2022).

for example the fitted size of $\sim 0.6\,\mathrm{days}$. On the other hand, the SED quite plainly tends towards a thin disk slope, similar to the super-Eddington AGN Mrk 142 (Cackett et al., 2020). All of this illustrates a fundamental challenge in continuum reverberation mapping studies of accretion disks: we are not observing a single, dominant accretion disk continuum, but a complex mixture of signals from different regions in the AGN. The key to accessing the underlying accretion disk structure then lies in disentangling these signatures.

4.5.3 The inner AGN structure in I Zw 1

We have here collected the most extensive set of directly measured sizes of internal AGN components from the optical disk through to the mid-IR dusty torus (this work, Huang et al., 2019). This is plotted in Fig. 4.11, which also includes the thin disk fit from Table 4.4, a thin disk with the fiducial size of $\tau_0 = 1.07\,\mathrm{ld}$, the self-gravitating radius R_{sg} of the disk, and the sublimation radius R_{sub}. As the lag we measure and that is described by Eq. 4.2 is the lag relative to the *g*-band, we correct the optical continuum lags by adding the absolute *g*-band size as fitted for a thin disk, $\tau_0 = 4.23\,\mathrm{ld}$. The H$\beta$ lag was determined relative to the *V*-band so we correct it by adding the resulting absolute *V*-band lag (Huang et al., 2019). Represented by the orange circles below $1\,\mu\mathrm{m}$ in Fig. 4.11, we detect optical emission of a fiducial accretion disk structure out to $\sim 0.01\,\mathrm{pc}$. This is also where the self-gravitating radius of the accretion disk is predicted to be, at $12\,\mathrm{ld} \simeq 0.01\,\mathrm{pc}$, as denoted by the lower dotted line (Lobban & King, 2022). The self-gravitating radius of the disk is where self-gravity in the disk starts to dominate over radiation pressure and the disk is expected to fragment. Therefore, it is possible that we are probing up to the outer edges of the accretion disk. Beyond these radii, we enter the region of the BLR. A measure of the region occupied by BLR gas is the radius derived from reverberation mapping of the Hβ emission line at $\sim 0.031\,\mathrm{pc}$ (Huang et al., 2019). This is indicated in Fig. 4.11 with the red triangle, and the shaded region covers the uncertainty. However, the BLR likely extends to both smaller and larger radii than this as the BLR has a radial ionization structure, with higher ionization lines found at smaller radii than lower ionization ones (e.g. Clavel et al., 1991). Classically, the inner boundary of the BLR is approximately given by the outer edge of the accretion disk and the outer boundary by the sublimation radius. The secondary reprocessor as fitted to the frequency-resolved lags covers the Hβ radius but also extends significantly inwards ($0.01 - 0.04\,\mathrm{pc}$), likely probing a larger region of the BLR. Notably, we see little indication of continuum reprocessing at a distance of $\sim 100\,\mathrm{ld}$, as that fit is strongly disfavoured. There is also evidence of winds launched from the BLR, a warm X-ray absorber with $v_{\mathrm{out}} \simeq 1750\,\mathrm{km\,s^{-1}}$ and an outflowing wind detected through absorption lines in the BLR spectrum with $v_{\mathrm{out}} \simeq 1950\,\mathrm{km\,s^{-1}}$ (Silva et al., 2018; Rogantini et al., 2022; Juráňová et al., 2024). Assuming that the outflow velocity must be at least the escape velocity as given by the virial velocity, the minimum launching radii of these outflowing components are $0.01 - 0.03\,\mathrm{pc}$. This places them towards the inner part of the fiducial BLR.

The outer edge of the BLR is delimited by the sublimation radius at $0.18\,\mathrm{pc}$, denoted by the upper dotted line in Fig. 4.11 (Section 3.4.1, GRAVITY Collaboration et al., 2020b). This is consistent with the inner dust radius of $224\,\mathrm{ld}$ ($0.19\,\mathrm{pc}$) determined by Landt (2023) using spectral fitting. This also describes the inner rim of the dusty torus. The infrared continuum measurements using optical interferometry of the hot dust ($2.2 - 4.6\,\mu\mathrm{m}$) indicates the presence of a wind launching region: a 'puffed-up' inner region of the dust disk where a dusty wind is launched through infrared radiation pressure (Chapter 3, Hönig, 2019). Reverberation mapping of the dust at $3.4 - 4.5\,\mu\mathrm{m}$ yields lags smaller than the optical interferometric measured sizes by a factor of $2.5 - 3.5$ (Lyu et al., 2019). This is similar to the behaviour observed between *K*-band reverberation and interferometric measurements, which are usually offset by a factor of $2 - 2.5$ (e.g. GRAVITY

Collaboration et al., 2024). An integral reason for this is the fact that these two measurements trace different sizes: reverberation mapping measures the response-weighted radius and optical interferometry the flux-weighted radius. Geometries that produce such offsets such as a bowl-shaped/concave inner dust structure have also been explored (e.g. GRAVITY Collaboration et al., 2024). However, the reverberation mapping results must be treated carefully as the lags are consistent with time intervals between observations of the IR light curve, indicating that the results may be spurious. Nevertheless, even accounting for a complex inner dusty torus edge of with different measurements of its size varying by a factor of $2 - 2.5$ does not significantly change the picture of the BLR and dusty torus locations presented here. While the outer edge of the BLR may already be at 0.1 pc, other measurements of the BLR size are well within radius. The entire fiducial BLR spans an entire order of magnitude in size which means that variations of a factor of a few in the outer edge radius are inconsequential in comparison. Finally, we then trace the cooler parts of the dust in the mid-IR out to $\sim 4\,\mathrm{pc}$ (Chapter 3, Burtscher et al., 2013).

Using this size-wavelength relation, we can examine the failed radiatively accelerated dust driven outflow BLR formation theory (Czerny & Hryniewicz, 2011; Baskin & Laor, 2018). In this model, the accretion disk extends into the BLR and out to the dusty torus. Temperatures of the accretion disk in this region are $\sim 1000\,\mathrm{K}$, which is less than the sublimation temperature ($\sim 1500\,\mathrm{K}$). Dust forms in the accretion disk atmosphere and is launched due to radiation pressure. At a certain height above the disk, the dust will sublime again due to strong irradiation and fall back down into the disk. The BLR is then constituted out of this failed wind. A central component of this theory is the presence of the accretion disk in the BLR. Extrapolating our fitted thin disk size to lower temperatures around $1000\,\mathrm{K}$ ($\sim 1 - 2\,\mu\mathrm{m}$, *JHK*-bands), as shown with the solid lines in Fig. 4.11, does extend it into the BLR. This is just the inner parts of the BLR, barely covering the $\mathrm{H}\beta$ radius. However, this is for a disk fit based on lags that are expected to include a significant contribution from a secondary reprocessor at larger radii, with a fitted τ_0 four times larger than the fiducial τ_0. If we consider a thin disk with the fiducial size, which is likely closer to the true size, also shown in Fig. 4.11, the accretion disk emitting in these wavelengths is outside of the BLR as denoted by the self-gravitating radius. Going down to the disk size as fitted to high frequency lags, smaller again by half, locates the relevant accretion disk sections even further inwards.

Similarly, Thorne et al. (2025) found that in 3C 273 the accretion disk is likely to overlap in its *K*-band region with the BLR, based on extending their reverberation mapping disk fit to longer wavelengths, up to $130 - 170\,\mathrm{days}$ in the *K*-band. The BLR radius is $145 \pm 35\,\mathrm{days}$ as determined using optical interferometry (GRAVITY Collaboration et al., 2018). The expected size in the *K*-band was estimated using the lag-wavelength spectrum fit that was several times larger than expected. As discussed in Section 4.5.1, this likely includes diffuse continuum reprocessing at larger scales. Frequency-resolved lags show results approaching the fiducial disk size (Lewin et al., 2023, 2024). The larger fiducial τ_0 in 3C 273 of $8.95\,\mathrm{days}$ gives an accretion disk *K*-band size of $88\,\mathrm{ld}$, significantly smaller than the BLR size from optical interferometry (Thorne et al., 2025; GRAVITY Collaboration et al., 2018). As in I Zw 1, the extension of the accretion disk into the BLR beyond its self-gravitating radius to temperatures $\sim 1000\,\mathrm{K}$ relies on the assumption that the measured

continuum lags overwhelmingly arise from the disk. However, based on our results and literature, this is likely to be false. Instead, assuming the predicted disk size, places this region of the disk at smaller radii, inconsistent with the measured BLR.

Furthermore, should we expect to be able to detect direct *K*-band emission from a disk in the BLR? The dominant *K*-band emission region in an AGN is the hot dust at the sublimation region. If we consider the ratio of the luminosity of the disk in the BLR to that of the torus in the *K*-band, we can approximate this as the ratio of the disk to torus area. This is approximately $r^2_{\rm disk}/r^2_{\rm torus}$, where $r_{\rm disk}$ is the distance of the disk to the centre and $r_{\rm torus}$ is the distance of the torus. In I Zw 1, if the *K*-band emission region of the disk is in the BLR, we can take $r_{\rm disk} \sim R_{\rm H\beta} = 0.031\,{\rm pc}$ (Huang et al., 2019). The measured size of the torus *K*-band emission region is $0.42\,{\rm pc}$, which gives $r^2_{\rm disk}/r^2_{\rm torus} \simeq 1\%$ (Chapter 3, GRAVITY Collaboration et al., 2024). In 3C 273, $r_{\rm disk} \sim R_{\rm BLR} = 0.12\,{\rm pc}$ and $r_{\rm torus} = 0.57\,{\rm pc}$, giving $r^2_{\rm disk}/r^2_{\rm torus} \simeq 4\%$ (GRAVITY Collaboration et al., 2018, 2020b). These results indicate that the putative disk *K*-band emission is only a small fraction of the dominant torus emission, and that it is incredibly difficult to detect the presence of a disk in the BLR even in spatially resolved studies such as reverberation mapping and optical interferometry.

4.6 Conclusions

In this paper, we present the reverberation mapping results of the optical continuum in the super-Eddington AGN I Zw 1 and collate the most extensive set of directly measured internal sizes of an AGN. We use the cross-correlation method and PyROA to evaluate the lags of three years of *uBgVriz*$_s$ light curves. These lag-wavelength spectra are fitted with a thin and a slim disk, and with a free power law index profile to probe the underlying accretion disk structure. We also calculate the lag as a function of variability timescale and the frequency-resolved lags. Finally, we isolate the AGN SED and fit the UV/optical SED profile. These results show that:

1. There is a continuum emitting secondary reprocessor at large radii consistent with the BLR, increasing lags significantly across all wavelengths, and likely resulting in an artificially inflated fitted accretion disk size.

2. The evidence for this secondary reprocessor consists of longer lags at longer variability timescales, and the need for an additional, secondary reprocessing component to reproduce the lags at low frequencies.

3. There are also indications that the source of this secondary reprocessor is diffuse continuum emission from hydrogen, such as the characteristic *u*-band excess in the lag-wavelength spectrum and an increase in the secondary reprocessor fraction in the *u*-band based on the modelling of the frequency-resolved lags, which both suggest the presence of the Balmer jump.

4. We cannot determine the underlying accretion disk profile, that is, we cannot distinguish between a standard thin disk and a slim disk that is expected for super-Eddington AGN, based on the lag-wavelength spectrum. The UV/optical SED profile trends towards a thin disk.

5. The actual disk size is likely to be on the order of the fiducial disk size ($\sim 1.07\,\mathrm{days}$ at $4495\,\text{Å}$) or even smaller ($\sim 0.6 \pm 0.4\,\mathrm{days}$ at $4495\,\text{Å}$), based on the high frequency lag-wavelength spectrum.

6. There is little difference between the results of the disk reverberation mapping for this super-Eddington object and other super- and sub-Eddington objects from literature. This indicates that there are very similar structures and processes responsible for the variable UV/optical continuum emission independent of accretion rate and/or that our observations and analysis techniques are not able to access the parameter spaces in which differences will manifest.

7. Considering the evidence that continuum reverberation mapping measures a combination of the disk and diffuse continuum at larger distances, and adjusting the fiducial disk size for this, the size-wavelength relation from the optical to the mid-infrared shows little evidence that the accretion disk extends into the BLR significantly. This disfavours the failed radiatively accelerated dust driven outflow BLR formation model.

Fourier analysis and frequency-resolved lags are shown to be capable of disentangling different signals that contribute to the continuum lags. Presumably, there is a combination of structures we measure when we perform disk reverberation mapping experiments. The key to isolating the underlying accretion disk structure is in the further development of these Fourier techniques and their optimisation for AGN light curves. Further, there lies significant power in combining directly measured sizes of the internal AGN structures from reverberation mapping and optical interferometry to study the interplay and relationship between internal structural components. The sample of objects with BLR and hot dust size measurements from optical interferometry is about to exponentially increase with the full commissioning of GRAVITY+ (GRAVITY+ Collaboration et al., 2022). Mid-infrared size measurements of the warm dust, especially the never before accessed $3 - 5\,\mu\mathrm{m}$ range, will also increase significantly as MATISSE also benefits from GRAVITY+. In the further future, the establishment of a km- or tens of km-baseline optical interferometer might enable direct observations of the accretion disk.

Chapter 5

Conclusions

> Don't force me to draw my own conclusions. I do have a very big pencil.
>
> *Raising Steam*
> Terry Pratchett

In this work, we investigated the physical origins of the dust winds in highly accreting AGN. Dusty polar winds are a part of the dusty torus and help to define and collimate the direction of radiative AGN feedback to the host galaxy. These winds are launched off the dusty disk due to radiation pressure from the central engine and are therefore sensitive to accretion disk parameters such as the shape of radiation and Eddington ratio. In our effort to study the effects of accretion rate on the dusty winds, we traced the dusty winds through their larger scale structure and direction down to their launching region and the driving mechanism, the accretion disk, in two highly accreting AGN, I Zw 1 and H0557-385. We focused on high spatial resolution techniques to resolve these internal structures of these AGN. For the dust in the infrared, we used optical interferometry which offers unprecedented angular resolution down to sub-mas. The accretion disk in the optical was studied using reverberation mapping, a time-resolved technique; however, through basic assumptions this can resolve the accretion disk structure on scales of light days. Furthermore, we demonstrated the power of combining these techniques and data to map the internal AGN structure and the connection between different AGN components.

In Chapter 3, we investigated the dusty torus structure in two highly accreting AGN, I Zw 1 and H0557-385; in particular we studied direction of the dusty winds and the wind launching region using optical interferometry primarily with VLTI/MATISSE. We developed a new data reduction method for faint MATISSE objects, described in Section 2.3. Using this method, we published the first MATISSE *LM*-band observations of Type 1 AGN. We further fitted the radiative transfer model CAT3D-WIND to the infrared SED of H0557-385. Combining these results with previous *N*-band results from literature enabled us to compile the size-wavelength relation from $2 - 13\,\mu\mathrm{m}$.

Together with comparisons against predictions for simple geometries, such as a disk, this allowed us to deduce the basic structure of the dusty torus in these AGN.

In Chapter 4, we studied the accretion disk structure in I Zw 1 using reverberation mapping with three years of optical monitoring with sub-daily cadence from Las Cumbres Observatory. We analysed this data using the classic cross correlation method and a running optimal average model (PyROA) to simultaneously fit all bands and deduce a driving light curve. We paid particular attention to different variability timescales and how these might trace different structures in the AGN by using PyROA modelling over different timescales and Fourier analysis to derive frequency-resolved lags. Further, we deconstructed the SED into AGN and host galaxy contributions, examined the internal extinction, and fitted the UV/optical slope to determine the shape of the red tail of the accretion disk emission. Using the results from this study, Chapter 3, and literature, we mapped the internal structure of I Zw 1 as a function of wavelength across $0.3 - 13\,\mu\mathrm{m}$. This corresponds to the outer parts of the accretion disk, the broad line region, and the dusty torus from the hot sublimation region to the warm mid-IR dust.

The structure of the dusty torus in highly accreting AGN appears to be affected by the accretion rate and is different in to slower accreting AGN. Firstly, there are indications of an absence of a *polar* dusty wind in both objects. Optical interferometric data in the *N*-band – which is expected to have strong polar dust contributions – does not show signs of polar elongations. CAT3D-WIND model fits to the infrared SED of H0557-385 prefer models with a low fraction of total mass in the wind and the largest available opening angles. Nevertheless, there are indications of dusty winds being launched in both objects. The size-wavelength relations show a flattening of sizes, i.e. size is independent of wavelength, within $5 - 10R_{\mathrm{sub}}$, particularly in the $2 - 8\,\mu\mathrm{m}$ wavelength range. This might indicate a puffed-up region which shadows outer parts of the disk. In the model of dusty winds launched by radiation pressure, we do expect a 'puffing-up', i.e. an increase in vertical height, where infrared radiation pressure vertically unbinds dust that is then blown out into the wind. Accordingly, this might imply that we are observing the wind launching region, which then means that winds *are* being launched, but not in a polar direction. Rather, the size-wavelength relations also imply a more disk-like structure and a wind with a large opening angle, indicating that the winds are orientated in a preferentially equatorial direction. This matches predictions when considering the anisotropy of accretion disk radiation in the scenario where winds are driven by radiation pressure: as the Eddington ratio increases, the opening angle of the wind increases, moving towards a more equatorial orientation (see Fig. 3.12). Likewise, several studies have shown that the covering fraction of the dusty torus decreases with increasing Eddington ratio (Ricci et al., 2017b, 2023; Ananna et al., 2022; Mizukoshi et al., 2024). It has been posited that this effect is due to a 'blowout' of dust, where at high Eddington ratios the AGN blows out the majority of non-equatorial dust, therefore reducing the covering fraction of the dusty torus (Alonso-Herrero et al., 2021; García-Burillo et al., 2021; Ricci et al., 2023). In fact, the high Eddington ratio of both objects puts them firmly in the theorised blowout region (see e.g. Fig. 4 in Alonso-Herrero et al., 2021). Therefore, our results could also be an indication of this blowout occurring; however, the physical difference between a blowout and a large wind opening angle is not directly evident.

As such, the low covering factors at large Eddington ratios might also be a result of predominantly equatorially orientated winds with large opening angles. Nevertheless, independent of the precise structure of the dusty torus, we do find indications that this dusty torus structure changes at high Eddington ratios.

In contrast to the dusty torus structure, the accretion disk structure does not appear to change significantly with Eddington ratio as far as we observe. More relevantly, disk reverberation mapping experiments in general probably do not measure solely the accretion disk as a source of reverberation signals, which we also found to be the case. Based on longer lags at longer variability timescales and longer low frequency lags which can only be reproduced with a secondary reprocessor, there is continuum emission at distances that correspond to the BLR, contributing to reverberation signals. This continuum may be hydrogen diffuse continuum emission as we detect the characteristic *u*-band excess and an increase in the secondary reprocessor fraction in the *u*-band, implying the presence of the Balmer jump. We are unable to precisely determine the temperature profile of the accretion disk, e.g. between a slim and a thin disk; that is, besides optically thick emission where temperature decreases as the radius increases. With regards to the disk size, we found indications that it might by on the order of the predicted size based on the Eddington ratio, or possibly smaller. These results are in fact similar to results from previous studies, for both sub- and super-Eddington AGN. This indicates that there are no currently measurable differences in accretion disk structure as a function of Eddington ratio. Rather, this implies a consistent Seyfert AGN structure (as illustrated in Fig. 1.1) across a large range of AGN parameters. Finally, we compiled the size-wavelength relation of I Zw 1 $0.3 - 13\,\mu\mathrm{m}$, mapping the accretion disk, BLR, and dusty torus. If we consider that there is significant contribution from a secondary reprocessor in the reverberation signals, this relation disfavours the failed radiatively accelerated dust driven outflow BLR formation model, as there is little evidence that the disk extends into the BLR at the relevant temperatures. In summary, we do not find any evidence for an Eddington ratio-dependant accretion disk structure, but we do uncover further information about the internal AGN structure.

In this study, we observe the physical origins of the dusty winds in highly accreting AGN from the wind driver, the accretion disk, over the wind launching region, to the dusty winds themselves. We find indications that the accretion disk structure as the driver does not differ significantly as a function of Eddington ratio. Further, since these are the first published high angular resolution observations of the putative wind launching region, we cannot make any statements as to its evolution with Eddington ratio. However, we do see evidence that the dusty winds themselves – especially their direction – changes with Eddington ratio, possibly having impacts on the feedback behaviour to the host galaxy.

This work provides important evidence that the structure of AGN emission, both from the central engine and on larger scales, is an essential AGN parameter and is at least partially driven by accretion rate. On internal AGN scales, the anisotropy of the accretion disk emission at high accretion rates creates a large opening angle of the dusty wind. This torus structure then guides the AGN feedback to the host galaxy, determining its direction. The impact of Eddington ratio on the direction of AGN feedback needs to be considered both in observational studies of the

AGN-galaxy connection and galaxy-scale simulations. In addition, the dusty torus structure and its dependence on accretion rate can also provide a pathway for AGN evolution. In strongly accreting objects, the dusty winds are orientated more equatorially and may remove more of the equatorial material that is the source of material for accretion. A lack of material then shifts the AGN into a lower accreting state, where winds are more polar and material can again accumulate in the equatorial plane, setting the AGN up for another burst of strong accretion. AGN emission cannot be assumed to be spherical because it impacts both the internal structure and evolution, and large-scale feedback to the galaxy.

The outlook for high angular resolution studies of AGN in the near future is very positive. The upgrade of GRAVITY into GRAVITY+ will significantly lower the magnitude limits for observations, opening up a large population of AGN to study (GRAVITY+ Collaboration et al., 2022). In the local Universe this means that a larger parameter space of AGN properties for which we can observe the hot dust. At larger redshifts, this means a substantial amount of AGN with direct black hole mass measurements enabling us to determine the black hole mass relation beyond the local Universe for the first time, as well as measuring the evolution of BLR with redshift. Some of these improvements will also map onto MATISSE through the AO upgrades and the GRA4MAT mode, where using GRAVITY as the fringe tracker increases integration times for MATISSE (Woillez et al., 2024). This will allow us for the first time to build a substantial sample of observations of the wind launching region in the *LM*-bands, investigating the evolution of this region with different AGN parameters such as black hole mass, Eddington ratio, luminosity, and inclination. Similarly, an improvement in the MATISSE *N*-band performance will enable us to couple these observations to the dusty wind properties. High spatial resolution mapping or the internal AGN structure from the accretion disk to the dusty torus is also more available than ever before: for example, 15 objects have both an LCO optical monitoring campaign and *K*-band observations from GRAVITY (AVA, GRAVITY Collaboration et al., 2020b, 2024). The availability of high cadence time series observation will also increase with the upcoming time domain survey LSST (Ivezić et al., 2019). A large sample of high spatial resolution size-wavelength relations, as we compiled for I Zw 1, will allow us to investigate the *resolved* internal AGN structure in its totality, as wells as the connection between the different components. We can examine the evolution of this structure as a function of different AGN parameters, especially Eddington ratio. We can further look at which points in the structure the impact of Eddington ratio becomes significant. Even further in the future we might construct a km- or tens of km-baseline optical interferometer; with this resolution we approach direct and resolved observations of the accretion disk (at least in differential phase).

Appendix A

Additional Data for Chapter 3

A.1 SED Modelling Results

Here we present the SED modelling results for H0667-385 using the CAT3D and CAT3D-WIND models in Table A.1, as described in Section 3.3.1.

A.2 I Zw 1 CAT3D and CAT3D-WIND Sample SED Fits

We present two sample fits to the SED of I Zw 1 with CAT3D and CAT3D-WIND to illustrate the problems in fitting the SED in Fig. A.1. The data used for fitting and shown in these plots is derived from the SED data presented in Fig. 3.6 and contained in Table A.2. First, the spectral

	i	$R_{\rm sub}$	a	N_0	h	a_w	θ_w	σ_θ	f_{wd}	$\tau_{\rm OD}$	$\chi^2_{\rm red}$
n	15	0.10	-2.25	7.5	0.25	-1.50	30	15	0.0	2.6	87
n	30	0.10	-2.25	7.5	0.25	-1.50	30	15	0.0	2.3	82
n	45	0.12	-2.25	5.0	0.25	-1.50	30	15	0.0	2.2	83
w	15	0.12	-2.5	5.0	0.3	-2.0	30	15	2.0	2.2	167
w	30	0.12	-2.5	5.0	0.4	-1.5	45	10	0.45	2.2	167
w	45	0.12	-2.5	5.0	0.4	-1.5	45	7	0.45	2.3	163

TABLE A.1: CAT3D and CAT3D-WIND SED modelling results for H0557-385. CAT3D models are indicated with n and CAT3D-WIND models are indicated with w. Model parameters are as follows: inclination of the AGN i in degrees, sublimation radius $R_{\rm sub}$, index a of the radial dust distribution power law in the disk, line-of-sight cloud number N_0, scale height h, index a_w of the wind dust distribution power law, wind half-opening angle θ_w in degrees, width of the wind cone σ_θ in degrees, ratio of wind-to-disk dust clouds f_{wd} (for more information see Hönig & Kishimoto, 2010, 2017). Additionally, we consider the host galaxy extinction with an optical depth of $\tau_{\rm OD}$. For CAT3D fits, a_w, θ_w, and σ_θ were held constant with $f_{wd} = 0$ to switch off the wind.

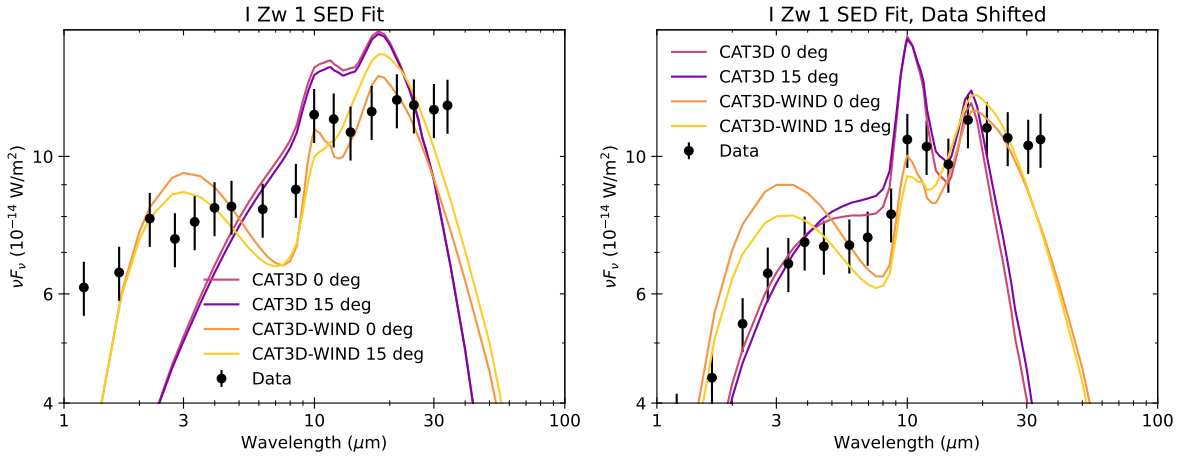

FIGURE A.1: Sample CAT3D and CAT3D-WIND SED fits for I Zw 1. Left: initial combined SED data; right: data $\leq 5\,\mu$m normalised independently to the rest of the data. Data combination and adjustment is described in the text.

data (AKARI, SPITZER, and VISIR) was re-binned with bins of $0.5\,\mu$m for AKARI, $2\,\mu$m for SPITZER, and $1\,\mu$m for VISIR. This was done to reduce the number of points in the spectra and therefore the weight of the spectra in the final combination of the SED data. These re-binned spectra were then adjusted to the flux level of the photometry. Finally, the average combination of the spectra and the photometry were evenly re-binned in log space and a fixed error of 10% was added so as to weigh the SED evenly. The fits were then performed with this data, as described for H0557-385 in Section 3.3.1 but without additional internal extinction. This time, we restricted the inclinations to $0 - 15$ degree, nearly face-on. The best fits for this set up are shown in the left plot in Fig. A.1. There appears to be a mismatch in the level of flux between $\lesssim 10\,\mu$m and $\gtrsim 10\,\mu$m that cannot be reproduced by the models. To possibly obtain a reasonable fit we tried to adjust the level of $\leq 5\,\mu$m flux independent to the rest of the data; this is shown in the right plot in Fig. A.1. We normalised this flux to the $4.6\,\mu$m photometry point. The best-fit SED models to this data are shown in the right plot in Fig. A.1. While this time, the near-IR slope is well-described by the CAT3D models, they massively overestimate the silicate feature. On the other hand, the CAT3D-WIND models fit the mid-IR features reasonably well but cannot replicate the near-IR flux and SED shape. There is clearly still a problem to reproduce both the near-IR and mid-IR SED simultaneously.

A.3 SED Data

We tabulate the SED data for I Zw 1 in Table A.2 and for H0557-385 in Table A.3. The assembly of the SED data is described in Section 3.2.2.

Type	λ (μm)	νF_ν (10^{-14}W/m^2)	Instrument	Obs. Date	Ext. Aper. Size
Phot.	1.2	6.15 ± 0.24	2MASS	2000-11-30	7”
"	1.6	6.50 ± 0.26^a	"	"	"
"	2.2	7.94 ± 0.16^a	"	"	"
"	3.4	7.64 ± 0.004^a	WISE	2010-07-11	8”.25
"	4.6	8.62 ± 0.005^a	"	"	"
"	22.1	12.9 ± 0.04^a	"	2010-07-10	16”.5
"	70.0	9.59 ± 0.03^a	Herschel/PACS	2011-07-24	12”
Phot.	8.99	10.1 ± 0.91^b	VLT/VISIR	2010-10-20	0.3”
"	11.74	12.2 ± 0.57^b	Subaru/COMICS	2006-10-04	"
"	11.88	11.3 ± 1.3^b	VLT/VISIR	2010-10-17	"
"	12.0	10.6 ± 1.9^b	"	–	"
Spec.	$2.5 - 5.0^c$	–	AKARI/IRC	2008-07-09	$7.3” \times 1'$
Spec.	$7.8 - 13.2^d$	–	VLT/VISIR	2010-10-20	0.4”
Spec.	$5.5 - 35.0^e$	–	SPITZER/IRS	2004-01-07	$11” \times 57”$
$F_{\rm tot}$	3.4	8.39 ± 1.23^f	VLTI/MATISSE	2021-09-25	–
$F_{\rm corr}$	3.4	6.67 ± 0.75^f	"	"	–
$F_{\rm tot}$	4.6	11.5 ± 3.02^f	"	"	–
$F_{\rm corr}$	4.6	10.3 ± 1.66^f	"	"	–
$F_{\rm corr}$	9.0	7.57 ± 1.07^g	VLTI/MIDI	2010-08-25	–
"	12.0	8.44 ± 1.77^g	"	"	–

TABLE A.2: SED data for I Zw 1. Types of measurement are as follows: Phot. is photometry, Spec. is spectrum, $F_{\rm tot}$ is total flux, and $F_{\rm corr}$ is correlated flux. References: [a] Shangguan et al. (2018), [b] Asmus et al. (2014), [c] Kim et al. (2015), [d] Jensen et al. (2017), [e] Shi et al. (2014), [f] this work, [g] Burtscher et al. (2013).

Type	λ (μm)	νF_ν (10^{-14}W/m^2)	Instrument	Obs. Date	Ext. Aper. Size
Phot.	1.0	1.29 ± 0.06^a	UKIRT/WFCAM	2009-12-13	$*$
"	1.2	1.73 ± 0.09^a	"	"	"
"	1.6	2.79 ± 0.14^a	"	"	"
"	2.2	4.99 ± 0.25^a	"	"	"
Phot.	3.6	11.7 ± 0.06^a	SPITZER/IRAC	2008-10-31	$*$
"	4.5	13.0 ± 0.06^a	"	"	"
"	5.7	14.1 ± 0.13^a	"	"	"
"	7.9	13.1 ± 0.06^a	"	"	"
Phot.	8.59	11.5 ± 0.38^b	VLT/VISIR	2009-09-07	0.33"
"	10.49	9.78 ± 0.54^b	"	2009-09-30	"
"	11.88	10.4 ± 1.49^b	"	2009-09-07	"
"	11.88	9.65 ± 0.42^b	"	2009-09-30	"
"	12.0	10.6 ± 1.07^b	"	–	"
"	12.81	11.2 ± 1.34^b	"	"	"
Phot.	12.0	13.2 ± 0.79^c	IRAS	1983-03-27	$4' \times 5'$
"	22.0	9.33 ± 0.47^c	"	"	"
"	52.0	1.86 ± 0.20^c	"	"	"
Spec.	$5.2 - 36.8^d$	–	SPITZER/IRS	2007-10-06	$11" \times 57"$
$F_{\rm tot}$	3.4	7.34 ± 1.81^e	VLTI/MATISSE	2021-09-25	–
$F_{\rm corr}$	3.4	4.86 ± 1.03^e	"	"	–
$F_{\rm tot}$	4.6	12.5 ± 4.59^e	"	"	–
$F_{\rm corr}$	4.6	8.07 ± 1.51^e	"	"	–
$F_{\rm corr}$	9.0	3.92 ± 0.97^f	VLTI/MIDI	2009-08-01	–
"	12.0	6.92 ± 1.30^f	"	"	–

TABLE A.3: SED data for H0557-385. Types of measurement are as follows: Phot. is photometry, Spec. is spectrum, $F_{\rm tot}$ is total flux, and $F_{\rm corr}$ is correlated flux. $*$: data was reduced to remove host galaxy contamination. For further details see Kishimoto et al. (2007, 2011b). References: [a] Kishimoto et al. (2011b), [b] Asmus et al. (2014), [c] Moshir et al. (1990), [d] Spitzer Heritage Archive, [e] this work, [f] Burtscher et al. (2013).

Appendix B

Additional Data for Chapter 4

B.1 I Zw 1 Spectrum

In parallel with our LCO 1 m photometric monitoring, we monitored variations in the optical spectrum of I Zw 1 using the LCO 2 m robotic telescopes (see AVA for more details). The Faulkes Telescope North (FTN) at Haleakala in Hawaii, and the Faulkes Telescope South (FTS) at Siding Springs Observatory in Australia are equipped with nearly-identical Floyds spectrographs[1]. We obtained 80 spectra taken in pairs in 40 epochs, throughout Year 2 and 4 (~ 15 per year). The spectra are cross-dispersed with 1st-order red spectra (5400-10000 Å) and 2nd-order blue spectra (3200-5700 Å) projected simultaneously on the CCD. The spectral resolution is $R \equiv \lambda/\Delta\lambda = 400$ on the blue end and $R = 700$ on the red end of each order. We used 600 s exposures, and employed the $6''$ slit, oriented at the parallactic angle, to minimize wavelength-dependent slit losses due to changes in seeing and airmass. Wavelength calibration and flat field lamp exposures were taken on each visit.

The spectra were downloaded from the LCO archive and extracted using the AGNFLOYDS pipeline[2]. To establish the absolute flux calibration, divide out telluric absorption features, and reduce fringing artifacts (although still evident at wavelengths larger than 7000 Å), we used the spectrum of the closest spectrophotometric standard star observed within 5 days.

We analysed the time-resolved spectroscopy with PrepSpec[3] to quantify variability in several broad emission lines. A similar PrepSpec analysis of NGC 5548 is described in full detail in Horne et al. (2021). Briefly, PrepSpec performs a maximum likelihood fit to the Floyds spectra at all epochs, adopting a simple (ABC) model for the spectral variations:

$$F(\lambda, t) = A(\lambda) + B(\lambda, t) + C(\lambda, t) \ . \tag{B.1}$$

[1] https://lco.global/observatory/instruments/floyds/
[2] https://github.com/svalenti/FLOYDSpipeline
[3] http://star-www.st-andrews.ac.uk/~kdh1/lib/prepspec/prepspec.tar.gz

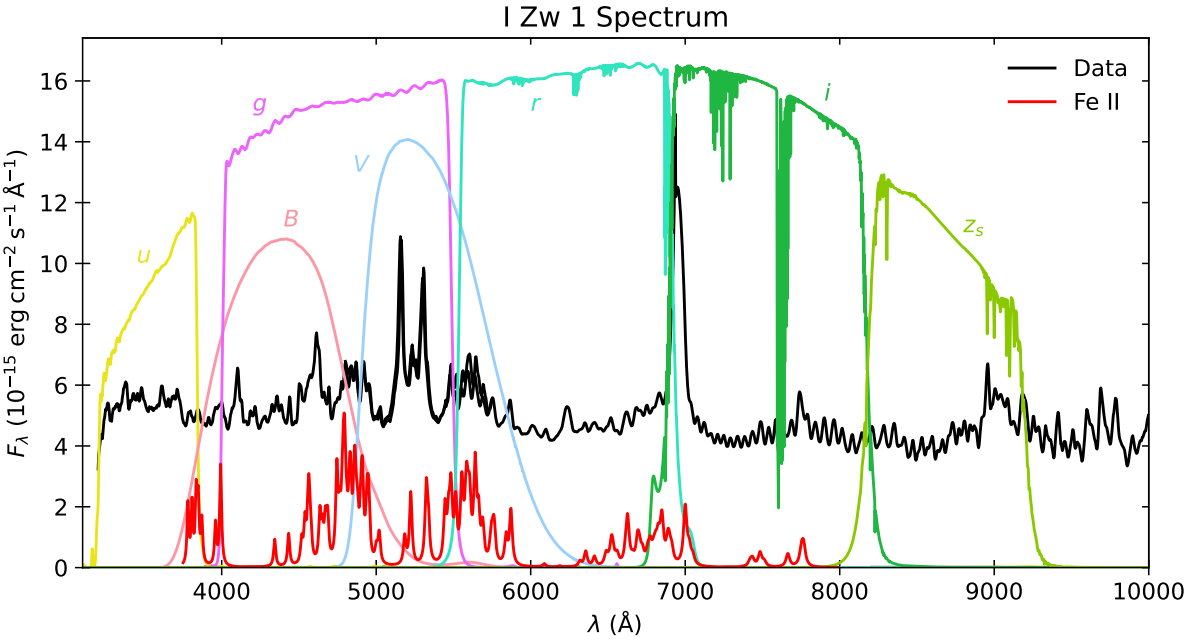

FIGURE B.1: The average spectrum of I Zw 1 over the LCO campaign in the observed frame (black lines), overlaid with the LCO filter transmission curves. The Fe II template by Véron-Cetty et al. (2004), which was created based on I Zw 1, is plotted with the red lines but does not indicate the actual amount of Fe II in I Zw 1.

This fit estimates the mean spectrum $A(\lambda)$, the broad emission-line variations $B(\lambda, t)$, and the continuum variations $C(\lambda, t)$. The full results of this analysis will be published in a following paper. Here, we just show the average spectrum across this campaign in Fig. B.1 to highlight the contribution of hydrogen, helium and Fe II lines to the broadband filters. We note that the oscillation pattern dominant in the continuum at > 7000 Å are caused by fringing interference artefacts in the detector. We also include the Fe II template from Véron-Cetty et al. (2004) to show the location of these prominent emission lines.

B.2 Additional Time Series Analysis Results

This section includes additional results of our time series analysis in Section 4.3. In Table B.1, we tabulate the peak correlation coefficients from the interpolated cross-correlation analysis in Section 4.3.1 for Years 2, 3, and 4. In Table B.2, we present the lags derived from PyROA modelling at different variability timescales as described in Section 4.3.2. For the PyROA fits we vary the width Δ of the Gaussian memory function with $\Delta = 3$, 5, 10, and 20 days. The lags are plotted in Fig. 4.4. Fig. B.2 shows the same frequency-resolved lags as Fig. 4.5 but overlaid with the model of a thin disk at an inclination of 60° with an Eddington ratio of 50. The frequency-resolved lags are described in Section 4.3.2.1, as well as the thin disk model and transfer function (Collier et al., 1999; Cackett et al., 2007; Starkey et al., 2016).

Band	$\lambda_{\rm eff}$ (Å)	Year 2 $r_{\rm peak}$	Year 3 $r_{\rm peak}$	Year 4 $r_{\rm peak}$
u	3540	0.95	0.96	0.89
B	4361	0.94	0.96	0.90
g	4770	1.00	1.00	1.00
V	5448	0.97	0.97	0.92
r	6215	0.93	0.96	0.85
i	7545	0.92	0.93	0.79
z_s	8700	0.85	0.84	0.58

TABLE B.1: The peak correlation coefficient $r_{\rm peak}$ calculated in the ICCF analysis with reference to the g-band in Section 4.3.1.

Band	$\lambda_{\rm eff}$ (Å)	$\Delta = 3$ τ (days)	$\Delta = 5$ τ (days)	$\Delta = 10$ τ (days)	$\Delta = 20$ τ (days)
u	3540	-0.28 ± 0.16	$-0.64^{+0.21}_{-0.20}$	-1.23 ± 0.30	$-1.78^{+0.56}_{-0.56}$
B	4361	-0.52 ± 0.17	$-0.66^{+0.22}_{-0.21}$	-0.89 ± 0.32	-1.62 ± 0.60
g	4700	0.00 ± 0.13	0.00 ± 0.17	0.00 ± 0.27	0.00 ± 0.55
V	5448	0.52 ± 0.14	0.59 ± 0.19	0.79 ± 0.28	1.50 ± 0.53
r	6215	2.18 ± 0.20	2.35 ± 0.24	2.31 ± 0.33	3.11 ± 0.56
i	7545	3.50 ± 0.24	$4.23^{+0.29}_{-0.30}$	5.38 ± 0.39	8.42 ± 0.62
z_s	8700	$4.78^{+0.65}_{-0.48}$	$5.73^{+0.52}_{-0.51}$	$6.54^{+0.66}_{-0.63}$	9.47 ± 0.86

TABLE B.2: Lags in days between each light curve and the reference light curve in the g-band, calculated with PyROA for different values of the light curve stiffness fitting parameter Δ. The lags are for PyROA fits with $\Delta = 3$, 5, 10, and 20 days as described in Section 4.3.2. The lags are plotted in Fig. 4.4.

B.3 LCO SED

Here we tabulate the LCO SED of the AGN; the faint and bright contours, the RMS, and the host galaxy contribution in Table B.3, which were calculated using flux-flux analysis as described in Section 4.4. Years 2, 3, and 4 of the LCO campaign are included. We present both the observed flux and flux corrected for Galactic extinction using $E(B-V) = 0.057$ (Schlafly & Finkbeiner, 2011; Fitzpatrick, 1999). The SED corrected for Galactic and internal extinction is plotted in Fig. 4.9 and 4.10.

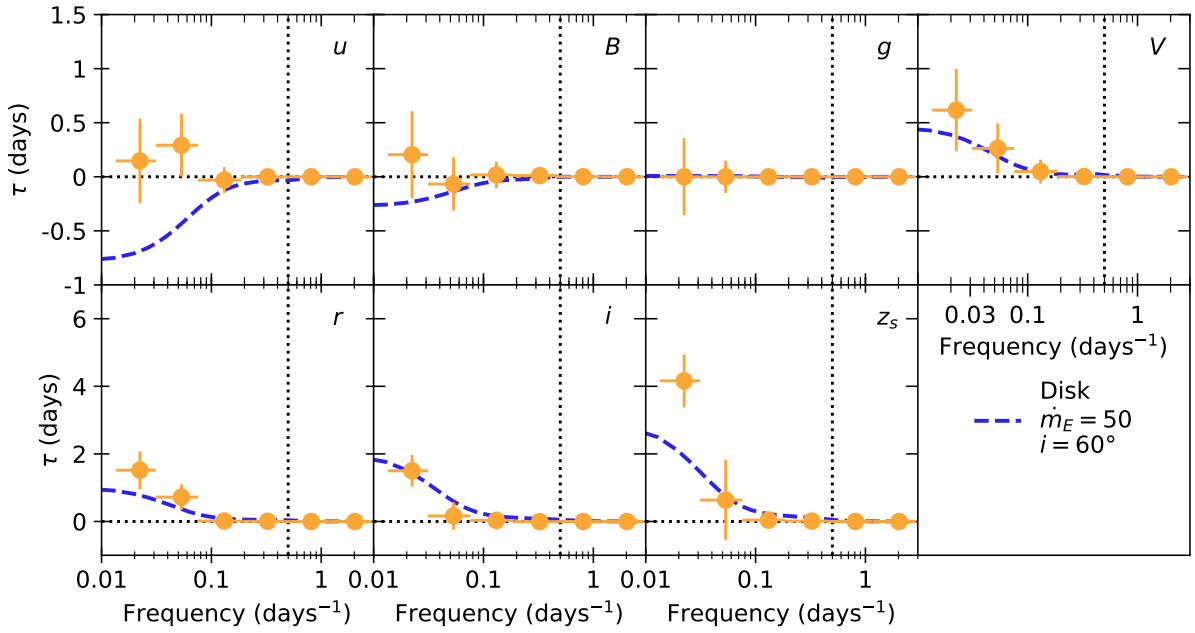

FIGURE B.2: The lag-frequency spectra as plotted in Fig. 4.5 combined with the prediction for a thin accretion disk with an inclination of 60° and $\dot{m}_E = 50$ (blue dashed line).

		observed				dereddened			
	$\lambda_{\rm eff}$ (Å)	$F_{\rm bright}$	$F_{\rm faint}$	$F_{\rm RMS}$	$F_{\rm gal}$	$F_{\rm bright}$	$F_{\rm faint}$	$F_{\rm RMS}$	$F_{\rm gal}$
u	3540	3.451 ± 0.003	2.061 ± 0.002	0.419 ± 0.001	0.006 ± 0.007	4.453 ± 0.003	2.659 ± 0.002	0.541 ± 0.001	0.008 ± 0.009
B	4361	4.798 ± 0.013	2.865 ± 0.010	0.583 ± 0.002	0.268 ± 0.009	5.955 ± 0.016	3.552 ± 0.012	0.722 ± 0.002	0.332 ± 0.011
g	4770	5.352 ± 0.011	3.196 ± 0.009	0.650 ± 0.001	0.624 ± 0.010	6.502 ± 0.014	3.883 ± 0.011	0.790 ± 0.002	0.758 ± 0.013
V	5448	6.792 ± 0.015	4.056 ± 0.012	0.825 ± 0.002	1.139 ± 0.013	7.981 ± 0.017	4.766 ± 0.014	0.969 ± 0.002	1.338 ± 0.015
r	6215	8.078 ± 0.022	4.824 ± 0.016	0.981 ± 0.003	1.467 ± 0.016	9.238 ± 0.025	5.517 ± 0.019	1.123 ± 0.003	1.677 ± 0.018
i	7545	9.871 ± 0.032	5.895 ± 0.023	1.199 ± 0.004	3.350 ± 0.019	10.90 ± 0.04	6.510 ± 0.025	1.324 ± 0.004	3.699 ± 0.021
z_s	8700	10.30 ± 0.05	6.152 ± 0.035	1.251 ± 0.006	3.890 ± 0.020	11.14 ± 0.06	6.651 ± 0.038	1.353 ± 0.007	4.206 ± 0.021

TABLE B.3: The LCO I Zw 1 SED calculated using the flux-flux analysis, as described in Section 4.4. All fluxes are in mJy. The 'observed' flux is flux as observed, without any extinction corrections. The 'dereddened' flux is corrected for line-of-sight Galactic extinction only, $E(B-V) = 0.057$ (Schlafly & Finkbeiner, 2011; Fitzpatrick, 1999). $F_{\rm bright}$ is the brightest AGN flux over the years 2, 3, and 4 of the campaign, $F_{\rm faint}$ is the faintest flux, and $F_{\rm RMS}$ is the AGN RMS flux. $F_{\rm gal}$ is the host galaxy flux.

References

Abramowicz, M. A., Czerny, B., Lasota, J. P., & Szuszkiewicz, E. 1988, ApJ, 332, 646, doi: 10.1086/166683

Abuter, R., Allouche, F., Amorim, A., et al. 2024, Nature, 627, 281, doi: 10.1038/s41586-024-07053-4

Ahumada, R., Allende Prieto, C., Almeida, A., et al. 2020, ApJS, 249, 3, doi: 10.3847/1538-4365/ab929e

Alonso-Herrero, A., Ramos Almeida, C., Mason, R., et al. 2011, ApJ, 736, 82, doi: 10.1088/0004-637X/736/2/82

Alonso-Herrero, A., García-Burillo, S., Hönig, S. F., et al. 2021, A&A, 652, A99, doi: 10.1051/0004-6361/202141219

Ananna, T. T., Urry, C. M., Ricci, C., et al. 2022, ApJ, 939, L13, doi: 10.3847/2041-8213/ac9979

Antonucci, R. 1993, ARA&A, 31, 473, doi: 10.1146/annurev.aa.31.090193.002353

Antonucci, R., Hurt, T., & Miller, J. 1994, ApJ, 430, 210, doi: 10.1086/174395

Antonucci, R. R. J., & Miller, J. S. 1985, ApJ, 297, 621, doi: 10.1086/163559

Asensio Ramos, A., & Ramos Almeida, C. 2009, ApJ, 696, 2075, doi: 10.1088/0004-637X/696/2/2075

Asmus, D., Gandhi, P., Hönig, S. F., Smette, A., & Duschl, W. J. 2015, MNRAS, 454, 766, doi: 10.1093/mnras/stv1950

Asmus, D., Hönig, S. F., & Gandhi, P. 2016, ApJ, 822, 109, doi: 10.3847/0004-637X/822/2/109

Asmus, D., Hönig, S. F., Gandhi, P., Smette, A., & Duschl, W. J. 2014, MNRAS, 439, 1648, doi: 10.1093/mnras/stu041

Balbus, S. A., & Hawley, J. F. 1991, ApJ, 376, 214, doi: 10.1086/170270

Baldwin, J. A., Ferland, G. J., Korista, K. T., Hamann, F., & LaCluyzé, A. 2004, ApJ, 615, 610, doi: 10.1086/424683

Barth, A. J., & Bentz, M. C. 2016, MNRAS, 458, L109, doi: 10.1093/mnrasl/slw030

Barth, A. J., Pancoast, A., Bennert, V. N., et al. 2013, ApJ, 769, 128, doi: 10.1088/0004-637X/769/2/128

Barvainis, R. 1987, ApJ, 320, 537

Baskin, A., & Laor, A. 2005, MNRAS, 358, 1043, doi: 10.1111/j.1365-2966.2005.08841.x

Baskin, A., & Laor, A. 2018, MNRAS, 474, 1970, doi: 10.1093/mnras/stx2850

Bennert, N., Jungwiert, B., Komossa, S., Haas, M., & Chini, R. 2006a, A&A, 456, 953, doi: 10.1051/0004-6361:20065319

Bennert, N., Jungwiert, B., Komossa, S., Haas, M., & Chini, R. 2006b, A&A, 459, 55, doi: 10.1051/0004-6361:20065477

Bentz, M. C., & Katz, S. 2015, PASP, 127, 67, doi: 10.1086/679601

Bentz, M. C., Markham, M., Rosborough, S., et al. 2023, ApJ, 959, 25, doi: 10.3847/1538-4357/ad08b8

Bentz, M. C., Williams, P. R., Street, R., et al. 2021, ApJ, 920, 112, doi: 10.3847/1538-4357/ac19af

Bentz, M. C., Denney, K. D., Grier, C. J., et al. 2013, ApJ, 767, 149, doi: 10.1088/0004-637X/767/2/149

Bertin, E., & Arnouts, S. 1996, A&AS, 117, 393, doi: 10.1051/aas:1996164

Blandford, R. D., & McKee, C. F. 1982, ApJ, 255, 419, doi: 10.1086/159843

Boroson, T. A., & Green, R. F. 1992, ApJS, 80, 109, doi: 10.1086/191661

Brandl, B. R., Bernard-Salas, J., Spoon, H. W. W., et al. 2006, ApJ, 653, 1129, doi: 10.1086/508849

Brandt, W. N., & Alexander, D. M. 2015, AA&ARv, 23, 1, doi: 10.1007/s00159-014-0081-z

Bridle, A. H., Hough, D. H., Lonsdale, C. J., Burns, J. O., & Laing, R. A. 1994, AJ, 108, 766, doi: 10.1086/117112

Bridle, A. H., & Perley, R. A. 1984, ARA&A, 22, 319, doi: 10.1146/annurev.aa.22.090184.001535

Brown, T. M., Baliber, N., Bianco, F. B., et al. 2013, PASP, 125, 1031, doi: 10.1086/673168

Burtscher, L., Meisenheimer, K., Tristram, K. R. W., et al. 2013, A&A, 558, A149, doi: 10.1051/0004-6361/201321890

Cackett, E. M., Chiang, C.-Y., McHardy, I., et al. 2018, ApJ, 857, 53, doi: 10.3847/1538-4357/aab4f7

Cackett, E. M., Horne, K., & Winkler, H. 2007, MNRAS, 380, 669, doi: 10.1111/j.1365-2966.2007.12098.x

Cackett, E. M., Zoghbi, A., & Ulrich, O. 2022, ApJ, 925, 29, doi: 10.3847/1538-4357/ac3913

Cackett, E. M., Gelbord, J., Li, Y.-R., et al. 2020, ApJ, 896, 1, doi: 10.3847/1538-4357/ab91b5

Cackett, E. M., Gelbord, J., Barth, A. J., et al. 2023, ApJ, 958, 195, doi: 10.3847/1538-4357/acfdac

Cai, Z.-Y., Wang, J.-X., Zhu, F.-F., et al. 2018, ApJ, 855, 117, doi: 10.3847/1538-4357/aab091

Carter, B. 1971, Phys. Rev. Lett., 26, 331, doi: 10.1103/PhysRevLett.26.331

Chan, C.-H., & Krolik, J. H. 2016, ApJ, 825, 67, doi: 10.3847/0004-637X/825/1/67

Chan, C.-H., & Krolik, J. H. 2017, ApJ, 843, 58, doi: 10.3847/1538-4357/aa76e4

Chen, Y.-J., Liu, J.-R., Zhai, S., et al. 2023, MNRAS, 522, 3439, doi: 10.1093/mnras/stad1136

Chiar, J. E., & Tielens, A. G. G. M. 2006, ApJ, 637, 774, doi: 10.1086/498406

Clavel, J., Wamsteker, W., & Glass, I. S. 1989, ApJ, 337, 236, doi: 10.1086/167100

Clavel, J., Reichert, G. A., Alloin, D., et al. 1991, ApJ, 366, 64, doi: 10.1086/169540

Coffey, D., Longinotti, A. L., Rodríguez-Ardila, A., et al. 2014, MNRAS, 443, 1788, doi: 10.1093/mnras/stu1294

Collier, S., Horne, K., Wanders, I., & Peterson, B. M. 1999, MNRAS, 302, L24, doi: 10.1046/j.1365-8711.1999.02250.x

Combes, F., García-Burillo, S., Audibert, A., et al. 2019, A&A, 623, A79, doi: 10.1051/0004-6361/201834560

Corporaal, A., Kluska, J., Van Winckel, H., et al. 2021, A&A, 650, L13, doi: 10.1051/0004-6361/202141154

Czerny, B., & Hryniewicz, K. 2011, A&A, 525, L8, doi: 10.1051/0004-6361/201016025

Czerny, B., Nikołajuk, M., Różańska, A., et al. 2003, A&A, 412, 317, doi: 10.1051/0004-6361:20031441

Davies, R., Baron, D., Shimizu, T., et al. 2020, MNRAS, 498, 4150, doi: 10.1093/mnras/staa2413

Dexter, J., & Agol, E. 2011, ApJ, 727, L24, doi: 10.1088/2041-8205/727/1/L24

Diamond-Stanic, A. M., & Rieke, G. H. 2010, ApJ, 724, 140, doi: 10.1088/0004-637X/724/1/140

Donnan, F. R., Horne, K., & Hernández Santisteban, J. V. 2021, MNRAS, 508, 5449, doi: 10.1093/mnras/stab2832

Donnan, F. R., Hernández Santisteban, J. V., Horne, K., et al. 2023, MNRAS, 523, 545, doi: 10.1093/mnras/stad1409

Draine, B. T., & Lee, H. M. 1984, ApJ, 285, 89, doi: 10.1086/162480

Drewes, F., Leftley, J. H., Hönig, S. F., Tristram, K. R. W., & Kishimoto, M. 2025, MNRAS, 537, 1369, doi: 10.1093/mnras/staf110

Du, P., Hu, C., Lu, K.-X., et al. 2015, ApJ, 806, 22, doi: 10.1088/0004-637X/806/1/22

Du, P., Lu, K.-X., Zhang, Z.-X., et al. 2016, ApJ, 825, 126, doi: 10.3847/0004-637X/825/2/126

Dullemond, C. P., Dominik, C., & Natta, A. 2001, ApJ, 560, 957, doi: 10.1086/323057

Edelson, R., Gelbord, J. M., Horne, K., et al. 2015, ApJ, 806, 129, doi: 10.1088/0004-637X/806/1/129

Edelson, R., Gelbord, J., Cackett, E., et al. 2017, ApJ, 840, 41, doi: 10.3847/1538-4357/aa6890

Edelson, R., Gelbord, J., Cackett, E., et al. 2019, ApJ, 870, 123, doi: 10.3847/1538-4357/aaf3b4

Event Horizon Telescope Collaboration, Akiyama, K., Alberdi, A., et al. 2019, ApJ, 875, L1, doi: 10.3847/2041-8213/ab0ec7

Event Horizon Telescope Collaboration, Akiyama, K., Alberdi, A., et al. 2022, ApJ, 930, L12, doi: 10.3847/2041-8213/ac6674

Fausnaugh, M. M., Denney, K. D., Barth, A. J., et al. 2016, ApJ, 821, 56, doi: 10.3847/0004-637X/821/1/56

Fausnaugh, M. M., Starkey, D. A., Horne, K., et al. 2018, ApJ, 854, 107, doi: 10.3847/1538-4357/aaaa2b

Fei, Q., Wang, R., Molina, J., et al. 2023, ApJ, 946, 45, doi: 10.3847/1538-4357/acbb05

Feltre, A., Hatziminaoglou, E., Fritz, J., & Franceschini, A. 2012, MNRAS, 426, 120, doi: 10.1111/j.1365-2966.2012.21695.x

Ferland, G. J., & Osterbrock, D. E. 1986, ApJ, 300, 658, doi: 10.1086/163841

Ferland, G. J., Peterson, B. M., Horne, K., Welsh, W. F., & Nahar, S. N. 1992, ApJ, 387, 95, doi: 10.1086/171063

Fischer, T. C., Crenshaw, D. M., Kraemer, S. B., & Schmitt, H. R. 2013, ApJS, 209, 1, doi: 10.1088/0067-0049/209/1/1

Fitzpatrick, E. L. 1999, PASP, 111, 63, doi: 10.1086/316293

Fritz, J., Franceschini, A., & Hatziminaoglou, E. 2006, MNRAS, 366, 767, doi: 10.1111/j.1365-2966.2006.09866.x

Fuller, L., Lopez-Rodriguez, E., Packham, C., et al. 2019, MNRAS, 483, 3404, doi: 10.1093/mnras/sty3338

Fuller, L., Lopez-Rodriguez, E., García-Bernete, I., et al. 2025, ApJS, 276, 64, doi: 10.3847/1538-4365/ad9907

Gámez Rosas, V., Isbell, J. W., Jaffe, W., et al. 2022, Nature, 602, 403, doi: 10.1038/s41586-021-04311-7

García-Bernete, I., Ramos Almeida, C., Landt, H., et al. 2017, MNRAS, 469, 110, doi: 10.1093/mnras/stx795

García-Bernete, I., Ramos Almeida, C., Alonso-Herrero, A., et al. 2019, MNRAS, 486, 4917, doi: 10.1093/mnras/stz1003

García-Burillo, S., Alonso-Herrero, A., Ramos Almeida, C., et al. 2021, A&A, 652, A98, doi: 10.1051/0004-6361/202141075

García-González, J., Alonso-Herrero, A., Hönig, S. F., et al. 2017, MNRAS, 470, 2578, doi: 10.1093/mnras/stx1361

Gardner, E., & Done, C. 2017, MNRAS, 470, 3591, doi: 10.1093/mnras/stx946

Gaskell, C. M., Goosmann, R. W., Antonucci, R. R. J., & Whysong, D. H. 2004, ApJ, 616, 147, doi: 10.1086/423885

Gaskell, M., Thakur, N., Tian, B., & Saravanan, A. 2022, Astronomische Nachrichten, 343, e210112, doi: 10.1002/asna.20210112

Gehrels, N., Chincarini, G., Giommi, P., et al. 2004, ApJ, 611, 1005, doi: 10.1086/422091

Gierliński, M., & Done, C. 2004, MNRAS, 349, L7, doi: 10.1111/j.1365-2966.2004.07687.x

Gitton, P. B., Leveque, S. A., Avila, G., & Phan Duc, T. 2004, in Society of Photo-Optical Instrumentation Engineers (SPIE) Conference Series, Vol. 5491, New Frontiers in Stellar Interferometry, ed. W. A. Traub, 944, doi: 10.1117/12.551377

Gliozzi, M., & Williams, J. K. 2020, MNRAS, 491, 532, doi: 10.1093/mnras/stz3005

Goad, M. R., Korista, K. T., & Ruff, A. J. 2012, MNRAS, 426, 3086, doi: 10.1111/j.1365-2966.2012.21808.x

González-Martín, O., Masegosa, J., García-Bernete, I., et al. 2019a, ApJ, 884, 10, doi: 10.3847/1538-4357/ab3e6b

González-Martín, O., Masegosa, J., García-Bernete, I., et al. 2019b, ApJ, 884, 11, doi: 10.3847/1538-4357/ab3e4f

González-Martín, O., Ramos Almeida, C., Fritz, J., et al. 2023, A&A, 676, A73, doi: 10.1051/0004-6361/202345858

González-Martín, O., Díaz-González, D. J., Martínez-Paredes, M., et al. 2025, MNRAS, doi: 10.1093/mnras/staf573

Gordon, K. D., Clayton, G. C., Misselt, K. A., Landolt, A. U., & Wolff, M. J. 2003, ApJ, 594, 279, doi: 10.1086/376774

Goulding, A. D., Alexander, D. M., Bauer, F. E., et al. 2012, ApJ, 755, 5, doi: 10.1088/0004-637X/755/1/5

GRAVITY Collaboration, Abuter, R., Accardo, M., et al. 2017, A&A, 602, A94, doi: 10.1051/0004-6361/201730838

GRAVITY Collaboration, Sturm, E., Dexter, J., et al. 2018, Nature, 563, 657, doi: 10.1038/s41586-018-0731-9

GRAVITY Collaboration, Amorim, A., Bauböck, M., et al. 2020a, A&A, 643, A154, doi: 10.1051/0004-6361/202039067

GRAVITY Collaboration, Dexter, J., Shangguan, J., et al. 2020b, A&A, 635, A92, doi: 10.1051/0004-6361/201936767

GRAVITY Collaboration, Pfuhl, O., Davies, R., et al. 2020c, A&A, 634, A1, doi: 10.1051/0004-6361/201936255

GRAVITY Collaboration, Amorim, A., Bauböck, M., et al. 2021a, A&A, 648, A117, doi: 10.1051/0004-6361/202040061

GRAVITY Collaboration, Amorim, A., Bauböck, M., et al. 2021b, A&A, 654, A85, doi: 10.1051/0004-6361/202141426

GRAVITY Collaboration, Perraut, K., Labadie, L., et al. 2021c, A&A, 655, A73, doi: 10.1051/0004-6361/202141624

GRAVITY Collaboration, Abuter, R., Aimar, N., et al. 2022, A&A, 657, L12, doi: 10.1051/0004-6361/202142465

GRAVITY+ Collaboration, Abuter, R., Alarcon, P., et al. 2022, The Messenger, 189, 17, doi: 10.18727/0722-6691/5285

GRAVITY Collaboration, Amorim, A., Bourdarot, G., et al. 2023, A&A, 669, A14, doi: 10.1051/0004-6361/202244655

GRAVITY Collaboration, Amorim, A., Bourdarot, G., et al. 2024, A&A, 684, A167, doi: 10.1051/0004-6361/202348167

GRAVITY+ Collaboration, Abuter, R., Allouche, F., et al. 2024, The Messenger, 193, 37, doi: 10.18727/0722-6691/5376

GRAVITY Collaboration, Amorim, A., Bourdarot, G., et al. 2024, A&A, 690, A76, doi: 10.1051/0004-6361/202450746

Grier, C. J., Pancoast, A., Barth, A. J., et al. 2017, ApJ, 849, 146, doi: 10.3847/1538-4357/aa901b

Grier, C. J., Peterson, B. M., Horne, K., et al. 2013, ApJ, 764, 47, doi: 10.1088/0004-637X/764/1/47

Guise, E., Hönig, S. F., Gorjian, V., et al. 2022, MNRAS, 516, 4898, doi: 10.1093/mnras/stac2529

Hagen, S., Done, C., & Edelson, R. 2024a, MNRAS, 530, 4850, doi: 10.1093/mnras/stae1177

Hagen, S., Done, C., Silverman, J. D., et al. 2024b, MNRAS, 534, 2803, doi: 10.1093/mnras/stae2272

Haidar, H., Rosario, D. J., Alonso-Herrero, A., et al. 2024, MNRAS, 532, 4645, doi: 10.1093/mnras/stae1596

Hao, C. N., Xia, X. Y., Mao, S., Wu, H., & Deng, Z. G. 2005, ApJ, 625, 78, doi: 10.1086/429716

Hatziminaoglou, E., Hernán-Caballero, A., Feltre, A., & Piñol Ferrer, N. 2015, ApJ, 803, 110. https://arxiv.org/abs/1502.05823

Henden, A. A., Levine, S., Terrell, D., et al. 2018, in American Astronomical Society Meeting Abstracts, Vol. 232, American Astronomical Society Meeting Abstracts #232, 223.06

Hernández Santisteban, J. V., Edelson, R., Horne, K., et al. 2020, MNRAS, 498, 5399, doi: 10.1093/mnras/staa2365

Hickox, R. C., & Alexander, D. M. 2018, ARA&A, 56, 625, doi: 10.1146/annurev-astro-081817-051803

Hönig, S. F. 2019, ApJ, 884, 171, doi: 10.3847/1538-4357/ab4591

Hönig, S. F., & Kishimoto, M. 2010, A&A, 523, A27, doi: 10.1051/0004-6361/200912676

Hönig, S. F., & Kishimoto, M. 2011, A&A, 534, A121, doi: 10.1051/0004-6361/201117750

Hönig, S. F., & Kishimoto, M. 2017, ApJ, 838, L20, doi: 10.3847/2041-8213/aa6838

Hönig, S. F., Kishimoto, M., Antonucci, R., et al. 2012, ApJ, 755, 149, doi: 10.1088/0004-637X/755/2/149

Hönig, S. F., Kishimoto, M., Gandhi, P., et al. 2010, A&A, 515, A23, doi: 10.1051/0004-6361/200913742

Hönig, S. F., Leipski, C., Antonucci, R., & Haas, M. 2011, ApJ, 736, 26, doi: 10.1088/0004-637X/736/1/26

Hönig, S. F., Kishimoto, M., Tristram, K. R. W., et al. 2013, ApJ, 771, 87, doi: 10.1088/0004-637X/771/2/87

Horne, K., De Rosa, G., Peterson, B. M., et al. 2021, ApJ, 907, 76, doi: 10.3847/1538-4357/abce60

Hu, C., Du, P., Lu, K.-X., et al. 2015, ApJ, 804, 138, doi: 10.1088/0004-637X/804/2/138

Huang, Y.-K., Hu, C., Zhao, Y.-L., et al. 2019, ApJ, 876, 102, doi: 10.3847/1538-4357/ab16ef

Isbell, J. W., Meisenheimer, K., Pott, J. U., et al. 2022, A&A, 663, A35, doi: 10.1051/0004-6361/202243271

Isbell, J. W., Pott, J. U., Meisenheimer, K., et al. 2023, A&A, 678, A136, doi: 10.1051/0004-6361/202347307

Isbell, J. W., Ertel, S., Pott, J. U., et al. 2025, Nature Astronomy, 9, 417, doi: 10.1038/s41550-024-02461-y

Israel, W. 1967, Physical Review, 164, 1776, doi: 10.1103/PhysRev.164.1776

Israel, W. 1968, Communications in Mathematical Physics, 8, 245, doi: 10.1007/BF01645859

Ivezić, Ž., Kahn, S. M., Tyson, J. A., et al. 2019, ApJ, 873, 111, doi: 10.3847/1538-4357/ab042c

Jaffe, W., Meisenheimer, K., Röttgering, H. J. A., et al. 2004, Nature, 429, 47, doi: 10.1038/nature02531

Jansen, F., Lumb, D., Altieri, B., et al. 2001, A&A, 365, L1, doi: 10.1051/0004-6361:20000036

Jensen, J. J., Hönig, S. F., Rakshit, S., et al. 2017, MNRAS, 470, 3071, doi: 10.1093/mnras/stx1447

Jin, C., Ward, M., Done, C., & Gelbord, J. 2012, MNRAS, 420, 1825, doi: 10.1111/j.1365-2966.2011.19805.x

Juráňová, A., Costantini, E., Kriss, G. A., et al. 2024, A&A, 686, A99, doi: 10.1051/0004-6361/202449544

Kakkad, D., Stalevski, M., Kishimoto, M., et al. 2023, MNRAS, 519, 5324, doi: 10.1093/mnras/stac3827

Kammoun, E. S., Dovčiak, M., Papadakis, I. E., Caballero-García, M. D., & Karas, V. 2021, ApJ, 907, 20, doi: 10.3847/1538-4357/abcb93

Kara, E., Barth, A. J., Cackett, E. M., et al. 2023, ApJ, 947, 62, doi: 10.3847/1538-4357/acbcd3

Kaspi, S., Smith, P. S., Netzer, H., et al. 2000, ApJ, 533, 631, doi: 10.1086/308704

Kellermann, K. I., Sramek, R., Schmidt, M., Shaffer, D. B., & Green, R. 1989, AJ, 98, 1195, doi: 10.1086/115207

Kim, D., Im, M., Kim, J. H., et al. 2015, ApJS, 216, 17, doi: 10.1088/0067-0049/216/1/17

Kishimoto, M., Hönig, S. F., Antonucci, R., et al. 2011a, A&A, 527, A121, doi: 10.1051/0004-6361/201016054

Kishimoto, M., Hönig, S. F., Antonucci, R., et al. 2009a, A&A, 507, L57, doi: 10.1051/0004-6361/200913512

Kishimoto, M., Hönig, S. F., Antonucci, R., et al. 2011b, A&A, 536, A78, doi: 10.1051/0004-6361/201117367

Kishimoto, M., Hönig, S. F., Beckert, T., & Weigelt, G. 2007, A&A, 476, 713, doi: 10.1051/0004-6361:20077911

Kishimoto, M., Hönig, S. F., Tristram, K. R. W., & Weigelt, G. 2009b, A&A, 493, L57, doi: 10.1051/0004-6361:200811062

Kishimoto, M., Anderson, M., ten Brummelaar, T., et al. 2022, ApJ, 940, 28, doi: 10.3847/1538-4357/ac91c4

Korista, K. T., & Goad, M. R. 2001, ApJ, 553, 695, doi: 10.1086/320964

Korista, K. T., & Goad, M. R. 2019, MNRAS, 489, 5284, doi: 10.1093/mnras/stz2330

Koshida, S., Minezaki, T., Yoshii, Y., et al. 2014, ApJ, 788, 159, doi: 10.1088/0004-637X/788/2/159

Koski, A. T. 1978, ApJ, 223, 56, doi: 10.1086/156235

Krolik, J. H. 2007, ApJ, 661, 52, doi: 10.1086/515432

Krolik, J. H., & Begelman, M. C. 1988, ApJ, 329, 702, doi: 10.1086/166414

Kubota, A., & Done, C. 2018, MNRAS, 480, 1247, doi: 10.1093/mnras/sty1890

Kubota, A., & Done, C. 2019, MNRAS, 489, 524, doi: 10.1093/mnras/stz2140

Kudoh, Y., Wada, K., Kawakatu, N., & Nomura, M. 2023, ApJ, 950, 72, doi: 10.3847/1538-4357/accc2b

Kudoh, Y., Wada, K., Kawakatu, N., & Nomura, M. 2024, ApJ, 977, 48, doi: 10.3847/1538-4357/ad8b42

Landt, H. 2023, Frontiers in Astronomy and Space Sciences, 10, 1256088, doi: 10.3389/fspas.2023.1256088

Laor, A., Jannuzi, B. T., Green, R. F., & Boroson, T. A. 1997, ApJ, 489, 656, doi: 10.1086/304816

Lawson, P. R., ed. 2000, Principles of Long Baseline Stellar Interferometry

Lawther, D., Goad, M. R., Korista, K. T., Ulrich, O., & Vestergaard, M. 2018, MNRAS, 481, 533, doi: 10.1093/mnras/sty2242

Le Bouquin, J. B., Berger, J. P., Lazareff, B., et al. 2011, A&A, 535, A67, doi: 10.1051/0004-6361/201117586

Leftley, J. H., Hönig, S. F., Asmus, D., et al. 2019, ApJ, 886, 55, doi: 10.3847/1538-4357/ab4a0b

Leftley, J. H., Tristram, K. R. W., Hönig, S. F., et al. 2021, ApJ, 912, 96, doi: 10.3847/1538-4357/abee80

Leftley, J. H., Tristram, K. R. W., Hönig, S. F., et al. 2018, ApJ, 862, 17, doi: 10.3847/1538-4357/aac8e5

Leftley, J. H., Petrov, R., Moszczynski, N., et al. 2024, A&A, 686, A204, doi: 10.1051/0004-6361/202348977

Leinert, C., Graser, U., Przygodda, F., et al. 2003, Ap&SS, 286, 73, doi: 10.1023/A:1026158127732

Lewin, C., Kara, E., Cackett, E. M., et al. 2023, ApJ, 954, 33, doi: 10.3847/1538-4357/ace77b

Lewin, C., Kara, E., Barth, A. J., et al. 2024, ApJ, 974, 271, doi: 10.3847/1538-4357/ad6b08

Lira, P., Videla, L., Wu, Y., et al. 2013, ApJ, 764, 159, doi: 10.1088/0004-637X/764/2/159

Lobban, A., & King, A. 2022, MNRAS, 511, 1992, doi: 10.1093/mnras/stac155

Lopez, B., Lagarde, S., Petrov, R. G., et al. 2022, A&A, 659, A192, doi: 10.1051/0004-6361/202141785

López-Gonzaga, N., Burtscher, L., Tristram, K. R. W., Meisenheimer, K., & Schartmann, M. 2016, A&A, 591, A47, doi: 10.1051/0004-6361/201527590

Lynden-Bell, D. 1969, Nature, 223, 690, doi: 10.1038/223690a0

Lyu, J., Rieke, G. H., & Smith, P. S. 2019, ApJ, 886, 33, doi: 10.3847/1538-4357/ab481d

Mandal, A. K., Woo, J.-H., Wang, S., et al. 2024, ApJ, 968, 59, doi: 10.3847/1538-4357/ad414d

Martínez-Ramírez, L. N., Calistro Rivera, G., Lusso, E., et al. 2024, A&A, 688, A46, doi: 10.1051/0004-6361/202449329

Mason, K. O., Breeveld, A., Much, R., et al. 2001, A&A, 365, L36, doi: 10.1051/0004-6361:20000044

McCully, C., Crawford, S., Kovacs, G., et al. 2018, astropy/astroscrappy: v1.0.5 Zenodo Release, v1.0.5, Zenodo, doi: 10.5281/zenodo.1482019

McLure, R. J., & Jarvis, M. J. 2002, MNRAS, 337, 109, doi: 10.1046/j.1365-8711.2002.05871.x

Menu, J., van Boekel, R., Henning, T., et al. 2015, A&A, 581, A107, doi: 10.1051/0004-6361/201525654

Miller, J. A., Cackett, E. M., Goad, M. R., et al. 2023, ApJ, 953, 137, doi: 10.3847/1538-4357/ace342

Minezaki, T., Yoshii, Y., Kobayashi, Y., et al. 2019, ApJ, 886, 150, doi: 10.3847/1538-4357/ab4f7b

Mizukoshi, S., Minezaki, T., Sameshima, H., et al. 2024, MNRAS, 532, 666, doi: 10.1093/mnras/stae1482

Mor, R., Netzer, H., & Elitzur, M. 2009, ApJ, 705, 298, doi: 10.1088/0004-637X/705/1/298

Morgan, C. W., Kochanek, C. S., Morgan, N. D., & Falco, E. E. 2010, ApJ, 712, 1129, doi: 10.1088/0004-637X/712/2/1129

Moshir, M., Kopan, G., Conrow, T., et al. 1990, IRAS Faint Source Catalogue, 0

Mundell, C. G., Wrobel, J. M., Pedlar, A., & Gallimore, J. F. 2003, ApJ, 583, 192, doi: 10.1086/345356

Narayan, R., & Yi, I. 1994, ApJ, 428, L13, doi: 10.1086/187381

Narayan, R., & Yi, I. 1995, ApJ, 452, 710, doi: 10.1086/176343

Nenkova, M., Sirocky, M. M., Ivezić, Ž., & Elitzur, M. 2008a, ApJ, 685, 147, doi: 10.1086/590482

Nenkova, M., Sirocky, M. M., Nikutta, R., Ivezić, Ž., & Elitzur, M. 2008b, ApJ, 685, 160, doi: 10.1086/590483

Nesvadba, N. P. H., Boulanger, F., Salomé, P., et al. 2010, A&A, 521, A65, doi: 10.1051/0004-6361/200913333

Netzer, H. 1987, MNRAS, 225, 55

Netzer, H. 1990, in Active Galactic Nuclei, ed. R. D. Blandford, H. Netzer, L. Woltjer, T. J. L. Courvoisier, & M. Mayor, 57–160

Netzer, H. 2015, ARA&A, 53, 365, doi: 10.1146/annurev-astro-082214-122302

Netzer, H. 2022, MNRAS, 509, 2637, doi: 10.1093/mnras/stab3133

Novikov, I. D., & Thorne, K. S. 1973, in Black Holes (Les Astres Occlus), ed. C. Dewitt & B. S. Dewitt, 343–450

Ogle, P., Boulanger, F., Guillard, P., et al. 2010, ApJ, 724, 1193, doi: 10.1088/0004-637X/724/2/1193

Ohsuga, K., Mineshige, S., Mori, M., & Umemura, M. 2002, ApJ, 574, 315, doi: 10.1086/340798

Ossenkopf, V., Henning, T., & Mathis, J. S. 1992, A&A, 261, 567

Padovani, P., & Urry, C. M. 1992, ApJ, 387, 449, doi: 10.1086/171098

Pahari, M., McHardy, I. M., Vincentelli, F., et al. 2020, MNRAS, 494, 4057, doi: 10.1093/mnras/staa1055

Panagiotou, C., Papadakis, I., Kara, E., et al. 2025, ApJ, 983, 132, doi: 10.3847/1538-4357/adbf95

Partington, E. R., Cackett, E. M., Kara, E., et al. 2023, ApJ, 947, 2, doi: 10.3847/1538-4357/acbf44

Peeters, E., Spoon, H. W. W., & Tielens, A. G. G. M. 2004, ApJ, 613, 986, doi: 10.1086/423237

Peterson, B. M., Ferrarese, L., Gilbert, K. M., et al. 2004, ApJ, 613, 682, doi: 10.1086/423269

Peterson, B. M., Denney, K. D., De Rosa, G., et al. 2013, ApJ, 779, 109, doi: 10.1088/0004-637X/779/2/109

Petrucci, P. O., Ursini, F., De Rosa, A., et al. 2018, A&A, 611, A59, doi: 10.1051/0004-6361/201731580

Petrucci, P. O., Paltani, S., Malzac, J., et al. 2013, A&A, 549, A73, doi: 10.1051/0004-6361/201219956

Pier, E. A., & Krolik, J. H. 1992a, ApJ, 399, L23, doi: 10.1086/186597

Pier, E. A., & Krolik, J. H. 1992b, ApJ, 401, 99, doi: 10.1086/172042

Pier, E. A., & Krolik, J. H. 1993, ApJ, 418, 673, doi: 10.1086/173427

Pogge, R. W. 1988, ApJ, 328, 519, doi: 10.1086/166309

Porquet, D., Reeves, J. N., O'Brien, P., & Brinkmann, W. 2004, A&A, 422, 85, doi: 10.1051/0004-6361:20047108

Pott, J.-U., Malkan, M. A., Elitzur, M., et al. 2010, ApJ, 715, 736, doi: 10.1088/0004-637X/715/2/736

Pozo Nuñez, F., Haas, M., Chini, R., et al. 2014, A&A, 561, L8, doi: 10.1051/0004-6361/201323178

Ramolla, M., Haas, M., Westhues, C., et al. 2018, A&A, 620, A137, doi: 10.1051/0004-6361/201732081

Ramos Almeida, C., Alonso-Herrero, A., Levenson, N. A., et al. 2014, MNRAS, 439, 3847, doi: 10.1093/mnras/stu235

Ramos Almeida, C., Levenson, N. A., Rodríguez Espinosa, J. M., et al. 2009, ApJ, 702, 1127, doi: 10.1088/0004-637X/702/2/1127

Ramos Almeida, C., Levenson, N. A., Alonso-Herrero, A., et al. 2011, ApJ, 731, 92, doi: 10.1086/165571

Ramos Almeida, C., Garcia-Bernete, I., Pereira-Santaella, M., et al. 2025, arXiv e-prints, arXiv:2504.01595, doi: 10.48550/arXiv.2504.01595

Rees, M. J., Silk, J. I., Werner, M. W., & Wickramasinghe, N. C. 1969, Nature, 223, 788, doi: 10.1038/223788a0

Reyes-Amador, O. U., Fritz, J., González-Martín, O., et al. 2024, MNRAS, 531, 1841, doi: 10.1093/mnras/stae1281

Reynolds, C. S. 2021, ARA&A, 59, 117, doi: 10.1146/annurev-astro-112420-035022

Ricci, C., Trakhtenbrot, B., Koss, M. J., et al. 2017a, ApJS, 233, 17, doi: 10.3847/1538-4365/aa96ad

Ricci, C., Trakhtenbrot, B., Koss, M. J., et al. 2017b, Nature, 549, 488, doi: 10.1038/nature23906

Ricci, C., Ichikawa, K., Stalevski, M., et al. 2023, ApJ, 959, 27, doi: 10.3847/1538-4357/ad0733

Rogantini, D., Costantini, E., Gallo, L. C., et al. 2022, MNRAS, 516, 5171, doi: 10.1093/mnras/stac2552

Rokaki, E., & Boisson, C. 1999, MNRAS, 307, 41, doi: 10.1046/j.1365-8711.1999.02565.x

Roming, P. W. A., Kennedy, T. E., Mason, K. O., et al. 2005, Space Sci. Rev., 120, 95, doi: 10.1007/s11214-005-5095-4

Rudy, R. J., Mazuk, S., Puetter, R. C., & Hamann, F. 2000, ApJ, 539, 166, doi: 10.1086/309222

Salpeter, E. E. 1964, ApJ, 140, 796, doi: 10.1086/147973

Sanders, D. B., Phinney, E. S., Neugebauer, G., Soifer, B. T., & Matthews, K. 1989, ApJ, 347, 29, doi: 10.1086/168094

Schartmann, M., Meisenheimer, K., Camenzind, M., et al. 2008, A&A, 482, 67, doi: 10.1051/0004-6361:20078907

Schinnerer, E., Eckart, A., & Tacconi, L. J. 1998, ApJ, 500, 147, doi: 10.1086/305714

Schlafly, E. F., & Finkbeiner, D. P. 2011, ApJ, 737, 103, doi: 10.1088/0004-637X/737/2/103

Schmitt, H. R., Donley, J. L., Antonucci, R. R. J., Hutchings, J. B., & Kinney, A. L. 2003, ApJS, 148, 327, doi: 10.1086/381224

Shakura, N. I., & Sunyaev, R. A. 1973, A&A, 24, 337

Shangguan, J., Ho, L. C., & Xie, Y. 2018, ApJ, 854, 158, doi: 10.3847/1538-4357/aaa9be

Shi, Y., Rieke, G. H., Ogle, P. M., Su, K. Y. L., & Balog, Z. 2014, ApJS, 214, 23, doi: 10.1088/0067-0049/214/2/23

Shimizu, T. T., Mushotzky, R. F., Meléndez, M., et al. 2017, MNRAS, 466, 3161, doi: 10.1093/mnras/stw3268

Siebenmorgen, R., Heymann, F., & Efstathiou, A. 2015, A&A, 583, A120, doi: 10.1051/0004-6361/201526034

Silva, C. V., Costantini, E., Giustini, M., et al. 2018, MNRAS, 480, 2334, doi: 10.1093/mnras/sty1938

Sobrino Figaredo, C., Haas, M., Ramolla, M., et al. 2020, AJ, 159, 259, doi: 10.3847/1538-3881/ab89b1

Stalevski, M., Fritz, J., Baes, M., Nakos, T., & Popović, L. Č. 2012, MNRAS, 420, 2756, doi: 10.1111/j.1365-2966.2011.19775.x

Stalevski, M., Ricci, C., Ueda, Y., et al. 2016, MNRAS, 458, 2288, doi: 10.1093/mnras/stw444

Stalevski, M., Tristram, K. R. W., & Asmus, D. 2019, MNRAS, 484, 3334, doi: 10.1093/mnras/stz220

Starkey, D. A., Horne, K., & Villforth, C. 2016, MNRAS, 456, 1960, doi: 10.1093/mnras/stv2744

Starkey, D. A., Huang, J., Horne, K., & Lin, D. N. C. 2023, MNRAS, 519, 2754, doi: 10.1093/mnras/stac3579

Suganuma, M., Yoshii, Y., Kobayashi, Y., et al. 2006, ApJ, 639, 46, doi: 10.1086/499326

Sun, M., Grier, C. J., & Peterson, B. M. 2018, PyCCF: Python Cross Correlation Function for reverberation mapping studies, Astrophysics Source Code Library, record ascl:1805.032

Swain, M., Vasisht, G., Akeson, R., et al. 2003, ApJ, 596, L163, doi: 10.1086/379235

Tadhunter, C., & Tsvetanov, Z. 1989, Nature, 341, 422, doi: 10.1038/341422a0

Temple, M. J., Matthews, J. H., Hewett, P. C., et al. 2023, MNRAS, 523, 646, doi: 10.1093/mnras/stad1448

Thorne, J. P., Landt, H., Huang, J., et al. 2025, MNRAS, 537, 3746. https://arxiv.org/abs/2502.08366

Trakhtenbrot, B., Ricci, C., Koss, M. J., et al. 2017, MNRAS, 470, 800, doi: 10.1093/mnras/stx1117

Tristram, K. R. W. 2007, PhD thesis, Max-Planck-Institute for Astronomy, Heidelberg

Tristram, K. R. W., Burtscher, L., Jaffe, W., et al. 2014, A&A, 563, A82, doi: 10.1051/0004-6361/201322698

Tristram, K. R. W., Impellizzeri, C. M. V., Zhang, Z.-Y., et al. 2022, A&A, 664, A142, doi: 10.1051/0004-6361/202243535

Urry, C. M., & Padovani, P. 1995, PASP, 107, 803, doi: 10.1086/133630

Uttley, P., Cackett, E. M., Fabian, A. C., Kara, E., & Wilkins, D. R. 2014, AA&ARv, 22, 72, doi: 10.1007/s00159-014-0072-0

Varga, J., Waters, L. B. F. M., Hogerheijde, M., et al. 2024, A&A, 681, A47, doi: 10.1051/0004-6361/202347535

Veilleux, S., Shopbell, P. L., Rupke, D. S., Bland-Hawthorn, J., & Cecil, G. 2003, AJ, 126, 2185, doi: 10.1086/379000

Venanzi, M., Hönig, S., & Williamson, D. 2020, ApJ, 900, 174, doi: 10.3847/1538-4357/aba89f

Véron-Cetty, M. P., Joly, M., & Véron, P. 2004, A&A, 417, 515, doi: 10.1051/0004-6361:20035714

Vestergaard, M., & Wilkes, B. J. 2001, ApJS, 134, 1, doi: 10.1086/320357

Vieliute, R., Hernández Santisteban, J. V., Horne, K., & Cornfield, H. 2025, RAS Techniques and Instruments, 4, rzaf021, doi: 10.1093/rasti/rzaf021

Vincentelli, F. M., McHardy, I., Cackett, E. M., et al. 2021, MNRAS, 504, 4337, doi: 10.1093/mnras/stab1033

Wada, K. 2012, ApJ, 758, 66, doi: 10.1088/0004-637X/758/1/66

Wada, K. 2015, ApJ, 812, 82, doi: 10.1088/0004-637X/812/1/82

Wada, K., Schartmann, M., & Meijerink, R. 2016, ApJ, 828, L19, doi: 10.3847/2041-8205/828/2/L19

Wang, J.-M., Szuszkiewicz, E., Lu, F.-J., & Zhou, Y.-Y. 1999, ApJ, 522, 839, doi: 10.1086/307686

Wang, J.-M., & Zhou, Y.-Y. 1999, ApJ, 516, 420, doi: 10.1086/307080

Weigelt, G., Hofmann, K. H., Kishimoto, M., et al. 2012, A&A, 541, L9, doi: 10.1051/0004-6361/201219213

Welsh, W. F. 1999, PASP, 111, 1347, doi: 10.1086/316457

Wilkins, D. R., Gallo, L. C., Costantini, E., Brandt, W. N., & Blandford, R. D. 2021, Nature, 595, 657, doi: 10.1038/s41586-021-03667-0

Wilkins, D. R., Reynolds, C. S., & Fabian, A. C. 2020, MNRAS, 493, 5532, doi: 10.1093/mnras/staa628

Williamson, D., Hönig, S., & Venanzi, M. 2019, ApJ, 876, 137, doi: 10.3847/1538-4357/ab17d5

Williamson, D., Hönig, S., & Venanzi, M. 2020, ApJ, 897, 26, doi: 10.3847/1538-4357/ab989e

Wilson, A. S., Shopbell, P. L., Simpson, C., et al. 2000, AJ, 120, 1325, doi: 10.1086/301532

Winkler, H. 1997, MNRAS, 292, 273, doi: 10.1093/mnras/292.2.273

Winkler, H., Glass, I. S., van Wyk, F., et al. 1992, MNRAS, 257, 659, doi: 10.1093/mnras/257.4.659

Winter, L. M., Mushotzky, R. F., Reynolds, C. S., & Tueller, J. 2009, ApJ, 690, 1322, doi: 10.1088/0004-637X/690/2/1322

Winter, L. M., Veilleux, S., McKernan, B., & Kallman, T. R. 2012, ApJ, 745, 107, doi: 10.1088/0004-637X/745/2/107

Woillez, J., Petrov, R., Abuter, R., et al. 2024, A&A, 688, A190, doi: 10.1051/0004-6361/202449702

Woo, J.-H., & Urry, C. M. 2002, ApJ, 579, 530, doi: 10.1086/342878

Wright, E. L., Eisenhardt, P. R. M., Mainzer, A. K., et al. 2010, AJ, 140, 1868, doi: 10.1088/0004-6256/140/6/1868

Yang, Q., Shen, Y., Liu, X., et al. 2020, ApJ, 900, 58, doi: 10.3847/1538-4357/aba59b

Yang, X., Yao, S., Gallo, L. C., et al. 2024, ApJ, 966, 151, doi: 10.3847/1538-4357/ad343c

Young, T. 1804, Philosophical Transactions of the Royal Society of London, 94, 1

Yu, Z., Kochanek, C. S., Peterson, B. M., et al. 2020, MNRAS, 491, 6045, doi: 10.1093/mnras/stz3464

Zhang, Z.-X., Du, P., Smith, P. S., et al. 2019, ApJ, 876, 49, doi: 10.3847/1538-4357/ab1099